PROGRAMA DE DOCTORADO EN CIENCIA Y TECNOLOGÍA

TESIS DOCTORAL

NANOPARTÍCULAS DE ÓXIDOS METÁLICOS: DE LA ÓPTICA A LA CATÁLISIS

PhD THESIS

METAL OXIDE NANOPARTICLES: FROM OPTICS TO CATALYSIS

AUTOR / AUTORA

ANDREA DIEGO RUCABADO

DIRECTOR / A / ES / AS

ROSA MARTÍN RODRÍGUEZ

ISRAEL CANO RICO

UNIVERSIDAD DE CANTABRIA

Escuela de Doctorado de la Universidad de Cantabria

Santander 2023

Universidad de Cantabria

Programa de Doctorado en Ciencia y Tecnología

TESIS DOCTORAL

Nanopartículas de óxidos metálicos: de la óptica a la catálisis

Ph.D Thesis

Metal oxide nanoparticles: from optics to catalysis

Andrea Diego Rucabado

Santander Noviembre 2023

Dª. Rosa Martín Rodríguez, Profesora Contratada Doctora del Dpto. de Química e Ingeniería de Procesos y Recursos de la Universidad de Cantabria, y D. Israel Cano Rico, Profesor Contratado Doctor del Dpto. de Química Inorgánica de la Universidad Complutense de Madrid

INFORMAN:

Que el trabajo que se presenta en esta memoria, titulado *Nanopartículas de óxidos metálicos: de la óptica a la catálisis*, ha sido realizado, bajo su dirección, por Dª. Andrea Diego Rucabado, y constituye su Tesis para optar al grado de Doctor por la Universidad de Cantabria.

Del mismo modo, emiten su conformidad para que esta sea depositada y se celebre, posteriormente, la correspondiente Lectura y Defensa.

Santander, Noviembre de 2023.

Fdo. Rosa Martín Rodríguez

Fdo. Israel Cano Rico

"I can never read all the books I want;
I can never be all the people I want and live all the lives I want.
I can never train myself in all the skills I want.
And why do I want?
I want to live and feel all the shades, tones and variations of mental and
physical experience possible in my life.
And I am horribly limited."

— Sylvia Plath

Agradecimientos

Quién iba a decirme que, después de este laaaargo periodo de escritura y reflexión, redactar esta parte me resultara tan complejo. Sin embargo, pasar por esta sección de puntillas sería tremendamente injusto con todos aquellos que han hecho posible llegar hasta aquí.

En primer lugar, y como no puede ser de otro modo, me gustaría agradecer a mis directores, Rosa e Isra, por el apoyo constante. Por estar todos estos años, siempre. Por aplacar las numerosas frustraciones y desilusiones, pero también por compartir los triunfos. Gracias por enseñar a esta incauta ingeniera lo mejor de los dos mundos. Sois unos directores increíbles, pero como personas... os salís. Qué suerte he tenido.

En segundo lugar, pero no menos importante, gracias a Rafa por contar conmigo en NCLas. Son innumerables las horas de fluorímetro y maratonianos project meetings que hemos compartido, pero si de alguien tenía que aprender Espectroscopía, no podía haber elegido mejor mentor. Eternamente agradecida por ser prácticamente un director más. El primer aguacate de mi cosecha (*if any, ever*) tiene nombre y apellido.

Thanks also to the European Community for the financial support to carry out this Thesis within the FET Open NCLas Project (Proposal: 829161) framework. This acknowledgement also holds for the international partners of the project at the AGH University in Poland, the University of Surrey in the UK, the Fraunhofer Institute for Ceramic Technologies and Systems (IKTS), the Leibniz Institute of Photonic Technology (IPHT) and LASOS in Germany.

Agradecer, también, a Vitrispan S.A. y, especialmente, a Eugenio por su colaboración y financiación en el proyecto de láminas de acero vitrificado basadas en nanopartículas de TiO_2 para aplicaciones fotocatalíticas.

Gracias a Imanol por contar con nosotros, surgiendo de ahí una fructífera colaboración y un capítulo más de esta Tesis. También, gracias a Jonathan Albo e Iván Merino del Departamento de Ingenierías Química y Biomolecular, por su buena disposición y numerosos experimentos tanto de fotoreducción de CO_2 como de MP-AES.

A todos aquellos que en innumerables ocasiones me han echado una mano con las diferentes técnicas de caracterización empleadas. Jesús González, Fidel Madrazo… ¡gracias! Mención especial merece Jose I. Espeso, por su siempre buena disposición y absoluta eficiencia con las medidas de XRD. Has conseguido que me reconcilie (un poco, pero poco, poco) con los rayos X.

Gracias a Alfredo Segura, de la Universidad de Valencia, por acogerme y formarme (en tiempo récord) en la técnica de PLD durante mi breve estancia aquel lejano y apocalíptico 2020.

A mis compañeros de CITIMAC. Corto pero intenso. Gracias por las comidas en las que las penas, compartidas, parecen menos penas. Por los martes temáticos. Por las conversaciones en las que juro y perjuro que no estaba, aunque todos digáis lo contrario (y probablemente estéis en lo cierto).

A Judith, por llegar y revolucionarlo todo. Por ser paño de lágrimas pero también la mejor cheerleader. Afortunada de poder llamarte amiga.

A mi familia y amigos/as, testigos de cuan larga experiencia. Gracias por compartir los éxitos y las frustraciones, aunque a día de hoy, cuatro años después, ninguno sepáis a ciencia cierta (nunca mejor dicho) qué narices hago.

Gracias a todos…y gracias a mí, que pa' eso lo he sudao' y llorao'.

Abstract

This Thesis aims to study the potential applications of metal oxide nanoparticles in the fields of optics and photocatalysis. For such a purpose, rare earth and transition metal ions have been selected as dopant species. Several synthesis procedures, namely combustion, molten salt, sol-gel Pechini, homogeneous precipitation and solvothermal methods, have been employed to optimize both the optical and photocatalytic properties of the obtained materials. Additionally, a wide variety of techniques have been applied to carry out an in-depth structural and optical characterization of the fabricated nanoparticles. In particular, X-ray diffraction, transmission electron microscopy, and microwave plasma-atomic emission, X-ray photoelectron and Raman spectroscopies have been used to study the structural features of the prepared samples. Likewise, absorption, excitation, luminescence and time-resolved spectroscopy experiments have been carried out to perform the optical characterization. The photoactivity of the synthesized catalysts has been evaluated through methylene blue degradation and CO_2 photoreduction tests.

The first part of this Thesis, devoted to optical materials, has been developed within the NanoCrystals in Fibre Lasers project. Firstly, the effect of the synthesis procedures on the optical performance of obtained the $Y_2O_3:Pr^{3+}$ nanoparticles has been thoroughly studied, demonstrating the crucial role of the fabrication conditions on their structural features, and thus on the resulting luminescent properties. Subsequently, the fabrication of nanoparticle-based optical composites for waveguide applications by means of pulsed laser deposition technique has been performed, proving the suitability of such an approach for the encapsulation and preservation of optically active nanomaterials.

The second part of this Thesis, focused on photocatalytic materials, has been developed within different collaborations. Firstly, a collaboration project with Vitrispan S.A. company has been carried out to develop transition-metal-doped TiO_2 nanoparticle-based enamel coatings on stainless-steel sheets for pollutant degradation purposes, showing the potential industrial application of such catalysts using visible solar irradiation. Secondly, along with the CITIMAC and the Chemical and Biomolecular Engineering Departments from the University of Cantabria, the catalytic performance of rare-earth-doped and transition metal/rare earth co-doped TiO_2 nanoparticles has been evaluated for the photoreduction of CO_2 to alcohols, proving the suitability of doping strategies for an increased light absorption and a boosted catalytic activity.

Resumen

Esta Tesis tiene por objeto estudiar las potenciales aplicaciones de nanopartículas de óxidos metálicos en los campos de la óptica y la fotocatálisis. Para ello, se han seleccionado iones de tierras raras y de metales de transición como dopantes. Con el fin de optimizar las propiedades ópticas y fotocatalíticas de los nanomateriales preparados, se han investigado diferentes métodos de síntesis, tales como combustión, sales fundidas, sol-gel Pechini, precipitación homogénea y solvotermal. Además, se ha empleado una gran variedad de técnicas para caracterizar estructural y ópticamente las nanopartículas fabricadas. Así, con el objeto de estudiar las características estructurales de las muestras preparadas, se han utilizado la difracción de rayos X, la microscopía electrónica de transmisión y diferentes técnicas espectroscópicas, como emisión atómica por plasma de microondas, fotoelectrónica de rayos X, y Raman. Del mismo modo, se han realizado experimentos de absorción, excitación, luminiscencia y espectroscopía resuelta en tiempo para llevar a cabo la caracterización óptica. Finalmente, se ha evaluado la fotoactividad de los catalizadores preparados mediante experimentos de degradación de azul de metileno y de fotoreducción de CO_2.

La primera parte de la Tesis, dedicada a materiales ópticos, se ha desarrollado en el marco del proyecto europeo NanoCrystals in Fibre Lasers. En primer lugar, se ha llevado a cabo un estudio exhaustivo del efecto de los diferentes métodos de síntesis empleados sobre las características ópticas de las nanopartículas de $Y_2O_3:Pr^{3+}$ obtenidas, poniendo de relieve el papel fundamental que ejercen las condiciones de síntesis sobre las cualidades y, por tanto, las propiedades luminiscentes del material preparado. Seguidamente, se han fabricado composites ópticamente activos basados en dichas nanopartículas mediante la técnica de deposición por láser pulsado para su uso potencial como

guía de ondas, manifestando así la idoneidad de este procedimiento para encapsular nanopartículas y preservar sus propiedades ópticas originales.

La segunda parte de la Tesis, enfocada en materiales fotocatalíticos, se ha elaborado a partir de diferentes proyectos de colaboración. En primer lugar, y a partir del interés mostrado por la empresa Vitrispan S.A, se han desarrollado recubrimientos de esmalte que contienen nanopartículas de TiO_2 dopadas con metales de transición sobre láminas de acero inoxidable. Dicho sistema se ha aplicado en la fotodegradación de contaminantes. Este trabajo pone de manifiesto la creciente atención existente hacia el uso industrial de tales materiales catalíticos empleando radiación solar visible como fuente de luz. Por otro lado, y en colaboración con el departamento CITIMAC y el departamento de Ingenierías Química y Biomolecular de la Universidad de Cantabria, se ha evaluado la actividad catalítica de nanopartículas de TiO_2 dopadas con elementos de tierras raras y co-dopadas con elementos de tierras raras y metales de transición en la fotoreducción de CO_2 a alcoholes, mostrando la eficacia de las estrategias de dopaje para incrementar la absorción de luz y la actividad de los catalizadores.

Table of contents

1 Introduction 1
References 5
2 Experimental techniques 9
2.1 Materials synthesis 10
2.2 Structural characterization techniques 19
2.3 Optical characterization techniques 22
2.4 Fabrication of optical composites 24
2.5 Fabrication of supported catalysts 26
2.6 Photocatalytic activity 28
References 31

Part I. Optical applications

3 Rare-earth doped metal oxide nanomaterials for optical applications 37
3.1 Introduction 37
3.2 Optical properties of doped insulating materials 39
3.3 Sesquioxides as host materials 45
3.4 Rare earth ions 46
References 51
4 Rare–earth doped yttria nanoparticles 55
4.1 State of the art 56
4.2 Synthesis of nanoparticles 57
4.3 Structural properties of nanoparticles 59
4.4 Effect of synthesis procedures on the structural properties of nanoparticles 64
4.5 Optical properties of nanoparticles 76

4.6 Effect of synthesis procedures on the optical properties of nanoparticles 80
4.7 Concluding remarks 89
References 90
5 Rare–earth doped composites 95
5.1 State of the art 96
5.2 Fabrication of optically active composites 98
5.3 Structural and optical properties of nanoparticles 99
5.4 Structural and optical properties of optically active composites 103
5.5 Concluding remarks 108
References 109

Part II. Photocatalytic applications

6 Doped metal oxide nanomaterials for photocatalytic applications 115
6.1 Introduction 115
6.2 Photocatalytic properties of semiconductors 117
6.3 Band gap engineering 121
References 125
7 Transition-metal doped titania nanoparticles for photocatalytic oxidation 129
7.1 State of the art 130
7.2 Fabrication of enamel coatings and photooxidation set-up 131
7.3 Characterization of nanoparticles and photocatalytic activity. 134
7.4 Characterization of enamel coatings and photocatalytic activity 154
7.5 Concluding remarks 160
References 161
8 Rare-earth and transition-metal doped titania nanoparticles for CO_2 photoreduction 167
8.1 State of the art 168
8.2 Fabrication of supported catalysts and photoreduction set-up 170
8.3 Structural and optical properties of nanoparticles 171
8.4 Photocatalytic activity of synthesized nanoparticles 179
8.5 Concluding remarks 187
References 189
9 Conclusions 195
Appendix A 199

Appendix B 201
Abbreviation list 207
List of publications 209
Grants and projects 211

1

Introduction

Nanomaterials have gained increasing popularity in the last decades due to their unique properties when compared with macroscopic (bulk) materials. Despite the apparent modern aspect of this research field, the use of nanomaterials has been reported to be present in ancient societies, dating back to *ca*. 7000 years ago [1]. Well-known examples of these old applications are the Lycurgus cup, the Damascus swords or the numerous rose windows of European medieval Cathedrals [2,3,4,5,6]. Nevertheless, it was not until the mid-20th century that miniaturization became widely acknowledged thanks to the development of semiconductor-based transistors, together with the famous lecture imparted by Prof. Richard Feynman entitled "There's plenty of room at the bottom" [7]. However, what makes nanomaterials so popular? The interest of such materials, whether natural, incidental or manufactured, does not only result from their size but from the effect of this on their features. Specifically, due to their restricted dimensions, nanomaterials show remarkable differences regarding their properties when compared with their bulk counterpart. Indeed, some structural, thermodynamic, electronic, spectroscopic, electromagnetic or chemical properties of materials may drastically change when the size is reduced to the nanoscale [8]. The main effects responsible for the properties change in a material when reducing the dimensionality are surface effects and quantum confinement [9]. The former is related to the large increase in the surface/volume ratio, which involves that a high fraction of atoms is located on the surface. These atoms present a different behavior than those from the bulk material due to the nature of the bonds they form. Specifically, atoms located in the core are highly coordinated, forming a higher number of bonds, and thus showing an increased stability. However, surface atoms are less coordinated and, as a result, they have more tendency to form new bonds with external molecules and they are more reactive. This feature holds great interest in the field of catalysis [9]. On the other hand, quantum size effects occur when the

size of nanomaterials is smaller than the exciton Bohr radius. This effect is particularly relevant in semiconductor nanoparticles (NPs), and its main manifestations are the band gap increase with decreasing particle size and the transition from energy bands to discrete energy levels. These quantum confinement effects give rise to new size-dependent optical and electronic properties of the material [1,8,10]. Interestingly, this year's Nobel prize in Chemistry has been awarded to M. G. Bawendi, L. E. Brus, and A. Yekimov for the discovery and development of quantum dots.

There are numerous procedures to prepare nanomaterials, which are usually classified in two basic approaches: top-down and bottom-up. The former refers to methods where bulk materials are "divided" into smaller fractions, *i.e.*, NPs, usually by means of physical techniques such as milling, ion sputtering or laser ablation [11,12,13]. Most of these do not allow a precise control of shape, size or homogeneity of the resulting nanomaterial [14]. Conversely, bottom-up methods consist in the use of atoms or molecules as building units to obtain nano-sized structures [15]. Some of the typically employed methods belonging to this category are wet chemical procedures such as sol-gel, homogeneous precipitation or solvothermal synthesis, which have proven to provide a better control of the structural parameters. In this approach, the possibility of modifying size, shape and homogeneity of the final material allows to tune both optical and electronic properties [16].

Due to these new characteristics, caused by size effects and fabrication approaches, new potential applications in a wide variety of research fields arise, from biomedicine [17] or catalysis [18] to optics [19]. Nevertheless, amid all the available materials at the nanoscale, metal oxide NPs have attracted a wide interest thanks to their particular features [20]. Specifically, these NPs present high chemical stability, keeping their original properties at high temperatures under diverse chemical environments, together with a noteworthy tolerance to mechanical stress and compatibility with organic compounds, providing a full range of plausible applications. Furthermore, their relatively high abundance, which directly impacts on the final cost of the material, makes metal oxide NPs an affordable option against other materials [14]. It is important to consider that these can be either insulating or semiconductor. According to this feature, their ultimate application may be very different, finding diverse potential uses as energy storage, drug delivery, optoelectronics, cosmetics, gas sensing, and development of anti-reflecting and self-cleaning surfaces, to name a few [11,16,21]. This is the particular case of Y_2O_3 and TiO_2 NPs, where the former

is an insulating compound which acts as host lattice and needs to incorporate optically active ions to be employed for optical applications, while TiO_2 is a wide-band-gap semiconductor material, commonly used for photocatalytic purposes.

This Thesis focuses on the synthesis and characterization of metal oxide NPs for different applications, specifically in the fields of optics and catalysis. An in-depth study of the effect of synthesis conditions on both the structural and optical properties has been carried out. In particular, Y_2O_3 and TiO_2 have been selected as metal oxides. Additionally, rare earth (RE) and transition metal (TM) doping ions have been used to assess their influence on both the optical and photocatalytic activity of the resulting materials. Specifically, the main aims of this Thesis are:

- To optimize the synthesis procedures of $Y_2O_3:Pr^{3+}$ NPs in order to achieve the best optical response of the material prior to fiber laser fabrication within the context of the NCLas European Project.
- To fabricate optical composites based on $Y_2O_3:Pr^{3+}$ NPs by means of pulsed laser deposition (PLD) technique for their potential application as waveguide material within the context of the NCLas European Project.
- To synthesize and incorporate pure and TM-doped TiO_2 NPs onto enamel coatings supported on stainless-steel sheets for their industrial application as catalyst in environmental organic pollutant degradation.
- To prepare pure, RE-doped and TM-RE-co-doped TiO_2 NPs for their use as catalysts in the CO_2 photoreduction to alcohols.

Firstly, considering the use of metal oxide NPs such as Y_2O_3 for optical applications, the introduction of RE and TM elements into metal oxide host matrixes has paved the way for the development of materials with increased power conversion efficiency in solar cells [22,23]. Additionally, potential uses as solid-state lasers, amplifiers, fluorescence lamps, and display and telecommunication devices have emerged thanks to the optical features due to RE-doping [24]. Specifically, characteristics such as high photostability, narrow emission lines, long fluorescence lifetimes, and easy functionalization make RE-doped metal oxide NPs very promising materials in the field of optics [25,26].

Secondly, when employing semiconductor metal oxide NPs for photocatalysis, such as TiO_2, an important limitation arises from their wide band gap. Indeed, only a small portion of the solar spectrum (*ca*. 5%) is taken advantage of since their absorption range is located in the ultraviolet (UV). As a result, the efficiency of the NPs can be severely handicapped, and thus their resulting applications [14]. To overcome this constraint, two possible strategies are available. Firstly, metal oxide NPs can be coupled with organic dyes [27,28] or metallic NPs presenting localized surface plasmon resonance [29,30]. The second approach involves the use of doping elements into the metal oxide host matrix, TM and RE being among the most common dopant elements. This strategy not only down-shifts NPs band gap, but also can introduce new energy levels within the original band gap to promote absorption in both the visible (Vis) and near infrared (NIR) regions, and ultimately induce new optical features [14]. As a result, TM- and RE-doped metal oxide NPs present a wide range of improved applications when compared with bare NPs. For instance, it is well known that the photocatalytic activity is enhanced after doping with RE ions such as Ce, Dy or Eu due to the promoted reduction of the band gap [10,31]. This redshift of the absorption range has also been described when using TM such as Cu, Mn, Ni or Co as doping elements [32,33,34].

The contents of this Thesis are organized in nine chapters as follows. Chapter 2 describes the experimental procedures for materials preparation and the characterization techniques that have been employed. After that, results are divided in two parts. Part I comprises Chapter 3, 4 and 5, and it is devoted to optical applications. Specifically, in Chapter 3, an introduction to rare earth doped metal oxide NPs for optical applications is presented. Chapter 4 focuses on the study of the effect of synthesis procedures on the structural and optical properties of Pr-doped Y_2O_3 NPs. Chapter 5 describes the preparation of composite films via PLD for Y_2O_3:Pr^{3+} NPs embedding and luminescence preservation. Part II includes Chapter 6, 7 and 8, and it is dedicated to photocatalytic applications. In Chapter 6, an introduction to RE- and TM-doped NPs with photocatalytic applications is reported. Chapter 7 is devoted to the use of pure, and Co and Mn-doped TiO_2 NPs in methylene blue dye photocatalytic degradation and to their incorporation in enamel coatings supported on stainless-steel sheets for ultimate industrial purposes. Chapter 8 describes the application of Ce-doped and Cu-Ce-co-doped TiO_2 NPs as catalysts for the photoreduction of CO_2 to alcohols. Finally, Chapter 9 presents the main conclusions achieved along the Thesis.

References

1 Vajtai, R. *Springer Handbook of nanomaterials*; Springer Berlin, 2013.

2 Freestone, I.; Meeks, N.; Sax, M.; Higgitt, C. The Lycurgus Cup – A Roman nanotechnology. *Gold Bulletin* **2007**, *40*, 270–277.

3 Reibold, M.; Paufler, P.; Levin, A. A.; Kochmann, W.; Pätzke, N.; Meyer, D. C. Carbon nanotubes in an ancient Damascus sabre. *Nature* **2006**, *444*, 286.

4 Hunault, M. O. J. Y.; Loisel, C.; Bauchau, F.; Lemasson, Q.; Pacheco, C.; Pichon, L.; Moignard, B.; Boulanger, K.; Hérold, M.; Calas, G.; Pallot-Frossard, I. Nondestructive redox quantification reveals glassmaking of rare french gothic stained glasses. *Anal. Chem*. **2017**, *89*, 6277–6284.

5 Pérez-Villar, S.; Rubio, J.; Oteo, J. L. Study of color and structural changes in silver painted medieval glasses. *J. Non-Cryst. Solids* **2008**, *354*, 1833–1844.

6 Capobianco, N.; Hunault, M. O. J. Y.; Balcon-Berry, S.; Galoisy, L.; Sandron, D.; Calas, G. The Grande Rose of the Reims Cathedral: an eight-century perspective on the colour management of medieval stained glass. *Sci. Rep*. **2019**, *9*, 3287.

7 Feynman, R. P. There's plenty of room at the bottom. *Eng. Sci*. **1960**, *23*, 22–36.

8 Rao, C. N. R.; Müller, A.; Cheetham, A. K. *The Chemistry of nanomaterials. Synthesis, properties and applications*. WILEY-VCH Verlag GmbH & Co, 2004.

9 Roduner, E. Size matters: why nanomaterials are different. *Chem. Soc. Rev*. **2006**, *35*, 583–592.

10 Mehtab, A.; Ahmed, J.; Alshehri, S. M.; Mao, Y.; Ahmad, T. Rare earth doped metal oxide nanoparticles for photocatalysis: a perspective. *Nanotechnology* **2022**, *33*, 142001.

11 Negrescu, A. M.; Killian, M. S.; Raghu, S. N. V.; Schmuki, P.; Mazare, A.; Cimpean, A. Metal oxide nanoparticles: review of synthesis, characterization and biological effects. *J. Funct. Biomater*. 2022, 13, 274.

12 Wender, H.; Migowski, P.; Feil, A. F.; Teixeira, S. R.; Dupont, J. Sputtering deposition of nanoparticles onto liquid substrates: recent advances and future trends. *Coord. Chem. Rev*. **2013**, *257*, 2468–2483.

13 Jamkhande, P. G.; Ghule, N. W.; Bamer, A. H.; Kalaskar, M. G. Metal nanoparticles synthesis: an overview on methods of preparation, advantages and disadvantages, and applications. *J. Drug Deliv. Sci. Technol*. **2019**, *53*, 101174.

14 Medhi, R.; Marquez, M. D.; Lee, T. R. Visible-light-active doped metal oxide nanoparticles: review of their synthesis, properties, and applications. *ACS Appl. Nano Mater*. **2020**, *3*, 6156–6185.

15 Vollath, D. *Nanomaterials. An introduction to synthesis, properties and applications*; John Wiley & Sons, 2013.

16 Nikam, A. V.; Prasad, B. L. V.; Kulkarni, A. A. Wet chemical synthesis of metal oxide nanoparticles: a review. *CrystEngComm* **2018**, *20*, 5091–5107.

17 Patra, J. K.; Das, G.; Fraceto, L. F.; Ramos Campos, E. V.; Rodriguez-Torres, M. del P.; Acosta-Torres, L. S.; Diaz-Torres, L. A.; Grillo, R.; Swamy, M. K.; Sharma, S.; Habtemariam, S.; Shin, H.-S. Nano based drug delivery systems: recent developments and future prospects. *J. Nanobiotechnol*. 2018, 16, 71.

18 Liu, L.; Corma, A. Metal catalysts for heterogeneous catalysis: from single atoms to nanoclusters and nanoparticles. *Chem. Rev*. **2018**, *118*, 4981–5079.

19 Pomerantseva, E.; Bonaccorso, F.; Feng, X.; Cui, Y.; Gogotsi, Y. Energy storage: the future enabled by nanomaterials. *Science* **2019**, *366*, eaan8285.

20 Chavali, M. S.; Nikolova, M. P. Metal oxide nanoparticles and their applications in nanotechnology. *SN Appl. Sci*. **2019**, *1*, 607.

21 Parashar, M.; Shukla, V. K.; Singh, R. Metal oxides nanoparticles via sol–gel method: a review on synthesis, characterization and applications. *J. Mater. Sci.: Mater. Electron*. **2020**, *31*, 3729–3749.

22 Kumar, V.; Pandey, A.; Swami, S. K.; Ntwaeaborwa, O. M.; Swart, H. C.; Dutta, V. Synthesis and characterization of Er^{3+}–Yb^{3+} doped ZnO upconversion nanoparticles for solar cell application. *J. Alloys Compd*. **2018**, *766*, 429–435.

23 Chava, R. K.; Kang, M. Improving the photovoltaic conversion efficiency of ZnO based dye sensitized solar cells by indium doping. *J. Alloys Compd*. **2017**, *692*, 67–76.

24 Gupta, S. K.; Sudarshan, K.; Kadam, R. M. Optical nanomaterials with focus on rare earth doped oxide: a review. *Mater. Today Commun*. **2021**, *27*, 102277.

25 Bouzigues, C.; Gacoin, T.; Alexandrou, A. Biological applications of rare-earth based nanoparticles. *ACS Nano* **2011**, *5*, 8488–8505.

26 Ninjbadgar, T.; Garnweitner, G.; Börger, A.; Goldenberg, L. M.; Sakhno, O. V.; Stumpe, J. Synthesis of luminescent ZrO_2:Eu^{3+} nanoparticles and their holographic sub-micrometer patterning in polymer composites. *Adv. Funct. Mater*. **2009**, *19*, 1819–1825.

27 Youssef, Z.; Colombeau, L.; Yesmurzayeva, N.; Baros, F.; Vanderesse, R.; Hamieh, T.; Toufaily, J.; Frochot, C.; Roques-Carmes, T.; Acherar, S. Dye-sensitized nanoparticles for heterogeneous photocatalysis: cases studies with TiO_2, ZnO, fullerene and graphene for water purification. *Dyes Pigm*. **2018**, *159*, 49–71.

28 Guillén, E.; Casanueva, F. F.; Anta, J. A.; Vega-Poot, A.; Oskam, G.; Alcántara, R.; Fernández-Lorenzo, C.; Martín-Calleja, J. Photovoltaic performance of nanostructured zinc oxide sensitised with xanthene dyes. *J. Photochem. Photobiol., A: Chem*. **2008**, *200*, 364–370.

29 Han, F.; Kambala, V. S. R.; Srinivasan, M.; Rajarathnam, D.; Naidu, R. Tailored titanium dioxide photocatalysts for the degradation of organic dyes in wastewater treatment: a review. *Appl. Catal., A* **2009**, *359*, 25–40.

30 Valenti, M.; Jonsson, M. P.; Biskos, G.; Schmidt-Ott, A.; Smith, W. A. Plasmonic nanoparticle-semiconductor composites for efficient solar water splitting. *J. Mater. Chem. A* **2016**, *4*, 17891–17912.

31 Ahmad, I.; Akhtar, M. S.; Ahmed, E.; Ahmad, M.; Keller, V.; Khan, W. Q.; Khalid, N. R. Rare earth co-doped ZnO photocatalysts: solution combustion synthesis and environmental applications. *Sep. Purif. Technol*. **2020**, *237*, 116328.

32 Khan, M. A.; Nain, P.; Ahmed, J.; Ahamed, M.; Kumar, S. Characterization and photocatalytic performance of hydrothermally synthesized Cu-doped TiO_2 NPs. *Opt. Mater*. **2022**, *133*, 112983.

33 Kuzmicheva, G. M.; Savinkina, E. V.; Obolenskaya, L. N.; Zubavichus, Y. V.; Murzin, V. Y.; Podbelskiy, V. V.; Sadovskaya, N. V. Synthesis of Mn-sensitized TiO_2 nanoparticles: influence of sequence of reagents on phase composition and photocatalytic activity. *J. Nanopart. Res*. **2015**, *17*, 406.

34 Kaur, R.; Singla, P.; Singh, K. Transition metals (Mn, Ni, Co) doping in TiO_2 nanoparticles and their effect on degradation of diethyl phthalate. *Int. J. Environ. Sci. Technol*. **2017**, *15*, 2359–2368.

2

Experimental techniques

This chapter comprises the experimental techniques and equipment employed to develop this Thesis. Firstly, the synthesis procedures for metal oxide NPs are described. A general description of each method developed for the preparation of Y_2O_3 and TiO_2-based materials is presented. Among them, the following bottom-up routes have been employed: combustion, sol-gel, molten salt, homogeneous precipitation, and solvothermal/hydrothermal synthesis. Additionally, different procedures to fabricate both optical composites and supported photocatalysts from the synthesized NPs are described in the chapter. PLD technique has been used to prepare the former, while vitrification process and carbon-paper deposition have been applied for the latter. Secondly, the structural characterization of the prepared NPs has been performed by means of X-ray diffraction (XRD), transmission electron microscopy (TEM), Raman spectroscopy, microwave plasma-atomic emission spectroscopy (MP-AES), and X-ray photoelectron spectroscopy (XPS). These techniques have provided useful information in terms of composition, crystalline phase, dopant concentration and oxidation state, vibrational modes, NP size and morphology, and agglomeration degree. The optical characterization has been carried out through spectroscopic techniques such as optical absorption, reflectance, photoluminescence and emission lifetime measurements. Emission and excitation spectra, and lifetime measurements have allowed the study of the optical properties of RE-doped Y_2O_3 NPs. Besides, the band gap modification achieved by doping TiO_2 NPs with RE and TM ions has been evaluated from the optical reflectance spectra. Additionally, absorption spectroscopy has been used to study the degradation of a chosen dye under UV irradiation catalyzed by synthesized TiO_2 NPs, and thus to investigate their photocatalytic performance.

Finally, the chapter also includes the procedures for the photocatalytic activity studies of bare and supported NPs. Firstly, the photocatalytic activity of pure and TM-doped TiO_2 NPs in the degradation of methylene blue (MB) has been evaluated. Secondly, the photocatalytic activity of pure, TM and TM-RE-codoped TiO_2 NPs has been investigated for CO_2 photoreduction to alcohols in a microreactor.

2.1. Materials synthesis

2.1.1. Synthesis of rare earth doped Y_2O_3 NPs

Since one the of main goals of this Thesis is to correlate the effect of different synthesis methods and their parameters with the structural and optical properties of the prepared NPs, several bottom-up procedures were adapted to synthesize Pr-doped Y_2O_3 NPs. For each method, the conditions were tuned and optimized to achieve the best optical performance of the resulting material. In this section, a general description of each synthesis procedure is presented, whereas an in-depth study of the modified parameters and their effect on the final NPs optical performance is developed in Chapter 4.

Combustion method

Combustion synthesis represents one of the simplest and fastest procedures to produce complex oxides [1]. The process is based on a redox reaction and three elements are required for it to take place: an oxidizer, a fuel (reducer) and the necessary temperature to trigger the reaction [2]. In this context, the fuel is burnt with an oxidizer producing an exothermic reaction. The typical reaction mechanism of the combustion method is described in Figure 2.1:

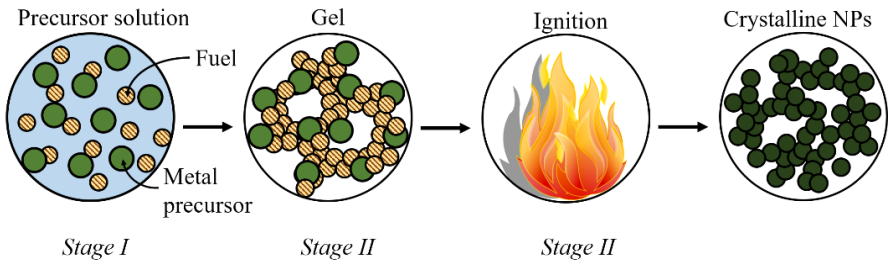

Figure 2.1. Schematic of the combustion method reaction mechanism.

This procedure can be described as a 3-stage method that begins with the dehydration of an aqueous mixture containing the organic fuel and the oxidizer to form a gel (Stages I and II). This oxidizer is usually a metal nitrate due to its good solubility in water and its low decomposition temperature. Then, the thermal decomposition of the resulting gel occurs through several exothermic reactions (Stage III). As a consequence, a large volume of gas is generated, promoting the expansion of the powder product and a fast decrease of temperature after reaction, ultimately leading to a high grade of dispersity and porosity of the solid [3].

In the present Thesis the combustion synthesis is one of the selected methods due to its simplicity, wide variety of achievable compositions, as well as high purity, homogeneity and surface area of the resulting powders [1,2]. A general description of the procedure performed in this Thesis is the following: rare earth nitrates ($RE(NO_3)_3$) were dissolved in a small volume of deionized water together with a fuel such as urea ($CO(NH_2)_2$). Then, the mixture was covered and heated up for the reaction to take place. Afterwards, a further annealing was applied to increase product purity and crystallinity. However, it is necessary to consider the role of the different involved parameters, such as fuel, metal precursors, reaction temperature, water content or annealing conditions [1,2,3]. Specifically, the effect of the thermal treatment on the prepared NPs has been studied since not only does it remove surface contamination but also modifies NP size and aggregation state [1].

Molten salt method

The molten salt synthesis procedure is considered as a simplistic alternative to wet-chemistry methods to obtain ceramic oxide powders in the nanoscale, such as titanates, ferrites and perovskites, to name a few [4]. Specifically, molten salt represents an easy route which provides crystalline, chemically pure, single-phase products. This method involves the use of a molten salt or a mixture of eutectic salts as a reaction medium, which enhances mobility and contact among reagents, and thus leads to higher reaction rates. Molten salt reaction occurs according to the 3-stage mechanism described in Figure 2.2:

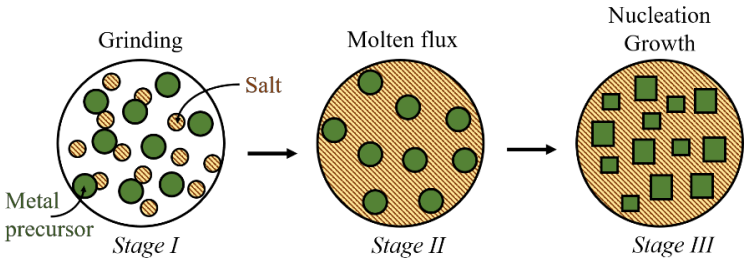

Figure 2.2. Schematic of the molten salt method reaction mechanism.

In Stage I, metal precursors are mixed with a salt or with a eutectic mixture to achieve a lower melting point. Then, in Stage II, the mixture is heated above the melting point of the salt in order to create a molten flux. At this temperature, precursor species start to disperse, dissociate, and rearrange, to later diffuse through the molten salt. At Stage III, NPs are formed by means of an initial nucleation followed by growth via solution-precipitation process [5,6].

There are several categories of molten salts, and they are classified into inert and reactive systems, being the former the most frequently used in molten salt synthesis [6]. Briefly, the procedure followed in this Thesis was as follows: $RE(NO_3)_3$ were mixed and ground in an agate mortar together with a large excess of salts. Then, the ground powder was heated above the melting point of the mixture of salts. A purification step by means of several washing and centrifugation cycles was required to purify the synthesized NPs. Parameters such as salt system, reaction time and temperature, amount of salt, and ratio between salts when using a eutectic mixture have been previously demonstrated to play a crucial role in the final characteristics of the resulting nanoparticles; namely, shape, morphology and physicochemical features [4,7]. It should be noted that product purification is a very important parameter to take into consideration, especially when synthesizing an optically active material. An exhaustive washing process is required to remove the remaining salts, which would be ultimately detrimental for luminescent properties. In this sense, the effect of the purification process has been studied in this Thesis.

Sol-gel Pechini method

The sol-gel synthesis method can be considered as one of the most popular procedures to prepare nano-sized powders and coatings [8]. This strategy allows to obtain different functional materials, particularly metal oxides, in

diverse forms such as thin films, wires or mesoporous materials [9], thus offering a wide variety of applications in the fields of magnetism, superconductivity, photocatalysis and optics, to name a few [10]. Sol-gel procedure involves the use of a colloidal solution, referred as sol, that derives to form a gel-type network as a result of several chemical reactions among metal alkoxides and solvents [8]. A general representation of these reactions is presented in Figure 2.3:

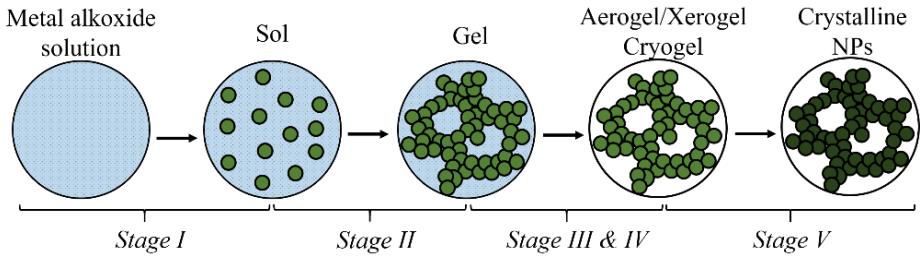

Figure 2.3. Schematic of the sol-gel method reaction mechanism.

Accordingly, sol-gel synthesis can be described as a 5-step process: hydrolysis, condensation, aging, drying and thermal decomposition. In the first step (hydrolysis), a mixture of metal alkoxides and solvents is prepared. The alkoxide functional group is removed and replaced by a newly formed hydroxyl (-OH) functional group. During the condensation step, the solvent (water/alcohol) is removed, thus forming the polymeric network composed of metal oxides linkages and obtaining the sol. Further growth of the polymeric network increases the viscosity of the solution leading to the formation of the gel. The polycondensation process continues together with the gel network precipitation during the aging step. Drying represents a critical step due to the different available methodologies and the effect that these may have on the resulting products. In this line, depending on the selected strategy, the final structure can be highly impacted, leading to the formation of aerogels, xerogels or cryogels. The last step involves a calcination process in order to remove the remaining hydroxyl groups and water molecules, and to obtain crystalline materials [8,11].

Nevertheless, the use of metal alkoxides is a limitation due to their instability or possible incompatibility with directing agents or templates. In this line, several efforts have been made to develop new methodologies based on sol-gel chemistry [9]. Precisely, sol-gel Pechini synthesis method, named after

the author of the original patent, represents an alternative procedure where metal alkoxides are substituted by metal salts [9]. Some of the main advantages offered by this modified route are the high purity of the resulting product and the precise control of the final composition [8]. Specifically, the sol-gel Pechini method involves the formation of a polymer network where metal ions are entrapped, delaying the thermal decomposition of the organic matrix, and thus allowing a higher control over particle growth. A typical sol-gel Pechini procedure consists in the preparation of an initial aqueous solution of metal salts and a chelating agent, usually citric acid, to form a solution of metal-citrate chelate complexes. Afterwards, a polyhydroxy alcohol is added while heating to initiate the polyesterification of chelates, forming a covalent network where metal ions are trapped. The resulting viscous liquid is then dried to form a gelatinous precursor, and a final thermal treatment is applied to remove organic compounds and to obtain the final metal oxide [8,9,10].

A simplified description of the employed procedure in this Thesis is as follows: $RE(NO_3)_3$ were dissolved in deionized water. Then, a chelating agent, such as citric acid ($(HOOCCH_2)_2C(OH)COOH$) or ethylenediaminetetraacetic acid (EDTA, $((HOOCCH_2)_2NCH_2)_2$) was added. Afterwards, a polyhydroxy alcohol was added while the mixture was moderately heated (below 100 ºC) for a short period of time. Then, the obtained sol was dried in a stove to obtain a gel. A final annealing step was required to remove the remaining organic reagents and to form the final NPs. Different parameters such as the type of chelating agent, the carboxylic acid/hydroxyl ratio or the employed alcohol can be tuned in order to optimize the final products. Specifically, the effect of the selected chelating agent and the thermal treatment conditions have been assessed in this Thesis, as these may lead to remarkable changes in terms of particle size, undesired phases formation [12] or particle morphology [9]. Firstly, the impact of the chelating agent on the resulting NPs can be attributed to differences in structure and degree of branching of the formed polyester, or to the diverse required temperatures for their thermal decomposition [9]. Also, modifying the number of reactive groups involved in the polyesterification process, by substituting both the chelating agent and the polyhydroxy alcohol, have been observed to lead to remarkable changes in terms of particle morphology [9].

Homogeneous precipitation method

The most popular and simple methodology to precipitate a hydroxide precursor in an aqueous medium is the alkali precipitation procedure. However, its lack of concentration homogeneity during the alkali precipitant formation leads to wide size distributions [13]. In contrast, the homogeneous precipitation synthesis is a very suitable method for the fabrication of well-defined particles with a very precise control of size and morphology. This has great interest in different application areas such as advanced ceramics and optics for the development of high-resolution displays. For the latter, the use of small-sized particles, with narrow size distributions and spherical shapes, is highly desired in order to improve resolution. These characteristics allow to obtain denser phosphor layers resulting from the better packing of spheres and to minimize light scattering on the surface [14,15].

Homogeneous precipitation synthesis consists in a cation precipitation process as a consequence of the thermal decomposition of urea, as represented in Figure 2.4:

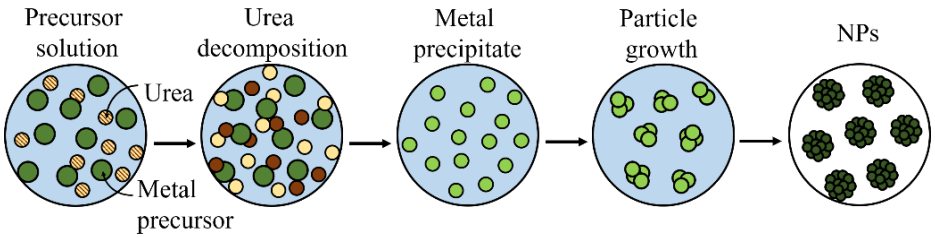

Figure 2.4. Schematic of the homogeneous precipitation method reaction mechanism.

It can be described as a 4-stage process. Briefly, the thermal decomposition of urea, which acts as a precipitation agent, takes place in an aqueous solution of metal precursors (Stage I). As a result, a slow and uniform release of precipitating ligands (mostly OH^- and CO_3^{2-}) occurs in the system (Stage II), avoiding the localized distribution of reagents, and therefore allowing a precise control of the nucleation and crystal growth processes (Stage III) [15,16]. A final thermal treatment is required to transform the metal precipitates into the desired metal oxides (Stage IV).

A representative description of the homogeneous precipitation method used in this Thesis is as follows: $RE(NO_3)_3$ were dissolved in a small volume

of deionized water. Afterwards, this solution was transferred to a well-stirred aqueous solution with a large excess of urea. The mixture was heated for a certain time to induce urea decomposition, and, after cooling down, the solid was washed by centrifugation. The product was dried and then annealed to obtain the final metal oxide. Accordingly, in order to control particle growth, *i.e.*, particle size, several parameters can be modified. Specifically, urea concentration and reaction time have been studied herein since they have a great relevance in particle size, and size distribution [13,17,18]. The use of urea in excess has been previously reported to lead to a remarkable reduction in particle size which can be related to an increased nuclei formation at the supersaturation critical point, suppressing in this way particle growth due to the initial consumption of reactants [17]. Likewise, longer reaction times have been described to promote increased particle sizes, which supports the hypothesis that the initial number of nuclei is constant during the process [18].

Solvothermal method

The solvothermal synthesis method is considered one of the most relevant procedures for preparation of nanomaterials thanks to its remarkable applications in fields such as catalysis, optoelectronics, magnetism or biomedicine, to name a few [19]. The solvothermal process consists in the heating of a solvent in a sealed vessel, bringing temperature near or well above the normal boiling point as a consequence of the increase of the autogenous pressure [20,21]. These conditions promote a higher solubility and reactivity of the metal precursors, allowing to carry out reactions at lower temperatures than other solid-state chemistry procedures. Additionally, unlike other wet-chemistry methods, the products can be obtained with quantitative yields and do not require a post-annealing treatment due to their exceptional crystallinity [5,21]. A general representation of the reaction mechanism is illustrated in Figure 2.5.

The solvothermal method can be described as a 2-step process: crystal nucleation and crystal growth. When the solubility of the solute is above its limit, that is, when the solution becomes supersaturated, the solute precipitates forming clusters. After the initial nucleation, crystals grow by means of: i) transport of growth units (with the same composition as nuclei and coming from the bulk solution), ii) attachment to the surface, iii) rearrangement of units over the surface, and iv) attachment of units to growth sites, which ultimately promotes bigger NP sizes [20].

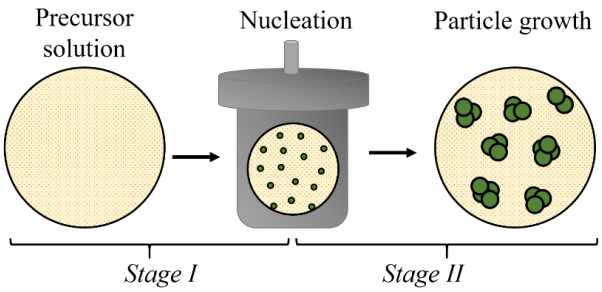

Figure 2.5. Schematic of the solvothermal method reaction mechanism.

A general description of the synthesis conditions followed for this procedure in the present Thesis is as follows: $RE(NO_3)_3$ were dissolved in a mixture of alcohol/deionized water. Then, the solution was transferred to a Teflon-lined stainless-steel autoclave, and heated up for a certain time for the reaction to occur. The obtained solid was collected and purified by centrifugation. Finally, a calcination step was applied to remove organic traces. Interestingly, parameters such as reaction temperature and time, the use of additives/surfactants, pH or solvent nature play an important role on both crystal nucleation and growth stages [5]. Specifically, reaction temperature, RE precursor concentration, type of alcohol and thermal treatment conditions have been evaluated in this Thesis. The former, *i.e.*, reaction temperature, has a great impact on the NPs synthesis since solvent properties dramatically change at high temperatures. A reduction of viscosity is experienced by the solvent when reaction temperature is increased, resulting in a higher mobility of the dissolved species. Besides, under such conditions, the dielectric constant of the solvent is remarkably affected, specially above its critical point, reducing the solubility of components, and thus leading to the supersaturation of the solution and ultimately increase of the nucleation rates, which will result in smaller NP sizes [20,22]. On the other hand, thermal treatment conditions have an impact on NP size, morphology and crystallinity. Regarding the solvent, depending on its nature, the method is defined as "hydrothermal" when using water, and "solvothermal" when using an organic solvent [20]. Water is the most widely solvent used in this type of procedure due to its great abundancy and low-toxic nature, together with its ability to dissolve many common metal salts and surfactants. Nevertheless, the use of organic solvents, such as polyols, has proven to allow for a more precise control of crystal phase, NP size and size distribution as a result of the higher temperatures and pressures that can be applied [20,22].

2.1.2. Synthesis of transition metal/rare earth doped TiO_2 NPs

Two of the previously described methods (precipitation and hydrothermal) were employed to prepare pure and doped/co-doped TiO_2 NPs, as a function of the final application. Firstly, since one of the main goals of this Thesis was to prepare vitrified supported catalysts based on the synthesized NPs as part of a collaboration project with Vitrispan S.A company, a precipitation method was selected. This procedure allows to achieve a good degree of crystallinity and purity in the final powders, and to use low temperatures for an easy control of NP size and shape [23]. Additionally, the precipitation method is easily scalable, which results remarkably relevant for its potential application in the industry. Secondly, a hydrothermal method was employed to synthesize pure and doped/co-doped TiO_2 NPs for their application as CO_2 reduction photocatalyst in a micro-reactor. This procedure allows to obtain crystalline products with a high degree of homogeneity at relatively low temperatures. Besides, it provides narrow NP size distributions, and simple particle size and morphology control [19]. However, the method is not suitable for large-scale production due to the limited volume available in the autoclave. A more detailed description of each procedure with the specific synthesis parameters is developed in Chapter 7 and 8, respectively.

Precipitation method

Titanium isopropoxide (TTIP, $Ti[OCH(CH_3)_2]_4$) was added dropwise to an aqueous solution of urea while stirring. After heating for a given time for the reaction to occur, the solid was washed and collected by centrifugation. An additional thermal treatment was applied to remove the remaining organic traces, or to tune NP size and the different TiO_2 crystalline phases ratio. For TM-doped NPs, stoichiometric amounts of the corresponding metal chloride were added to the aqueous urea solution prior to the addition of TTIP.

Hydrothermal method

An acidified aqueous solution (pH 1) was prepared by adding concentrated HNO_3 to deionized water. Next, TTIP was added dropwise while stirring. The mixture was heated to reduce the total volume and then transferred to a Teflon-lined stainless-steel autoclave. After heating for a certain time, the solid was washed and collected by centrifugation. For RE-doped and RE-TM co-doped

NPs, stoichiometric amounts of the corresponding metal nitrates were dissolved into the acidified aqueous solution prior to the addition of TTIP.

2.2. Structural characterization techniques

2.2.1. X-ray diffraction

XRD is a versatile and non-destructive technique that provides useful information such as phase identification, sample purity, lattice parameters and crystallite size [24]. In this work, XRD was employed to determine sample composition, crystalline structure and NP size distribution of all prepared NPs.

XRD measurements were performed in a Bruker D8 Advanced diffractometer equipped with a Cu tube (wavelength: $<K\alpha_{1,2}> = 1.5418$ Å) and a fast LYNXEYE 1D-detector at the Department of CITIMAC of the University of Cantabria. Samples were typically measured in the 10°–120° range (2θ) for both phase identification and structural refinements. XRD patterns were analyzed by the Rietveld method using FullProf [25]. In addition, the Thompson-Cox-Hastings pseudo-Voigt approach [26] was used to reproduce the shape of the diffraction peaks, and Gaussian and Lorentzian contributions were considered for strain and size effects, respectively.

2.2.2. Transmission electron microscopy

TEM has become one of the most efficient and popular tools to perform microstructural characterization of nanomaterials. Accordingly, TEM technique was employed to obtain information about both morphology and particle size of the studied samples.

TEM images were acquired using a JEOL JEM 1011 microscope equipped with a high-resolution CCD camera (Gatan, Pleasanton, United States) at the IDIVAL institute. Dispersions of powder samples in ethanol (EtOH) under ultrasonic vibration were prepared and dropped over copper grids for the analysis. After complete drying at room temperature (RT), grids were placed in the specimen rod prior to its introduction into the microscope. To estimate NP size distribution, up to 300 particles per sample were measured from TEM images using ImageJ software for particle counting and OriginPro 9.0 software for particle size distribution fitting.

2.2.3. Microwave plasma-atomic emission spectroscopy

MP-AES can be considered a rather recent analytical technique which displays several advantages such as low maintenance cost, safety, inexpensive and non-flammable gases requirement, multi-element capability, good detection limits and fast analysis. As a result, all these features have turned it into a promising routine analytical technique for multi-analyte determination of elements [27,28]. In this way, MP-AES was employed for Ce and Cu concentration determination in doped TiO_2 NPs.

MP-AES measurements were performed at the Department of Chemical and Biomolecular Engineering of the University of Cantabria to determine the accurate Cu and Ce dopants concentrations in the analyzed photocatalysts. To this end, 0.2 g of powder samples were weighted and digested with HNO_3 (69%, suprapur) at 210 ºC in a Plasma Microwave (Ethos One, Millestone). Afterwards, the samples were diluted and analyzed with a microwave plasma-atomic emission spectrometer (MP-AES 4200, Agilent Technologies). This setup employs nitrogen plasma as excitation source and a solid-state CCD detector. A linear external calibration was also performed to accurately determine the actual Ce and Cu concentrations in the studied photocatalysts.

2.2.4. X-ray photoelectron spectroscopy

XPS is a powerful technique for surface characterization due to the great amount of information it provides. Both qualitative and quantitative results can be obtained through XPS analysis. From the resulting bands, elemental determination can be performed as each element exhibits a characteristic spectrum. In addition, from peak heights and areas, or changes in binding energies (chemical shift), information such as elemental concentration and oxidation state can be obtained [29]. In this context, XPS technique was used to determine the oxidation state of the elements in the studied Cu-Ce-doped TiO_2 samples.

XPS measurements were performed in a SPECS system equipped with a Phoibos 150 1D-DLD analyzer and Al Kα monochromatic radiation source (1486.7 eV) located at the Department of Organic and Inorganic Chemistry of the University of the Basque Country. Powder samples were dispersed on a conductive tape, and no further modifications were applied for the samples

supported in gas diffusion layers to obtain the XPS spectra. An initial analysis was carried out to determine the present elements in the samples (wide scan: step energy 1 eV, dwell time 0.1 s, pass energy 80 eV), and, afterwards, detailed analyses of the detected elements were performed (detail scan: step energy 0.08 eV, dwell time 0.1 s, pass energy 30 eV) with an electron exit angle of 90°. The spectrometer was initially calibrated with Ag (Ag $3d_{5/2}$, 368.26 eV). Spectra were fitted using CasaXPS 2.3.16 software, which models Gauss-Lorentzian contributions, after background subtraction (Shirley).

2.2.5. Raman spectroscopy

Among the numerous existing forms of light-matter interaction, the vast majority of methods employed to detect vibrations in either molecules or condensed matter are based on infrared absorption and Raman spectroscopies. These techniques allow to obtain information about the chemical structure, identify substances and determine quantitatively or semi-quantitatively the amount of a certain compound in a sample in a wide range of physical states [30]. However, the possibility of examining aqueous solutions together with its non-destructive and non-invasive character makes Raman spectroscopy an optimal technique to characterize materials, especially in the biological and medical fields [31]. In this line, Raman spectra were recorded for phase identification.

Unpolarized confocal micro-Raman measurements were performed by means of a triple monochromator Raman spectrometer (Horiba-Jobin-Yvon, Model T64000), in subtractive-mode backscattering configuration, equipped with a liquid-N_2-cooled CCD detector. The 488 nm line of an Ar^+–Kr^+ laser was focused on the sample with a 20× objective, and the laser power was kept below 4 mW in order to avoid laser-heating effects. The laser spot was 2 μm in diameter, and the spectral resolution was better than 0.6 cm^{-1} for all spectra. Complementary measurements were performed with a SM245 spectrophotometer from Spectral Products, equipped with a CCD detector and a solid-state laser emitting at 785 nm, focused with a 20× objective. Spectra were recorded with a resolution higher than 5 cm^{-1}, a laser power of 150 mW and an acquisition time of 60 seconds. Both instruments are located at the High Pressure and Spectroscopy Group of the University of Cantabria.

2.3. Optical characterization techniques

2.3.1. Absorption spectroscopy

Light absorption measurements in the UV-Vis and IR regions are based on the attenuating effect that a light beam experiences when passing through a material. Additionally, complementary information can be obtained by means of reflectance spectra for powder samples, which is defined as the ratio of reflected light by the sample and that of a standard surface measured under the same experimental conditions. Reflectance spectra can be obtained in two modes: i) direct reflectivity or ii) diffuse reflectivity. The use of an integrating sphere is required for the latter [32]. In this Thesis, absorption measurements allowed thin films thickness and photocatalytic activity determination, while reflectance spectra were measured to analyze RE optical transitions and TiO_2 band gap modification.

Absorption spectra at RT of the prepared samples were obtained in the 200–1800 nm spectral range with a Cary 6000i (Varian) equipment. The spectrometer contains two light sources: a quartz halogen lamp for Vis/IR measurements, and a deuterium lamp for the UV region. In addition, it is equipped with two detectors: a photomultiplier (PMT) (Hamamatsu R928) and an InGaAs detector for the Vis and near IR regions, respectively. Spectral resolution can be optimized down to $\Delta\lambda = 0.01$ nm, and maximum absorption can be detected up to 8. For powder samples, diffuse reflectance experiments were performed using an integrating sphere (DRA 1800) coated with polytetrafluoroethylene (PTFE), which exhibits NIR superior performance compared to traditional coatings, maintaining UV–Vis capabilities. Diffuse reflectance measurements of the NPs were made relative to a baseline using PTFE as a standard reference material. Additionally, reflectance spectra were converted into absorbance by the available software of the device by default. On the other hand, absorption spectra of liquid samples were recorded using quartz cuvettes with path lengths of 1 cm.

2.3.2. Luminescence spectroscopy

The most common techniques to characterize optical materials consist in using a continuous wave light source and recording the intensity versus wavelength (or energy). In this line, two possible options are available: emission and

excitation scans [32]. Interestingly, and in contrast to absorption, both emission and excitation are selective techniques.

RT emission and excitation spectra were recorded using a FLSP920 spectrofluorometer from Edinburgh Instruments, equipped with double monochromators in emission and excitation, located at the Department of Applied Physics of the University of Cantabria. A continuous Xe-lamp of 450 W was used as an excitation source. Emission was detected with an electrically cooled photomultiplier tube R928P (Hamamatsu, Shizuoka, Japan).

2.3.3. Luminescence lifetime spectroscopy

When the aforementioned spectrofluorometer includes pulsed light sources and a time detection system, luminescence lifetime measurements can also be carried out. For this purpose, both single excitation and emission wavelengths are selected, and emission intensity versus time is recorded [33]. This kind of experiments provides useful information regarding electronic structure and coordination environment of the emitting species, such as quantum yield of both radiative and non-radiative processes, presence of coordinated water molecules or ligands, and detection of different emitting ions in the sample [33].

Lifetime measurements were carried out with the previously described FLSP920 spectrofluorometer, using a pulsed Xe-lamp of 60 W. The luminescence decay curves of Pr^{3+}-doped Y_2O_3 NPs were fitted to a double exponential function, thus obtaining average emission lifetimes according to [34]:

$$< \tau > = \frac{A_1 \cdot \tau_1^2 + A_2 \cdot \tau_2^2}{A_1 \cdot \tau_1 + A_2 \cdot \tau_2} \qquad \text{(eqn. 2.1)}$$

where $A_i \cdot \tau_i$ represents the contribution of the i-th component.

2.4. Fabrication of optical composites

2.4.1. Fabrication of optically active composites by pulsed laser deposition

PLD is a promising technology that provides an efficient stoichiometric transfer from a pre-pressed solid target to the so-obtained thin film over a substrate. The principle of this technique is rather simple in contrast to the complex mechanisms that occur. Briefly, a laser beam is focused on the surface of a solid target inside a vacuum chamber. The impact of high-power pulsed laser energy leads to the ejection of material forming a dense plasma which expands symmetrically with respect to the normal of the target. This plasma is referred to as plume and it is formed by both neutral and ionized species that will eventually reach the substrate to condense and grow a film (Figure 2.6) [35,36,37].

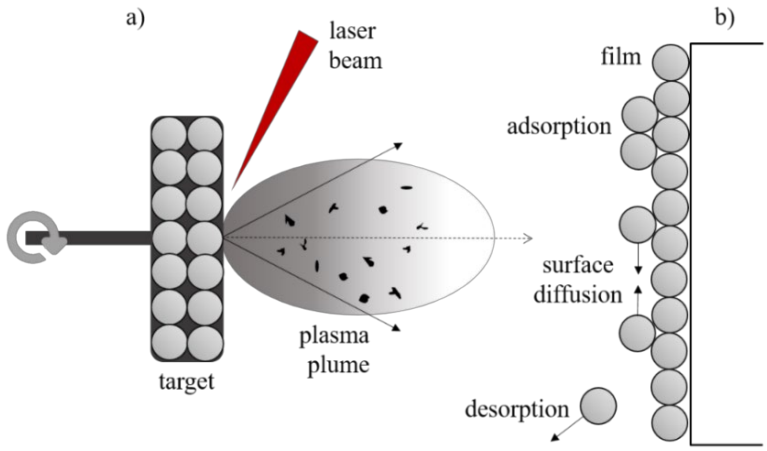

Figure 2.6. a) Schematic of the ablation and deposition processes; b) atom interactions during thin film deposition.

In order to control the thin film growth, several parameters that play a crucial role can be tuned. Among them, substrate temperature, substrate composition, vacuum level, background gas or laser energy highly influence the deposition process. Specifically, it is necessary for the substrate to present both good chemical and lattice compatibility with the material to be deposited. Otherwise, chemical reactions between the substrate and the film may inhibit epitaxial growth and promote the formation of undesired phases [38]. In addition, lattice compatibility is demanded to avoid induced strain or defects in

the deposited film [37]. Finally, when growing thin films for optical applications, some additional requirements must be taken into account regarding substrate selection: good transmission, lower refractive index than the deposited material and low cost, to name a few [38]

Another aspect to consider is substrate temperature. High temperatures promote epitaxial growth and good crystallinity in the films due to the desorption of impurities and surface diffusion of atoms [37]. Nevertheless, extremely high temperatures must be avoided to inhibit possible re-evaporation processes of deposited atoms. In addition, the vacuum level is especially relevant to guarantee the absence of undesired impurities. The choice of an appropriate pressure range has important effects on the stoichiometry of the films, as species can be evaporated or desorbed. On the other hand, the use of a reactive background gas is of special interest when growing metal oxide thin films, since an oxidizing species is required. Another purpose for using a reactive atmosphere is to modify the kinetic energy of the plume, and thus the thin film growth. In this sense, pressure and atmosphere not only influence the thickness, but also crystallinity and composition [37,39].

It must be noted that another critical factor is the energy source. Short pulses of high energy density are required for laser ablation. Consequently, the laser wavelength will have a direct impact on the composition of the plume, since material can be ejected as single atoms, binary or even ternary species, and thus on the final composition of the film. According to this, the selection of the appropriate laser wavelength should be in line with the absorption properties of the target material not only to achieve ablation, but also to avoid target destruction as a consequence of energy transfer, also known as “laser-induced breakdown” [37,40].

Optical composites of Pr^{3+}-doped Y_2O_3 NPs were prepared by means of PLD technique. This method was employed to embed the luminescent Y_2O_3-based NPs and protect their optical properties. The optical composites were prepared during a short research stay at the Department of Applied Physics of the University of Valencia, under the supervision of Prof. Alfredo Segura. The experimental setup consists of a multi-target PLD system equipped with a T-shape vacuum chamber. A rotatory pump and a turbomolecular pump were employed to achieve the vacuum conditions inside the chamber. A pressure of *ca*. 10^{-7} mbar was reached initially, while a final pressure of *ca*. 10^{-5} mbar was maintained during the deposition cycles. The deposition chamber also includes

a background gas controller, allowing the use of oxidizing atmospheres. In our case, O_2 was employed as background gas to facilitate the transfer of metal oxide from the target to the substrate. Additionally, different substrates (fused silica (FS), MgO (MO), sapphire C (SC) and sapphire R (SR)) were introduced simultaneously during the experiment and heated using a temperature controller. All deposition experiments were performed heating the substrates up to 600 ºC in order to promote an ordered growth of the material structure over the substrate. On the other hand, a quadrupled Nd:YAG laser (266 nm) with a repetition rate of 10 Hz and an energy of 10 mJ/pulse was used as ablating source for the target.

A more detailed description of the fabrication of thin films and optically active composites is developed in Chapter 5. Briefly, for the preparation of the target, high purity powders of the desired species were selected. A certain amount of the desired target composition was dispersed in EtOH to achieve a good grade of homogeneity. After drying overnight (o.n.) in a stove, the powders were pressed to form a pellet. Next, the prepared pellet was mildly heated at 100 ºC to remove adsorbed water molecules. Afterwards, a slow calcination was applied up to 1200 ºC and kept at that temperature for 24 h more. Finally, the sample was slowly cooled down to RT. On the other hand, material ejection from the target was carried out by means of a Nd:YAG laser. Thin films were grown over different substrates located at 4 cm of distance from the target. For the incorporation of the NPs, these were synthesized by solvothermal synthesis and dispersed in EtOH. The NPs suspension was deposited over the thin films and dried at RT. Afterwards, an additional deposition cycle was performed to obtain the composite. The number of deposition cycles and NPs concentration was modified in order to obtain different composite structures.

2.5. Fabrication of supported catalysts

Depending on their ultimate application, two different strategies were employed to prepare supported catalysts. Vitrified supported catalysts were fabricated for MB photodegradation experiments, while carbon-paper deposited catalysts were prepared by means of ink airbrushing for photoreduction of CO_2 to alcohols.

2.5.1. Fabrication of vitrified supported catalysts

The vitrified supported catalysts were prepared at Vitrispan S.A. company. Two types of enamels were deposited on stainless steel sheets (AC01EK quality with 0.08% carbon content): (i) a base enamel, and (ii) a coat enamel. In both cases, the precursors (enamel frit, clay, $NaAlO_2$, urea and water) were ground in a ball mill to obtain a suspension with a density of *ca*. 1.75–1.80 $g \cdot mL^{-1}$. The base enamel was deposited onto the stainless-steel sheets and dried at 100 °C. Subsequently, this base enamel was vitrified by heating at 840 °C for 3 minutes (min). After cooling down, the coat enamel was deposited over the vitrified base enamel, dried at 100 °C and vitrified by heating at 830 °C for 3 min. The resulting vitrified coat enamel showed a thickness of *ca*. 150 μm, while the base enamel exhibited a thickness of *ca*. 120 μm.

To prepare the supported photocatalyst (5 wt.% of photoactive material), TiO_2 NPs were mixed with a serigraph-type oil (mainly composed of acrylic resins and propylene glycol ester in a 2:5 w:w ratio) to obtain an appropriate viscosity. The mixture was deposited on the prepared support (enamel onto stainless steel sheets) by indirect serigraphy and vitrified by heating at 700 °C for 15 min.

2.5.2. Fabrication of carbon-paper supported catalysts

Photocatalytically active surfaces were prepared in the Department of Chemical and Biomolecular Engineering of the University of Cantabria. To this end, surfaces with 1 cm^2 area were manufactured by homogeneous deposition of active TiO_2 NPs onto porous carbon paper supports (Toray TGP-H-60). This procedure was already described in detail elsewhere by Albo *et al*. [41]. Briefly, TiO_2 NPs were dispersed with Nafion (5 wt.%, Alfa Aesar, copolymer polytetrafluoroethylene) acting as a binder, and isopropanol (Sigma-Aldrich) as a vehicle, with a 70/30 (photocatalyst/Nafion) mass ratio and 3 wt.% of total solids (photocatalyst + Nafion) in the dispersion. The resulting dispersion was sonicated for 30 min, and then airbrushed over the carbonaceous support, which was originally covered by a paper mask with a square hole of 1 cm^2. The deposition process was carried out at 100 ºC to ensure the complete evaporation of the solvent during the accumulation of photocatalytic layers. A total mass loading per photoelectrode was set to 2 $mg \cdot cm^{-2}$ [42], which was experimentally determined by continuous weighing.

2.6. Photocatalytic activity

The synthesized TiO_2-based NPs were employed as photocatalysts for different cutting-edge applications, namely pollutants degradation and CO_2 photoreduction to alcohols. Firstly, the use of bare NPs and vitrified supported catalysts for MB dye degradation was assessed. MB dye was selected to evaluate the organic compound removal ability of the prepared nanomaterials. Secondly, the utilization of supported NPs as catalysts for the continuous photoreduction of CO_2 to alcohols was studied in a planar optofluidic microreactor.

2.6.1. Methylene blue degradation

The photocatalytic performance of undoped and TM-doped TiO_2 NPs was investigated in the degradation of a MB aqueous solution under UV radiation according to the ISO 10678 International Standard method [43]. For comparison purposes, all the samples were studied using the same experimental conditions.

The non-supported NPs were dispersed in an aqueous solution of MB. Then, the reaction mixture was irradiated from the top with a UV LED lamp (395 nm, 22 W) under vigorous stirring at RT. A more detailed description of the experimental conditions is presented in Chapter 7. In the case of supported NPs, the catalytic material was shaped in the form of a plate (5 × 5 cm^2) and subsequently irradiated with the UV lamp for 48 h as stated by the ISO 10678. The plate was placed over three methacrylate pieces in order to achieve an adequate stirring of the solution, and thus concentration homogeneity. Next, the MB aqueous solution was added and the degradation assay was carried out under the same conditions as described for non-supported NPs. As a control experiment, the supported photocatalyst was placed in the same MB aqueous solution and kept in the dark for 24 h. A slight reduction of the MB solution concentration due to an adsorption process was observed.

The absorbance of the MB solution was measured by extracting aliquots at different times, and the photocatalytic activity of the material was determined from the degradation rate, d. This degradation rate results from the reduction of the absorbance, A, which is proportional to the MB solution concentration, C, according to:

$$d\ (\%) = \frac{C_0 - C}{C_0} \cdot 100 = \frac{A_0 - A}{A_0} \cdot 100 \qquad \text{(eqn. 2.2)}$$

where C_0 and A_0 are the initial solution concentration and absorbance, respectively. The obtained values were appropriately corrected with the previously mentioned adsorption contribution in all photocatalytic activity measurements (% MB degradation).

2.6.2. CO_2 photoreduction to alcohols

On the other hand, the RE-doped and RE-TM-co-doped TiO_2 NPs were employed as catalysts for the continuous photoreduction of CO_2 to alcohols in a planar optofluidic microreactor.

In this setup, located at the Department of Chemical and Biomolecular Engineering of the University of Cantabria, photoactive electrodes are assembled in a tailor-made designed planar optofluidic microreactor equipped with a reaction microchamber of 1 cm^2 and 75 µL for the continuous light-driven conversion of CO_2 into alcohols. The light-responsive electrodes are sandwiched between two highly transparent polymethylmethacrylate (Altuglas-Arkema) plates and a stainless-steel plate on the top. The prepared surfaces are placed in the reaction microchamber and irradiated with UV (peak at 365 nm) or Vis (peak at 450 nm) LED lights with a light intensity of E = 5 $mW \cdot cm^{-2}$, measured by a radiometer (Photoradiometer Delta OHM) and controlled by adjusting the LED intensity and the distance between the transparent microreactor and the LED. An infrared thermometer controls the temperature during the reaction. An in-depth description of the experimental setup and photoreactor details can be found elsewhere [42,44].

Light-driven CO_2 reduction experiments were carried out in continuous mode by duplicate for 180 min under ambient conditions. The stability of the photoelectrodes was additionally evaluated in the long-term (6 h). A CO_2 saturated 0.5 M $KHCO_3$ (PanReac, >99.5%) aqueous solution was prepared at RT with ultra-pure water (18.2 MΩ cm at 273 K, MilliQ Millipore system) and supplied to the microchamber with a peristaltic pump (Minipuls 3 Gilson) at a flow rate of 100 $\mu L \cdot min^{-1}$. Blank tests in the dark and without CO_2 were also performed. The optofluidic microreactor was placed in a ventilated dark box, and the temperature was controlled with an infrared thermometer (*ca*. 20 °C). The concentration of alcohols in each sample was analyzed by duplicate in a

headspace gas chromatograph (GCMS-QP2010 Ultra Shimadzu) equipped with a flame ionization detector. An average concentration was obtained for each point, which was used to calculate the product formation rates (relative standard deviation < 15%). To ensure an accurate determination of alcohols concentration, external calibration samples (by triplicate) were prepared in a wide range of concentrations.

The performance of the process was analyzed in terms of: i) production rate of alcohols (*r*), *i.e.*, product yield per gram of photocatalyst and time ($\mu mol \cdot g^{-1} \cdot h^{-1}$); and ii) apparent quantum yield (*AQY*), which represents the ratio between the rate of electrons transferred towards a certain product and the rate of incident photons on the surface of the photoactive material. *AQY* values were determined according to:

$$AQY = \frac{n_e}{n_p} \cdot 100 \qquad \text{(eqn. 2.3)}$$

where n_e is the rate of required electrons for methanol (CH_3OH) and ethanol (C_2H_5OH) formation, defined as the number of evolved molecules (mol) multiplied by the number of reacted electrons (6 and 12 e^- for CH_3OH and C_2H_5OH, respectively) and the Avogadro number (mol^{-1}). n_p represents the rate of incident photons on the surface and it is obtained as follows:

$$n_p = \frac{E \cdot A \cdot t \cdot \lambda}{h \cdot c} \qquad \text{(eqn. 2.4)}$$

where *E* is the light intensity ($W \cdot m^{-2}$), *A* is the irradiation area (m^2), *t* is the reaction time (s), λ is the wavelength peak (nm), *h* is the Planck's constant, and *c* is the speed of light.

References

1 Shea, L. E.; McKittrick, J.; Lopez, O. A. Synthesis of red-emitting, small particle size luminescent oxides using an optimized combustion process. *J. Am. Ceram. Soc*. **1996**, *79*, 3257–3265.

2 Carlos, E.; Martins, R.; Fortunato, E.; Branquinho, R. Solution combustion synthesis: towards a sustainable approach for metal oxides. *Chem. Eur. J*. **2020**, *26*, 9099–9125

3 Varma, A.; Mukasyan, A.; Rogachev, A. S.; Manukyan, K. V. Solution combustion synthesis of nanoscale materials. *Chem. Rev*. **2016**, *116*, 14493−14586.

4 Mao, Y.; Park, T. -J.; Wong, S. S. Synthesis of classes of ternary metal oxide nanostructures. *Chem. Commun*. **2005**, 5721–5735.

5 Mao, Y.; Park, T. -J.; Zhang, F.; Zhou, H.; Wong, S. S. Environmentally friendly methodologies of nanostructure synthesis. *Small* **2007**, *3*, 1122–1139.

6 Gupta, S. K.; Mao, Y. A review on molten salt synthesis of metal oxide nanomaterials: status, opportunity, and challenge. *Prog. Mater. Sci*. **2021**, *117*, 100734.

7 Yoon, K. H.; Cho, Y. S.; Kang, D. H. Molten salt synthesis of lead-based relaxors. *J. Mater. Sci.* **1998**, *33*, 2977−2984.

8 Navas, D.; Fuentes, S.; Castro-Alvarez, A.; Chavez-Angel, E. Review on sol-gel synthesis of perovskite and oxide nanomaterials. *Gels* **2021**, *7*, 275.

9 Danks, A. E.; Hall, S. R.; Schnepp, Z. The evolution of ‘sol–gel’ chemistry as a technique for materials synthesis. *Mater. Horiz*. **2016**, *3*, 91−112.

10 Dimesso, L. Pechini processes: an alternate approach of the sol–gel method, preparation, properties, and applications. In *Handbook of Sol-Gel Science and Technology*. Springer Cham. 2016.

11 Parashar. M.; Shukla, V. K.; Singh, R. Metal oxides nanoparticles via sol–gel method: a review on synthesis, characterization and applications. *J. Mater. Sci.: Mater. Electron*. **2020**, *31*, 3729–3749.

12 Motta, M.; Deimling, C. V.; Saeki, M. J.; Lisboa-Filho, P.N. Chelating agent effects in the synthesis of mesoscopic-size superconducting particles. *J. Sol-Gel Sci. Technol*. **2008**, *46*, 201–207.

13 Venkatachalam, N.; Saito, Y.; Soga, K. Synthesis of Er^{3+} doped Y_2O_3 nanophosphors. *J. Am. Ceram. Soc*. **2009**, *92*, 1006–1010.

14 Qin, H.; Tan, X.; Huang, W.; Jiang, J.; Jiang, H. Application of urea precipitation method in preparation of advanced ceramic powders. *Ceram. Int*. **2015**, *41*, 11598–11604.

15 Li, J. -G.; Li, X.; Sun, X.; Ishigaki, T. Monodispersed colloidal spheres for uniform Y_2O_3:Eu^{3+} red-phosphor particles and greatly enhanced luminescence by simultaneous Gd^{3+} doping. *J. Phys. Chem. C* **2008**, *112*, 11707–11716.

16 Xu, X.; Sun, X.; Liu, H.; Li, J.-G.; Li, X.; Huo, D.; Liu, S. Synthesis of monodispersed spherical yttrium aluminum garnet (YAG) powders by a homogeneous precipitation method. *J. Am. Ceram. Soc*. **2012**, *95*, 3821–3826.

17 Fukushima, S.; Furukawa, T.; Niioka, H.; Ichimiya, M.; Sannomiya, T.; Miyake, J.; Ashida, M.; Araki, T.; Hashimoto, M. Synthesis of Y_2O_3 nanophosphors by homogeneous precipitation method using excessive urea for cathodoluminescence and upconversion luminescence bioimaging. *Opt. Mater. Express* **2016**, *6*, 831–831.

18 Sordelet, D.; Akinc, M. Preparation of spherical, monosized Y_2O_3 precursor particles. *J. Colloid Interface Sci*. **1988**, *122*, 47–59.

19 Byrappa, K.; Adschiri, T. Hydrothermal technology for nanotechnology. *Prog. Cryst. Growth Charact. Mater*. **2007**, *53*, 117−166.

20 Li, J.; Wu, Q.; Wu, J. Synthesis of nanoparticles via solvothermal and hydrothermal methods. In *Handbook of nanoparticles.* Springer Cham, 2015.

21 Cushing, B. L.; Kolesnichenko, V. L.; O'Connor, C. J. Recent advances in the liquid-phase syntheses of inorganic nanoparticles. *Chem. Rev*. **2004**, *104*, 3893–3946.

22 Lai, J.; Niu, W.; Luque, R.; Xu, G. Solvothermal synthesis of metal nanocrystals and their applications. *Nano Today* **2015**, *10*, 240–267.

23 Nyamukamba, P.; Okoh, O.; Mungondori, H.; Taziwa, R.; Zinya, S. Synthetic methods for titanium dioxide nanoparticles: a review. In *Titanium Dioxide - Material for a Sustainable Environment*. InTech 2018, 151-174.

24 Holder, C. F.; Schaak, R. E. Tutorial on powder X-ray diffraction for characterizing nanoscale materials. *ACS Nano* **2019**, *13*, 7359–7365.

25 Rodríguez-Carvajal, J. Recent advances in magnetic structure determination by neutron powder diffraction. *Phys. B: Condens. Matter* **1993**, *192*, 55–69.

26 Thompson, P.; Cox, D. E.; Hastings, J. B. Rietveld refinement of Debye-Scherrer synchrotron X-ray data from Al_2O_3. *J. Appl. Cryst*. **1987**, *20*, 79–83.

27 Balaram, V. Microwave plasma atomic emission spectrometry (MP-AES) and its applications – A critical review. *Microchem. J*. **2020**, *159*, 105483.

28 Khandpur, R. S. Atomic emission spectroscopy: microwave plasma. In *Compendium of biomedical instrumentation*. John Wiley & Sons Ltd, 2020, 1, 121–124.

29 Hollander, J. M.; Jolly, W. L. X-ray photoelectron spectroscopy. *Acc. Chem. Res*. **1970**, *3*, 193–200.

30 Smith, E; Dent, G. *Modern Raman spectroscopy. A practical approach*. John Wiley and Sons Ltd, 2005.

31 Jones, R. R.; Hooper, D. C.; Zhang, L.; Wolverson, D.; Ventsislav, K. V. Raman techniques: fundamentals and frontiers. *Nanoscale Res. Lett*. **2019**, *14*, 1–34.

32 García Solé, J.; Bausá, L. E.; Jaque, D. *An introduction to the optical spectroscopy of inorganic solids*. John Wiley and Sons Ltd, 2005.

33 Morris, D. E.; de Bettencourt-Dias, A. Spectroscopic techniques and instrumentation. In *Luminescence of lanthanide ions in coordination compounds and nanomaterials*. John Wiley and Sons Ltd, 2005.

34 Fišerová, E.; Kubala, M. Mean fluorescence lifetime and its error. *J. Lumin*. **2012**, *132*, 2059–2064.

35 Sans Tresserras, J. Á. Electronic structure of ZnO–based wide band gap semiconductors: growth and characterization of the transparent conducting oxide ZnO:Ga and the semimagnetic alloy $Zn_{1-X}Co_xO$ and their high pressure phases. PhD Thesis, Universidad de Valencia, 2007.

36 Christen, H. M.; Eres, G. Recent advances in pulsed–laser deposition of complex oxides. *J. Phys.: Condens. Matter* **2008**, *20*, 264005.

37 Shepelin, N. A.; Tehrani, Z. P.; Ohannessian, N.; Schneider, C. W.; Pergolesi, D.; Lippert, T. A practical guide to pulsed laser deposition. *Chem. Soc. Rev*. **2023**, *52*, 2294–2321.

38 Korzenski, M. B.; Lecoeur, Ph.; Mercey, B.; Chippaux, D.; Raveau, B.; Desfeux, R. PLD–grown Y_2O_3 thin films from Y metal: an advantageous alternative to films deposited from yttria. *Chem. Mater*. **2000**, *12*, 3139–3150.

39 Norton, D. P. Synthesis and properties of epitaxial electronic oxide thin–film materials. *Mater. Sci. Eng. R* **2004**, *43*, 139–247.

40 İleri, B. Lattice matching of epitaxial rare–earth–doped dielectric PLD–films. PhD Thesis, Universität Hamburg, 2007.

41 Albo, J.; Sáez, A.; Solla-Gullón, J.; Montiel, V.; Irabien, A. Production of methanol from CO_2 electroreduction at Cu_2O and Cu_2O/ZnO-based electrodes in aqueous solution. *Appl. Catal. B Environ*. **2015**, *176–177*, 709–717.

42 Albo, J.; Qadir, M. I.; Samperi, M.; Fernandes, J. A.; de Pedro, I.; Dupont, J. Use of an optofluidic microreactor and Cu nanoparticles synthesized in ionic liquid and embedded in TiO_2 for an efficient photoreduction of CO_2 to methanol. *Chem. Eng. J.* **2021**, *404*, 126643.

43 ISO 10678:2010, *Fine ceramics (advanced ceramics, advanced technical ceramics) – Determination of photocatalytic activity of surfaces in aqueous medium by degradation of methylene blue*.

44 Albo, J.; García, G. Enhanced visible-light photoreduction of CO_2 to methanol over Mo_2C/TiO_2 surfaces in an optofluidic microreactor. *React. Chem. Eng*. **2021**, *6*, 304–312.

Part I

Optical Applications

3

Rare-earth doped metal oxide nanomaterials for optical applications

This chapter consists in a general introduction to RE doped metal oxides and their applications in the field of optics. Firstly, an overview about the interest of nanomaterials for optical applications and the project that motivated Part I of this Thesis is presented. Subsequently, the relevance of metal oxide nanomaterials and the effect of host matrixes on optically active dopant ions are detailed. Finally, the most important optical features of RE ions and the main non-radiative mechanisms that can take place are included.

3.1. Introduction

As previously described in Chapter 1, nanomaterials have experienced an increasing interest in a wide range of fields. Among them, optics could be considered the most popular one due to the noteworthy number of applications in this research area [1,2]. For such a purpose, there are different types of available optical nanomaterials. Plasmonic nanomaterials present size and shape-dependent optical properties, and the ability of transforming chemical/physical stimulus into optical signals, which results of great interest for diagnostics, therapeutic technologies, and spectroscopic applications [3,4]. Likewise, quantum dots also present tunable optical features because of the effect of their size and shape on emission and absorption processes [5,6]. These materials exhibit remarkable properties such as high stability, large stokes shift and emission tunability, which makes them very promising when compared with organic dyes [7,8]. Some interesting applications include bioimaging, photonics and optoelectronics [9,10,11]. Additionally, luminescent NPs doped

with optically active RE or TM ions also allow to develop new optical devices like plasma display panels, field emission displays, cathode ray tubes, X-ray detectors, LEDs or fiber lasers, to name a few [12,13,14,15]. Specifically, RE-doped NPs show several advantages, namely narrow emission lines, high color purity and long emission lifetimes [16,17]. Moreover, the luminescent features of these materials are only slightly affected by the environment [18]. In this regard, the use of metal oxides as host matrix is an interesting approach to embed RE ions. Some of their most relevant advantages include simple fabrication, non-hazardous nature, remarkable chemical and thermal stability, and high band gap, resulting in suitable transparency in the Vis range [1,2,19,20].

This Part I, devoted to RE-doped metal oxide nanomaterials for optical applications, which comprises Chapters 3, 4 and 5, has been developed within the NanoCrystals in Fibre Lasers (NCLas) project. NCLas is a Future and Emerging Technologies (FET) project (Proposal: 829161 H2020-FET-OPEN), funded by the European Commission, whose main goal is to develop new fiber lasers based on novel hybrid nanosintering processes [21]. For such a purpose, the fabrication of new optical materials based on the incorporation of functional crystalline NPs into a mixture of amorphous glass NPs is sought. The combination of these materials has been pursued for a long time due to their remarkable properties. Specifically, NPs doped with intentional impurity ions present a wide variety of optical properties such as narrow emission lines, high quantum efficiencies or numerous laser transitions along the spectral range, to name a few [22,23]. On the other hand, multicomponent oxide glasses exhibit outstanding chemical resistance, tunable refractive index, appropriate optical quality and reduced fabrication cost [24]. Thus, the combination of these independent components is a promising strategy to obtain high-quality hybrid optical materials at a reduced fabrication cost. Besides, their individual preparation processes allow for a precise and flexible control of NP size and crystal phase. Figure 3.1 depicts a general representation of the fabrication process developed in the frame of the mentioned NCLas project. Firstly, optical NPs and glass NPs are prepared independently. Then, both materials are mixed at RT and sintered with the use of the minimum heat to melt the mixture without achieving the point of liquefaction, hence allowing the optical NPs to survive and keep their original functionality.

Nevertheless, as the first-ever implementation of this new nanosintering process, some difficulties have arisen during the fabrication

process. Firstly, due to the high temperatures required during the melting process, certain glass matrixes have induced optical NPs dissolution, thus promoting a mixture of phases and loss of functionality. Furthermore, such optical NPs have also boosted nucleation and crystallization of the glass NPs, resulting in undesired scattering losses. To overcome these obstacles, some strategies such as modifying functional NPs or glass NPs composition to increase compatibility, or the use of core-shell structures to protect the functional NPs have been considered within the NCLas project. However, the study of compatibility and stability of both functional and glass NPs is beyond the scope of this Thesis. In this sense, this Thesis focuses on the initial steps of the fabrication process of the mentioned novel hybrid optical materials, specifically on the synthesis and optimization of the optically active NPs as well as on the fabrication of optical composites by means of PLD technique as an alternative for laser waveguide preparation.

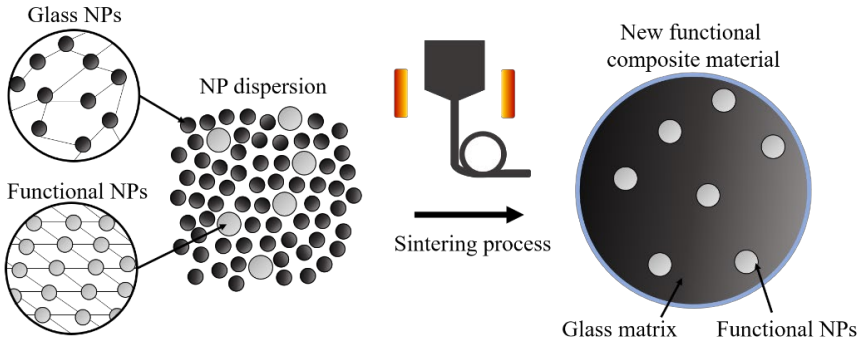

Figure 3.1. Schematic representation of the fabrication process of novel hybrid optical materials based on functional NPs and glass NPs carried out within the NCLas project.

3.2. Optical properties of doped insulating materials

Optical materials based on doped insulators consist of two components: i) host material, and ii) activators or dopant ions. The former has two different roles. Firstly, the host matrix presents a passive role by defining the spatial location of the dopant ions. Secondly, it also takes part in the luminescent behavior of the material by influencing the optical properties of the dopants. In this sense, the energy levels and the kinetics of the luminescence processes of the activator can be altered by the selected host matrix [25].

As described in Chapter 1, metal oxide NPs are promising candidates as host matrix. Concretely, their high chemical stability results of great interest since they may keep their original properties at high temperatures under diverse chemical environments. In fact, this feature makes metal oxide NPs a very suitable lattice for optical applications, and, specifically, for the ultimate goal of the NCLas project.

3.2.1. Optical centers in a static crystalline environment

The spectroscopically active ions intentionally introduced within the structure of a host matrix to induce new optical features can also be referred as "optically active centers". Accordingly, the impact of the host matrix on the optical features of the dopant ion, when compared with those of the corresponding free ion, can be understood by means of the coordination complex idea, AB_n. In such a structure, a dopant ion A (the central ion) is surrounded by lattice ions B (ligand ions) at a distance *a*. An octahedral arrangement is commonly employed for optical dopants in solids, as depicted in Figure 3.2. Assuming the ideal static situation where the distance *a* remains fixed and B ligands act as point charges, an electric field will be generated, leading to a perturbation of the central ion A. This interaction is defined as crystal field, and the Hamiltonian can be written as [26,27]:

$$H = H_{FI} + H_{CF} \qquad \text{(eqn. 3.1)}$$

where H_{FI} and H_{CF} are the Hamiltonians related to the free ion A and the crystal field, respectively. The latter results from the interaction of the valence electrons of A with the electrostatic field generated by B ligands. Additionally, the free ion term can be written as:

$$H_{FI} = H_0 + H' + H_{SO} \qquad \text{(eqn. 3.2)}$$

where H_0 is the central field Hamiltonian (effect of the electric field caused by the inner and outer-shell electrons on the valence electrons), H' is related to Coulomb interactions over outer electrons, and H_{SO} represents the spin-orbit interactions.

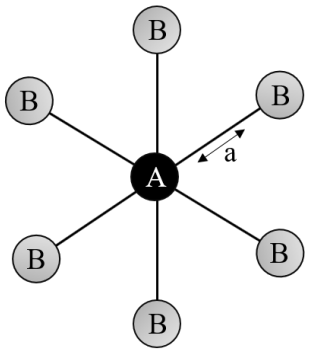

Figure 3.2. Schematic representation of an optically active center, AB_6.

Three different approaches can be considered depending on the relative importance of the crystal field term H_{CF} when compared with the remaining three terms relative to the free ion:

- Weak crystal field: $H_{CF} << H_{SO}, H', H_0$. The energy levels of the free ion A are slightly affected by the crystal field. In this sense, H_{CF} acts as a perturbation of the $^{2S+1}L_J$ states. This approach is very suitable for trivalent RE ions whose optically active *4f* ions are shielded from the field generated by B ligands by the outer filled *5s* and *5p* shells.
- Intermediate crystal field: $H_{SO} << H_{CF} < H'$. In this case the crystal field interaction dominates over the spin-orbit, which is initially neglected, and it is considered as a perturbation of the $^{2S+1}L_J$ states. TM ions as centers in some crystals are included in this approach.
- Strong crystal field: $H_{SO} < H' < H_{CF}$. The crystal field interactions dominate over both spin-orbit and electron-electron interactions. This also applies for TM ions in some crystalline environments and for *f-d* transitions of RE ions.

3.2.2. The configurational coordinate diagram

For the previous description of the effect of the host lattice on the optical features of the dopant ion by means of crystal field theory, an ideal static model was assumed. However, in real optical centers the central ion A is located in the dynamic environment of a vibrating lattice, thus experiencing changes in its electronic states. Consequently, a new term considering the lattice, H_L, must be included in the Hamiltonian:

$$H = H_{FI} + H_{CF} + H_L \qquad \text{(eqn. 3.3)}$$

Taking into account this coupling between the dopant ion A and the dynamic lattice, the resulting effect on the optical spectra can be studied through the configurational coordinate diagram [18]. Such a diagram represents the potential energy curves of the ground and excited electronic states of the central ion as a function of the configurational coordinate, Q.

Figure 3.3 displays a simplistic representation of such a coupling where only the vibrational modes of B ligands are considered. In this sense, the potential energy curves can be described by parabolas in line with the harmonic oscillator approximation. The lowest parabola represents the ground state, whose minimum is located at Q_0. Likewise, the excited state is also represented by a parabola. It should be noted that a slight shift of its equilibrium distance Q_0' is promoted as a consequence of changes in the chemical bond [18,28].

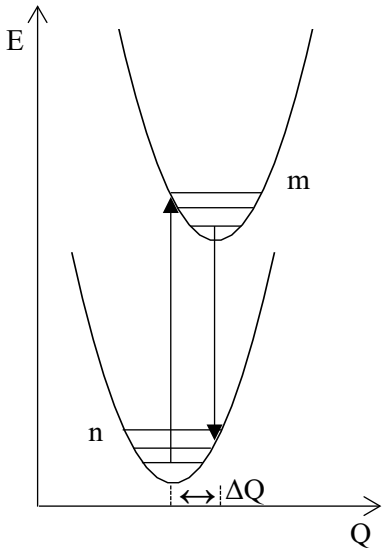

Figure 3.3. Configurational coordinate diagram of the AB_6 optically active center.

The electronic transitions are represented in the diagram as vertical lines. Accordingly, assuming that this system is at 0 K, so the lowest vibrational level (n = 0) is the only one populated, absorption takes place from this 0 level to the edge of the upper parabola, *i.e.*, the excited state. Conversely, emission occurs from the lowest level of the excited state parabola (m = 0) to the ground state, showing its maximum value at lower energies than the absorption process. This is known as *Stokes shift* and results of great relevance so absorption and emission bands do not overlap, and thus reabsorption processes of the optical center can be avoided. This shift is usually measured by means of the displacement of the parabolas' minimum, $\Delta Q = Q_0' - Q_0$. Therefore, since ΔQ also represents the strength of the coupling interaction between the electrons of the dopant ion A and the vibrations, the larger ΔQ, the broader the absorption bands, and thus the stronger lattice-ion coupling. Furthermore, the band broadening will also be increased by high temperatures, since these promote the population of other vibrational levels of the ground state (n = 1, 2…) [27,28].

3.2.3. Light absorption and emission processes

The transitions between energy levels may lead to different processes. Absorption occurs when transitions from lower energy levels to higher energy levels take place, while transitions to lower energy levels give rise to emission

processes. The former needs the atom to absorb the required energy to be promoted to a higher energy state, thus absorption is a stimulated process. Conversely, since atoms have a natural tendency to return to the ground state and lose the excess energy, emission can be referred to as spontaneous emission. This relaxation from excited states can occur through different mechanisms: radiative and non-radiative processes [27]. When a purely radiative transition takes place, the spontaneous emission between two energy levels is determined by the Einstein A coefficient. If the excited state presents a population N at a time *t*, the radiative emission rate is described as:

$$\left(\frac{dN}{dt}\right)_{radiative} = -AN \qquad \text{(eqn. 3.4)}$$

$$N(t) = N(0)\, e^{\left(-\frac{t}{\tau_{rad}}\right)} \qquad \text{(eqn. 3.5)}$$

where τ_{rad} is the radiative lifetime of such a spontaneous emission.

In this sense, the emission of photons at a given time is proportional both to the Einstein coefficient and to the number of optical centers in the excited state [27].

3.2.4. Non-radiative transitions

As previously described, despite the optically-active nature of RE or TM ions, non-radiative processes, which compete with radiative de-excitation, can also take place when the center returns to the ground state. Accordingly, these can be classified in three categories [18,26,28]:

- Multiphonon relaxation: This de-excitation mechanism is the most relevant competing process against emitting relaxation. The electronic excitation is partially transformed into vibrational energy. In this sense, multiphonon relaxation takes place down to the lowest excited state (for instance, from m = 2 to m = 0, Figure 3.3). Hence, if radiative emission occurs, it takes place from this lowest excited state (m = 0, Figure 3.3). This relaxation mechanism can be explained though the configurational coordinate diagram when strong electron-lattice coupling exists, *i.e.*, in TM systems, where there is a crossover point of the ground state and excited state parabolas. On the other hand, in the case or RE ions, due to their weak coupling interaction resulting from the *4f* electrons shielding,

no such a crossover from the parabolas is generated. Therefore, these ions present a small stokes shift, *i.e.*, the parabolas are almost parallel and the optical spectrum consists of sharp lines from pure electronic transitions. Besides, according to the so-called energy gap's law, in the case of *f-f* transitions of RE ions, multiphonon relaxation processes are dominant when the energy separation between excited levels is lower than six times the maximum energy phonon of the host material.

- Energy transfer: Non-radiative energy transfer occurs when an excited center, referred as donor (D^*), returns to the ground state (D) by transmitting the absorbed excitation energy to a second center located nearby, denominated acceptor (A). Consequently, the center A is promoted to an excited state A^*, from which this new excited center returns to the ground state by emitting its characteristic radiation. A schematic representation of the mechanism is as follows:

$$D^* + A \rightarrow D + A^*$$

The energy transfer has been described to occur via two different processes, namely dipole-dipole interaction and exchange interaction. Such processes are *D-A* distance dependent, the latter requiring very short *D-A* distances to take place.

- Concentration quenching: An expected consequence of an increased ion concentration would be an improved emission intensity due to the higher number of emitting centers. However, this is certain up to a concentration limit, from which the intensity starts to decrease. This threshold is defined as concentration quenching, and it is a consequence of the reduced distance between optical centers, thus favoring energy transfer mechanisms. It can be attributed to the presence of defects or trace ions that may act as acceptors, referred to as killers or quenching traps. Additionally, migration of the emission energy can occur among identical optical centers by means of cross relaxation processes due to resonant energy transfer. As a result of the different non-radiative processes, relaxation becomes no longer purely radiative. Thus, it is important to consider that the measured lifetime τ includes both radiative and non-radiative rates, and therefore τ can be expressed as [18,29]:

$$\frac{1}{\tau} = \frac{1}{\tau_{rad}} + \frac{1}{\tau_{nonrad}} \qquad \text{(eqn. 3.6)}$$

In most real cases, deviations from single exponential behavior of the emission decay intensity, which is proportional to the density of centers per unit time $(dN/dt)_{radiative}$ (eqn. 3.4), can be expected.

3.3. Sesquioxides as host materials

RE oxides, RE_2O_3 (RE = lanthanide, Y, Sc), also referred to as sesquioxides, are a promising group of materials due to their unique chemical and physical properties. In particular, RE sesquioxides present high thermal conductivity (almost twice as high as that of YAG), which allows to carry out an efficient extraction of heat even for high-power lasers. Besides, their low phonon energy minimizes non-radiative relaxation processes, resulting in larger energy storage times and improved optical performance. All these features together with their wide transparency range from the UV to the mid-IR and their lower refractive index make RE sesquioxides very promising materials as host matrix for applications in the field of optics [20,30,31].

RE sesquioxides can be found as five different polymorphs (A-, B-, C-, H-, and X-RE_2O_3) depending on the cation and temperature. Specifically, below 2000 ºC, the following three crystalline phases can be obtained [32,33,34]:

- A-type (hexagonal, $P\bar{3}m1$): Stable structure for RE = La, Ce, Pr, and Nd.
- B-type (monoclinic, $C2/m$): Stable structure for RE = Sm, Eu, and Gd. However, these can also exist in the C-form.
- C-type (cubic, $Ia3$): Stable structure for RE = Tb, Dy, Ho, Er, Tm, Yb, Lu, Y, and Sc.

3.3.1. Yttrium oxide

Among all the available RE sesquioxides, yttrium oxide or yttria (Y_2O_3) is an interesting candidate as host matrix for the aforementioned applications. Specifically, the maximum phonon energy in bulk yttria is 600 cm^{-1} [35]. Besides, this material presents a wide transparency range from 0.2 to 8 µm with a band gap of 5.6 eV, making it optically inert in the Vis and mid-IR spectral range [30,36].

Y_2O_3 crystallizes in the cubic C-type phase, which is its most stable form almost until its melting temperature (*ca*. 2400 ºC) [37]. Figure 3.4 displays the body-centered bixbyite cubic structure containing twice the primitive cell, *i.e*., a total of 80 atoms. The oxygen atoms are located on the 48e sites, while Y^{3+} cations are present in six-fold coordination occupying two non-equivalent sites, C_2 (non-centrosymmetric) and S_6 (centrosymmetric). Specifically, 24 out of the total 32 sites exhibit C_2 symmetry (at 24d Wyckoff position), while the remaining 8 show S_6 symmetry (at 8b Wyckoff position). Thus, the C_2:S_6 site ratio is 3:1. Trivalent optically active RE ions are incorporated randomly to both crystallographic sites when substituting Y^{3+} [38,39]. In this sense, the spectroscopic behavior of the introduced dopant is expected to differ from one site to another, thus enabling to tune the optical properties of the material.

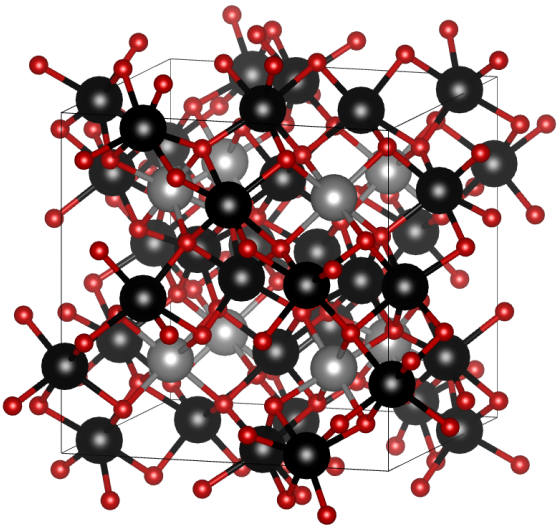

Figure 3.4. Unit cell of C-Y_2O_3, with the two available crystallographic sites (black, C_2; gray, S_6) for Y^{3+} ions. O^{2-} is plotted in red.

3.4. Rare earth ions

Lanthanides, commonly referred to as RE elements, comprise those located in the sixth period of the periodic table after lanthanum, where the filling of the 4*f* valence orbital begins. These elements are usually incorporated in crystals as ions upon ionization. In this regard, +3 is the most stable oxidation state, $[Xe]4f^{n-1}$ being its electronic configuration. For some electronic configurations, RE ions can also be present in +4 and +2 stable valence states. Interestingly,

these 4*f* electrons are responsible for the optical transitions of RE ions, thus leading to different luminescent properties as a function of the oxidation state. Trivalent RE ions may lack *5d*, *6s* and some *4f* electrons, experiencing sublevel transitions within the *4f* electronic configuration. Conversely, divalent RE ions, which possess an additional electron when compared with RE^{3+} ions, present $f \rightarrow d$ interconfigurational optical transitions; hence, displaying different spectroscopic behavior [18,40].

3.4.1. Optical properties of trivalent rare earth ions in crystals

As previously described, electrons from the unfilled *4f* shell, screened by the filled *5s* and *5p* outer shells, are responsible for the optical transitions of RE^{3+} ions. As a consequence of this shielding effect, *4f* valence electrons are predominantly unaffected by the ligand ions in the surroundings, as they are located deeper into the ion, resulting in sharp emission bands from the *f-f* transitions similar to the free ions. In this regard, the effect of the crystal field is minor and spin-orbit transitions are stronger due to electrons closer to the nucleus: $H_{cryst} < H_{SO}$ [18,25]. This dominant effect of the spin-orbit interaction leads to slight perturbations of the $^{2S+1}L_J$ states of RE^{3+} ions when these are incorporated into crystals. Consequently, the effect of the crystal field promotes small energy shifts of such states, and the resulting spectrum is barely affected when RE^{3+} ions are incorporated into different host matrixes [18].

Figure 3.5 displays the Dieke diagram, which is a very useful tool to predict or to assign energy transitions of a RE^{3+} optical spectrum. Specifically, the Dieke diagram illustrates the energy of the $^{2S+1}L_J$ states of the different RE^{3+} ions in $LaCl_3$ as host matrix. The magnitude of the crystal field splitting is represented by the width of the lines, while the center of gravity of each multiplet shows the approximated position of the $^{2S+1}L_J$ states of the free ion. Both energy splitting and center of gravity of the multiplets can be slightly affected when changing from $LaCl_3$ to another host matrix. However, most characteristics remain unmodified. Additionally, the previously determined light-emitting levels can be identified from the represented semicircles below the multiplet lines.

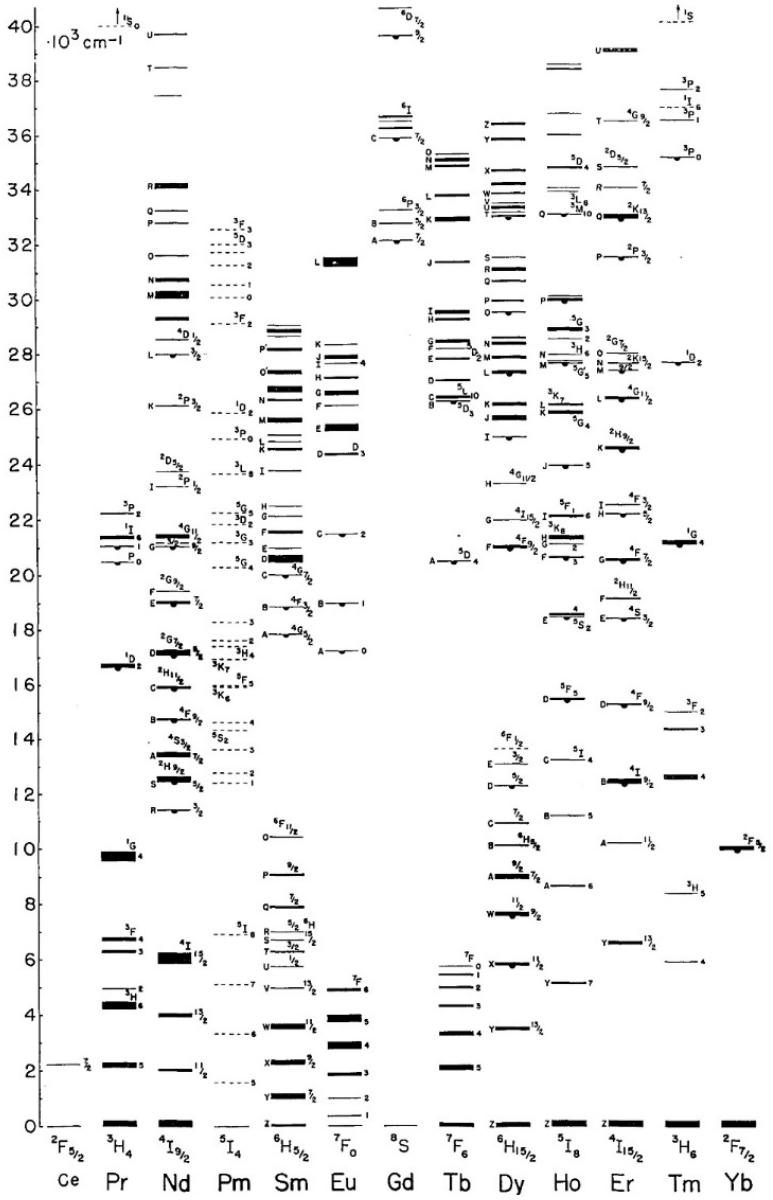

Figure 3.5. Dieke diagram for trivalent RE ions in $LaCl_3$ [41]. The width of the lines indicates the crystal-field splitting. Semicircles represent the emitting levels.

Different transitions can be identified from the obtained absorption and emission spectra of RE^{3+} ions in crystals, which can be classified in two categories: intraconfigurational and interconfigurational. The former occur

within the *4f* shell. Therefore, due to the weak crystal field effect, the intraconfigurational transitions are barely affected by the surrounding ligands and covalency effects. As a result, the shift between the coordinate diagram parabolas from the ground and excited states is very small or zero; hence, resulting in weak and narrow absorption and emission lines. Although *f-f* transitions are parity-forbidden, they become partially allowed as a consequence of the non-inversion symmetry of the crystal field. On the other hand, two types of interconfigurational transitions can be considered. Firstly, $4f^n \rightarrow 4f^{n-1}5d$ transitions, which are more common for RE^{3+} ions with tendency to gain an electron and become RE^{2+}. This leads to intense and broad absorption and emission bands, generally in the UV region, given that they are parity-allowed transitions. Secondly, the charge transfer interconfigurational transitions can be observed when RE^{3+} ions are incorporated into a crystal. In this case, a charge-transfer state is generated from which an allowed transition to the $4f^n$ occurs. Specifically, excitation takes place from the RE^{3+} ground state to the charge-transfer state of a ligand of the host matrix, such as Cl^- or O^{2-} anions. Subsequently, de-excitation occurs to the excited state of the RE^{3+} ion via non-radiative process. Emission is then originated from the excited state parabola of the RE^{3+} to the lowest parabola, that is, the RE^{3+} ground state. This last transition is detected in the resulting spectrum in the form of emission lines [18,25].

3.4.2. Praseodymium

Praseodymium in trivalent state (Pr^{3+}) results of great interest owing to its efficient luminescent emission in a wide range of wavelengths, from the Vis to the near-IR spectral regions. Both interconfigurational and intraconfigurational transitions can occur when doping inorganic host lattices with Pr^{3+} ions, resulting in diverse applications. Among them, Pr^{3+} transitions have been used as scintillators thanks to the allowed $5d \rightarrow 4f$ transitions. On the other hand, blue and red emissions of Pr^{3+} hold suitable potential for lasing applications, while IR emission can be employed for optical amplification [42,43,44,45].

Within the frame of the NCLas project, Pr^{3+}-based lasers were proposed as an alternative to the currently used laser systems, such as Ti:sapphire or optical parametric oscillators. These lasers show high performance, but they are not suitable to be used in facilities like hospitals due to their high cost, use complexity and bulky volume. Conversely, fiber lasers are compact, efficient and meet the optical requirements for biophotonics. However, the existing fiber

lasers present an important limitation regarding their emission wavelengths, which are out of the biomedical optical windows. In this context, the proposed Pr^{3+}-doped yttria fiber laser represents an alternative solution to overcome such constraints by covering both the first and second biological windows.

References

1 Gupta, S. K.; Sudarshan, K.; Kadam, R. M. Optical nanomaterials with focus on rare earth doped oxide: a review. *Mater. Today Commun*. **2021**, *27*, 102277.

2 Bharmoria, P.; Ventura, S. P. M. Optical applications of nanomaterials. In: *Nanomaterials for healthcare, energy and environment*. Springer, 2019.

3 Valenti, M.; Jonsson, M. P.; Biskos, G.; Schmidt−Ott, A.; Smith, W. A. Plasmonic nanoparticle-semiconductor composites for efficient solar water splitting. *J. Mater. Chem. A* **2016**, *4*, 17891–17912.

4 Kravets, V. G.; Kabashin, A. V.; Barnes, W. L.; Grigorenko, A. N. Plasmonic surface lattice resonances: a review of properties and applications. *Chem. Rev*. **2018**, *118*, 5912–5951.

5 Baker, S. N.; Baker, G. A. Luminescent carbon nanodots: emergent nanolights. *Angew. Chem., Int. Ed*. **2010**, *49*, 6726–6744.

6 Yoffe, A. D. Semiconductor quantum dots and related systems: electronic, optical, luminescence and related properties of low dimensional systems. *Adv. Phys*. **2001**, *50*, 1–208.

7 Resch-Genger, U.; Grabolle, M.; Cavaliere-Jaricot, S.; Nitschke, R.; Nann, T. Quantum dots versus organic dyes as fluorescent labels. *Nat. method*s **2008**, *5*, 763–775.

8 Chen, Y.; Rosenzweig, Z. Luminescent CdS quantum dots as selective ion probes. *Anal. Chem*. **2002**, *74*, 5132–5138.

9 Wolfbeis, O. S. An overview of nanoparticles commonly used in fluorescent bioimaging. *Chem. Soc. Rev*. **2015**, *44*, 4743–4768.

10 Huang, Y.; Duan, X.; Lieber, C. S. Nanowires for integrated multicolor nanophotonics. *Small* **2004**, *1*, 142–147.

11 Konstantatos, G.; Badioli, M.; Gaudreau, L.; Osmond, J.; Bernechea, M.; de Arquer, F. P. G.; Gatti, F.; Koppens, F. H. L. Hybrid graphene–quantum dot phototransistors with ultrahigh gain. *Nat. Nanotechnol*. **2012**, *7*, 363–368.

12 Urquhart, P. Review of rare earth doped fibre lasers and amplifiers. *IEE Proc*. *J. Optoelectron*. **1988**, *135*, 385–407.

13 Kim, C. H.; Kwon, I. E.; Park, C. H.; Hwang, Y. J.; Bae, H. S.; Yu, B. Y.; Pyun, C. H.; Hong, G. Y. Phosphors for plasma display panels. *J. Alloys Compd*. **2000**, *311*, 33–39.

14 Ronda, C. R. Recent achievements in research on phosphors for lamps and displays. *J. Lumin*. **1997**, *72*, 49–54.

15 Leskelä, M. Rare earths in electroluminescent and field emission display phosphors. *J. Alloys Compd*. **1998**, *275*, 702–708.

16 Bouzigues, C.; Gacoin, T.; Alexandrou, A. Biological applications of rare-earth based nanoparticles. *ACS Nano* **2011**, *5*, 8488–8505.

17 Ninjbadgar, T.; Garnweitner, G.; Börger, A.; Goldenberg, L. M.; Sakhno, O. V.; Stumpe, J. Synthesis of luminescent ZrO_2:Eu^{3+} nanoparticles and their holographic sub-micrometer patterning in polymer composites. *Adv. Funct. Mater*. **2009**, *19*, 1819–1825.

18 García Solé, J.; Bausá, L. E.; Jaque, D. *An introduction to the optical spectroscopy of inorganic solids*. John Wiley & Sons Ltd, 2005.

19 Chavali, M. S.; Nikolova, M. P. Metal oxide nanoparticles and their applications in nanotechnology. *SN Appl. Sci*. **2019**, *1*, 607.

20 Sanghera, J.; Kim, W.; Villalobos, G.; Shaw, B.; Baker, C.; Frantz, J.; Sadowski, B.; Aggarwal, I. Ceramic laser materials: past and present. *Opt. Mater.* **2013**, *35*, 693–699.

21 *NanoCrystals in Fibre Lasers*. https://www.nclas.eu . (Accessed 05-06-2023).

22 Weber, M. J.; Rare earth lasers. In: *Handbook on the physics and chemistry of rare earths*. North-Holland, 1979.

23 Reisfeld, R.; Jørgensen, C. K. *Lasers and excited states of rare earths*. Springer Berlin, 1977.

24 Wang, W. C.; Zhou, B.; Xu, S. H.; Yang, Z. M.; Zhang, Q. Y. Recent advances in soft optical glass fiber and fiber lasers. *Prog. Mater. Sci*. **2019**, *101*, 90–171.

25 Ruvalcaba Cornejo, C. Luminescence in rare earth ion-doped oxide compounds. In: *Luminescence - An outlook on the phenomena and their applications.* InTech, 2016.

26 Henderson, B.; Imbusch, G. F. *Optical spectroscopy of inorganic solids*. Clarendon Press, 1989

27 Fox, M. *Optical properties of solids*. Oxford University Press, 2001.

28 Blasse, G.; Grabmaier, B. C. *Luminescent materials*. Springer-Verlag, 1994.

29 Morris, D. E.; de Bettencourt-Dias, A. Spectroscopic techniques and instrumentation. In *Luminescence of lanthanide ions in coordination compounds and nanomaterials*. John Wiley and Sons Ltd, 2005

30 Kränkel, C.; Uvarova, A.; Guguschev, C.; Kalusniak, S.; Hülshoff, L.; Tanaka, H.; Klimm, D. Rare-earth doped mixed sesquioxides for ultrafast lasers. *Opt. Mater. Express* **2022**, *12*, 1074–1091.

31 Bär, S.; Petermann, K.; Huber, G. Sesquioxides as host materials for rare-earth-doped bulk lasers and active waveguides. In: *Rare earth oxide thin films. Topics in applied physics*. Springer, 2006.

32 Zinkevich, M. Thermodynamics of rare earth sesquioxides. *Prog. Mater. Sci*. **2007**, *52*, 597–647.

33 Warshaw, I.; Roy, R. Polymorphism of the rare earth sesquioxides[1]. *J. Phys. Chem*. **1961**, *65*, 2048–2051.

34 Roth, R. S.; Schneider, S. J. Phase equilibria in systems involving the rare-earth oxides. Part I. Polymorphism of the oxides of the trivalent rare-earth ions. *J. Res. Natl. Bur. Stand. A Phys. Chem*. **1960**, *64A*, 309–316.

35 De Mello Donegá, C.; Meijerink, A.; Blasse, G. Non-radiative relaxation processes of the Pr^{3+} ion in solids. *J. Phys. Chem. Solids* **1995**, *56*, 673–685.

36 Das, G. K.; Tan, T. T. Y. Rare-earth-doped and codoped Y_2O_3 nanomaterials as potential bioimaging probes. *J. Phys. Chem. C* **2008**, *112*, 11211–11217.

37 Swamy, V.; Dubrovinskaya, N. A.; Dubrovinsky, L. S. High-temperature powder X-ray diffraction of yttria to melting point. *J. Mater. Res*. **1999**, *14*, 456–459.

38 Mandel, M. Paramagnetic resonance of Yb^{3+} in yttrium oxide. *Appl. Phys. Lett*. **1963**, *2*, 197–198.

39 Concas, G.; Spano, G.; Bettinelli, M.; Speghini, A. Distribution of Eu^{3+} dopant ions in C_{3i} and C_2 sites of the nanocrystalline Sc_2O_3:Eu phosphor. *Z. Naturforsch. A* **2008**, *63*, 210–216.

40 De Bettencourt-Dias, A. *Luminescence of lanthanide ions in coordination compounds and nanomaterials*. John Wiley & Sons Ltd, 2014.

41 Dieke, G. H. *Spectra and energy levels of rare earth ions*. Wiley Interscience Publishers, 1968.

42 Mallur, S. B.; Babu, P. K. Optical properties of praseodymium (Pr^{3+}) doped bismuth boro-tellurite glasses containing CdSe nanoparticles. *Mater. Res. Bull*. **2022**, 111651.

43 Rodnyĭ, P. A.; Mishin, A. N.; Potapov, A. Luminescence of trivalent praseodymium in oxides and fluorides. *Optic Spectrosc.* **2002**, *93*, 714–721.

44 Liang, Y. J.; Liu, F.; Chen, Y. F.; Wang, X. L.; Sun, K. N.; Pan, Z. W. Red/near-infrared/short-wave infrared multi-band persistent luminescence in Pr^{3+}-doped persistent phosphors. *Dalton Trans.* **2017**, *46*, 11149–11153.

45 Zhuravleva, M.; Novoselov, A.; Yoshikawa, A.; Pejchal, J.; Nikl, M.; Fukuda, T. Crystal growth and scintillation properties of Pr-doped $YAlO_3$. *Opt. Mater.* **2007**, *30*, 171–173.

4

Rare–earth doped yttria nanoparticles

This chapter describes the fabrication of rare-earth doped Y_2O_3 NPs using several bottom-up methods. The preparation procedure has been demonstrated to be critical for both the structural and optical properties of the obtained NPs. Considering such a matter, this study focuses on the assessment and optimization of synthesis procedures to achieve the best optical performance of the resulting material. It should be noted that this chapter includes the research performed within the NCLas project, focused on the development of new fiber lasers based on hybrid materials of functional NPs and glass NPs. Thus, several synthesis procedures and their respective parameters have been studied and compared to optimize the required structural and optical features of the NPs. To maximize the emission efficiency, the luminescence lifetime has been used as an accurate parameter to compare the Pr^{3+}-doped NPs prepared by different methods, since it does not depend on the configuration of the optical experimental setup.

The main goals of this chapter are:

1. To synthesize Y_2O_3:Pr^{3+} NPs by different synthesis methods.
2. To perform an in-depth structural and optical characterization of the as-prepared NPs.
3. To study the effect of different synthesis parameters for each procedure on the structural and optical features of the resulting nanomaterials.
4. To assess and determine the optimal concentration of Pr^{3+} ions to achieve the best optical performance of the NPs.

4.1. State of the art

As described in Chapter 3, RE-doped sesquioxides have experienced an increasing interest due to their remarkable optical and mechanical properties, offering a wide variety of applications. Among them, optics has proven to be the most popular, resulting in the development of fiber lasers, amplifiers, plasma display panels or fluorescence lamps [1,2,3,4]. In particular, numerous studies about Y_2O_3 doped with different RE ions for such optical applications have been published, namely Eu^{3+} [5,6,7,8], Er^{3+} [9,10,11], Yb^{3+} [12,13,14] and Tb^{3+} [15,16,17]. However, the number of publications is less abundant in the case of Pr^{3+}-doped yttria, despite its potential application in the first and second biological windows. In this sense, some of the synthesis methods employed to obtain Y_2O_3:Pr^{3+} NPs are laser heated pedestal growth [18], flame-fusion or Verneuil method [19], thermal decomposition [20], solvent evaporation [21], co-precipitation [22] or sol–gel [23]. Nevertheless, remarkable differences can be detected among the results presented in such studies. Specifically, variations regarding structural features such as NP size, dopant concentration, crystalline phase or presence of defects are observed, which have an ultimate effect on their optical properties, particularly emission intensity and lifetime.

In this context, as previously described, the NCLas project has as its main goal the fabrication of fiber lasers based on composite materials from the mixture of optically active Y_2O_3:Pr^{3+} NPs and glass NPs. However, some requirements must be considered for such an application. Firstly, a particular NP size as well as narrow NP dimension distribution is essential in order to avoid surface effects and light scattering processes [24,25]. On the other hand, maximizing RE emission efficiency is crucial. Specifically, given that the ultimate aim is to develop fiber lasers in which population inversion is necessary, achieving the longest possible emission decay rates results of great advantage [26]. Accordingly, NPs structural characteristics and the presence of surface contamination can be controlled by tuning the synthesis procedure to therefore enhance the optical response of the material [27,28]. Precisely, among all the available methods from both top-down and bottom-up approaches as described in Chapter 1, chemical synthesis routes allow for a more precise control of the fabrication conditions, and thus of the resulting properties of the material. Therefore, synthesis procedures deserve an in-depth systematic evaluation.

4.2. Synthesis of nanoparticles

Y_2O_3:Pr^{3+} NPs were prepared by five different adapted synthesis methods: combustion [29], molten salt [30], sol-gel Pechini [12], homogeneous precipitation [31], and solvothermal [32]. The effect of diverse parameters on the structural and optical properties of the as-prepared nanomaterials were studied. The synthesis conditions and the modified parameters for each procedure are described in this section.

4.2.1. Combustion method

$Y(NO_3)_3$ (2.61 mmol), the stoichiometric amount of $Pr(NO_3)_3$ for a given Pr^{3+} concentration and urea (6.82 mmol) were dissolved in deionized water (3 mL). The mixture was covered with a watch glass and heated up to 500 ºC for 10 min in a furnace. Then, the effect of annealing on the as-synthesized Y_2O_3:Pr^{3+} NPs was tested by calcinating the sample at 900 ºC for 4 h using a heating ramp of 5 °C/min.

Studied parameter: annealing.

4.2.2. Molten salt method

$Y(NO_3)_3$ (7.84 mmol) and the stoichiometric amount of $Pr(NO_3)_3$ for a given Pr^{3+} concentration were mixed and ground with $NaNO_3$ and KNO_3 (235.2 mmol each, 30 equivalents (eq) regarding total amount of RE) in an agate mortar for 15 min. The well-mixed powder was then heated up to 500 °C in a ceramic crucible for 3 h with a heating ramp of 5 °C/min. After naturally cooling down to RT, the so-obtained solid was washed with deionized water followed by centrifugation (5-10 washing cycles) until no crystallization of salts was observed in the supernatant. Afterwards, the purified Y_2O_3:Pr^{3+} NPs were dried o.n. at 100 °C.

Studied parameter: number of washing cycles.

4.2.3. Sol−gel Pechini Method

$Y(NO_3)_3$ (20 mmol) and the stoichiometric amount of $Pr(NO_3)_3$ for a given Pr^{3+} concentration were dissolved in deionized water (200 mL) under vigorous stirring. Then, citric acid or EDTA as a chelating agent (2 eq regarding the amount of lanthanides) was added over the obtained solution. The final mixture

was heated up to 90 ºC for 15 min. Afterwards, polyethylene glycol (2.01 mmol) was added to the solution, which was stirred at 90 °C for another 15 min. The obtained sol was kept at 90 °C for 24 h in a stove without stirring, leading to the formation of a gel. Finally, the gel was fired at the chosen temperature (800 or 900 °C) for the required time (16 or 24 h).

Studied parameters: chelating agent, annealing temperature, annealing time.

4.2.4. Homogeneous precipitation method

$Y(NO_3)_3$ (1.43 mmol) and the stoichiometric amount of $Pr(NO_3)_3$ for a given Pr^{3+} concentration were dissolved in deionized water (3 mL). Next, this solution was added over a well-stirred aqueous solution of urea in large excess (0.46-4.16 mol/L, 360 mL as final volume). The resulting mixture was heated up to 85 ºC for 45-180 min. After the reaction mixture was cooled down to RT, the solid was washed with deionized water and centrifuged three times. The solid was then suspended in EtOH (50 mL) to avoid the aggregation of preformed NPs and dried o.n. at 60 °C. Finally, the solid was fired at 800 °C for 3 h with a heating ramp of 5 °C/min.

Studied parameters: urea concentration, reaction time.

4.2.5. Solvothermal method

$Y(NO_3)_3$ (5.04 or 10.07 mmol) and the corresponding stoichiometric amount of $Pr(NO_3)_3$ for a given Pr^{3+} concentration were added to a mixture of a specific alcohol (EtOH or ethylene glycol (EG)) and deionized water (19:1, 60 mL as final volume). The resulting mixture was mildly heated up while stirring to dissolve the lanthanide salts. Next, the solution was introduced into a Teflon-lined stainless-steel autoclave, which was sealed and heated up at the chosen temperature (180 or 220 °C) for 24 h. Then, the reaction mixture was naturally cooled down to RT, and the so-obtained solid was washed and centrifuged with EtOH:H_2O (1:1) once, and with deionized water three additional times. Finally, the solid was dried o.n. at 70 °C in a stove and calcined at the chosen temperature (800, 900 or 1000 °C) for the required time (4 or 8 h) with a heating ramp of 5 °C/min.

Studied parameters: RE precursors concentration, alcohol, reaction temperature, annealing temperature and time.

4.3. Structural properties of nanoparticles

Initially and prior to the study and optimization of the synthesis methods and their respective parameters, a complete and general structural characterization of the material is presented. According to this, Y_2O_3:Pr^{3+} (0.1% mol) NPs were prepared through the five aforementioned procedures and characterized by means of XRD, TEM, and Raman and absorption spectroscopies before parameter optimization. In particular, the initial conditions studied in sections 4.3 and 4.5 of the evaluated methods were as follows:

- Combustion: No annealing applied.
- Molten salt: 5 washing cycles.
- Sol-gel Pechini: Citric acid as chelating agent, annealed at 800 ºC for 16 h.
- Homogeneous precipitation: 1.35 mol/L as urea concentration, 2 h as reaction time.
- Solvothermal: $RE(NO_3)_3$ (5.04 mmol), ethylene glycol (EG), reaction at 180 ºC, annealed at 800 ºC for 4 h.

Figure 4.1 shows the refined XRD patterns of NPs prepared using the described methods under the initial conditions, namely combustion, molten salt, sol-gel Pechini, homogeneous precipitation and solvothermal. As it can be observed, all of them fit perfectly to the single cubic Y_2O_3 crystalline phase, whereas no traces from remaining impurities were detected, pointing out the high purity these synthesis methods provide. Differences in terms of NP size can be expected from XRD peak broadening. In this regard, the effect of both the synthesis methods and their modified parameters on crystallite size will be discussed in section 4.4.

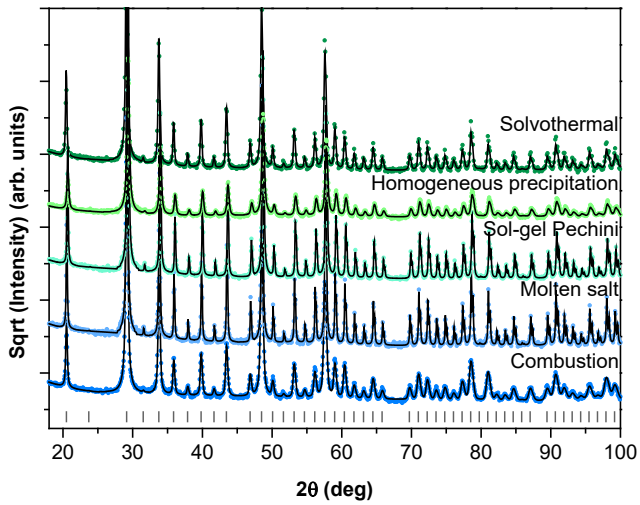

Figure 4.1. Rietveld refinement of XRD diffraction patterns of $Y_2O_3:Pr^{3+}$ (0.1% mol) NPs prepared by different synthesis methods. Vertical lines correspond to c-Y_2O_3 Bragg reflections.

Since all prepared NPs present the cubic Y_2O_3 crystalline structure, up to 120 vibrational modes can be expected from the crystal space group (T_h^7, $Ia\bar{3}$, Z=16) in the Raman spectra. The irreducible representations of the optical and acoustic vibrational modes are as follows [33,34]:

$$\Gamma_{op+ac} = 4\ A_g + 4\ E_g + 14\ T_g + 5\ A_{2u} + 5\ E_u + 17\ T_u,$$

Among these 120 modes, E and T modes are double and triple degenerate, respectively. 51 of them are grouped into 17 infrared active modes of T_u symmetry and 54 into 22 Raman active modes (4 A_g + 4 E_g + 14 T_g). Consequently, up to 22 lines would be expected in the Raman spectra. Nevertheless, only a reduced number of lines was experimentally observed, probably as a result of the superposition of different types of transitions.

Figure 4.2 displays the Raman spectra of the synthesized NPs. All samples present similar spectra whose Raman peaks observed in the 0-600 cm^{-1} range were assigned as reported in references [34,35], the most intense band being centered at around 376.4 cm^{-1} and attributed to a T_g vibration. On the other hand, Raman peaks detected below 200 cm^{-1}, *i.e.*, in the region of the external lattice vibrations, are associated to pure Y^{3+} vibrations [34].

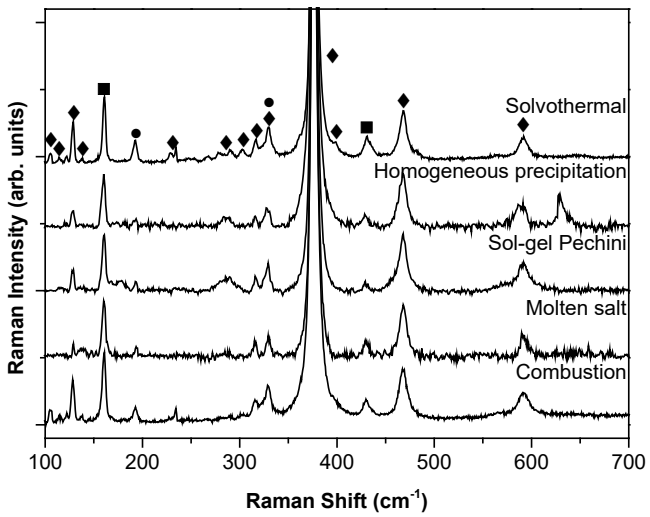

Figure 4.2. Normalized Raman spectra of Y_2O_3:Pr^{3+} (0.1% mol) NPs prepared through different synthesis methods. ♦: T_g mode; ■: A_g mode, ●: E_g mode.

Raman frequencies, peak width (full width at half maximum height, FWHM) and their symmetry assignment are collected in Table A.1 (Appendix A). The data were obtained by fitting the peaks to Lorentzian functions. No effect of either NP size or synthesis method on the FWHM Raman peaks was observed within the experimental resolution (0.6 cm^{-1}). A shift of the most intense band located at *ca.* 376.4 cm^{-1} towards lower frequencies would be expected upon decreasing the NP size [36]. However, this Raman peak did not present any remarkable displacement independently of the synthesis method or NP size, and thus there is no confinement effect due to the size (Figure 4.3).

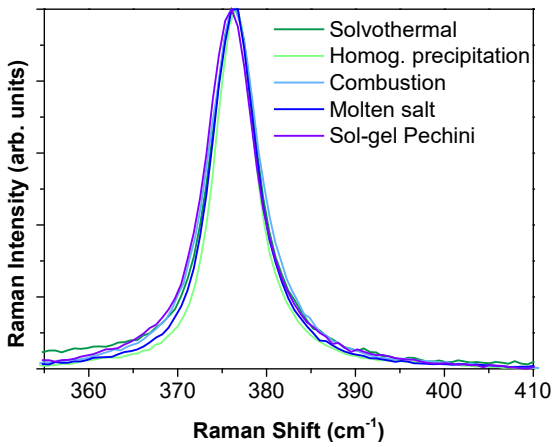

Figure 4.3. Comparison of the normalized most prominent Raman peak of Y_2O_3:Pr^{3+} (0.1% mol) NPs prepared through different synthesis methods.

Figure 4.4 shows TEM images of the prepared NPs by means of the five described methods. As it can be observed, different morphologies and size ranges can be obtained as a function of the selected synthesis route. Specifically, NPs synthesized through combustion procedure presented highly irregular shape, particle sizes below 10 nm and a noteworthy degree of aggregation, prior to annealing (Figure 4.4a). Conversely, molten salt method provided well-defined polyhedral NPs with increased average size, *ca*. 60 nm, and a good degree of crystallinity (Figure 4.4b). Likewise, sol-gel Pechini synthesis yielded crystalline, polyhedral NPs in the 30-40 nm range. However, a remarkable agglomeration was observed (Figure 4.4c). Spherical particles formed by the agglomeration of smaller NPs were obtained from the homogeneous precipitation method. These spherical particles showed a very good dispersion and average sizes of *ca*. 260 nm, while the smaller NPs presented an average size of *ca*. 20 nm (Figure 4.4d). Finally, solvothermal synthesis provided polyhedral NPs with some aggregation and an average size of *ca*. 30 nm (Figure 4.4e).

All things considered, the employed synthesis methods provided Pr-doped yttria NPs with different average sizes and morphologies, but the same crystalline structure and vibrational peaks, as confirmed by means of XRD, Raman spectroscopy and TEM measurements. The influence of the size will be discussed in the following sections of the chapter. Firstly, analyses in terms of particle size, size distribution and aggregation were carried out by evaluation of XRD patterns and TEM images, and they are presented in section 4.4. Secondly, the effect of these parameters is key to understand the optical properties of the prepared NPs, which will be discussed after the structural study, in section 4.6.

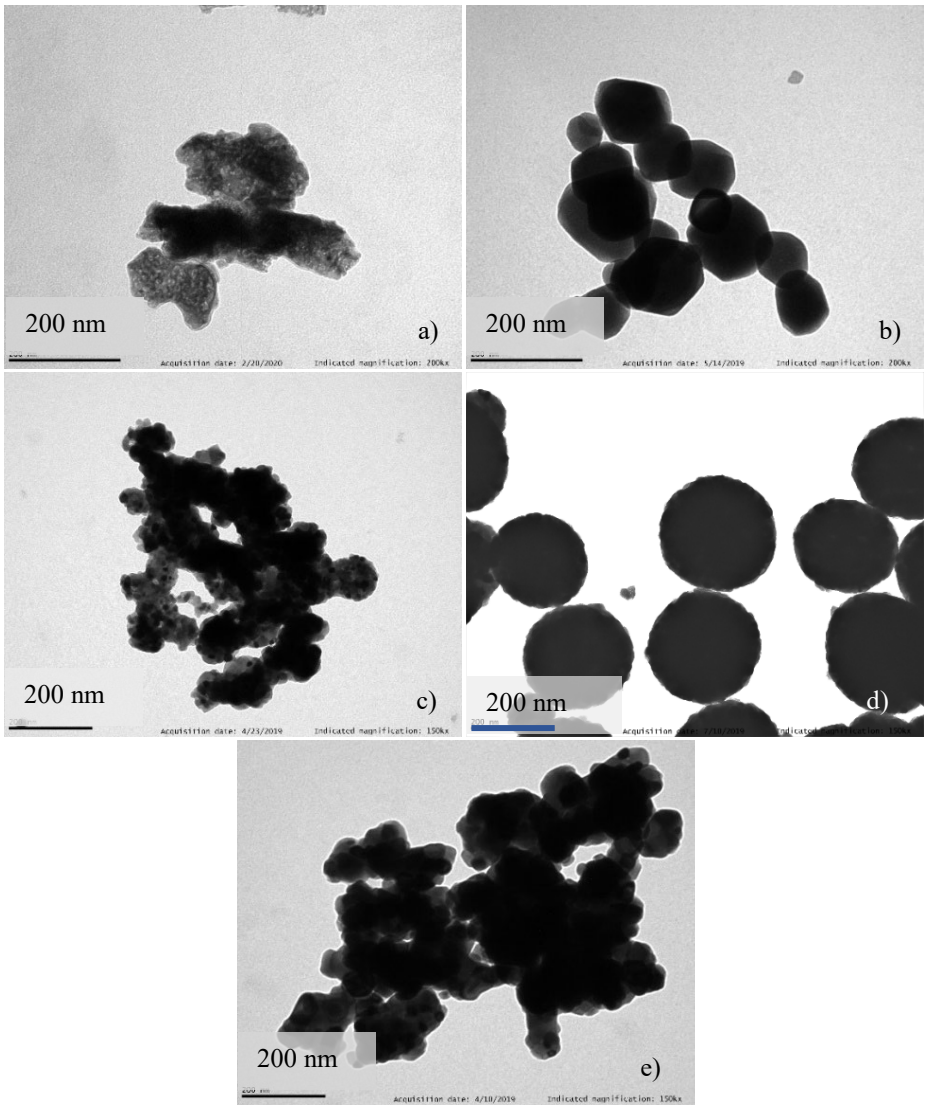

Figure 4.4. TEM images of Y_2O_3:Pr^{3+} (0.1% mol) NPs synthesized via: a) combustion; b) molten salt; c) sol-gel Pechini; d) homogeneous precipitation; e) solvothermal.

4.4. Effect of synthesis procedures on the structural properties of nanoparticles

4.4.1. Combustion method

For NPs prepared through the combustion method, only the influence of the thermal treatment was studied. Specifically, the as-prepared material was heated up to 900 ºC to increase crystallinity and particle size. Figure 4.5a displays the TEM image of the obtained NPs prior to the calcination step. This procedure provided highly agglomerated NPs before applying the thermal treatment, with particle sizes below 10 nm. Due to the reduced size of the obtained material, and in order to avoid surface effects, which are detrimental for the optical properties, a thermal treatment was applied to promote not only a better crystallinity but also to induce NP growth. Figure 4.5b displays a representative TEM image of the NPs calcined at 900ºC for 4 h. The annealed NPs showed a high agglomeration degree with particle sizes in the 10-40 nm range.

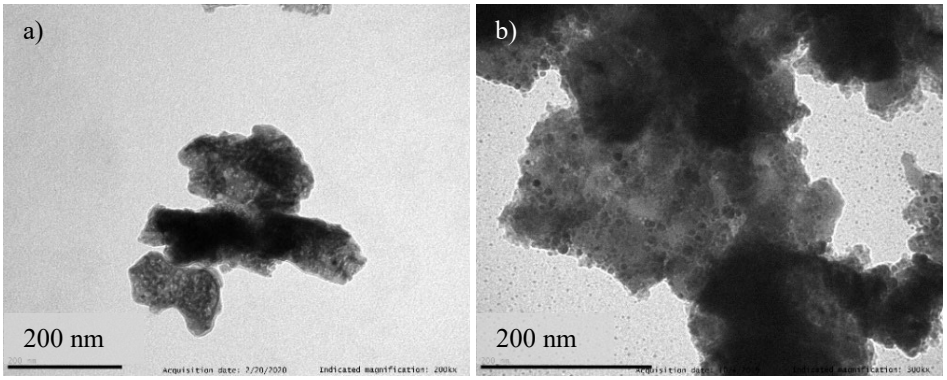

Figure 4.5. TEM images of Y_2O_3:Pr^{3+} (0.1% mol) NPs prepared by combustion method: a) without any thermal treatment; b) after annealing at 900 ºC for 4 h.

Figure B.1 (Appendix B) presents the XRD diffraction pattern and Rietveld refinement of the calcined Pr^{3+}-doped Y_2O_3 NPs. Only a single cubic phase (S.G. $Ia\bar{3}$) was used for the refinement and no impurity phases were detected within the experimental uncertainty. A particle size of 35 ± 5 nm was estimated from XRD analysis, in good agreement with TEM results.

4.4.2. Molten salt method

As previously described, the purification step is particularly relevant when preparing materials for optical applications. In this regard, although molten salt synthesis provides pure, single-phase products, it requires to remove remaining of the employed salts for eutectic mixtures. Therefore, the effect of washing cycles on the optical properties was studied.

Figure 4.6 shows the TEM images of NPs obtained by molten salt after 10 washing cycles. Such a method produces crystalline, polyhedral and well dispersed Y_2O_3: Pr^{3+} NPs, with an average size of 70 ± 20 nm. This result is in good agreement with the NP size obtained from XRD pattern refinement (77 ± 4 nm, Figure B.2). As expected, no structural variations were detected when modifying the number of washing cycles during the purification process, *i.e.*, after 5 cycles (Figure B.2).

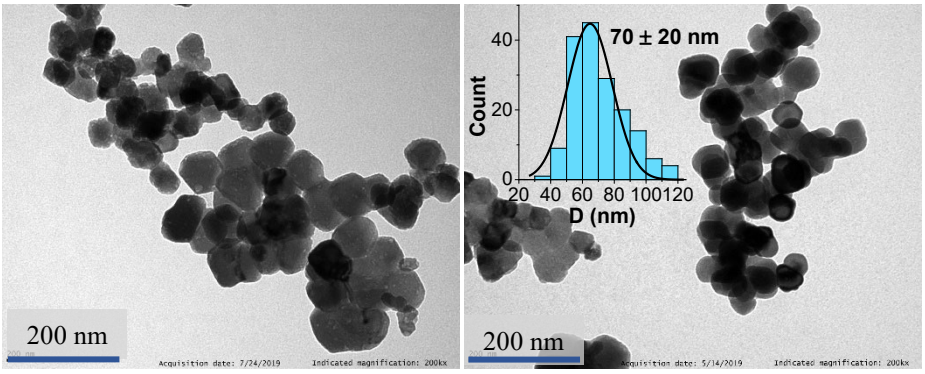

Figure 4.6. TEM image and average particle size of Y_2O_3:Pr^{3+} (0.1% mol) NPs prepared by molten salt method after 10 washing cycles.

4.4.3. Sol−gel Pechini method

For sol-gel Pechini method different parameters were modified to study their effect on the structural and optical properties of the prepared NPs. In this context, the type of hydroxyl carboxylic acid or chelating agent, together with the annealing conditions, *i.e.*, calcination time and temperature, were tuned and assessed (Table 4.1).

Initially, citric acid was employed as chelating agent. After gel formation, the sample was fired at 800 ºC for 16 h to yield the metal oxide NPs

(Table 4.1, entry 1). As observed from TEM images (Figure 4.7a), a presumably organic layer was formed around the $Y_2O_3:Pr^{3+}$ NPs, which promotes agglomeration under such preparation conditions. For this reason, the calcination time was increased up to 24 h, and no changes in the surrounding layer but a slight increase in NP size were observed by TEM (Figure 4.7b), in good agreement with XRD results (Figure B.3, Table 4.1, entry 2).

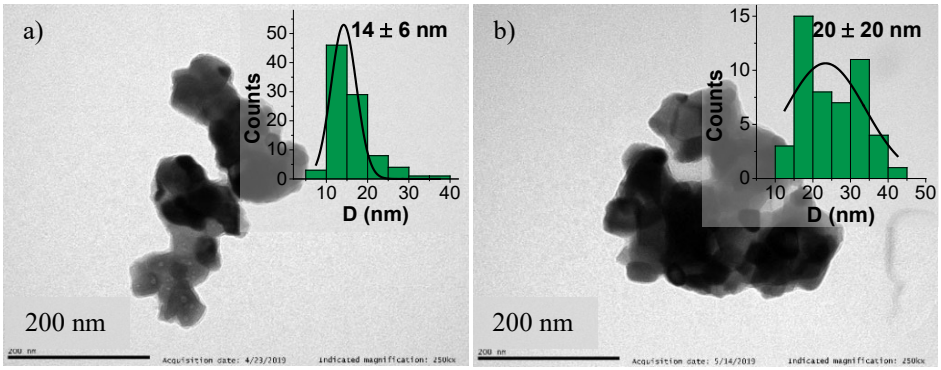

Figure 4.7. TEM images and average particle sizes of $Y_2O_3:Pr^{3+}$ (0.1% mol) NPs prepared by sol-gel Pechini method using citric acid as chelating agent and treating the NPs at 800 ºC for: a) 16 h and b) 24 h.

Table 4.1. Optimization parameters for the synthesis of $Y_2O_3:Pr^{3+}$ NPs by sol-gel Pechini method, and NPs size estimation.

Entry	CA	t_{CAL} (h)	T_{CAL} (ºC)	$Size_{TEM}$ (nm)	$Size_{XRD}$ (nm)	Observations
1	Citric acid	16	800	14 ± 6	27 ± 1	Surrounding organic layer; aggregated
2	Citric acid	24	800	20 ± 20	33 ± 1	Surrounding organic layer; aggregated
3	Citric acid	16	900	26 ± 6 60 ± 16	42 ± 3	Well dispersed
4	EDTA	16	900	40 ± 12	38 ± 2	Aggregated

CA: chelating agent; t_{CAL}: calcination time; T_{CAL}: calcination temperature.

On the other hand, after increasing the annealing temperature up to 900 ºC for 16 h, the complete removal of the surrounding layer was confirmed by TEM images (Figure 4.8). Under such synthesis conditions, the NPs presented polyhedral morphology and two size distributions, 26 ± 6 and 60 ± 16 nm (Table 4.1, entry 3). In addition, the crystallite size was determined via XRD

pattern refinement, providing an average size of 42 ± 3 nm (Figure B.4), which is in good agreement with TEM results.

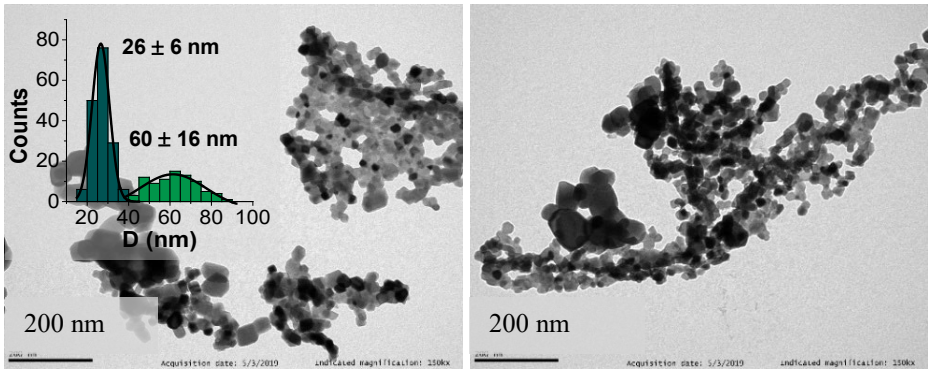

Figure 4.8. TEM images and average particle size of $Y_2O_3:Pr^{3+}$ (0.1% mol) NPs prepared by sol-gel Pechini method using citric acid as chelating agent and treating the NPs at 900 ºC for 16 h.

After optimizing the thermal treatment conditions, the effect of the chelating agent was analyzed and citric acid was replaced by EDTA, (Table 4.1, entry 4). In this case, the NPs presented a single size distribution with an average size of 40 ± 12 nm, which was estimated from TEM images (Figure 4.9) and matches with XRD results (38 ± 2 nm, Figure B.5). However, the use of EDTA as chelating agent proved to be detrimental for NPs dispersion, leading to a high degree of agglomeration.

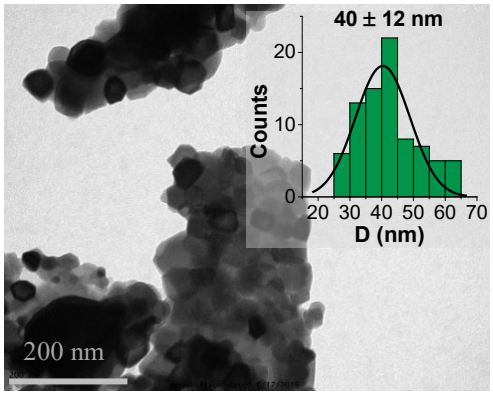

Figure 4.9. TEM image and average particle size of $Y_2O_3:Pr^{3+}$ (0.1% mol) NPs prepared by sol-gel Pechini method using EDTA as chelating agent and treating the NPs at 900 ºC for 16 h.

4.4.4. Homogeneous precipitation method

Homogeneous precipitation method is characterized for yielding well-dispersed, large spherical particles (200-300 nm) formed by smaller NPs with sizes ranging from 20 to 30 nm [31,37]. According to this, different parameters were modified and assessed to reduce the sphere size while maintaining the appropriate degree of dispersion and NPs size. Specifically, the influence of reaction time and urea concentration was analyzed. Figure 4.10 shows the obtained spheres with an average size of 260 ± 30 nm (and a residual amount of spheres with 100 ± 14 nm size) when using the non-tuned conditions described by Geitenbeek *et al*. [31], namely, 1.35 mol/L of urea and 2 h as reaction time (Table 4.2, entry 1). As previously described, these big and spherical particles are formed by smaller NPs, which was confirmed by XRD pattern refinement, providing an average crystallite size of 20 ± 2 nm (Figure B.6).

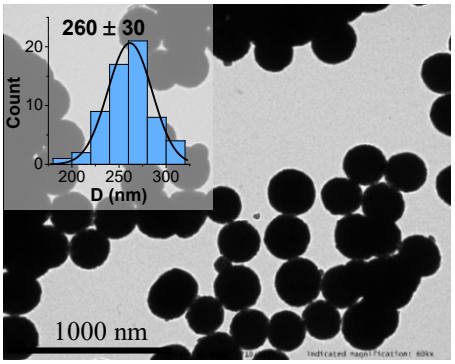

Figure 4.10. TEM image and average particle size of Y_2O_3:Pr^{3+} (0.1% mol) NPs prepared by homogeneous precipitation method using a urea concentration of 1.35 mol/L as originally described by Geitenbeek *et al*. [31].

Table 4.2. Optimization of urea concentration for the synthesis of Y_2O_3:Pr^{3+} NPs by homogeneous precipitation method.

Entry	[Urea] (mol/L)	$Size_{TEM}$ (nm)	$Size_{XRD}$ (nm)	Observations
1	1.35	260 ± 30	20 ± 2	Well-dispersed
2	0.46	340 ± 40	27 ± 3	Well-dispersed spheres
3	2.31	220 ± 30	21 ± 2	Well-dispersed spheres
4	3.93	170 ± 60 70 ± 40	22 ± 2	Well-dispersed spheres, two size distributions
5	4.16	160 ± 40 50 ± 14	22 ± 3	Well-dispersed spheres, two size distributions

Reaction time: 2h.

Firstly, the effect of urea concentration was evaluated. This synthesis parameter proved to have a critical impact on both dispersion and size of spherical NPs. In this sense, the initial urea concentration, 1.35 mol/L, was reduced to 0.46 mol/L (Table 4.2, entry 2), leading to an accused increase in the spherical particle size as detected via TEM images (Figure 4.11a). Indeed, very well-dispersed spheres of *ca*. 340 ± 40 nm were obtained in contrast to the average size of 260 ± 30 nm observed when using the original synthesis conditions (1.35 mol/L, Table 4.2, entry 1, Figure 4.10). On the other hand, the average crystallite size estimated by XRD showed a slight increase, being 27 ± 3 and 20 ± 2 nm for 0.46 and 1.35 mol/L of urea (Figure B.6), respectively. Conversely, when urea concentration was increased to 2.31 mol/L (Table 4.2, entry 3), a slight reduction in the size of spherical particles was detected. Accordingly, an average size of *ca*. 220 ± 30 nm was determined from TEM images (Figure 4.11b). No changes in terms of crystallite size were detected from XRD patterns, showing an average NP size of 21 ± 2 and 20 ± 2 nm for 2.31 and 1.35 mol/L of urea (Figure B.6), respectively. Interestingly, when a larger concentration of urea was employed, *i.e.*, 3.93 mol/L, two size distributions were observed (Table 4.2, entry 4). Specifically, the spheres experienced a decrease in size from 260 ± 30 nm to 170 ± 60 nm and 70 ± 40 nm (Figure 4.11c). However, the crystallite size did not undergo relevant differences (22 ± 2 nm) when compared with the original size of 20 ± 2 nm (Figure B.6). Finally, a further increase of urea concentration up to 4.16 mol/L (Table 4.2, entry 5) led to the formation of even smaller spherical particles with two size distributions, namely 160 ± 40 and 50 ± 14 nm (Figure 4.11d). In addition, no appreciable changes in terms of crystallite size were obtained, being 22 ± 3 and 20 ± 2 nm for 4.16 and 1.35 mol/L of urea (Figure B.6), respectively. Therefore, an excessive urea concentration (Table 4.2, entries 4 and 5) not only reduces the spherical particle size but also is detrimental for size homogeneity due to the remarkable promotion of ungrown nuclei.

Figure 4.12 displays particle size evolution as a function of urea concentration. As it can be observed, the average particle size decreases for higher urea concentrations. In this context, the use of an excess of urea leads to a noteworthy reduction of spherical NPs size until reaching a convergence size where a further increase of the amount of urea will not lead to smaller particles. This trend has already been reported by Fukushima *et al*. [38]. As described by the LaMer model (Figure 4.13) [39,40], the formation of nanoparticles in

solution consists in three main stages: i) rapid generation of monomers, ii) nuclei formation at supersaturation point, and iii) nanoparticle growth.

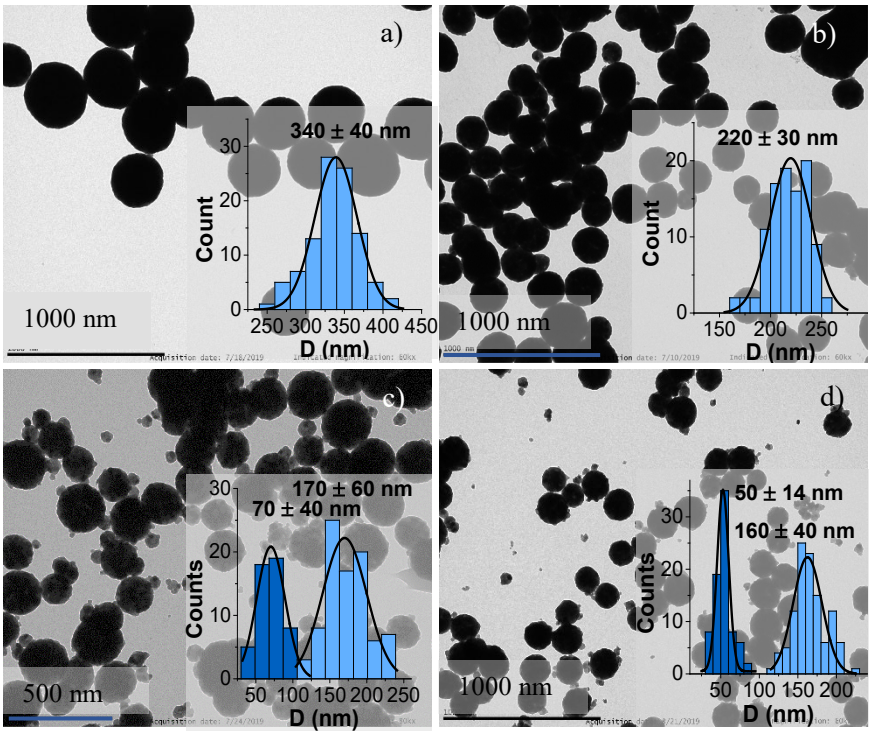

Figure 4.11. TEM images and average particle sizes of Y_2O_3:Pr^{3+} (0.1% mol) NPs prepared by homogeneous precipitation method using different urea concentrations. a) 0.46 mol/L, b) 2.31 mol/L, c) 3.93 mol/L, and d) 4.16 mol/L.

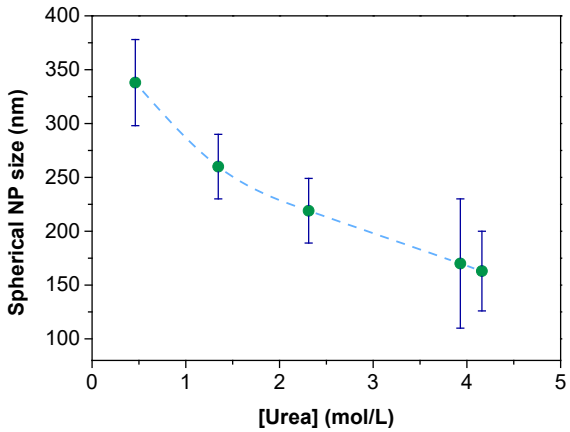

Figure 4.12. Average size of Y_2O_3:Pr^{3+} (0.1% mol) NPs prepared through homogeneous precipitation as a function of urea concentration. Dashed lines connecting dots are plotted just for reader's convenience.

According to this, a higher concentration of urea would increase the initial monomer production (Stage I), and thus the consumption of metal precursor. Consequently, the number of generated nuclei at Stage II would be larger and the final particle growth (Stage III) would be limited due to the lack of reactants [38]. As it can be observed from Figure 4.11, this model is in good agreement with our results, where an excess of urea led to:

- A remarkable reduction of the spherical NPs average size.
- An increased number of ungrown nuclei.
- A negligible effect on agglomeration.

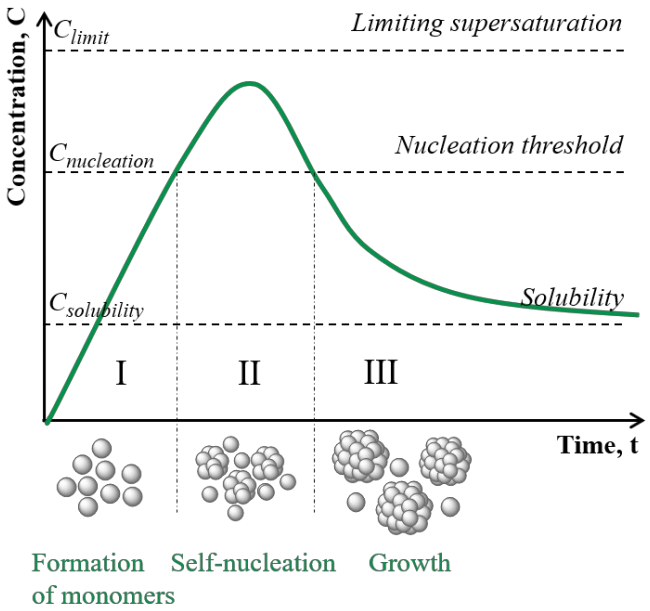

Figure 4.13. LaMer model for monodisperse nanoparticle formation.

Secondly, reaction time was also assessed. Specifically, 45-, 90-, 120- and 180-min reaction times were evaluated (Table 4.3). Figure 4.14 shows the TEM images of synthesized NPs under such conditions. No remarkable differences in terms of morphology or size were detected. Indeed, the spherical morphology remained stable at different reaction times, from 45 mins to 180 mins. Additionally, no particle growth or generation of new small NPs were detected when increasing reaction time, which indicates that: i) NP size converges at early reaction times, *i.e.*, 45 mins, regardless the reaction time

once precursors are consumed [6], and ii) the initial number of nuclei remains constant along the synthesis process [37].

Table 4.3. Optimization of reaction time for the synthesis of Y_2O_3:Pr^{3+} NPs by homogeneous precipitation method.

Entry	t_R (min)	$Size_{TEM}$ (nm)	Observations
1	45	270 ± 50	Well-dispersed spheres
2	90	250 ± 50	Well-dispersed spheres
3*	120	260 ± 30	Well-dispersed spheres
4	180	270 ± 60	Well-dispersed spheres

* Original conditions as described in reference [31]. Urea concentration: 1.35 mol/L.
t_R: reaction time.

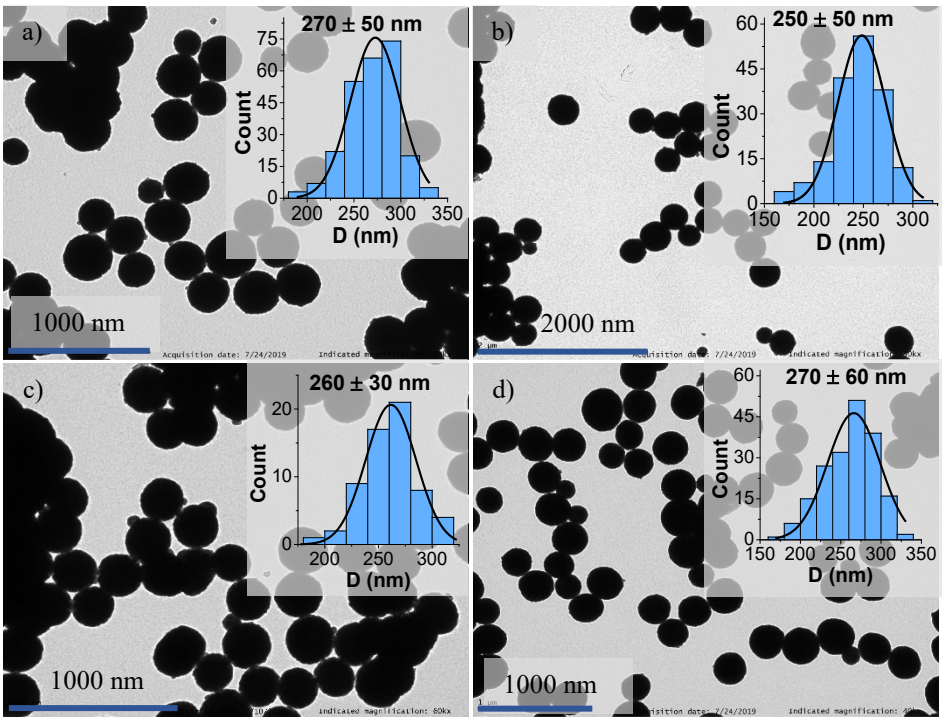

Figure 4.14. TEM images and average particle sizes of Y_2O_3:Pr^{3+} (0.1% mol) NPs prepared by homogeneous precipitation method, modifying reaction time. a) 45 mins, b) 90 mins, c) 120 mins, and d) 180 mins.

4.4.5. Solvothermal method

Finally, Y_2O_3:Pr^{3+} NPs were also synthetized via solvothermal method. The influence of several synthesis parameters, specifically RE precursors concentration, type of alcohol, reaction temperature, and annealing time and temperature, was studied. The original conditions described in reference [32] required the reaction mixture to be heated up to 180 ºC for 24 h in a Teflon-lined stainless-steel autoclave. Then, the resulting product was calcined at 800 °C for 4 h (Table 4.4, entry 1). NPs obtained under these conditions present polyhedral morphology, exhibiting some agglomeration and an average size of *ca*. 35 ± 20 nm as observed from TEM images (Figure 4.15a), in agreement with the crystallite size of 21 ± 1 nm estimated from XRD measurements (Figure B.7). Additionally, a surrounding layer was also detected.

Table 4.4. Optimization parameters for the synthesis of Y_2O_3:Pr^{3+} NPs by solvothermal method.

Entry	Alcohol	T_R (ºC)	T_{CAL}/t_{CAL} (ºC) / (h)	$Size_{TEM}$ (nm)	$Size_{XRD}$ (nm)	Observations
1	EG	180	800 / 4	35 ± 20	21 ± 1	Some aggregation, surrounding layer
2	EG	180	900 / 4	40 ±20	31 ± 3	Slight aggregation
3*	EG	180	900 / 4	40 ± 20	43 ± 3	Strong aggregation
4	EtOH	180	900 / 4	30 ± 14	–	Strong aggregation
5	EG	180	900 / 8	–	–	Strong aggregation
6	EG	220	900 / 4	45 ±18	36 ± 1	Slight aggregation
7	EG	220	1000 / 4	70 ± 30	53 ± 5	Slight aggregation

* Effect of twofold concentration of RE precursors. T_R: reaction temperature; T_{CAL}: calcination temperature; t_{CAL}: calcination time.

Firstly, in order to remove such a layer, the annealing temperature was increased up to 900 ºC (Table 4.4, entry 2). This modification did not have any effect on NP morphology, but promoted an increase in their average size up to 40 ± 20 nm, as observed from TEM images (Figure 4.15b), which was consistent with XRD analysis (31 ± 3 nm, Figure B.7). Additionally, the

surrounding layer was successfully removed. Secondly, the effect of RE precursors concentration was analyzed. In this context, the amount of RE-nitrates was doubled (Table 4.4, entry 3) to increase the average NP size to fulfill the particle size requirements within the NCLas project. As in the previous case, this increase in the amount of RE precursors did not seem to have any impact on the polyhedral morphology of the original NPs. XRD analysis showed a grain size of 43 ± 3 nm (Figure B.8), which was in good agreement with that observed by TEM (40 ± 20 nm, Figure 4.16), indicating NPs with single domain structure. Nevertheless, a noteworthy increase in NP aggregation was promoted.

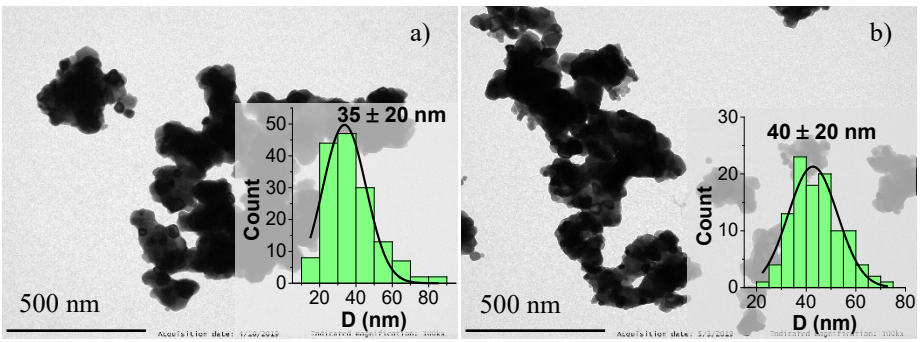

Figure 4.15. TEM images and average particle sizes of $Y_2O_3:Pr^{3+}$ (0.1% mol) NPs synthesized via solvothermal method at 180 ºC for 24 h followed by calcination at: a) 800 ºC for 4 h, and b) 900 ºC for 4 h.

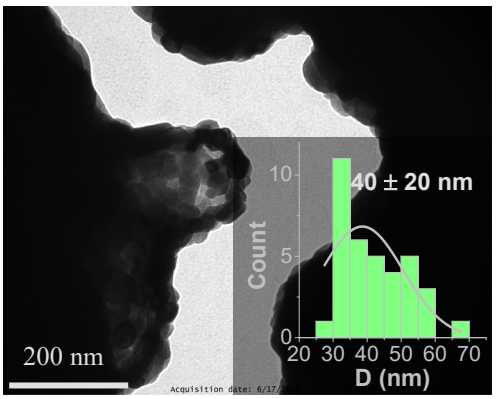

Figure 4.16. TEM image and average particle size of $Y_2O_3:Pr^{3+}$ (0.1% mol) NPs synthesized via solvothermal method at 180 ºC for 24 h using a two-fold RE precursors concentration (10.07 mmol), followed by calcination at 900 ºC for 4 h.

Afterwards, the effect of the alcohol was assessed by replacing EG with EtOH (Table 4.4, entry 4). The NPs showed a decrease in the average size down to 30 ±14 nm, as observed from TEM images (Figure 4.17). Unfortunately, the use of EtOH also seems to negatively impact NPs dispersion, leading to a strong increase in agglomeration and the presence of the above-mentioned surrounding layer.

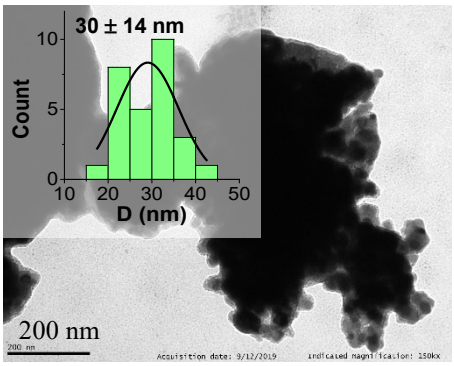

Figure 4.17. TEM image and average particle size of $Y_2O_3:Pr^{3+}$ (0.1% mol) NPs synthesized via solvothermal method at 180 ºC for 24 h using EtOH, followed by calcination at 900 ºC for 4 h.

After determining the optimal RE precursors concentration, annealing temperature and type of alcohol, the annealing time was also evaluated. In this way, the calcination time was increased up to 8 h (Table 4.4, entry 5). An increase in the average NP size was expected due to the longer crystal growth process. However, under such conditions, a dramatic promotion of NP agglomeration was observed, and therefore it was not possible to determine the NP average size from TEM images (Figure 4.18).

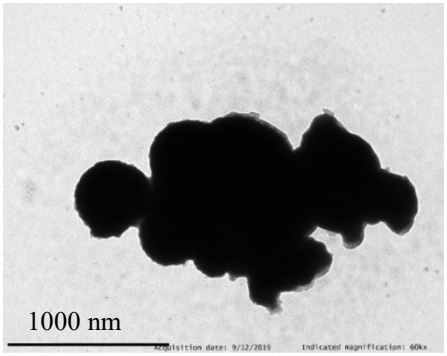

Figure 4.18. TEM image of $Y_2O_3:Pr^{3+}$ (0.1% mol) NPs synthesized via solvothermal method at 180 ºC for 24 h followed by calcination at 900 ºC for 8 h.

Finally, the effect of reaction temperature was studied. To this end, the autoclave temperature was increased up to 220 ºC for 24 h (Table 4.4, entry 6). Figure 4.19a displays the NPs obtained under such conditions, which present 45 ± 18 nm in size, while no surrounding layer was observed. An average crystallite size of 36 ± 1 nm was determined from the refined XRD pattern (Figure B.9), in line with TEM estimations. Additionally, the annealing temperature was also increased up to 1000 ºC to promote a larger particle size (Table 4.4, entry 7). In this case, TEM images (Figure 4.19b) showed polyhedral NPs with a slight agglomeration degree and an average size of *ca.* 70 ± 30 nm, in agreement with XRD results (53 ± 5 nm, Figure B.9).

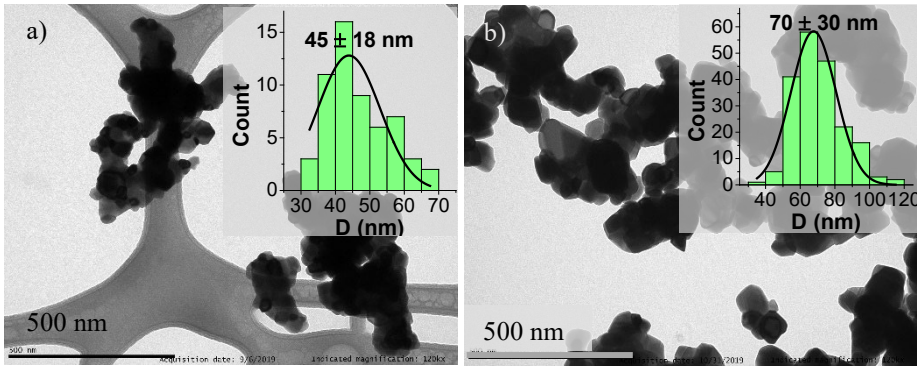

Figure 4.19. TEM images and average particle sizes of Y_2O_3:Pr^{3+} (0.1% mol) NPs synthesized via solvothermal method at 220 ºC for 24 h followed by calcination at: a) 900 ºC for 4 h, and b) 1000 ºC for 4 h.

4.5. Optical properties of nanoparticles

The optical properties of all Pr^{3+}-doped Y_2O_3 NPs prepared prior to optimization, as described at the beginning of section 4.3, were analyzed in detail by means of reflectance and luminescence spectroscopy. Specifically, Figure 4.20 shows the absorption spectrum of 1% mol Pr^{3+}-doped Y_2O_3 NPs obtained via sol-gel Pechini method [12] as a representative example. The spectrum is dominated by a broad band centered below 400 nm, ascribed to the interconfigurational $4f^2 \rightarrow 4f^15d^1$ transition of Pr^{3+} ions in the cubic Y_2O_3 host matrix. Low-intensity sharp peaks were also identified in the infrared region, which are assigned to *f-f* intraconfigurational transitions. Specifically, absorption peaks detected at *ca.* 1000 nm correspond to the transitions from the ground state to the $^1G_4$ excited state. In addition, the peaks located in the 1300-1800 nm region are attributed to transitions from the $^3H_4$ ground state to the ^3F_J

multiplets [20]. The jump in absorbance intensity at 800 nm is due to the change of detector and diffraction grating, not corrected by the baseline correction.

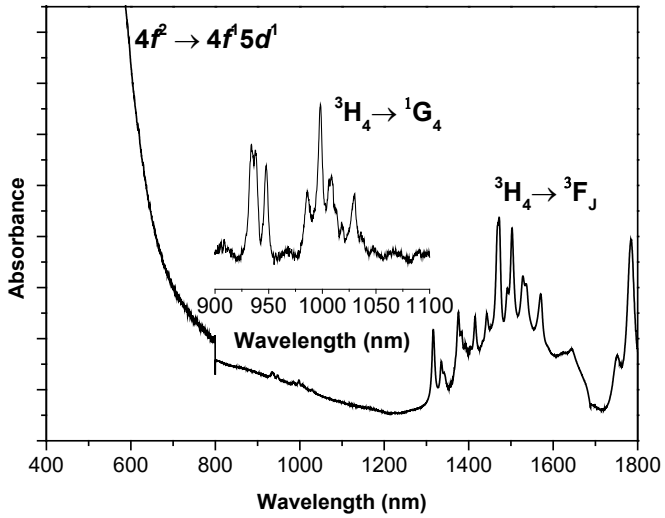

Figure 4.20. Absorption spectrum of Y_2O_3:Pr^{3+} (1% mol) NPs prepared through sol-gel Pechini method, as described in section 4.3.

In terms of luminescence, excitation and emission spectra of Pr^{3+} at the two available crystallographic sites (C_2 and S_6) were recorded for NPs prepared by the five studied synthesis methods. As a representative example, Figure 4.21 shows the RT excitation spectra of NPs obtained by the unmodified solvothermal method (section 4.3), monitoring the emission from the $^1D_2$ multiplet to the $^3H_4$ ground state (λ_{em} = 717 and 603 nm for C_2 and S_6, respectively). Spectra from both sites are dominated by broad bands in the UV region attributed to the interconfigurational $4f^2 \rightarrow 4f^1 5d^1$ transition of Pr^{3+}, considering that Y_2O_3 shows no absorption in this spectral range [20]. As reported by Aumüller *et al*. [22], this interconfigurational transition takes place at higher energies at C_2 sites than at S_6 sites for sesquioxides. According to this, the broad excitation band located at 280 nm is ascribed to Pr^{3+} ions at C_2 sites, whereas the band centered at 317 nm is assigned to Pr^{3+} ions at S_6 sites. Additionally, the sharp lines identified in the 430-520 nm range are attributed to the intraconfigurational transitions from the ground state to the ^3P_J + $^1I_6$ multiplets.

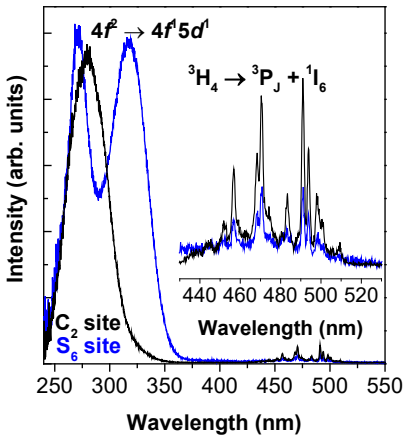

Figure 4.21. Excitation spectra at C_2 and S_6 sites (black, λ_{em} = 717 nm; blue, λ_{em} = 603 nm, respectively) of Y_2O_3:Pr^{3+} (0.1% mol) NPs prepared by solvothermal method as described in section 4.3. The inset shows a zoom of the intraconfigurational *f-f* transitions of Pr^{3+}.

Figure 4.22 compares the RT excitation spectra of NPs obtained by the five employed synthesis procedures. In terms of optical performance of the resulting materials, relevant differences arising from the synthesis procedure can be observed (Figure 4.22a and 4.22b). Among all the assessed samples, Y_2O_3:Pr^{3+} NPs obtained through the molten salt method presented the lowest intensity in the excitation spectra from both crystallographic sites. This can be attributed to the absence of thermal treatment, which eliminates remaining traces from precursors and salts and usually leads to more crystalline NPs. Conversely, NPs prepared by the sol-gel Pechini synthesis displayed the most intense excitation bands, which could be associated to their higher crystallinity as a result of the long calcination times (16 h).

Figure 4.23a shows the RT emission spectra of Y_2O_3:Pr^{3+} NPs prepared by the solvothermal method. Such spectra were generated upon direct excitation of Pr^{3+} in the UV region at 292 and 330 nm for ions located at C_2 and S_6 sites, respectively. As it can be observed, the emission spectrum of Pr^{3+} at C_2 sites is about an order of magnitude more intense than that from S_6 sites, which is in good agreement with their 3:1 ratio and the absence of inversion center for the C_2 site. Both emission spectra are dominated by peaks located between 600 and 670 nm which are ascribed to transitions from the $^1D_2$ excited state to the $^3H_4$ ground state. Additionally, transitions from the $^1D_2$ multiplet to the $^3H_5$ excited state were also detected in the 700-750 nm range. Furthermore, emission transitions in the IR spectral range from the $^1D_2$ multiplet to both the $^3H_6$ and $^3F_2$ excited states in the 820-910 and 920-970 nm ranges were recorded,

respectively. On the other hand, no resulting emission from the $^3P_0$ excited state was detected, as expected, this being a common feature of sesquioxides with cubic structure [20,41]. Figure 4.23b displays the schematic representation of the energy level diagram of Pr^{3+} obtained from the transitions detected in the emission spectra.

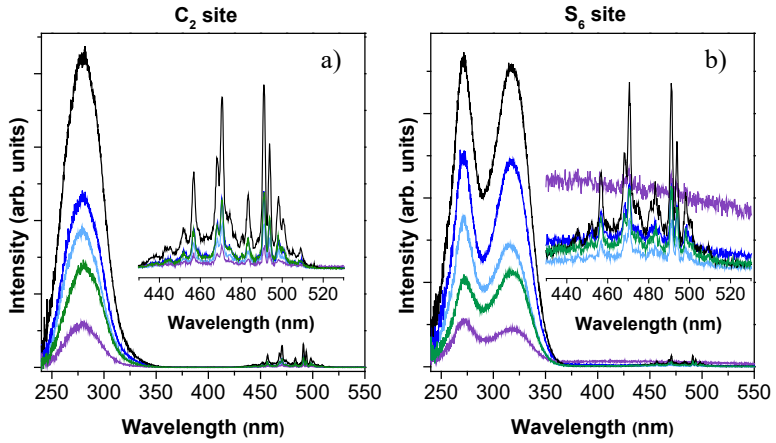

Figure 4.22. Excitation spectra at a) C_2 site (λ_{em} = 717 nm) and b) S_6 site (λ_{em} = 603 nm) of Y_2O_3:Pr^{3+} (0.1% mol) NPs prepared by combustion (light blue), molten salt (violet), sol-gel Pechini (black), homogeneous precipitation (green), and solvothermal (dark blue) synthesis as described in section 4.3.

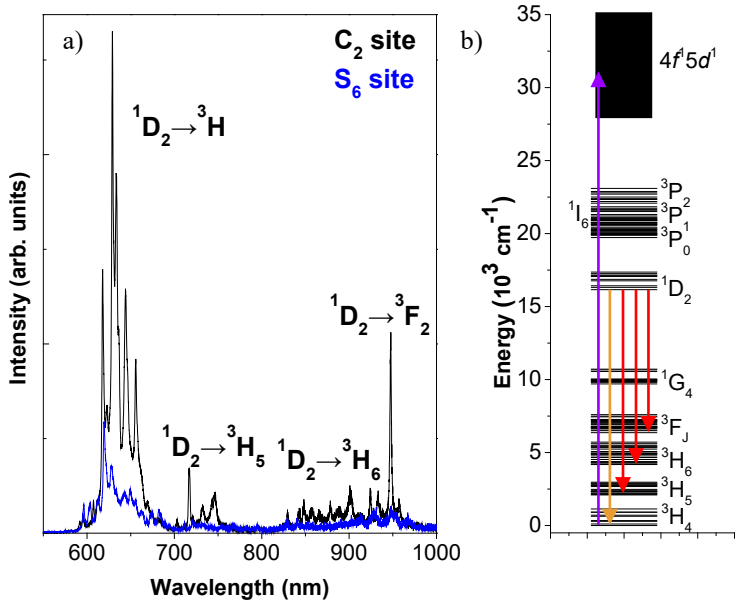

Figure 4.23. a) Emission spectra at C_2 and S_6 sites (black, λ_{exc} = 292 nm; blue, λ_{exc} = 330 nm, respectively) of Y_2O_3:Pr^{3+} (0.1% mol) NPs prepared by solvothermal synthesis as described in section 4.3; b) energy level diagram of Pr^{3+}.

Figure 4.24 compares the RT Vis emission spectra of NPs obtained by the different studied synthesis procedures at both C_2 and S_6 crystallographic sites. As in the case of the recorded excitation spectra, important differences in terms of intensity were detected in the Pr^{3+} emission spectra from both crystallographic sites. Likewise, Y_2O_3:Pr^{3+} NPs obtained by the molten salt method displayed the lowest intensity in both emission spectra, while NPs prepared through the sol-gel Pechini synthesis presented the most intense peaks. Apart from crystallinity, these differences in terms of intensity can be attributed to various features, such as Pr^{3+} distribution, size and surface effects. However, the luminescence intensity can be a complex magnitude to carry out comparisons among different samples. In this regard, the luminescence lifetime was selected as a more accurate parameter to perform a proper comparison of the optical properties after tuning synthesis conditions, since it does not depend on the geometry or configuration of the experimental setup.

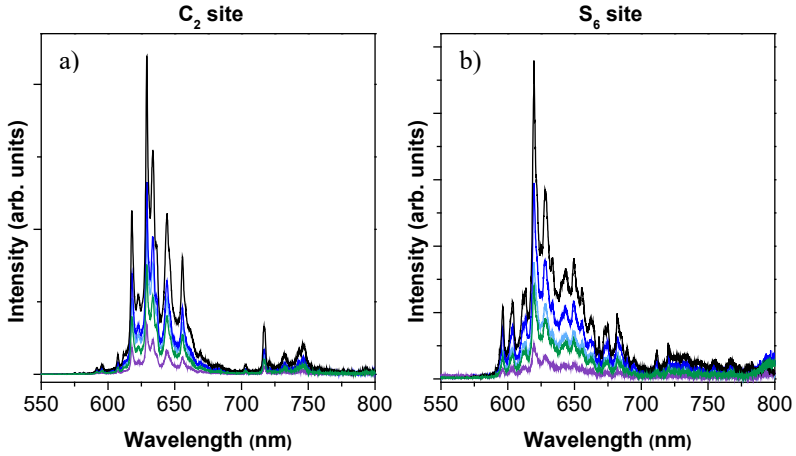

Figure 4.24. Emission spectra at a) C_2 (λ_{exc} = 292 nm) and b) S_6 (λ_{exc} = 330 nm) sites of Y_2O_3:Pr^{3+} (0.1% mol) NPs prepared by combustion (light blue), molten salt (violet), sol-gel Pechini (black), homogeneous precipitation (green), and solvothermal (dark blue) synthesis as described in section 4.3.

4.6. Effect of synthesis procedures on the optical properties of nanoparticles

As previously mentioned, the study of the optical performance of RE-doped oxides, and in particular the influence of the synthesis method on the luminescence properties of Pr^{3+}-doped Y_2O_3 NPs, holds great importance from both fundamental and applied points of view. In this regard, an in-depth study

and comparison of the optical quality of synthesized materials have been carried out. After optimization of the structural features of the NPs, the effect of these on the optical properties has been evaluated. Luminescence intensity is a complex magnitude for comparison purposes since it is highly dependent on the experimental setup configuration. Consequently, the average emission lifetime was chosen as a more accurate parameter to assess and quantitatively compare the optical properties of the synthesized NPs.

Time evolution of the $^1D_2 \rightarrow {}^3H_4$ emission transition detected at 629 nm was recorded after direct excitation into the ^3P_J manifold at 491 nm for all prepared samples. All luminescence decay curves were fitted to a double-exponential behavior that can be attributed to the excitation of both sites and the overlap of emission peaks (Figures 4.21 and 4.23a). Additionally, energy transfer between both crystallographic sites cannot be excluded at RT, which could also promote this bi-exponential behavior. Consequently, the shorter lifetime component is assigned to Pr^{3+} ions at the C_2 site, while the longer decay time corresponds to Pr^{3+} at the S_6 site [42,43].

Several parameters were tuned and optimized for the five studied synthesis methods not only to achieve the most suitable structural properties, but also to maximize the luminescence lifetime. Assuming that all the evaluated synthesis procedures promote a similar occupancy of both crystallographic sites, differences in terms of emission lifetime values can be ascribed to factors such as NP size, Pr^{3+} distribution, crystallinity, and remaining reagent traces or molecules adsorbed at the NPs surface.

Firstly, Figure 4.25 shows the luminescence decay curves of the Pr^{3+} $^1D_2 \rightarrow {}^3H_4$ emission transition at RT for Y_2O_3:Pr^3 NPs prepared via combustion and molten salt method. The NPs synthesized through the former procedure showed an increase in the average emission lifetime of *ca*. 50%, from 114 to 173 μs, after applying a thermal treatment at 900 ºC (Table 4.5, Figure 4.25a). This improvement can be attributed not only to a better crystallinity, but also to the complete removal of organic residues, which represents an important channel for non-radiative relaxation processes. Besides, calcination promoted particle growth from below 10 nm to *ca*. 40 nm, which had a positive effect on emission lifetime by reducing surface effects.

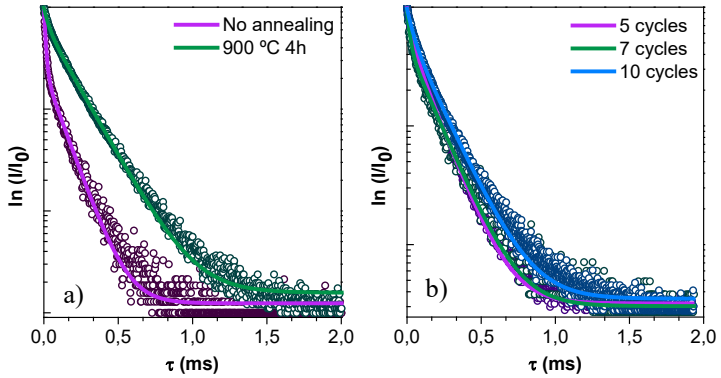

Figure 4.25. Luminescence decay curves of the Pr^{3+} $^1D_2 \rightarrow {}^3H_4$ emission of $Y_2O_3:Pr^{3+}$ (0.1% mol) NPs prepared by: a) combustion method, and b) molten salt method.

Table 4.5. Luminescence lifetime of the Pr^{3+} $^1D_2 \rightarrow {}^3H_4$ emission transition at RT for $Y_2O_3:Pr^{3+}$ (0.1% mol) NPs prepared by combustion method.

Entry	T_{CAL} (ºC)	τ (µs)
1	–	114
2	800	173

T_{CAL}: calcination temperature.

The previously described detrimental effect of remaining impurities on the optical properties was also observed for NPs prepared through molten salt method. In this case, the average emission lifetime experienced a progressive enhancement when the number of washing cycles was increased (Table 4.6, Figure 4.25b). Specifically, the estimated lifetime values after 5, 7 and 10 washing cycles were 128, 138 and 160 µs, showing an increase of 8 and 25%, respectively.

Table 4.6. Luminescence lifetime of the Pr^{3+} $^1D_2 \rightarrow {}^3H_4$ emission transition at RT for $Y_2O_3:Pr^{3+}$ (0.1% mol) NPs prepared by molten salt method.

Entry	Number of washing cycles	τ (µs)
1	5	128
2	7	138
3	10	160

Secondly, Figure 4.26 compares the obtained luminescence decay curves of NPs prepared via sol-gel Pechini. It was observed that longer times and higher temperatures during the annealing step had a positive effect on the luminescence average lifetime (Table 4.7, Figure 4.26a). Indeed, an improvement of *ca*. 10% was observed after extending the annealing process

from 16 h to 24 h, the average emission lifetimes values being 104 and 114 µs, respectively (Table 4.7, entries 1 and 2). A higher calcination temperature also led to a better optical performance of the material, obtaining an average emission lifetime of 118 µs when firing the sample at 900 ºC (Table 4.7, entry 3), exceeding the original result by 13%. The enhanced optical performance observed upon the annealing step optimization can be attributed to both the removal of the surrounding organic layer and to a better final crystallinity of the NPs. Next, the effect of the chelating agent was assessed. In this way, replacing citric acid by EDTA promoted a better result in terms of the average emission lifetime, leading to an increase of 20%, from 104 to 125 µs (Figure 4.26b, Table 4.7, entries 1 and 4). This lifetime enhancement can be ascribed to the monodisperse-size distribution shown by the NPs when using EDTA (see Figure 4.9). However, given that high aggregation was also promoted, the improvement in radiative lifetime was not remarkable enough to consider EDTA as a better chelating agent.

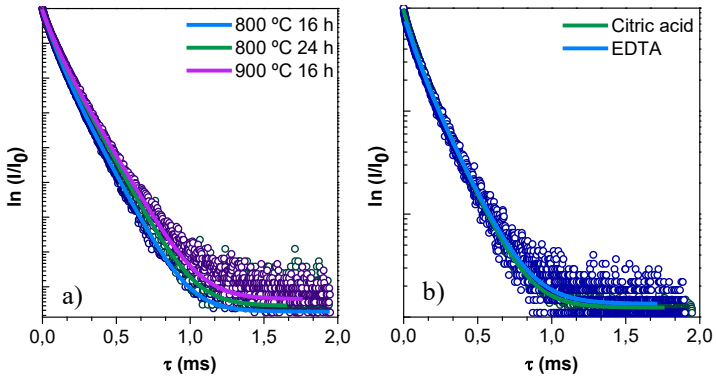

Figure 4.26. Luminescence decay curves of the Pr^{3+} $^1D_2 \rightarrow {}^3H_4$ emission of $Y_2O_3:Pr^{3+}$ (0.1% mol) NPs prepared by sol-gel Pechini method modifying: a) thermal treatment conditions, and b) chelating agent.

Table 4.7. Luminescence lifetime of the Pr^{3+} $^1D_2 \rightarrow {}^3H_4$ emission transition at RT for $Y_2O_3:Pr^{3+}$ (0.1% mol) NPs prepared by sol-gel Pechini method.

Entry	CA	t_{CAL} (h)	T_{CAL} (ºC)	τ (µs)
1	Citric acid	16	800	104
2	Citric acid	24	800	114
3	Citric acid	16	900	118
4	EDTA	16	900	125

CA: chelating agent; t_{CAL}: calcination time; T_{CAL}: calcination temperature.

Thirdly, Figure 4.27 presents the luminescence decay curves of NPs prepared via homogeneous precipitation. Such samples also showed relevant

differences regarding the optical properties when modifying the synthesis procedure. Interestingly, the unmodified conditions (1.35 mol/L of urea and a reaction time of 2 h) provided well-dispersed spheres with an average emission lifetime of 172 µs, remarkably higher than those measured for the synthesis methods previously described, namely combustion, molten salt and sol-gel Pechini, even after optimization of the synthesis conditions (Table 4.8, entry 1). However, tuning the synthesis parameters not only allowed a reduction of the spherical NPs size while keeping their optimal dispersion and crystallinity, but also an improvement of their luminescence decay rates. Specifically, urea concentration proved to be critical for the spherical NP size and dispersion, and thus changes regarding emission lifetime were expected. In this sense, different lifetimes ranging from 150 to 190 µs were obtained for different urea concentrations (Figure 4.27a, Table 4.8). However, even though a clear correlation between both parameters could not be accomplished as values did not follow any tendency, it is interesting to remark that most of the experiments provided longer emission decay rates than the original synthesis conditions.

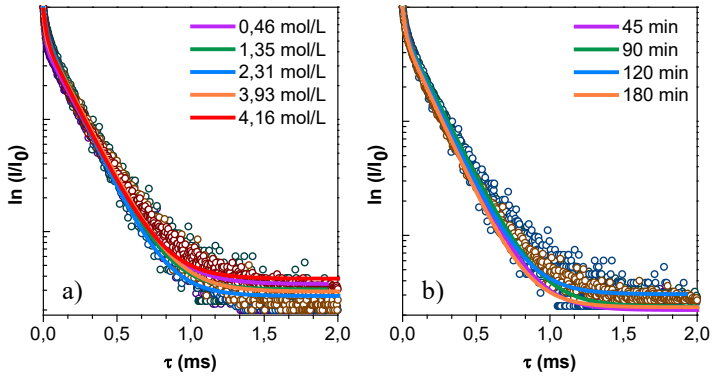

Figure 4.27. Luminescence decay curves of the Pr^{3+} $^1D_2 \rightarrow {}^3H_4$ emission of $Y_2O_3:Pr^{3+}$ (0.1% mol) NPs prepared by homogeneous precipitation method modifying: a) urea concentration, and b) reaction time

Table 4.8. Luminescence lifetime of the Pr^{3+} $^1D_2 \rightarrow {}^3H_4$ emission transition at RT of $Y_2O_3:Pr^{3+}$ (0.1% mol) NPs prepared by homogeneous precipitation method as a function of urea concentration.

Entry	[Urea] (mol/L)	τ (µs)
1	1.35	172
2	0.46	190
3	2.31	150
4	3.93	190
5	4.16	184

On the other hand, as previously observed from TEM images (Figure 4.14), reaction time had little effect on the spherical particle size. Accordingly, no remarkable changes were expected in the emission lifetime. In this sense, NPs prepared with different reaction times presented almost equal decay rate values, ranging from 172 to 179 µs (Table 4.9), as it can be noted from the superposition of decay curves (Figure 4.27b).

Table 4.9. Luminescence lifetime of the Pr^{3+} $^1D_2 \rightarrow {}^3H_4$ emission transition at RT of $Y_2O_3:Pr^{3+}$ (0.1% mol) NPs prepared by homogeneous precipitation method as a function of reaction time.

Entry	t_R (min)	τ (µs)
1	45	172
2	90	178
3	120	172
4	180	179

t_R: reaction time.

Finally, the effect of tuning the synthesis conditions for the solvothermal method was studied. Figure 4.28 shows the luminescence decay curves of NPs prepared by such a synthesis procedure. This provided the longest emission decay rates when compared with the other methods, even for the unmodified conditions ($RE(NO_3)_3$ (5.04 mmol), EG, reaction at 180 ºC, annealed at 800 ºC for 4 h). Specifically, the original synthesis procedure yielded agglomerated, polyhedral NPs with an average luminescence lifetime of 198 µs (Table 4.10, entry 1). As expected, modifications that promoted a strong aggregation of NPs, such as increasing annealing time, changing the type of alcohol, or increasing RE nitrates concentration, led to dramatic decreases in the average lifetime values, from 17 to 32% reduction (Table 4.10, entries 3-5, Figure 4.28a). Conversely, applying higher temperatures in both the reaction and annealing steps yielded NPs with longer luminescence lifetime values due to the improved crystallinity and surrounding layer removal (Table 4.10, entries, 2, 6 and 7, Figure 4.28b). Specifically, radiative decays of 223 and 216 µs were obtained when the reaction temperature was increased up to 220 ºC, and the calcination occurred at 900 and 1000 ºC, respectively (Table 4.10, entries 6 and 7).

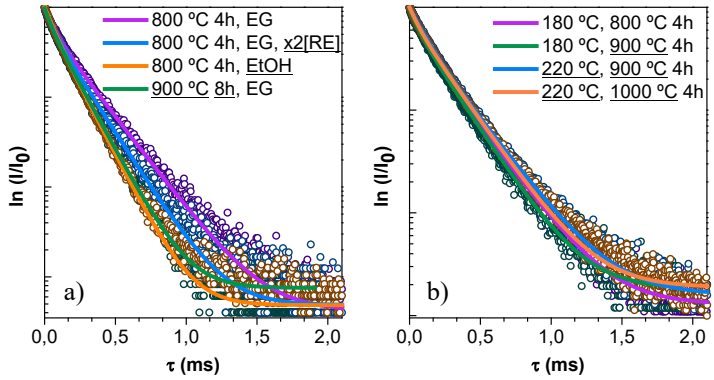

Figure 4.28. Luminescence decay curves of the Pr^{3+} $^1D_2 \rightarrow {}^3H_4$ emission of $Y_2O_3:Pr^{3+}$ (0.1% mol) NPs prepared by solvothermal method modifying: a) annealing time and temperature, type of alcohol, and RE nitrates concentration, and b) reaction and calcination temperatures. Modified parameters appear underlined.

The variations of emission decay rates associated to non-radiative processes can be ascribed to factors such as NP size, calcination temperature, presence of impurities, trap defects associated related to the synthesis procedure, and small fluctuations in Pr^{3+} concentration, to name a few. According to the obtained results, an increase in the NP size generally led to a reduction of surface effects, and thus to an improvement of luminescence properties, *i.e.*, an increase of the luminescence lifetime. Conversely, a higher agglomeration degree of the NPs seems to have a detrimental effect on the optical properties, generating a reduction of the average emission decay rate.

Table 4.10. Luminescence lifetime of the Pr^{3+} $^1D_2 \rightarrow {}^3H_4$ emission transition at RT for $Y_2O_3:Pr^{3+}$ (0.1% mol) NPs prepared by solvothermal method.

Entry	**Alcohol**	**T_R (ºC)**	**T_{CAL} / t_{CAL} (ºC) / (h)**	**τ (μs)**
1	EG	180	800 / 4	198
2	EG	180	900 / 4	202
3*	EG	180	900 / 4	144
4	EtOH	180	900 / 4	163
5	EG	180	900 / 8	135
6	EG	220	900 / 4	223
7	EG	220	1000 / 4	216

* Effect of twofold concentration of RE precursors. T_R: reaction temperature; T_{CAL}: calcination temperature; t_{CAL}: calcination time.

The NPs synthesized in this chapter present average sizes larger than 20 nm, together with a low Pr^{3+} concentration (0.1%). These structural and doping conditions were selected to minimize possible surface effects and concentration quenching. Particle size has a great influence on the optical properties of the material when the surface to volume ratio is large, *i.e.*, in very small NPs, which is related to both the higher concentration of surface Pr^{3+} ions and the adsorption of molecules from the environment. This is in good agreement with our results, where in all cases a higher calcination temperature promoted not only a better crystallinity of the material, but also a reduction of quenching due to surface effects as a consequence of crystal growth, ultimately resulting in longer radiative decays [26,44]. On the other hand, a low dopant concentration decreases both the amount of superficial RE ions and the distance between optically active dopants, thus reducing the probability of non-radiative processes ascribed to cross relaxation processes [45].

To investigate the aforementioned concentration quenching effect, the emission lifetime dependence on Pr^{3+} concentration was studied for combustion, sol-gel Pechini, homogeneous precipitation, and solvothermal methods (Figure 4.29, Table 4.11). For such a purpose, the dopant concentration was increased up to 2% mol. A progressive decrease in the emission lifetimes was detected when increasing the Pr^{3+} content, thus confirming the optimal 0.1% mol Pr^{3+} concentration, regardless of the synthesis procedure.

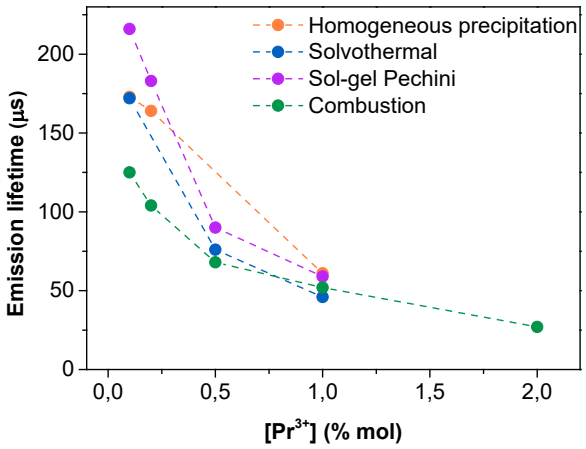

Figure 4.29. Dependence of the average lifetime on Pr^{3+} concentration for NPs obtained through the different synthesis methods. Dashed lines connecting dots are plotted just for reader's convenience.

Table 4.11. Average emission lifetime values as a function of Pr^{3+} concentration for NPs obtained through combustion, solvothermal, homogeneous precipitation, and sol-gel Pechini methods.

	Synthesis method	**Pr^{3+} concentration (%mol)**				
		0.1	0.2	0.5	1	2
τ (μs)	Combustion	173	164	–	61	–
	Sol-gel Pechini	125	104	68	52	27
	Homogeneous precipitation	172	–	76	46	–
	Solvothermal	216	183	90	59	–

Overall, the exhaustive tuning and optimization of the different synthesis parameters performed for each studied method have allowed to improve the optical properties of Y_2O_3:Pr^{3+} NPs, resulting in longer luminescence lifetimes for the Vis red Pr^{3+} emission ($^1D_2 \rightarrow {}^3H_4$). Table 4.12 compares the optimized average emission decay times of NPs prepared by each synthesis procedure. Remarkable differences in the obtained lifetimes were detected depending on the preparation route, the solvothermal method being the one providing the longest lifetime value. Besides, this synthesis method is highly reproducible, time-efficient, and yields NPs with appropriate size and dispersion degree.

The emission decay rate of bulk 0.1% mol Pr^{3+}-doped yttria has been reported to be 124 μs [46], while some authors have described values of 110-115 μs for the same material in the nanoscale [23,47]. To the best of our knowledge, the lifetime achieved in this Thesis for Y_2O_3:Pr^{3+} NPs prepared by solvothermal method (223 μs) is the longest luminescence emission lifetime reported to date for 0.1% mol Pr^{3+}-doped yttria NPs. Specifically, a lifetime of 180 μs was the longest value previously reported for Y_2O_3:Pr^{3+} (0.1% mol) NPs, prepared via the citrate complexation method and with average particle sizes in the 25-30 nm range [48]. Thus, it is worth noting that two of the optimized synthesis procedures studied herein provide Y_2O_3:Pr^{3+} (0.1% mol) NPs with luminescence lifetime values exceeding the published values so far. Specifically, an improvement of up to *ca*. 25% of the optical performance of the material was achieved in this Thesis

Table 4.12. $^1D_2 \rightarrow {}^3H_4$ Pr^{3+} average lifetimes of $Y_2O_3:Pr^{3+}$ (0.1% mol) NPs after optimization of the different synthesis methods.

Synthesis method	**τ (μs)**
Combustion	173
Molten salt	160
Sol-gel Pechini	118
Homogeneous precipitation	190
Solvothermal	223

4.7. Concluding remarks

The main conclusions obtained along this chapter are the following:

- The preparation of pure cubic $Y_2O_3:Pr^{3+}$ NPs has been achieved through five different bottom-up methods.
- A good grade of crystallinity has been obtained regardless of the synthesis procedure.
- The selection of the synthesis method has proven to be crucial for both the structural and optical properties of the resulting material.
- Structural features such as NP size and dispersion have demonstrated to be highly dependent on the fabrication strategy.
- Emission of Pr^{3+} ions has been detected for the two available crystallographic sites (C_2 and S_6) in the Y_2O_3 host matrix.
- No emission from the ^3P_J manifold has been observed regardless of the synthesis method, as expected for Pr^{3+}-doped sesquioxides.
- The average luminescence lifetime has been employed as the most accurate parameter for comparison purposes among the different assessed methods.
- The solvothermal synthesis has proven to be the best suited method to produce $Y_2O_3:Pr^{3+}$ NPs with superior optical properties. Specifically, this procedure has provided the most intense luminescence and the longest decay rates.

References

1 Weber, M. J.; Rare earth lasers. In: *Handbook on the physics and chemistry of rare earths*. North-Holland, 1979.

2 Reisfeld, R.; Jørgensen, C. K. *Lasers and excited states of rare earths*. Springer Berlin, 1977.

3 Ronda, C. R. Recent achievements in research on phosphors for lamps and displays. *J. Lumin*. **1997**, *72–74*, 49–54.

4 Leskelä, M. Rare earths in electroluminescent and field emission display phosphors. *J. Alloys Compd*. **1998**, *275–277*, 702–708.

5 Ye, T.; Guiwen, Z.; Weiping, Z.; Shangda, X. Combustion synthesis and photoluminescence of nanocrystalline Y_2O_3: Eu phosphors. *Mater. Res. Bull*. **1997**, *32*, 501–506.

6 Li, J. G.; Li, X.; Sun, X.; Ishigaki, T. Monodispersed colloidal spheres for uniform Y_2O_3:Eu^{3+} red-phosphor particles and greatly enhanced luminescence by simultaneous Gd^{3+} doping. *J. Phys. Chem. C* **2008**, *112*, 11707–11716.

7 Dhanaraj, J.; Jagannathan, R.; Kutty, T. R. N.; Lu, C. H. Photoluminescence characteristics of Y_2O_3:Eu^{3+} nanophosphors prepared using sol-gel thermolysis. *J. Phys. Chem. B* **2001**, *105*, 11098–11105.

8 Meltzer, R. S.; Feofilov, S. P.; Tissue, B.; Yuan, H. B. Dependence of fluorescence lifetimes of Y_2O_3:Eu^{3+} nanoparticles on the surrounding medium. *Phys. Rev. B* **1999**, *60*, 14012–14015.

9 Riseberg, L. A.; Moos, H. W. Multiphonon orbit-lattice relaxation of excited states of rare-earth ions in crystals. *Phys. Rev.* **1968**, *174*, 429–438.

10 Capobianco, J. A.; Vetrone, F.; Boyer, J. C.; Speghini, A.; Bettinelli, M. Enhancement of red emission ($^4F_{9/2}$→$^4I_{15/2}$) via upconversion in bulk and nanocrystalline cubic Y_2O_3:Er^{3+}. *J. Phys. Chem. B* **2002**, *106*, 1181–1187.

11 Vetrone, F.; Boyer, J. C.; Capobianco, J. A.; Speghini, A.; Bettinelli, M. Concentration-dependent near-infrared to visible upconversion in nanocrystalline and bulk Y_2O_3:Er^{3+}. *Chem. Mater*. **2003**, *15*, 2737–2743.

12 Martín-Rodríguez, R.; Valiente, R.; Polizzi, S.; Bettinelli, M.; Speghini, A.; Piccinelli, F. Upconversion luminescence in nanocrystals of $Gd_3Ga_5O_{12}$ and $Y_3Al_5O_{12}$ doped with Tb^{3+}-Yb^{3+} and Eu^{3+}-Yb^{3+}. *J. Phys. Chem. C* **2009**, *113*, 12195–12200.

13 Chang, N. C.; Gruber, J. B.; Leavitt, R. P.; Morrison, C. A. Optical spectra, energy levels, and crystal-field analysis of tripositive rare earth ions in Y_2O_3. I. Kramers ions in C_2 sites. *J. Chem. Phys*. **1982**, *76*, 3877–3889.

14 Matsuura, D. Red, green, and blue upconversion luminescence of trivalent-rare-earth ion-doped Y_2O_3 nanocrystals. *Appl. Phys. Lett*. **2002**, *81*, 4526–4528.

15 Goldburt, E. T.; Kulkarni, B.; Bhargava, R. N.; Taylor, J.; Libera, M. Size dependent efficiency in Tb doped Y_2O_3 nanocrystalline phosphor. *J. Lumin*. **1997**, *72*, 190–192.

16 Hao, J.; Studenikin, S. A.; Cocivera, M. Blue, green and red cathodoluminescence of Y_2O_3 phosphor films prepared by spray pyrolysis. *J. Lumin*. **2001**, *93*, 313–319.

17 Flores-Gonzalez, M. A.; Ledoux, G.; Roux, S.; Lebbou, K.; Perriat, P.; Tillement, O. Preparing nanometer scaled Tb-doped Y_2O_3 luminescent powders by the polyol method. *J. Solid State Chem*. **2005**, *178*, 989–997.

18 Guyot, Y.; Moncorgé, R.; Merkle, L. D.; Pinto, A.; McIntosh, B.; Verdun, H. Luminescence properties of Y_2O_3 single crystals doped with Pr^{3+} or Tm^{3+} and codoped with Yb^{3+}, Tb^{3+} or Ho^{3+} ions. *Opt. Mater*. **1996**, *5*, 127–136.

19 Krupke, W. F. Optical absorption and fluorescence intensities in several rare-earth doped Y_2O_3 and LaF_3 single crystals. *Phys. Rev*. **1966**, *145*, 325–337.

20 Srivastava, A. M.; Renero-Lecuna, C.; Santamaría-Pérez, D.; Rodríguez, F.; Valiente, R. Pressure-induced Pr^{3+} $^3P_0$ luminescence in cubic Y_2O_3. *J. Lumin*. **2014**, *146*, 27–32.

21 Alarcón-Flores, G.; García-Hipolito, M.; Aguilar-Frutis, M.; Zaleta-Alejandre, E.; Chacón, E.; Ramos-Brito, F.; Carmona-Téllez, S.; Guzmán-Mendoza, J.; Falcony, C. Synthesis and characterization of Y_2O_3:Pr^{3+} phosphor powders by simple solvent evaporation. *Ceram. Int*. **2015**, *41*, 743–748.

22 Aumüller, G. C.; Köstler, W.; Grabmaier, B. C.; Frey, R. Luminescence properties of Pr^{3+} in cubic rare earth oxides. *J. Phys. Chem. Solids* **1994**, *8*, 767–772.

23 Dudek, M.; Jusza, A.; Anders, K.; Lipinska, L.; Baran, M.; Piramidowicz, R. Luminescent properties of praseodymium doped Y_2O_3 and $LaAlO_3$ nanocrystallites and polymer composites. *J. Rare Earths* **2011**, *29*, 1123–1129.

24 Nikam, A. V.; Prasad, B. L. V.; Kulkarni, A. A. Wet chemical synthesis of metal oxide nanoparticles: a review. *Cryst. Eng. Comm*. **2018**, *20*, 5091–5107.

25 Medhi, R.; Marquez, M. D.; Lee, T. R. Visible-light-active doped metal oxide nanoparticles: review of their synthesis, properties, and applications. *ACS Appl. Nano Mater*. **2020**, *3*, 6156–6185.

26 Sudarsan, V.; van Veggel, F. C. J. M.; Herring, R. A.; Raudsepp, M. Surface Eu^{3+} ions are different than ''bulk'' Eu^{3+} ions in crystalline doped LaF_3 nanoparticles. *J. Mater. Chem*. **2015**, *15*, 1332–1342.

27 Haque, F. Z.; Nandanwar, R.; Singh, P.; Dharavath, K.; Syed, F. F. Effect of different acids and solvents on optical properties of SiO_2 nanoparticles prepared by the sol-gel process. *Silicon* **2018**, *10*, 413–419.

28 Kumar, K.; Rai, S. B.; Rai, D. K. Upconversion and concentration quenching in Er^{3+}-doped TeO_2-Na_2O binary glasses. *J. Non-Cryst. Solids* **2007**, *353*, 1383–1387.

29 Martín-Rodríguez, R.; Valiente, R.; Pesquera, C.; González, F.; Blanco, C.; Potin V.; Marco de Lucas, M. C. Optical properties of nanocrystalline-coated Y_2O_3:Er^{3+}, Yb^{3+} obtained by mechano-chemical and combustion synthesis. *J. Lumin*. **2009**, *129*, 1109–1114.

30 Mao, Y.; Tran, T.; Guo, X.; Huang, J. Y.; Shih, C. K.; Wang, K. L.; Chang, J.P. Luminescence of nanocrystalline erbium-doped yttria. *Adv. Funct. Mater*. **2009**, *19*, 748–754.

31 Geitenbeek, R. G.; Salzmann, B. B. V.; Nieuwelink, A. E.; Meijerink, A.; Weckhuysen, B. M. Chemically and thermally stable lanthanide-doped Y_2O_3 nanoparticles for remote temperature sensing in catalytic environments. *Chem. Eng. Sci*. **2018**, *198*, 235–240.

32 Yang, J.; Gu, J.; Yang, R.; Shang, Q.; Yang, J. Hydrothermal synthesis Y_2O_3:Yb^{3+}/Er^{3+} nanospheres with upconversion luminescence from green to red. *NSNM* **2016**, *2*, 41–45.

33 Repelin, Y.; Proust, C.; Husson, E.; Beny, J. M. Vibrational spectroscopy of the C-form of yttrium sesquioxide. *J. Solid State Chem*. **1995**, *118*, 163–169.

34 Ibáñez, J.; Sans, J. A.; Cuenca-Gotor, V.; Oliva, R.; Gomis, Ó.; Rodríguez-Hernández, P.; Muñoz, A.; Rodríguez-Mendoza, U.; Velázquez, M.; Veber, P.; Popescu, C.; Manjón, F. J. Structural and lattice-dynamical properties of Tb_2O_3 under compression: a comparative study with rare-earth and related sesquioxides. *Inorg. Chem*. **2020**, *59*, 9648–9666.

35 Abrashev, M. V.; Todorov, N. D.; Geshev, J. Raman spectra of R_2O_3 (R–rare earth) sesquioxides with C-type bixbyite crystal structure: a comparative study. *J. Appl. Phys*. **2014**, *116*, 103508.

36 Bruch, C.; Krüger, J. K.; Unruh, H. -G.; Krauss, W.; Zimmermeier, B.; Beck, C.; Hempelmann, R. Inelastic light scattering and phonon-confinement in nanocrystalline Y_2O_3. *Ber. Bunsenges. Phys. Chem*. **1997**, *101*, 1761–1764.

37 Sordelet, D.; Akinc, M. Preparation of spherical, monosized Y_2O_3 precursor particles. *J. Colloid Interface Sci*. **122**, *1988*, 47–59.

38 Fukushima, S.; Furukawa, T.; Niioka, H.; Ichimiya, M.; Sannomiya, T.; Miyake, J.; Ashida, M.; Araki, T.; Hashimoto, M. Synthesis of Y_2O_3 nanophosphors by homogeneous precipitation method using excessive urea for cathodoluminescence and upconversion luminescence bioimaging. *Opt. Mater. Express* **2016**, *6*, 831–843.

39 LaMer, V. K.; Dinegar, R. H. Theory, production and mechanism of formation of monodispersed hydrosols. *J. Am. Chem. Soc*. **1950**, *72*, 4847–4854.

40 Thanh, N. T. K.; Maclean, N.; Mahiddine, S. Mechanisms of nucleation and growth of nanoparticles in solution. *Chem. Rev*. **2014**, *114*, 7610–7630.

41 De Mello Donegá, C.; Meijerink, A.; Blasse, G. Non-radiative relaxation processes of the Pr^{3+} ion in solids. *J. Phys. Chem. Solids* **1995**, *56*, 673–685.

42 Hunt Jr., R. B.; Pappalardo, R. G. Fast excited-state relaxation of Eu-Eu pairs in commercial Y_2O_3:Eu^{3+} phosphors. *J. Lumin*. **1985**, *34*, 133–146.

43 Pappalardo, R. G.; Hunt Jr., R. B. Dye-laser spectroscopy of commercial Y_2O_3:Eu^{3+} phosphors. *J. Electrochem. Soc*. **1985**, *132*, 721–730.

44 Secu, C. E.; Matei, E.; Negrila, C.; Secu, M. The influence of the nanocrystals size and surface on the Yb/Er doped LaF_3 luminescence properties. *J. Alloys Compd*. **2019**, *791*, 1098–1104.

45 Benz, F.; Strunk, H. P. Rare earth luminescence: a way to overcome concentration quenching. *AIP Adv*. **2012**, *2*, 042115.

46 Guyot, Y.; Moncorgé, R.; Merkle, L. D.; Pinto, A.; McIntosh, B.; Verdun, H. Luminescence properties of Y_2O_3 single crystals doped with Pr^{3+} or Tm^{3+} and codoped with Yb^{3+}, Tb^{3+} or Ho^{3+} ions. *Opt. Mater*. **1996**, *5*, 127–136.

47 Jusza, A.; Lipinska, L.; Baran, M.; Olszyna, A.; Jastrzebska, A.; Gil, A.; Mergo, P.; Piramidowicz, R. Praseodymium doped nanocrystals and nanocomposites for application in white light sources. *Opt. Mater*. **2019**, *95*, 109247.

48 Avram, D.; Cojocaru, B.; Florea, M.; Tiseanu, C. Advances in luminescence of lanthanide doped Y_2O_3: case of S_6 sites. *Opt. Mater. Express* **2016**, *6*, 1635–1643.

5

Rare–earth doped composites

This chapter describes the fabrication of optically active composites based on RE doped NPs by means of the PLD technique. The development of thin films holds great potential for use in different applications such as passive and active waveguide structures, integrated optics, optical communications, sensors or interface technologies, for example [1]. To this end, and within the NCLas project, the development of luminescent NP-based composites for its ultimate application as waveguide was proposed. An in-depth structural and optical characterization of the active NPs has been carried out prior to their incorporation into the sandwich-like prepared structures. Afterwards, pure Y_2O_3 thin films have been deposited by PLD in order to encapsulate the NPs. The resulting structures have been structurally and optically characterized through different techniques, confirming the optimal preservation of the original properties of the initial RE-doped NPs.

The main goals of this chapter are:

1. To prepare and perform an in-depth structural and optical characterization of the optically active Pr^{3+}-doped Y_2O_3 NPs.
2. To fabricate optically active composites using different substrates by means of the PLD technique.
3. To fully characterize the prepared thin film composites by several structural and optical characterization techniques.
4. To demonstrate the potential application of PLD method for encapsulation and preservation of active nanomaterials for further optical applications in the field of optoelectronics.

5.1. State of the art

The development of composite films has experienced increasing popularity in recent years, especially in the fields of energy harvesting [2,3,4] and optics [5,6,7]. For the former, the use of RE-based films is an appropriate solution to reduce energy losses caused by spectral mismatch in silicon solar cells. Specifically, these composites allow to downshift the spectra of the incident light to wavelengths in the range of higher solar cell efficiency [8]. Regarding the optics field, RE-doped nanocomposites provide a suitable alternative to boost the scarce red component of the white light emitting diodes (WLEDs) spectra [9]. Furthermore, RE-based composite films serve as an additional solution to the limitation of RE doping concentration in glasses, which is related to low solubility rates and strong tendency to form clusters, and ultimately leads to fluorescence quenching [10,11,12]. Moreover, these materials offer an advantageous alternative for the development of planar waveguide lasers as a consequence of the resulting high optical gain in a small device [13].

For such purposes, selecting the most convenient material becomes crucial. In this context, some of the required features include low optical losses, low phonon energy and ability to be doped. Among the wide variety of available host matrixes, the use of Y_2O_3 for thin films has drawn remarkable attention thanks to its excellent electronic and mechanical properties. Indeed, yttria presents a high refractive index (1.7−1.9), large band gap, high thermal conductivity (twice higher than YAG), low phonon energy, and broad transparency range (0.2−8 μm). All these features, together with its high stability up to *ca*. 2400 ºC and its easiness to incorporate RE elements as doping ions due to their similar ionic radii, make Y_2O_3 a potential candidate for laser applications [13,14,15].

There are several methods available for thin film growth, which can be classified in two approaches: chemical and/or physical. The former comprises techniques in which a precursor in liquid-phase undergoes a chemical reaction to generate a thin film over a substrate [16]. Some of these include spin coating [5,17], electrodeposition [18,19] or spray pyrolysis [20,21]. On the other hand, physical deposition techniques involve mechanical or thermodynamic processes in which the material is vaporized to later be deposited onto a substrate [16], the most important procedures being laser molecular beam epitaxy [22,23], radio frequency magnetron sputtering [24,25], and PLD [26,27,28]. Among all these methods, as described in section 2.4.1, PLD

represents a promising technology due to its efficient stoichiometric transfer from a pre-pressed solid target to the so-obtained thin film over a substrate. Nevertheless, due to the rather complex character of the deposition process, this technique presents some limitations, particularly for industrial applications. The highly forward–directed nature of the ablation system results in great deposition efficiencies. However, remarkable differences in deposition rates occur within distances on the centimeter scale. As a result, modifications on the substrate and plume position are required to achieve homogeneous film thicknesses along vast areas [29]. Moreover, the PLD process often generates particles at the micron scale during the ejection step, which has proven to be detrimental due to changes in the refractive index, thermal conductivity, and promotion of polycrystalline growth. This is also especially relevant for the development of waveguides, since these particles increase light scattering, giving rise to higher optical loss. To overcome this drawback, strategies such as the use of velocity filters, shadow masks or two lasers focused on different perpendicular targets have been employed [29,30]. On the other hand, when fabricating materials for optical applications, achieving an appropriate distribution of the luminescent ions is crucial to avoid non-radiative processes. In this sense, the development of optically active composites based on NPs and thin films by means of PLD is a suitable alternative to overcome some of such limitations. Specifically, the external incorporation of luminescent NPs between deposited thin films allows to tune the structural and optical properties of the luminescent material, and to achieve a homogeneous distribution of the NPs along the composite surface.

5.2. Fabrication of optically active composites

In this section, the potential application of PLD technique to prepare luminescent composites through the encapsulation of active NPs is described. To this end, NPs were prepared and then introduced between deposited thin films. Different substrates were employed for thin film growth. In addition, two structures were proposed to assess both the optimal NP concentration and the appropriate number of deposition cycles, in order to obtain the best optical response of the composites.

5.2.1. Synthesis of active Pr-doped yttria nanoparticles

Optically active Y_2O_3:Pr^{3+} (0.2% mol) NPs were prepared using the modified solvothermal method described by Yang *et al*. [31], employing some of the optimized parameters described in Chapter 4 (section 4.4.5). Specifically, $Y(NO_3)_3$ (5.04 mmol) and $Pr(NO_3)_3$ (0.01 mmol) were dissolved in a mixture of EG and deionized H_2O (19:1, 60 mL as final volume). The resulting mixture was heated up while stirring to achieve the complete dissolution of reagents. Next, the solution was transferred to a Teflon-lined stainless-steel autoclave, where the reaction took place at 180 ºC for 24 h. After naturally cooling down to RT, the precipitate was separated and purified by washing with deionized H_2O (3 x 100 mL) and EtOH:H_2O (1:1) (1 x 100 mL). The obtained solid was dried in a stove o.n. at 70 ºC. A final thermal treatment at 900 ºC was applied for 4 h with a heating ramp of 5 ºC/min.

5.2.2. Preparation of thin films by pulsed laser deposition

The optically active composites were prepared as follows: a pure Y_2O_3 target was obtained by grinding 3 g of yttria, which was homogeneously dispersed in *ca*. 20 mL of EtOH. The mixture was kept o.n. in a stove at 50 ºC to remove the solvent, and subsequently pressed to form a pellet. The pellet was firstly heated at 100 ºC for 2 h, and then fired with a slow heating rate up to 1200 ºC. This temperature was maintained for 24 h followed by a slow cooling down to RT. For thin-film growth, a multi-target PLD system was used. A quadrupled Nd:YAG laser at the wavelength of 266 nm with 10 Hz repetition rate and a pulse energy of 10 mJ was employed. The substrate-target distance was fixed at 4 cm and the substrates were heated up to 600 ºC during the simultaneous deposition process, for which O_2 was used as background gas at $2 \cdot 10^{-5}$ mbar.

Under these conditions, an initial thin film of Y_2O_3 was prepared through a 4-h deposition cycle onto the four different substrates as the foundation of the composites. Then, a layer of Y_2O_3:Pr^{3+} (0.2% mol) NPs was deposited by adding 50 or 100 µL of NPs dispersed in EtOH at 1 mg/mL concentration. Finally, after EtOH evaporation, an additional thin film of Y_2O_3 was deposited by PLD. Firstly, the composite samples prepared with a single layer of 50 µL of NPs will be referred to as *X1*, where *X* identifies the kind of substrate (FS, SC, SR, MO). Secondly, this process was carried out with two intercalated layers of 100 µL of NPs between Y_2O_3 thin films. These samples will be referred to as *X2*, *i.e.*, two double NP layers and an additional deposition cycle. A representative schematic of the preparation procedure of *X1* is shown in Figure 5.1.

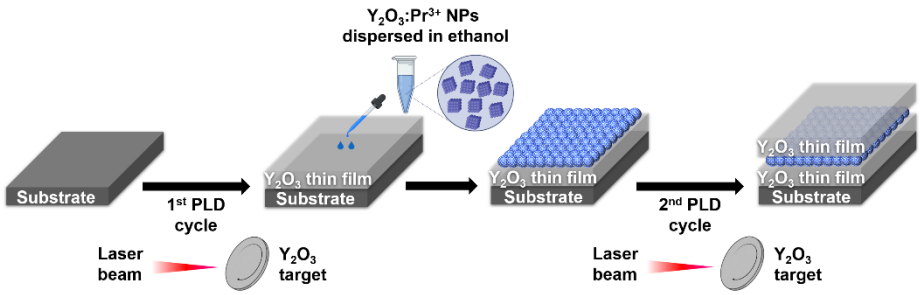

Figure 5.1. Schematic of the preparation procedure of *X1* samples.

5.3. Structural and optical properties of nanoparticles

The structural and optical features of the active NPs were analyzed in detail prior to their incorporation between thin films generated by PLD. In this context, XRD and TEM techniques were employed to structurally characterize the NPs, *i.e.*, to determine the phase composition and the average NP size. On the other hand, the optical properties of the synthesized NPs were studied by means of luminescence spectroscopy. Specifically, excitation and emission spectra were obtained, and the temporal evolution of the $^1D_2 \rightarrow {}^3H_4$ luminescent transition was recorded after excitation into the ^3P_J manifold.

5.3.1. Structural characterization

As described in section 5.2.1, Y_2O_3:Pr^{3+} (0.2% mol) NPs were prepared through solvothermal synthesis. The in-depth study carried out in Chapter 4 demonstrated that this procedure allows a precise control of structural properties, and thus an optimized optical performance of the resulting material. Besides, low active ion concentrations, such as 0.1–0.2% mol Pr^{3+}, avoid concentration quenching, thus providing the longest emission decay rates and the highest photoluminescence intensities, as previously shown in section 4.5.

As described in Chapter 4, the solvothermal method leads to the formation of NPs with pure Y_2O_3 cubic phase (space group $Ia\bar{3}$), which was confirmed by the recorded XRD pattern (Figure 5.2). No other crystalline phases were required to fit the pattern due to the total absence of remaining impurities after the thermal treatment at 900 ºC. Additionally, an average crystallite size of 52 ± 5 nm was obtained from the Rietveld refinement.

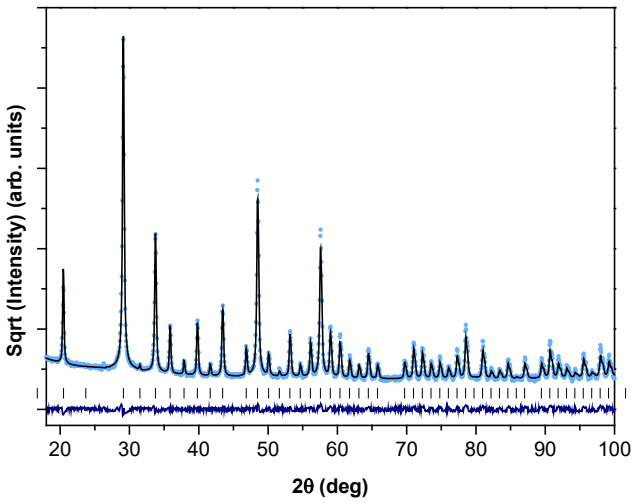

Figure 5.2. Rietveld refinement of the XRD pattern for the synthesized Y_2O_3:Pr^{3+} (0.2% mol) NPs. Vertical lines correspond to c-Y_2O_3 Bragg reflections.

TEM images (Figure 5.3) showed that slightly agglomerated NPs with polyhedral morphology were obtained, as expected. No surrounding layer was detected as a result of the optimized conditions during the annealing step. In addition, an average NP size of 45 ± 18 nm was determined, in good agreement with XRD results.

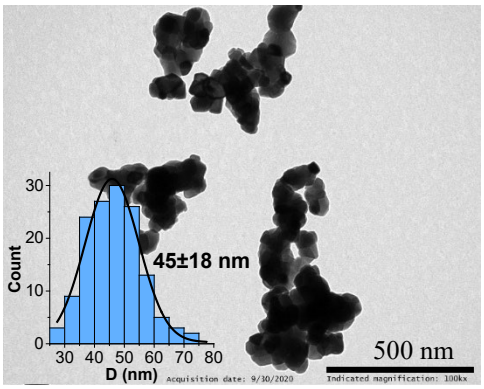

Figure 5.3. TEM image and average particle size of prepared $Y_2O_3:Pr^{3+}$ (0.2% mol) NPs prior to their incorporation between the deposition thin films.

5.3.2. Optical characterization

The RT excitation spectrum of the $Y_2O_3:Pr^{3+}$ (0.2% mol) NPs was obtained after monitoring the emission from the $^1D_2$ multiplet to the $^3H_4$ ground state at 629 nm (Figure 5.4a). As previously described, the broad band centered at *ca.* 280 nm dominates the spectrum, which mainly results from the inter-configurational transition $4f^2 \rightarrow 4f^15d^1$ of Pr^{3+} ions located at C_2 sites. Nevertheless, contribution of S_6 sites cannot be ruled out due to both excitation and emission spectra overlap of the two crystallographic sites. From 425 to 525 nm, sharp lines related to intra–configurational transitions of Pr^{3+} from the $^3H_4$ ground state to the ^3P_J + $^1I_6$ multiplets are also detected. The RT emission spectrum of the synthesized NPs was obtained upon direct excitation at λ_{exc} = 290 nm (Figure 5.4b). This wavelength allows us to obtain predominantly the spectrum corresponding to Pr^{3+} ions placed at the C_2 crystallographic site in the host lattice, which shows stronger luminescence than Pr^{3+} ions located on the S_6 site, in agreement with the 3:1 ratio of the two sites and the lack of center of symmetry [32]. Again, no emission of Pr^{3+} from the ^3P_J excited states was detected [32]. The photoluminescence spectrum consists of peaks located at 600–670 nm range, assigned to the $^1D_2 \rightarrow {}^3H_4$ transition, and bands between 700 and 750 nm, characteristic of the $^1D_2 \rightarrow {}^3H_5$ emission.

The temporal evolution of the $^1D_2 \rightarrow {}^3H_4$ luminescent transition at 629 nm was studied after excitation into the ^3P_J excited states at 491 nm (Figure 5.5). The emission decay curve was fitted to a double exponential, leading to an average lifetime of $<\tau>$ = 177 μs. The observed bi-exponential behavior can

be ascribed to the emission of Pr^{3+} ions from C_2 and S_6 crystallographic sites, since both present peaks at this excitation wavelength, as previously described [32].

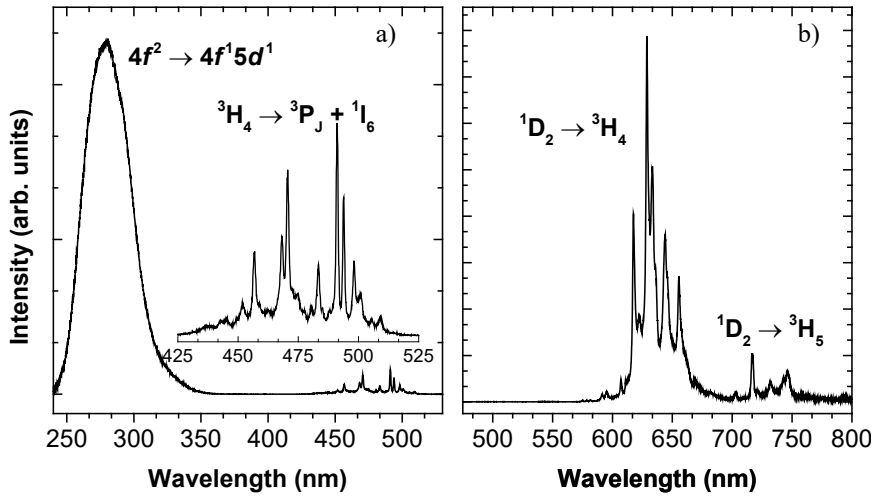

Figure 5.4. (a) Excitation spectrum (λ_{em} = 629 nm) of Y_2O_3:Pr^{3+} (0.2% mol) NPs. The inset shows a zoom of the intra-configurational *f-f* transitions of Pr^{3+} ions. (b) Emission spectrum (λ_{exc} = 290 nm) of Y_2O_3:Pr^{3+} (0.2% mol) NPs (C_2 sites).

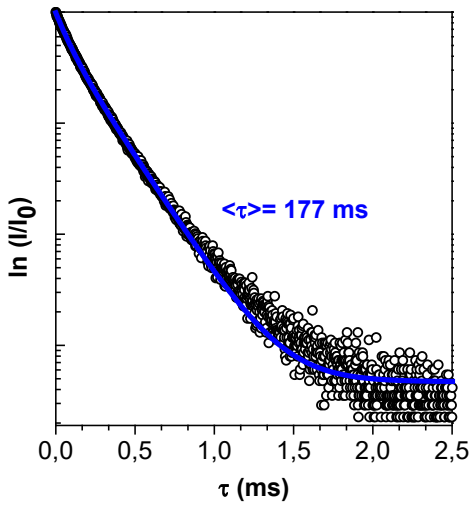

Figure 5.5. Luminescence decay curve of Pr^{3+} $^1D_2 \rightarrow {}^3H_4$ emission (λ_{ex} = 491 nm; λ_{em} = 629 nm) of Y_2O_3:Pr^{3+} (0.2% mol) NPs prepared by solvothermal method.

5.4. Structural and optical properties of optically active composites

As described in section 5.2, the composite samples are referred to as *X1* or *X2*, where *X* identifies the kind of substrate (FS, SC, SR, MO) and the following number represents the number of NPs layers between Y_2O_3 thin films. The resulting sandwich-like structure for both types of samples, *X1* and *X2*, is represented in Figure 5.6.

The structural and optical characterization of the prepared composites was carried out using different techniques. Specifically, absorption spectroscopy was employed to estimate the thickness of the deposited thin films. Additionally, XRD was used to determine the phase of the grown Y_2O_3 layers. On the other hand, the optical properties of the sandwich-like structures were studied by means of luminescence spectroscopy in order to verify the preservation of the NPs after the deposition cycles.

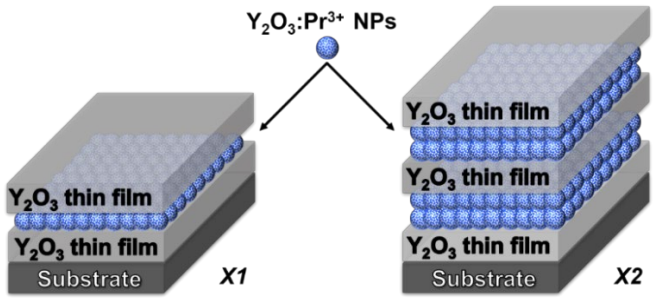

Figure 5.6. Schematic of the two types of structures obtained (*X1* and *X2* composites) after the deposition procedure.

5.4.1. Structural characterization

Firstly, the total thickness of the composites was quantified through the analysis of the interferences detected in the absorption spectra (Figure 5.7), according to equation 5.1 [33]:

$$d = \frac{\lambda_1 \lambda_2}{2(\lambda_1 n_2 - \lambda_2 n_1)} \qquad \text{(eqn. 5.1)}$$

where n_i is the refractive index at λ_i and d is the thickness of the thin–film composite. Since the Pr^{3+} concentration of Y_2O_3 NPs is as low as 0.2%

mol, the refractive index was considered homogeneous, and equal to the value for pure Y_2O_3 along the multilayer structure. Values for n_i were taken from reference [34].

The thin films had different thicknesses depending on their position with respect to the target during the PLD deposition process, which is due to the highly forward-directed nature of the ablation process [29]. The estimated thickness values of both *X1* and *X2* composites are shown in Table 5.1. In particular, the *SR* composite showed the smallest thickness, while the other three samples displayed similar values within the experimental uncertainty. This is related to the fact that the SR substrate was located farther from the target than the other substrates.

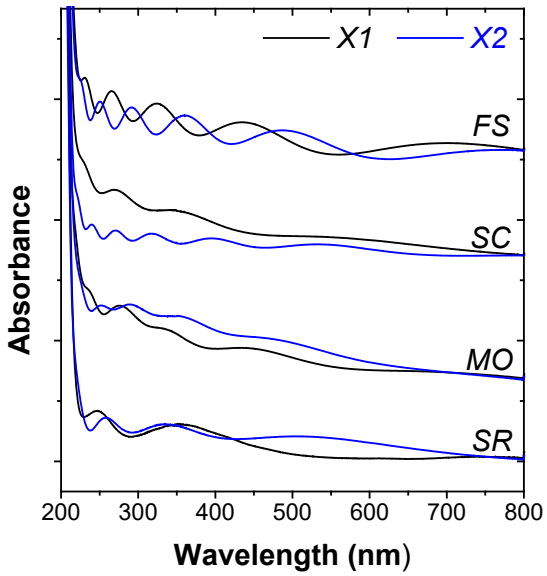

Figure 5.7. Absorption spectra of the thin–film composites on different substrates.

Table 5.1. Thickness values of the prepared composites estimated from the absorption spectra and the interference pattern according to equation 5.1.

	Thickness (nm)			
	FS	*SC*	*MO*	*SR*
X1	285 ± 3 nm	231 ± 13 nm	313 ± 3 nm	159 ± 5 nm
X2	321 ± 5 nm	356 ± 5 nm	340 ± 23 nm	220 ± 5 nm

As a representative example, Figure 5.8 shows the XRD pattern of *FS1* and *FS2* composites in comparison with that of the bare *FS* substrate. Firstly, a broad peak was observed at *ca*. 22º, which is common to the three XRD patterns, and thus attributed to the amorphous SiO_2 substrate contribution. A few additional broad peaks were also detected. The peak broadening could be related to induced tensions within the thin films during the deposition process and to the lattice mismatch with the substrate. These peaks were assigned to the crystalline reflections of c-Y_2O_3, and therefore to the thin films, the (222) peak being the most intense one. Furthermore, both (332) and (444) peaks from *FS2* sample exhibit slightly higher intensity when compared with *FS1* sample due to their different number of deposition cycles. Finally, and as expected, no additional diffraction peaks from the NPs could be detected as a consequence of their reduced concentration and the overlap of their reflections with those of the thin films due to their same composition.

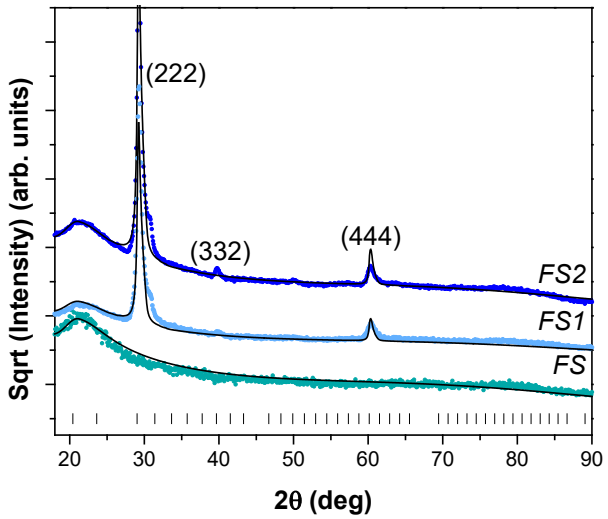

Figure 5.8. Rietveld refinement of XRD diffraction patterns of *FS1* and *FS2* composites, and *FS* bare substrate for comparison purposes. Vertical lines correspond to c-Y_2O_3 Bragg reflections.

5.4.2. Optical characterization

To study the optical properties of the composites, emission and excitation spectra together with luminescence decay curves were compared with those from the original bare NPs prior to encapsulation. In this regard, the emission and excitation spectra of *X1* composites, *i.e.*, those containing a single layer of

active NPs, displayed both lower intensity and resolution due to the reduced concentration of NPs. For that reason, the optical characterization was focused on *X2* composites, *i.e.*, those including two layers of NPs with twofold concentration per layer.

Figure 5.9a shows a comparison between the RT normalized excitation spectra of the non-supported Y_2O_3:Pr^{3+} (0.2% mol) NPs and the *FS2* composite as a representative example of the PLD samples, when monitoring the emission from the $^1D_2$ multiplet (λ_{em} = 629 nm). Both spectra are dominated by broad bands centered at *ca*. 273 and 279 nm for the composite and the NPs, respectively, which are ascribed to the inter–configurational transition $4f^2 \rightarrow 4f^15d^1$ of Pr^{3+}. Additionally, intra–configurational transitions from the ground state to the ^3P_J + $^1I_6$ multiplets were also detected in the 430–520 nm range. As expected, the spectra of the composites displayed lower intensity and resolution than those of the powder NPs.

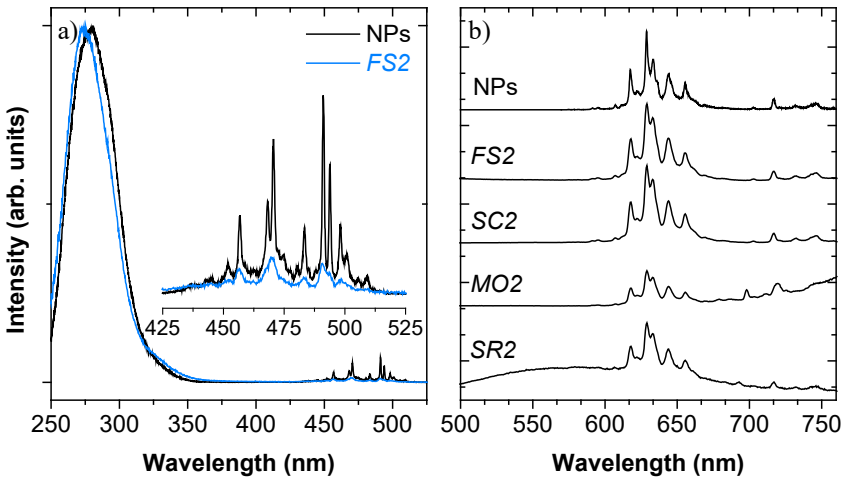

Figure 5.9. a) Comparison between the normalized excitation spectra (λ_{em} = 629 nm) of Y_2O_3:Pr^{3+} (0.2% mol) NPs and the double-layered composite deposited on the *FS2* substrate ; b) Comparison between the normalized emission spectra (λ_{ex} = 290 nm) of Y_2O_3:Pr^{3+} (0.2% mol) NPs and the double-layered *X2* composites after NPs encapsulation between pure Y_2O_3 thin films.

Figure 5.9b presents the RT normalized emission spectra of the prepared composites and that of the non-supported Y_2O_3:Pr^{3+} (0.2% mol) NPs for comparison purposes. The characteristic photoluminescence bands previously assigned to the transitions $^1D_2 \rightarrow {}^3H_4$ and $^1D_2 \rightarrow {}^3H_5$ were detected after direct excitation in the UV region (λ_{exc} = 290 nm). In addition, no differences in terms of emission band position and intensity ratio were observed

between the original NPs and the resulting composites. Interestingly, *FS* and *SC* composites exhibit the highest intensities and the best spectral resolution among the studied substrates.

Concerning the emission lifetime, the temporal evolution of the $^1D_2 \rightarrow {}^3H_4$ transition intensity was recorded at 629 nm after direct excitation into the ^3P_J manifold at 491 nm. No changes in terms of the bi-exponential behavior were observed when compared with the initial NPs, since emission occurs from the two available crystallographic sites (Figure 5.10) [32]. Furthermore, slight decreases from 8% up to 20% of the original emission lifetime were observed due to the encapsulation of the optically active NPs between deposition thin films (Table 5.2). Specifically, these lower emission decay rates can be ascribed to the change in the refractive index from air to yttria, which is particularly relevant for Pr^{3+} ions located close to the NPs surface [35].

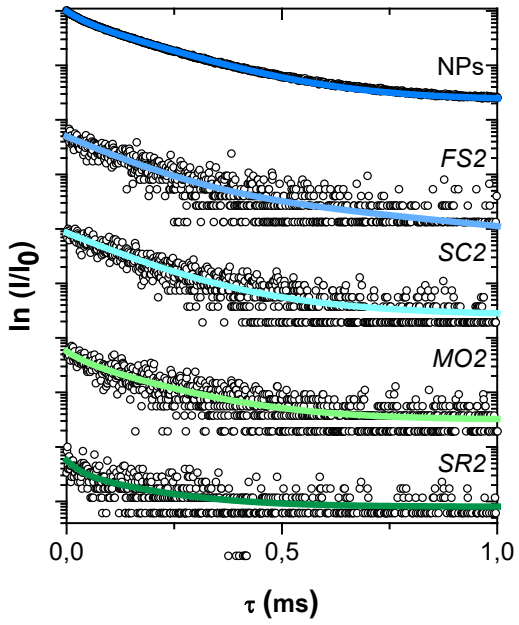

Figure 5.10. Luminescence intensity decay curves of the Pr^{3+} $^1D_2 \rightarrow {}^3H_4$ emission (λ_{ex} = 491 nm; λ_{em} = 629 nm) for the initial NPs and the prepared *X2* composites.

Table 5.2. Average luminescence lifetimes of the Pr^{3+} $^1D_2 \rightarrow {}^3H_4$ emission transition of $Y_2O_3:Pr^{3+}$ (0.2% mol) NPs and *X2* composites with NPs embedded between pure Y_2O_3 thin films.

	NPs	**Composites**			
		FS2	*SC2*	*MO2*	*SR2*
τ (μs)	177	153	155	163	141

5.5. Concluding remarks

The main conclusions obtained along this chapter are the following:

- Optically active composites based on luminescent $Y_2O_3:Pr^{3+}$ NPs embedded between pure yttria thin films have been successfully fabricated by means of PLD technique.
- Pure cubic Y_2O_3 thin films with thicknesses ranging from 159 to 356 nm have been obtained as a function of the position of the substrates and the number and duration of deposition cycles.
- The optical characterization has shown that this approach is a suitable encapsulation method that leads to an optimal preservation of the luminescent features of the initial $Y_2O_3:Pr^{3+}$ NPs.
- This strategy has proven to be very promising for the development of high-optical-quality thin films, showing great potential for different applications in the field of luminescent materials.

References

1 Bär, S.; Petermann, K.; Huber, G. Sesquioxides as host materials for rare-earth-doped bulk lasers and active waveguides. In: *Rare earth oxide thin films. Topics in applied physics*. Springer, 2006.

2 Trabelsi, F.; Mercier, F.; Blanquet, E.; Crisci, A.; Salhi, R. Synthesis of upconversion TiO_2:Er^{3+}–Yb^{3+} Nanoparticles and deposition of thin films by spin coating technique. *Ceram. Int*. **2020**, *46*, 28183–28192.

3 Kalytchuk, S.; Gupta, S.; Zhovtiuk, O.; Vaneski, A.; Kershaw, S.V.; Fu, H.; Fan, Z.; Kwok, E. C. H.; Wang, C. –F.; Teoh, W. Y.; Rogach, A. L. Semiconductor nanocrystals as luminescent down–shifting layers to enhance the efficiency of thin–film CdTe/CdS and crystalline Si solar cells. *J. Phys. Chem. C* **2014**, *118*, 16393–16400.

4 Bouras, K.; Schmerber, G.; Rinnert, H.; Aureau, D.; Park, H.; Ferblantier, G.; Colis, S.; Fix, T.; Park, C.; Kim, W. K.; Dinia, A.; Slaoui, A. Structural, optical and electrical properties of Nd–doped SnO_2 thin films fabricated by reactive magnetron sputtering for solar cell devices. *Sol. Energy Mater. Sol. Cells* **2016**, *145*, 134–141.

5 Zhang, X.; Chen, R.; Wang, P.; Shu, J.; Zhang, H.; Song, H.; Xu, J.; Zhang, P.; Xu, J. A Soft chemistry–based route to enhanced photoluminescence of terbium ions and tin oxide nanocrystals codoped silica thin films. *Appl. Surf. Sci*. **2018**, *452*, 96–101.

6 Khanlary, M. R.; Hajinorozi, A.; Baghshahi, S. Influence of Ce doping concentration on the structural and optical properties of sol–gel derived ZnO:Ce nanostructures. *J. Inorg. Organomet. Polym.* **2015**, *25*, 1521–1528.

7 Lee, B.I.; Jeong, H.; Byeon, S. H. Layer-by-layer deposition of highly transparent multifunctional Gd_2O_3:RE/SiO_2 (RE = Eu and Tb) films. *Eur. J. Inorg. Chem.* **2014**, *21*, 3298–3304.

8 Van Der Ende, B. M.; Aarts, L.; Meijerink, A. Lanthanide ions as spectral converters for solar cells. *Phys. Chem. Chem. Phys*. **2009**, *11*, 11081-11095.

9 Cao, X.; Sun, S.; Lu, B.; Liu, Y.; Ma, R.; Cao, H.; Ma, H.; Huang, H. Spectral photoluminescence properties of YAG: Ce, R (R: Gd^{3+}, Pr^{3+}, Gd^{3+} and Pr^{3+}) transparent fluorescent thin film prepared by pulse laser deposition. *J. Lumin*. **2020**, *223*, 117222.

10 Monteil, A.; Chaussedent, S.; Alombert–Goget, G.; Gaumer, N.; Obriot, J.; Ribeiro, S. J. L.; Messaddeq, Y.; Chiasera, A.; Ferrari, M. Clustering of rare earth in glasses, aluminum effect: experiments and modeling. *J. Non–Cryst. Solids* **2004**, *348*, 44–50.

11 Kokou, L.; Du, J. Rare rarth ion clustering behavior in europium doped silicate glasses: simulation size and glass structure effect. *J. Non–Cryst. Solids* **2012**, *358*, 3408–3417.

12 Aitken, B. G.; Ponader, C. W.; Quimby, R.S. Clustering of rare earths in GeAs sulfide glass. *C. R. Chim*. **2002**, *5*, 865–872.

13 Pearce, S. J.; Parker, G. J.; Charlton, M. D. B.; Wilkinson, J. S. Structural and optical properties of yttrium oxide thin films for planar waveguiding applications. *J. Vac. Sci. Technol., A* **2010**, *28*, 1388–1392.

14 Ramana, C. V.; Mudavakkat, V. H.; Kamala Bharathi, K.; Atuchin, V. V.; Pokrovsky, L. D.; Kruchinin, V. N. Enhanced optical constants of nanocrystalline yttrium oxide thin films. *Appl. Phys. Lett*. **2011**, *98*, 031905.

15 Laversenne, L.; Kairouani, S.; Guyot, Y.; Goutaudier, C.; Boulon, G.; Cohen–Adad, M.Th. Correlation between dopant content and excited–state dynamics properties in Er^{3+}–Yb^{3+}–codoped Y_2O_3 by using a new combinatorial method. *Opt. Mater*. **2002**, *19*, 59–66.

16 Lee, E.; Terblans, J. J.; Craciun, V.; Swart, H. C. Structural and luminescence properties of Y_2O_3:$Bi_{2.0\ mol\%}$,$Yb_{10.0\ mol\%}$ thin films prepared using the pulsed laser deposition and spin coating technique. *Surf. Interfaces* **2019**, *16*, 101–107.

17 Zaręba–Grodź, I.; Pązik, R.; Tylus, W.; Mielcarek, W.; Hermanowicz, K.; Stręk, W.; Maruszewski, K. Europium–doped silica–titania thin films obtained by the sol–gel method. *Opt. Mater*. **2007**, *29*, 1103–1106.

18 Zhang, Z.; Kitada, A.; Fukami, K.; Yao, Z.; Murase, K. Electrodeposition of an iron thin film with compact and smooth morphology using an ethereal electrolyte. *Electrochim. Acta* **2020**, *348*, 136289.

19 Sayem Rahman, A. S. M.; Islam, M. A.; Shorowordi, K. M. Electrodeposition and characterization of copper oxide thin films for solar cell applications. *Procedia Eng*. **1985**, *34*, 133–146.

20 Hao, J.; Studenikin, S. A.; Cocivera, M. Blue, green and red cathodoluminescence of Y_2O_3 phosphor films prepared by spray pyrolysis. *J. Lumin*. **2001**, *93*, 313–319.

21 Kanarjov, P.; Reedo, V.; Oja Acik, I.; Matisen, L.; Vorobjov, A.; Kiisk, V.; Krunks, M.; Sildos, I. Luminescent materials based on thin metal oxide films doped with rare earth ions. *Phys. Solid State* **2008**, *50*, 1727–1730.

22 Feofilov, S. P.; Korovin, A. M.; Kulinkin, A. B.; Kuzin, D. S.; Smirnov, A. N.; Sokolov, N. S.; Suturin, S. M.; Yagovkina, M. A. Modified radiative lifetime of Eu^{3+} ions in Y_2O_3 thin films on Al_2O_3 substrates. *J. Lumin.* **2021**, *230*, 117754.

23 Seifarth, O.; Schubert, M. A.; Giussani, A.; Klenov, D. O.; Schmeißer, D.; Schroeder, T. Single crystalline $Pr_{2-X}Y_xO_3$ (X=0–2) dielectrics on Si with tailored electronic and crystallographic structure. *J. Appl. Phys*. **2010**, *108*, 103709.

24 Balestrieri, M.; Gallart, M.; Ziegler, M.; Bazylewski, P.; Ferblantier, G.; Schmerber, G.; Chang, G. S.; Gilliot, P.; Muller, D.; Slaoui, A.; Colis, S.; Dinia, A. Luminescent properties and energy transfer in Pr^{3+} doped and Pr^{3+}–Yb^{3+} co–doped ZnO thin films. *J. Phys. Chem*. **2014**, *118*, 13775–13780.

25 Kavitha, V. S.; Reshmi Krishnan, R.; Sreeja Sreedharan, R.; Suresh, K.; Jayasankar, C. K.; Mahadevan Pillai, V. P. Tb^{3+}–doped WO_3 thin films: a potential candidate in white light emitting devices. *J. Alloys Compd*. **2019**, *788*, 429–445.

26 Korir, P. C.; Dejene, F. B. The effect of deposition time on the structural, morphological and luminescence properties of Y_2O_2S:Eu^{3+} thin films prepared by pulsed laser deposition. *Appl. Phys. Mater. Sci. Process* **2018**, *124*, 1–9.

27 Ali, A. G.; Dejene, B. F.; Swart, H. C. Temperature dependence of structural and luminescence properties of Eu^{3+}–doped Y_2O_3 red–emitting phosphor thin films by pulsed laser deposition. *Appl. Phys. A* **2016**, *122*, 382.

28 Sans, J. A.; Segura, A.; Mollar, M.; Marí, B. Optical properties of thin films of ZnO prepared by pulsed laser deposition. *Thin Solid Films* **2004**, *453–454*, 251–255.

29 Norton, D. P. Synthesis and properties of epitaxial electronic oxide thin–film materials. *Mater. Sci. Eng. R* **2004**, *43*, 139–247.

30 Prentice, J. J. Pulsed laser deposition of thin-film oxides for waveguide lasers. PhD Thesis, University of Southampton, 2020.

31 Yang, J.; Gu, J.; Yang, R.; Shang, Q.; Yang, J. Hydrothermal synthesis Y_2O_3:Yb^{3+}/Er^{3+} nanospheres with upconversion luminescence from green to red. *NSNM* **2016**, *2*, 41–45.

32 Aumüller, G. C.; Köstler, W.; Grabmaier, B. C.; Frey, R. Luminescence properties of Pr^{3+} in cubic rare earth oxides. *J. Phys. Chem. Solids* **1994**, *8*, 767–772.

33 Swanepoel, R. Determination of the thickness and optical constants of amorphous silicon. *J. Phys. E Sci. Instrum*. **1983**, *16*, 1214.

34 Nigara, Y. Measurement of the optical constants of yttrium oxide. *Jpn*. *J. Appl. Phys*. **1968**, *7*, 404–408.

35 Meltzer, R. S.; Feofilov, S. P.; Tissue, B.; Yuan, H. B. Dependence of fluorescence lifetimes of Y_2O_3:Eu^{3+} nanoparticles on the surrounding medium. *Phys. Rev. B* **1999**, *60*, 14012–14015.

Part II

Photocatalytic Applications

6

Doped metal oxide nanomaterials for photocatalytic applications

This chapter consists in a general introduction to TM and RE-doped metal oxides and their applications in the field of photocatalysis. Firstly, an overview about the relevance of nanomaterials in the area of photocatalysis and the research projects that motivated this Part II of the Thesis are described. Then, the interest of semiconductor materials and, specifically, metal oxides and their most significant features for their application as photocatalysts are detailed. Finally, strategies to improve the photocatalytic activity such as band gap engineering based on TM- and RE-doping are presented.

6.1. Introduction

The use of nanomaterials in the field of photocatalysis has experienced an exponentially growing interest in the last decades, resulting from the increasing pollution levels and the consideration of the sunlight as a never-ending source of energy [1]. An important advantage of the use of nanomaterials for photocatalytic purposes when compared with their bulk version arises from their large surface area, which provides a higher number of active sites for electrochemical reactions [2]. In this sense, nanomaterials based on a wide variety of compositions have found numerous applications, such as degradation of organic pollutants and heavy metals, water splitting, carbon dioxide (CO_2) photoreduction, air purification, self-cleaning, or N_2 fixation for NH_3 production, to name a few [2,3]. Some of the available materials for such purposes comprise: plasmonic metal NPs [4,5], organic nanostructures [6,7], and inorganic semiconductors [1]. The former take advantage of the surface

plasmon resonance effect to display an enhanced absorption cross section, in both Vis and NIR spectral regions, resulting of great interest for solar energy harvesting [8]. However, these NPs frequently need to be stabilized on other materials such as metal oxides or carbon supports in order to become active for certain reactions, thus acting as an antenna for the support itself [8,9]. On the other hand, organic nanomaterials are attracting growing interest in the field of photocatalysis due to their remarkable solubility in organic solvents, simple tunability of photophysical properties, and plausible fabrication through green synthesis methods using fruits, plants, or recycled plastics as sustainable precursor sources [10,11,12,13]. Some examples of this type of catalysts include carbon quantum dots, fullerenes, and covalent organic frameworks (COFs) [7,11,14]. Nevertheless, inorganic semiconductors are considered as the most popular materials for photocatalytic applications. Metal oxides, metal nitrides, metal sulfides or oxynitrides are included in this group. Specifically, metal oxide NPs, such as TiO_2, Fe_2O_3, WO_3, ZnO, MoO_3 or ZrO_2, and metal sulfide NPs, including CdS, CuS, $AgIn_5S_8$ or ZnS, are predominantly used due to their narrow band gap and unique electronic structure resulting from their unoccupied conduction band (CB) and occupied valence band (VB) [2,15]. Among them, titanium (IV) oxide (TiO_2), also known as titanium dioxide or titania, is the most widely used metal oxide photocatalyst owing to its low toxicity, chemical stability, low cost, and remarkable abundance [6].

In this context, the Part II of this Thesis, which comprises Chapters 6, 7 and 8, is devoted to the synthesis, characterization and photocatalytic applications of TM- and RE-doped metal oxide nanomaterials. It has been developed in the frame of two different research projects aiming at the development of TiO_2-based catalysts. Firstly, a collaboration project with Vitrispan S.A. company, whose results are compiled in Chapter 7, was carried out. The main goal of this research project was to study the incorporation of doped and undoped TiO_2 NPs onto vitrified stainless-steel sheets for its potential industrial application in pollutant photodegradation. Secondly, the results included in Chapter 8 arise from a collaboration with the CITIMAC and the Chemical and Biomolecular Engineering Departments from the University of Cantabria. The main purpose was to optimize the photoreduction of CO_2 to produce alcohols mediated by TiO_2 NPs-based catalysts within a planar optofluidic microreactor.

6.2. Photocatalytic properties of semiconductors

The mechanism of action of semiconductors in a photocatalytic process can be described as follows: firstly, photoexcitation takes place when the energy of the incident radiation matches or exceeds the band gap energy (E_g) of the semiconductor. Consequently, the photo-excited electrons (e^-_{CB}) transit from the VB to the CB, thus generating an equal number of vacant sites (holes, h^+_{VB}) in the VB, which gives rise to an electron/hole e^-_{CB}/h^+_{VB} pair as represented in Figure 6.1. Then, charge separation and transportation occur. In this sense, the components of e^-_{CB}/h^+_{VB} pair are separated and transferred to the active sites on the surface of the catalyst. However, charge recombination can simultaneously take place. Due to the competing nature between migration and charge recombination processes, a fraction of e^-_{CB} and h^+_{VB} may radiatively or non-radiatively recombine dissipating the absorbed energy, or be trapped by defects on the catalyst surface, therefore reducing the quantum efficiency of the photocatalytic process. Finally, the photocatalyzed redox reaction takes place, where e^-_{CB}/h^+_{VB} react with adsorbed species on the catalyst surface. In this context, reducing charge recombination is of great importance in order to increase the quantum efficiency of the catalyst. Specifically, given that structural defects are highly detrimental for efficient charge separation and migration processes of e^-_{CB}/h^+_{VB} pairs, improving the crystallinity of the catalytic material is key to minimize trapping and recombination sites. On the other hand, the use of semiconductor nanomaterials is also a suitable strategy since smaller particle sizes lead to shorter distances between generated photoinduced charges and surface active sites, thus reducing the probability of recombination [16].

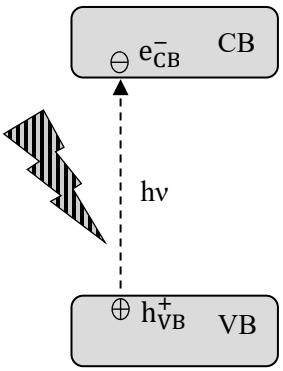

Figure 6.1. Schematic representation of the basic photoexcitation mechanism of semiconductors.

6.2.1. Photooxidation mechanism

Firstly, during the aforementioned photocatalyzed redox reaction, a photooxidation process can occur. This transformation results of great interest for the degradation of pollutants or organic compounds like MB dye. In this context, the photogenerated positive holes (h^+_{VB}, eqn. 6.1) perform as powerful oxidants, oxidizing water or OH^- and leading to the formation of $^{\cdot}OH$ radicals

at the semiconductor surface (eqn. 6.2 and 6.3). On the other hand, e^-_{CB} act as strong reducing agents and can interact with O_2 to generate superoxide ($O_2^{\cdot-}$), which might react with H^+ yielding hydroperoxyl ($^{\cdot}OOH$) radicals (eqn. 6.5 and 6.7). All these radicals are extremely reactive oxidants and might degrade organic compounds and pollutants by an oxidation process (eqn. 6.4, 6.6, and 6.8) [16,17,18].

$$\text{Semiconductor} + h\nu \longrightarrow h^+_{VB} + e^-_{CB} \quad \text{(eqn. 6.1)}$$

$$h^+_{VB} + H_2O \longrightarrow H^+ + {}^{\bullet}OH \quad \text{(eqn. 6.2)}$$

$$h^+_{VB} + OH^- \longrightarrow {}^{\bullet}OH \quad \text{(eqn. 6.3)}$$

$${}^{\bullet}OH + \text{organic molecule} \longrightarrow \longrightarrow \longrightarrow CO_2 + H_2O \quad \text{(eqn. 6.4)}$$

$$e^-_{CB} + O_2 \longrightarrow O_2^{\bullet-} \quad \text{(eqn. 6.5)}$$

$$O_2^{\bullet-} + \text{organic molecule} \longrightarrow \longrightarrow \longrightarrow CO_2 + H_2O \quad \text{(eqn. 6.6)}$$

$$O_2^{\bullet-} + H^+ \longrightarrow {}^{\bullet}OOH \quad \text{(eqn. 6.7)}$$

$${}^{\bullet}OOH + \text{organic molecule} \longrightarrow \longrightarrow \longrightarrow CO_2 + H_2O \quad \text{(eqn. 6.8)}$$

6.2.2. Photoreduction mechanism

Secondly, photoreduction reactions have also experienced an increasing interest as they can be not only a strategy for pollutant mitigation such as CO_2 but also a green route to obtain fuels and chemicals [19]. CO_2 photocatalytic reduction is often performed in the presence of H_2O as reducing agent, providing the necessary electrons and protons, at ambient temperature and pressure [20]. Specifically, h^+_{VB} holes oxidize H_2O molecules, forming both hydroxyl radicals and hydrogen ions together with molecular oxygen (eqn. 6.9 and 6.10), while e^-_{CB} reduce CO_2. The latter, however, results of higher complexity and, as a consequence, the accurate mechanism towards certain products is still unclear, thus hindering selectivity control [21,22]. Three pathways have been proposed as possible mechanisms: the formaldehyde pathway, the carbene pathway, and the glyoxal pathway, providing different single-carbon or multiple-carbon products [23]. On the other hand, due to the high chemical stability and inert nature of the CO_2 molecule, a single-electron reaction to induce CO_2 reduction is highly implausible because of the large negative standard potential of the process. Instead, multi-electron reactions, in

which transference of electrons, protons and radicals, rupture of C-O bonds, and generation of C-H bonds take place, are more favorable. The number of involved electrons is linked to the final product. In the case of methanol, a single carbon product, the reduction process requires six electrons (eqn. 6.11), while the formation of ethanol, which presents two carbon atoms, involves twelve electrons (eqn. 6.12) [20,21,22,23]. Despite methanol and ethanol being the products of interest in this Thesis, related to their great market value as fuels, other reduction reactions can take place, thus competing for the available electrons and yielding different products as carbon monoxide, formic acid, formaldehyde, or methane, to name a few. Accordingly, the control of selectivity plays a crucial role in order to maximize alcohol production rates and to avoid the generation of side products [20].

$$h^+_{VB} + H_2O \longrightarrow {}^{\bullet}OH + H^+ \qquad \text{(eqn. 6.9)}$$

$$2h^+_{VB} + H_2O \longrightarrow 1/_2\, O_2 + 2H^+ \qquad \text{(eqn. 6.10)}$$

$$CO_2 + 6H^+ + 6e^-_{CB} \longrightarrow CH_3OH + H_2O \qquad \text{(eqn. 6.11)}$$

$$2CO_2 + 12H^+ + 12e^-_{CB} \longrightarrow CH_3CH_2OH + 3H_2O \qquad \text{(eqn. 6.12)}$$

6.2.3. Metal oxides as photocatalysts

The industrial application of photocatalysts establishes a certain number of requirements to be fulfilled. High activity results fundamental, while increased resistance to poisoning and stability at high temperatures after prolonged application are also demanded. Other features such as mechanical and chemical stability or attrition resistance are highly desired. In this sense, despite showing the highest photocatalytic activities, noble metal catalysts are expensive and exhibit low stability at high temperatures, resulting in deactivation due to sintering processes [24]. On the other hand, binary metal sulfides display insufficient stability and remarkable toxicity [25]. Therefore, metal oxides are a suitable alternative as photocatalysts for potential industrial applications. Not only are they resistant to both poisoning and deactivation, but also are easily modified or combined with other species to enhance their photocatalytic performance [25].

Among all the available metal oxides, TiO_2 has been the most popular photocatalyst since the first report by Fujishima and Honda in 1972, in which this semiconductor was employed for the photoelectrochemical splitting of

water [26]. This is related to its remarkable properties, such as high stability, low toxicity, outstanding photoactivity resulting from its high redox potential, and tunable band gap [2,6,15]. Some applications developed since then comprise: detoxification of effluents, self-cleaning surfaces, water splitting for hydrogen production, photoreduction of CO_2 to alcohols, or solar energy harvesting [1,16].

TiO_2 can crystallize in different polymorphs, anatase, rutile and brookite being the most relevant ones. Rutile is the thermodynamically stable phase, while anatase and brookite are metastable and undergo an irreversible transformation towards rutile phase at *ca*. 600 ºC [27]. These three crystalline phases consist in TiO_6 octahedra (Ti^{4+} is six-coordinated to O^{2-}), but they show differences regarding the distortion of the octahedron units and shared edges or corners as represented in Figure 6.2 [28]. Specifically, tetragonal anatase is formed by corner-sharing octahedra, forming (001) planes. Rutile is characterized by edge-sharing octahedra at (001) planes, resulting in a tetragonal structure. Finally, orthorhombic brookite presents both corner- and edge-sharing octahedra. These differences in terms of lattice features lead to diverse mass densities and electronic band structures [15,27,28].

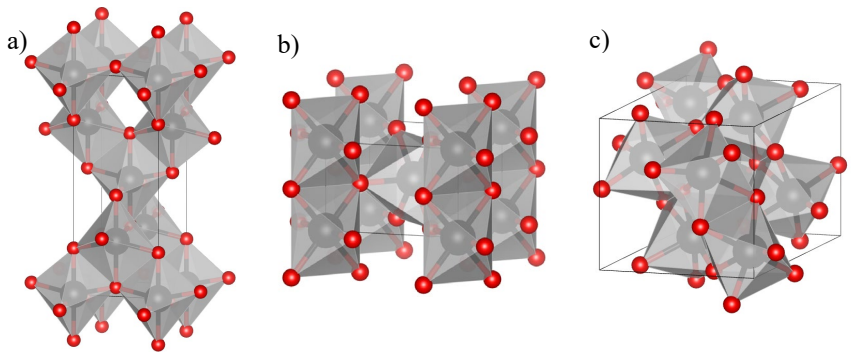

Figure 6.2. Crystalline structures of TiO_2: a) anatase, b) rutile, and c) brookite.

Band gap values of bulk TiO_2 have been reported to be 3.2, 3.0 and 3.4 eV for anatase, rutile and brookite, respectively. Accordingly, TiO_2-based photocatalysts display high performance under UV irradiation. However, given that only *ca*. 5% of the solar spectrum comprises UV radiation, these wide band gap values represent a non-negligible constraint for the industrial use of TiO_2 [15,25]. Consequently, many efforts have been made to increase the photocatalytic efficiency of this semiconductor using natural solar irradiation. Firstly, it has been reported that nanosized TiO_2 promotes a better separation of e^-_{CB}/h^+_{VB} pairs, thus leading to a decrease of recombination processes [27].

However, excessively reducing the particle size may increase surface recombination, therefore resulting in a detrimental effect on the photocatalytic activity [6]. Other strategies are focused on band gap optimization in order to extend the light absorption range of TiO_2. Some of these include: doping, fabrication of heterojunctions with metals or other semiconductors, or surface sensitization [15,25,29].

6.3. Band gap engineering

Among the aforementioned approaches, doping is one of the most effective strategies to improve the photocatalytic activity. The introduction of metal or non-metal ions within the semiconductor lattice leads to the generation of new impurity energy levels between the VB and CB of the catalyst, which can not only shift the light absorption towards the Vis spectral region, but also promote separation and mobility of e^-_{CB}/h^+_{VB} pairs [23,28]. In this context, the substitution of O atoms by non-metallic elements such as N, C, B or S has been widely studied. Nevertheless, despite reporting enhanced photocatalytic activities, small reductions of less than 0.3 eV of the original E_g value were obtained. Furthermore, in some metal oxide catalysts, the introduction of such anions may lead to the complete destruction of the crystalline structure as a consequence of the full substitution of O atoms, resulting in the formation of oxynitrides, oxysulfides or sulfides [1]. On the other hand, cation-doping of semiconductor catalysts with TM or RE ions is a popular strategy to extend light absorption to the Vis range. Indeed, it has been described that using RE and TM elements for such a purpose increases the activity of the photocatalytic system due to both the generated energy levels between the VB and CB and the electron transfer between the host and the doping ions [15]. However, some considerations need to be taken into account when doping with TM and RE ions. Firstly, these species may not be incorporated within the structure but remain on the catalyst surface, thus ending up being detrimental for the photocatalytic activity by blocking surface active sites [27]. Secondly, although the introduction of these elements has been observed to increase the photocatalytic efficiency, attributed to enhanced charge separation and extended absorption range, rapid charge recombination processes have also been reported due to exchangeable redox states of such doping species [25].

6.3.1. Transition metal ions

Transition metals comprise those elements located in the fourth period of the periodic table. In ionic solids, these tend to lose their outermost 4*s* and some 3*d* electrons, the electronic configuration of TM ions being $1s^2 2s^2 2p^6 3s^2 3p^6 3d^n$, where n < 10 [30]. The 3*d* orbitals, which are responsible for the optical transitions of TM ions, present a relatively large radius and lie on the outer shell of the ion. As a consequence of this lack of shielding, 3*d* orbitals have strong ion-lattice coupling, and thus are very sensitive to the crystalline environment. Accordingly, optical spectra of TM ions can present broad and intense bands, in contrast to the sharp, narrow bands of RE ions [30,31]. In this sense, and in line with the "strong crystal field" approach described in Chapter 3, electron-electron and crystal-field interactions dominate over spin-orbit interactions, resulting in noteworthy differences between the electronic states of the ion in the solid and those of the free ion depending on the complex symmetry [31].

The energy of TM excited states has been determined by Tanabe and Sugano, and is represented in the so-called Tanabe-Sugano diagrams. These diagrams comprise a graphical representation of the energy of the electronic states of $3d^n$ ions (2 < n < 8) as a function of the octahedral crystal field strength (Δ, defined as 10Dq) [30,32]. On the utmost left-side of the diagram, the energy levels of the free ion, denoted as $^{2S+1}$L, are represented. The energy separation of these states is determined by the Racah parameters (A, B, C), which describe the strength of the electrostatic interactions between the electrons. Indeed, the energy level splitting is represented as a function of the ratio between the latter and the crystal-field strength, *i.e.*, in Δ/B units, for a given C/B ratio [33]. In this sense, the effect of the crystal field may promote the degeneracy of these $^{2S+1}$L levels, being L referred to as A (no degeneracy), E (twofold degeneracy) or T (threefold degeneracy) [32]. In the case of tetrahedral symmetry of the system, the relationship between crystal-field strength is given by:

$$10Dq\ (\text{octahedral}) = -\frac{9}{4} Dq\ (\text{tetrahedral})$$

Therefore, the energy level scheme in tetrahedral symmetry is the same as that in octahedral symmetry, but with negative 10Dq. As a representative example, Figure 6.3 shows the Tanabe-Sugano diagram for a $3d^5$ configuration in an octahedral crystal field, characteristic of Mn^{2+}, one of the TM ions object of study in this Part II of the Thesis. Thus, Tanabe-Sugano diagrams are a useful

tool for interpretation of the optical properties of TM ions, specifically the position and width of absorption bands [32]. This has great interest in photocatalysis as it provides a strategy to predict and develop materials with a more efficient absorption of incident light.

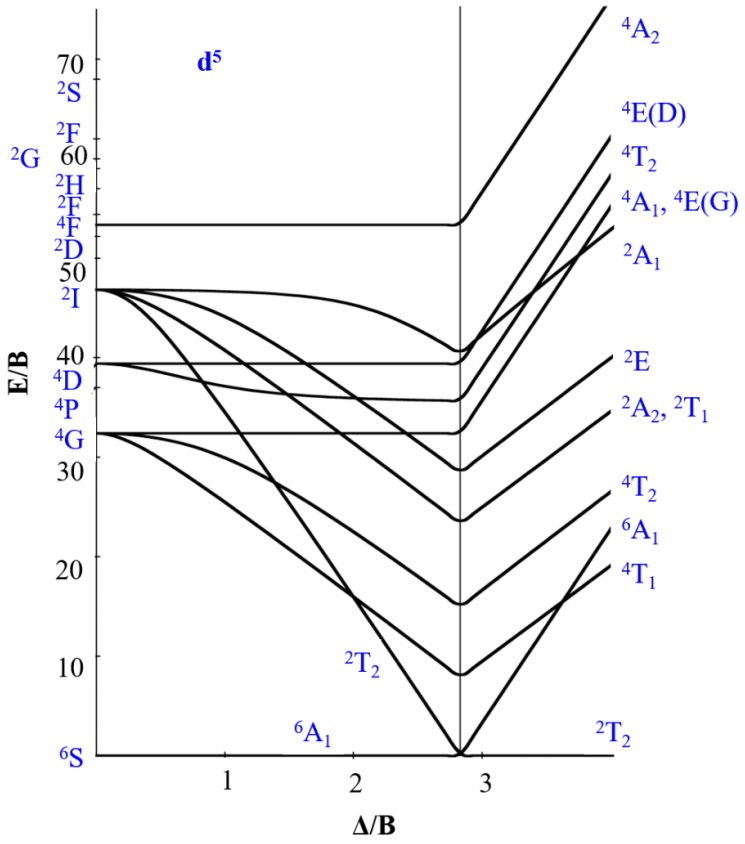

Figure 6.3. Tanabe-Sugano energy-level diagram for a $3d^5$ ion in octahedral symmetry.

6.3.2. Rare earth ions

As described in Chapter 4, RE^{3+} ions are characterized by their unfilled 4*f* shell, whose electrons are responsible for their optical properties. In this sense, 4*f* orbitals are shielded by the outer shells, *i.e.*, 5*s* and 5*p*, resulting in sharp, narrow bands from *f-f* transitions due to the weak crystal field contribution. Additional *f-d* transitions may be observed for both trivalent and divalent RE ions, giving rise to different spectroscopic response of the material [30,34]. Useful information about RE ions electronic transitions can also be obtained

from the Dieke diagram, for spectra interpretation, as previously explained in Chapter 4.

From the photocatalytic point of view, the introduction of RE ions as doping species within the semiconductor lattice is an interesting approach. Specifically, from the transitions of *f* orbital electrons a red-shift of the absorption edge of the material is expected [35]. It has also been reported that RE-doping promotes the formation of complexes of these dopant ions with Lewis bases on the catalyst surface, thus increasing both adsorption capacity and adsorption rate [36]. Furthermore, the introduction of RE ions into the TiO_2 structure inhibits phase transformation from anatase to rutile [37,38]. This has been described to lead to a better photocatalytic performance of the material due to the higher activity displayed by an appropriate ratio of both phases [39,40].

References

1 Tong, H.; Ouyang, S.; Bi, Y.; Umezawa, N.; Oshikiri, M.; Ye, J. Nano-photocatalytic materials: possibilities and challenges. *Adv. Mater*. **2011**, *24*, 229–251.

2 Bilal Tahir, M.; Rafique, M.; Shahid Rafique, M. *Nanotechnology and photocatalysis for environmental applications*. Elsevier, 2020.

3 Kumar, A.; Rana, S.; Wang, T.; Dhiman, P.; Sharma, G.; Du, B.; Stadler, F. J. Advances in S-scheme heterojunction semiconductor photocatalysts for CO_2 reduction, nitrogen fixation and NOx degradation. *Mater. Sci. Semicond. Process* **2023**, *168*, 107869.

4 Linic, S.; Aslam, U.; Boerigter, C.; Morabito, M. Photochemical transformations on plasmonic metal nanoparticles. *Nat. Mater*. **2015**, *14*, 567–576.

5 Gawande, M. B.; Goswami, A.; Felpin, F.-X.; Asefa, T.; Huang, X.; Silva, R.; Zou, X.; Zboril, R.; Varma, R. S. Cu and Cu-Based nanoparticles: synthesis and applications in catalysis. *Chem. Rev*. **2016**, *116*, 3722–3811.

6 Qu, X.; Alvarez, P. J. J.; Li, Q. Applications of nanotechnology in water and wastewater treatment. *Water Res*. **2013**, *47*, 3931–3946.

7 Ying Lim, S.; Shen, W.; Gao, Z. Carbon quantum dots and their applications. *Chem. Soc. Rev*. **2015**, *44*, 362–381.

8 Sarina, S.; Waclawik, E. R.; Zhu, H. Photocatalysis on supported gold and silver nanoparticles under ultraviolet and visible light irradiation. *Green Chem*. **2013**, *15*, 1814.

9 Haruta, M. Gold as a novel catalyst in the 21st century: preparation, working mechanism and applications. *Gold Bull*. **2004**, *37*, 27–36.

10 Bobo, M. V.; Kuchta, J. J.; Vannucci, A. K. Recent advancements in the development of molecular organic photocatalysts. *Org. Biomol. Chem* **2021**, *19*, 4816–4834.

11 Yan, C.; Dong, J.; Chen, Y.; Zhou, W. -J.; Peng, Y.; Zhang, Y.; Wang, L. -N. Organic photocatalysts: from molecular to aggregate level. *Nano Res*. **2022**, *15*, 3835–3858.

12 Chahal, S.; Macairan, J.-R.; Yousefi, N.; Tufenkji, N.; Naccache, R. Green synthesis of carbon dots and their applications. *RSC Adv*. **2021**, *11*, 25354–25363.

13 Elessawy, N. A.; El-Sayed, E. M.; Ali, S. M.; Elkady, M. F.; Elnouby, M.; Hamad, H. A. One-pot green synthesis of magnetic fullerene nanocomposite for adsorption characteristics. *J. Water Process. Eng*. **2020**, *34*, 101047.

14 Romero, N. A.; Nicewicz, D. A. Organic photoredox catalysis. *Chem. Rev*. **2016**, *116*, 10075–10166.

15 Etacheri, V.; Di Valentin, C.; Schneider, J.; Bahnemann, D.; Pillai, S. C. Visible-light activation of TiO_2 photocatalysts: advances in theory and experiments. *J. Photochem. Photobiol., C* **2015**, *25*, 1–29.

16 Zhou, H.; Qu, Y.; Zeid, T.; Duan, X. Towards highly efficient photocatalysts using semiconductor nanoarchitectures. *Energy Environ. Sci*. **2012**, *5*, 6732.

17 Morelli, S.; Pérez, R.; Querejeta, A.; Muñoz, J.; Lusvarghi, L.; Gualtieri, M. L.; Bolelli, G.; Grande, H. -J. Photocatalytic enamel/TiO_2 coatings developed by electrophoretic deposition for methyl orange decomposition. *Ceram. Int*. **2018**, *44*, 16199–16208.

18 Le, H. A.; Linh, L. T.; Chin, S.; Jurng, J. Photocatalytic degradation of methylene blue by a combination of TiO_2-anatase and coconut shell activated carbon. *Powder Technol*. **2012**, *225*, 167–175.

19 Portela, R.; Hernández-Alonso, M. D. Environmental applications of photocatalysis. In: *Design of advanced photocatalytic materials for energy and environmental applications*. Springer, 2013, 35–66.

20 Navarro-Jaén, S.; Virginie, M.; Bonin, J.; Robert, M.; Wojcieszak, R.; Khodakov, A. Y. Highlights and challenges in the selective reduction of carbon dioxide to methanol. *Nat. Rev. Chem*. **2021**, *5*, 564–579.

21 Wang, Y.; Chen, E.; Tang, J. Insight on reaction pathways of photocatalytic CO_2 conversion. *ACS Catal*. **2022**, *12*, 7300–7316.

22 Lundberg, D. J.; Parviz, D.; Kim, H. -A.; Lebowitz, M.; Lu, R.; Strano, M. S. Universal kinetic mechanism describing CO_2 photoreductive yield and selectivity for semiconducting nanoparticle photocatalysts. *J. Am. Chem. Soc*. **2022**, *144*, 13623–13633.

23 Habisreutinger, S. N.; Schmidt-Mende, L.; Stolarczyk, J. K. Photocatalytic reduction of CO_2 on TiO_2 and other semiconductors. *Angew. Chem. Int. Ed*. **2013**, *52*, 7372–7408.

24 Li, D.; Hao, C.; Liu, H.; Zhang, R.; Li, Y.; Guo, J.; Vilancuo, C. C.; Guo, J. Photocatalytic CO_2 conversion to ethanol: a concise review. *Catalysts* **2022**, *12*, 1549.

25 Ibhadon, A.; Fitzpatrick, P. Heterogeneous photocatalysis: recent advances and applications. *Catalysts* **2013**, *3*, 189–218.

26 Fujishima, A.; Honda, K. Electrochemical photolysis of water at a semiconductor electrode. *Nature* **1972**, *238*, 37–38.

27 Pelaez, M.; Nolan, N. T.; Pillai, S. C.; Seery, M. K.; Falaras, P.; Kontos, A. G.; Dunlop, P. S. M.; Hamilton, J. W. J.; Byrne, J. Anthony.; O'Shea, K.; Entezari, M. H.; Dionysiou, D. D. A review on the visible light active titanium dioxide photocatalysts for environmental applications. *Appl. Catal., B* **2012**, *125*, 331–349.

28 Ma, Y.; Wang, X.; Jia, Y.; Chen, X.; Han, H.; Li, C. Titanium dioxide-based nanomaterials for photocatalytic fuel generations. *Chem. Rev*. **2014**, *114*, 9987–10043.

29 Wang, Y.; Wang, Q.; Zhan, X.; Wang, F.; Safdar, M.; He, J. Visible light driven type II heterostructures and their enhanced photocatalysis properties: a review. *Nanoscale* **2013**, *5*, 8326.

30 García Solé, J.; Bausá, L. E.; Jaque, D. *An introduction to the optical spectroscopy of inorganic solids*. John Wiley & Sons Ltd, 2005.

31 Fox, M. *Optical properties of solids*. Oxford University Press, 2001.

32 Blasse, G.; Grabmaier, B. C. *Luminescent materials*. Springer-Verlag, 1994

33 Tanabe, Y.; Sugano, S. On the absorption spectra of complex ions. I. *J. Phys. Soc. Jpn*. **1954**, *9*, 753–766.

34 De Bettencourt-Dias, A. *Luminescence of lanthanide ions in coordination compounds and nanomaterials*. John Wiley & Sons Ltd, 2014

35 Nasir, M.; Bagwasi, S.; Jiao, Y.; Chen, F.; Tian, B.; Zhang, J. Characterization and activity of the Ce and N co-doped TiO_2 prepared through hydrothermal method. *Chem. Eng. J*. **2014**, *236*, 388–397.

36 Tang, X.; Xue, Q. L.; Qi, X.; Cheng, C.; Yang, M.; Yang, T.; Chen, F.; Qiu, F.; Quan, X. DFT and experimental study on visible-light driven photocatalysis of rare-earth-doped TiO_2. *Vacuum* **2022**, *200*, 110972.

37 Liu, H.; Yu, L.; Chen, W.; Li, Y. The progress of nanocrystals doped with rare earth ions. *J. Nanomater.* **2012**, *2012*, 235879.

38 Cacciotti, I.; Bianco, A.; Pezzotti, G.; Gusmano, G. Synthesis, thermal behaviour and luminescence properties of rare earth-doped titania nanofibers. *Chem. Eng. J*. **2011**, *166*, 751–764.

39 Luttrell, T.; Halpegamage, S.; Tao, J.; Kramer, A.; Sutter, E.; Batzill, M. Why is anatase a better photocatalyst than rutile? - Model studies on epitaxial TiO_2 films. *Sci. Rep.* **2014**, *4*, 4043.

40 Žerjav, G.; Žižek, K.; Zavašnik, J.; Pintar, A. Brookite vs. rutile vs. anatase: what's behind their various photocatalytic activities? *J. Environ. Chem. Eng*. **2022**, *10*, 107722.

7

Transition-metal doped titania nanoparticles for photocatalytic oxidation

This chapter describes the use of photocatalytic materials containing pure and TM doped TiO_2 NPs for the degradation of pollutants. To this end, different TiO_2-based nanocatalysts have been prepared by a precipitation method, which has been optimized prior to TM-doping. Next, a complete structural and optical characterization of the resulting NPs has been carried out. Afterwards, the photocatalytic activity of these NPs has been assessed through the degradation of MB dye in water as a model reaction. Then, the active NPs have been supported onto stainless-steel sheets, as part of a collaboration project with Vitrispan S.A. company. Likewise, after an in-depth structural and optical characterization, the photocatalytic activity of the supported catalysts has been investigated. Finally, the recyclability of these materials has been also studied.

The main goals of this chapter are:

1. To synthesize and perform an in-depth structural and optical characterization of the photocatalytically active pure and TM-doped TiO_2 NPs.
2. To carry out photodegradation experiments catalyzed by non-supported NPs.
3. To identify the optimal preparation conditions of the catalytic materials for further deposition onto enamel coatings on stainless steel surfaces.
4. To fully characterize the supported catalysts by means of structural and optical techniques.

5. To perform photocatalytic degradation experiments mediated by the pure and TM-doped TiO_2 NPs supported onto enamel coatings on stainless steel surfaces.

7.1. State of the art

Air and water contamination has become one of the most urgent environmental problems to overcome nowadays [1,2,3]. Specifically, the presence of atmospheric pollutants such as CO_x, NO_x and SO_x, as well as pesticides, pharmaceuticals and dyes dissolved in aqueous media represent some of the most concerning issues [4,5]. To remediate such a situation, different decontamination strategies based on advanced oxidation processes have been evaluated making use of the high reactivity of oxygen radicals ($^{\cdot}OH$, , $O_2^{\cdot-}$, $^{\cdot}OOH$) for pollutant degradation. Among these processes, photocatalytic oxidation is an advantageous alternative since no use of additional chemical species is required and no generation of waste streams is promoted [6,7]. Consequently, photooxidative degradation, which is a catalyst-mediated process, has become an important research area [7,8,9]. In particular, catalytic materials based on semiconductors have generated increasing interest, TiO_2 being one of the most popular one, due to the features described in Chapter 6 [10,11,12]. Nevertheless, an important limitation for its industrial application arises from its wide band gap. Accordingly, the introduction of TM ions as dopant species to extend light absorption of the catalyst towards the Vis spectral region has been widely studied, leading to an enhanced photocatalytic activity [13,14,15]. This improvement has been attributed to the creation of oxygen vacancies, due to the lower oxidation states of some TM-doping ions, and the induced narrowing of the band gap that promotes a redshift [13,16]. Moreover, TM ions have also been reported to restrain crystal growth, thus yielding reduced particle sizes, which might result in a higher photocatalytic activity owing to the increased active surface [6,17].

Particularly, Mn is a promising dopant species for Ti^{4+} substitution due to its similar ionic radius [18]. Firstly, it has been widely described that, among 3*d* TM elements, Mn is especially suitable to promote a TiO_2 band gap narrowing, introducing new intermediate energy states [6,19]. Secondly, Mn cations can exist in a variety of oxidation states, thus favouring charge separation [20]. Specifically, Mn^{2+} ions can act like hole traps, while Mn^{3+} and Mn^{4+} ions can act as electron traps [21]. In this sense, despite the lack of control

over the presence of different oxidation states in the resulting catalyst, such a mixture has been described to be advantageous. This is related to the fact that photogenerated charges are attracted by the different Mn cations, and thus their lifetime is increased yielding an enhanced photocatalytic activity [21]. Co has also been extensively studied as dopant for photocatalytic applications such as degradation of dyes, oxidation of NO and CO pollutants, as well as hydrogen production [22]. Co-doped TiO_2 NPs have been reported to display enhanced photoactivity under Vis irradiation due to created oxygen vacancies and new generated intermediate states from *d-d* transitions of Co^{2+}. Specifically, a broad absorption band centered at *ca*. 600 nm appears, thus promoting a redshift and a remarkable increase of absorbed Vis light [23,24]. Interestingly, numerous authors have described that upon heating above 500 ºC, Co-doped TiO_2 catalysts experience the formation of $CoTiO_3$ ilmenite phase as well as anatase-rutile transformation, both further increasing Vis light absorption [24,25].

Finally, the support is also an important factor that must be considered when using TiO_2-based nanomaterials for catalytic applications. The support is relevant not only to ensure recovery and recyclability of the catalysts but also to avoid possible health and environmental issues, especially when performing pollutant degradation in water streams or indoor locations [9]. In this sense, the immobilization of nanosized TiO_2 on glazed surfaces [26,27,28] and their incorporation into enamel coatings [29,30,31] have been extensively studied, leading to new smart photocatalytic materials with self-cleaning properties for different applications. Specifically, the use of such new functional materials has been described for sanity wares [32], coating for high solar power receivers [33], or construction elements as floorings, glasses, tunnels and subway panels [27,29,30,34,35,36], to name a few.

7.2. Fabrication of enamel coatings and photooxidation set-up

7.2.1. Synthesis of pure and transition-metal doped titania nanoparticles

Photoactive NPs were prepared following a precipitation method previously developed by Lusvardi *et al*., and described in section 2.1.2 [37]. This procedure was selected due to its simplicity, high reproducibility and easy scaling-up, as this chapter of the Thesis was developed under a collaboration project with Vitrispan S.A. company for potential industrial applications.

For undoped samples, an 80-mL aqueous solution of urea (32.5 mmol) was prepared. Then, 20 mL (65.2 mmol) of TTIP were added dropwise over this solution (1:0.5 Ti:urea ratio). The mixture was vigorously stirred at 50 ºC for 60 minutes, and then at 85 ºC for the reaction to occur. Nanocrystalline TiO_2 powder was obtained after complete solvent evaporation. For TM-doped NPs, stoichiometric amounts of the corresponding metal chloride for a 5% mol concentration (cobalt and manganese) were added to the urea solution prior to TTIP addition. Table 7.1 displays the different prepared photocatalysts and their nomenclature as a function of the calcination temperature and TM employed as doping ion.

In a first series of experiments, a subsequent calcination process at different temperatures for 2 h was performed for the undoped NPs to remove the excess of urea and increase the rutile ratio. After determining that 600 ºC was the most suitable annealing temperature, the effect of this calcination temperature was also assessed on TM-doped NPs.

Table 7.1. Summary of the undoped and TM-doped TiO_2 NPs prepared via precipitation method.

Photocatalytic material	**TM content (% mol)**	**T_{CAL} (ºC)**	**Nomenclature**
TiO_2	–	–	$RTTiO_2$
	–	600	$600TiO_2$
	–	800	$800TiO_2$
Mn/TiO_2	5	–	$RTMnTiO_2$
	5	600	$600MnTiO_2$
Co/TiO_2	5	–	$RTCoTiO_2$
	5	600	$600CoTiO_2$

T_{CAL}: calcination temperature

7.2.2. Fabrication of nanoparticle-based enamel coatings

As described in section 2.5.1, the supported catalysts were prepared at Vitrispan S.A. company through a vitrification process over stainless-steel sheets. Given that the vitrification process requires further annealing at 700 ºC, NPs without previous thermal treatment were selected to prepare the supported catalysts in order to avoid a high degree of sintering and the presence of pure rutile phase.

Specifically, $RTTiO_2$, $RTMnTiO_2$ and $RTCoTiO_2$ samples were selected to this end.

The resulting supported catalysts are displayed in Figure 7.1, and their corresponding nomenclature is included in Table 7.2.

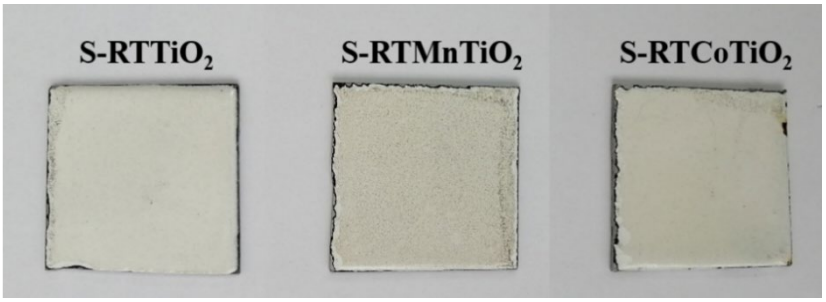

Figure 7.1. Photographs of supported photocatalysts containing the synthesized undoped and TM-doped TiO_2 NPs.

Table 7.2. Summary of the undoped and TM-doped TiO_2 NPs supported onto enamel coatings on stainless steel surfaces.

Photocatalytic NPs	**Nomenclature of supported sample**
$RTTiO_2$	S-$RTTiO_2$
$RTMnTiO_2$	S- $RTMnTiO_2$
$RTCoTiO_2$	S- $RTCoTiO_2$

7.2.3. Methylene blue degradation

As defined in section 2.6.1, the photocatalytic activity of both non-supported and supported NPs in the degradation of MB in water was studied according to the ISO 10678:2010 regulation [38]. The specific conditions for non-supported nanocatalysts are as follows: undoped or TM-doped TiO_2 NPs (10 mg) were dispersed in an aqueous solution of MB (150 mL, C_0 = 10 µM). The mixture was irradiated from the top with a UV light (395 nm, 22 W) at RT under vigorous stirring, as depicted in Figure 7.2. The extraction of small volume aliquots for MB absorbance measurements was performed at different times (t = 0, 1, 8 and 24 h).

For supported NPs, the resulting sheets were immersed in a MB aqueous solution (100 mL, C_0 = 10 μM). In the same way as for the powder NPs, the extraction of MB solution aliquots was carried out at t = 0, 1, 8 and 24 h for absorbance measurements.

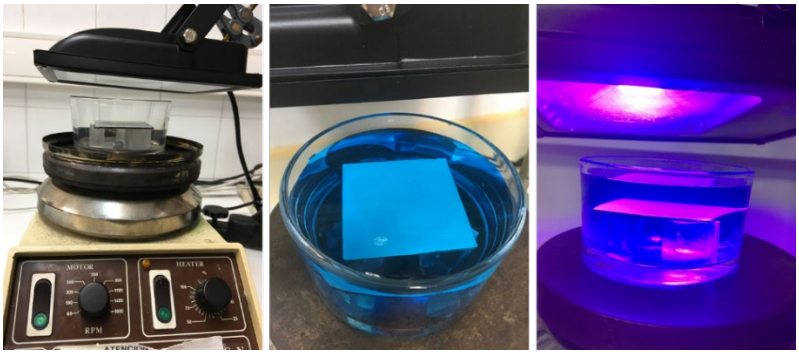

Figure 7.2. Setup for MB photocatalytic degradation studies.

7.3. Characterization of nanoparticles and photocatalytic activity

Different techniques were employed to perform the structural and optical characterization of the synthetized photocatalytic materials prior to their deposition onto enamel surfaces. In this way, the influence of NP size, anatase/rutile/brookite ratio and TM doping was studied. The photocatalytic activity of the non-supported NPs was then assessed.

7.3.1. Structural characterization

7.3.1.1. Undoped TiO_2 samples

An initial study of the effect of annealing temperature on the structural features of the synthesized NPs was carried out. In this line, the undoped TiO_2 NPs were characterized before and after calcination at both 600 and 800 ºC. Figure 7.3 shows the XRD patterns of the obtained NPs. Due to the low temperature of the synthesis reaction (85 ºC), anatase is the most abundant phase in the non-calcined NPs ($RTTiO_2$) [39] (Table 7.3, entry 1). However, a non-negligible amount of brookite phase was also generated. A thermal treatment was subsequently applied in order to promote the formation of rutile phase, which requires higher temperatures [39], to ultimately study the effect of the

anatase/rutile/brookite ratio on the photocatalytic activity. It was described that the photocatalytic activity is maximized for an anatase:rutile ratio of *ca*. 60:40 [40], although there is an open controversy concerning the synergistic effect between these phases [41,42]. The improved photocatalytic activity is ascribed by several authors to the heterojunction behavior of anatase-rutile mixture that favors e^-_{CB}/h^+_{VB} trapping, leading to an enhanced charge separation [43,44]. Besides, it is important to consider that owing to the lack of extensive studies of brookite phase, related to its complex fabrication, the vast majority of publications do not consider the effect of such a phase in this synergistic effect, although brookite is a photoactive phase as well [45,46]. However, the comparison of the different crystalline phases is difficult and may be affected by various physicochemical features of TiO_2 phases, in particular particle size, surface area or defect formation.

As expected, the XRD patterns showed the formation of rutile phase as a consequence of the calcination process. Specifically, a temperature of 600 ºC gave rise to up to 8% of rutile phase, while no traces of brookite were detected (Table 7.3, entry 2). At 800 ºC, an almost complete formation of rutile phase was observed (Table 7.3, entry 3).

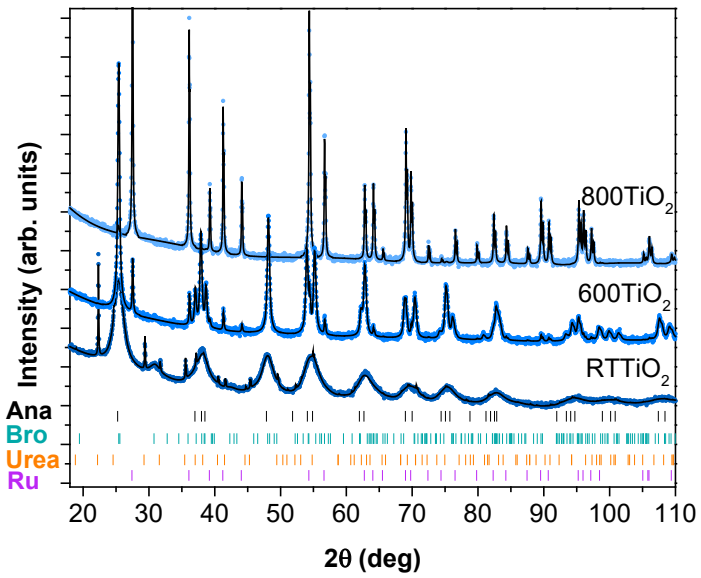

Figure 7.3. Refinement of XRD diffraction patterns of undoped TiO_2 NPs before and after thermal treatment at 600 and 800 ºC. Ana, Bro, Ru and Urea correspond to the Bragg positions of anatase, brookite and rutile phases, and urea, respectively.

Table 7.3. Summary of sizes and anatase/rutile/brookite ratios obtained by XRD and TEM for undoped TiO_2 NPs. Ana, Ru and Bro correspond to anatase, rutile and brookite phases, respectively.

Sample	**T_{CAL} (ºC)**	**Ana:Ru:Bro**	**$Size_{Ana}$ (nm)**	**$Size_{Ru}$ (nm)**	**$Size_{Bro}$ (nm)**	**$Size_{TEM}$ (nm)**
$RTTiO_2$[a]	–	68 : – : 32	5 ± 1	–	3 ± 1	5 ± 3
$600TiO_2$	600	92 : 8 : –	30 ± 1	59 ± 1	–	35 ± 10
$800TiO_2$	800	1 : 99 : –	–	102 ± 4	–	70 ± 75

[a] 10% urea. T_{CAL}: calcination temperature.

Numerous authors have studied the phase transformation mechanism of TiO_2 upon heating, this being dependent on many factors such as particle size, pH or surface chemistry [47]. It is well known that anatase to rutile transformation occurs when increasing the temperature. However, there is no clear knowledge about whether anatase transforms to brookite or *vice versa*, which might be related to the scarce number of studies on brookite when compared with the other TiO_2 phases. Zhang et *al*. reported that, if particle sizes of the three TiO_2 phases are similar, anatase is the most stable form for crystal sizes below 11 nm, brookite is the most stable for size ranges between *ca*. 11 and 35 nm, and rutile is the most stable for crystal sizes above 35 nm [48]. Nevertheless, while this study described anatase → brookite → rutile to be the conversion sequence, Ye at *al*. provided results that contradict the former by reporting brookite → anatase → rutile as the actual transformation [49]. This discrepancy can be attributed to the different crystallite size presented in both studies, proving indeed that this parameter plays a crucial role in the phase transition mechanism modifying its direction [48,49].

Considering this, our results seem to be in good agreement with the brookite → anatase → rutile phase transformation sequence. Specifically, the average NP size was observed to increase with the calcination temperature (Table 7.3), which can be related to sintering processes, as expected. In this line, due to the very small crystallite size for both anatase and brookite phases (<5 nm) in the $RTTiO_2$ NPs, and the higher stability of anatase in this size range, an increase in temperature (600 ºC) promoted the brookite → anatase transformation (Table 7.3, entries 1 and 2). The amount of anatase phase increased progressively during the annealing process, most likely at the expense of the small brookite NPs. Interestingly, anatase ↔ brookite transformation has been previously described as a reversible process in certain size regions [48,50]. Furthermore, Zhu *et al*. [51] described that there is a critical brookite grain size

(D_c) that determines the direction of the phase transformation mechanism between anatase and brookite. In this way, there are three possible scenarios depending on D_c and brookite grain size (D_b):

i) $D_b = D_c$: anatase and brookite transform directly to rutile.
ii) $D_b > D_c$: anatase transforms to brookite, and then brookite directly to rutile.
iii) $D_b < D_c$: brookite transforms to anatase, and then anatase to rutile.

Accordingly, D_c is determined by the following expression:

$$D_c = \frac{192.6 D_a}{5.7 D_a + 65} \qquad \text{(eqn. 7.1)}$$

where D_a is the anatase grain size.

Therefore, as the undoped NPs (RTTiO$_2$) exhibit D_a value of 5 nm, the estimated critical grain size of brookite (D_c) is 10.3 nm. Consequently, given that the brookite phase in RTTiO$_2$ NPs presents an average crystallite size of 3 nm (D_b), a brookite → anatase transformation is expected, in good agreement with our results (Table 7.3, entries 1 and 2). On the other hand, the formation of larger crystallite sizes (>50 nm) led to the generation of rutile phase (8%). Upon increased heating (800 ºC), the NP size experienced a further growth, and thus a complete transformation to rutile phase, proving indeed the crucial role of particle size in the phase transformation mechanism. Additionally, traces of urea from the synthesis process in the non-calcined NPs were identified by XRD analysis. In this line, it can be concluded that the annealing step not only promoted the rutile phase formation and crystalline growth, but also the removal of remaining organic traces, which could be ultimately detrimental for the photocatalytic activity.

Figure 7.4 displays the obtained TEM images of the synthesized NPs, which support the described particle growth trend. NPs initially presented rounded morphology and an average particle size of *ca*. 5 nm, experiencing a transformation towards polyhedral shape and an increased particle size upon heating at 600 ºC. Higher temperatures up to 800 ºC promoted further particle growth as well as an increased degree of agglomeration.

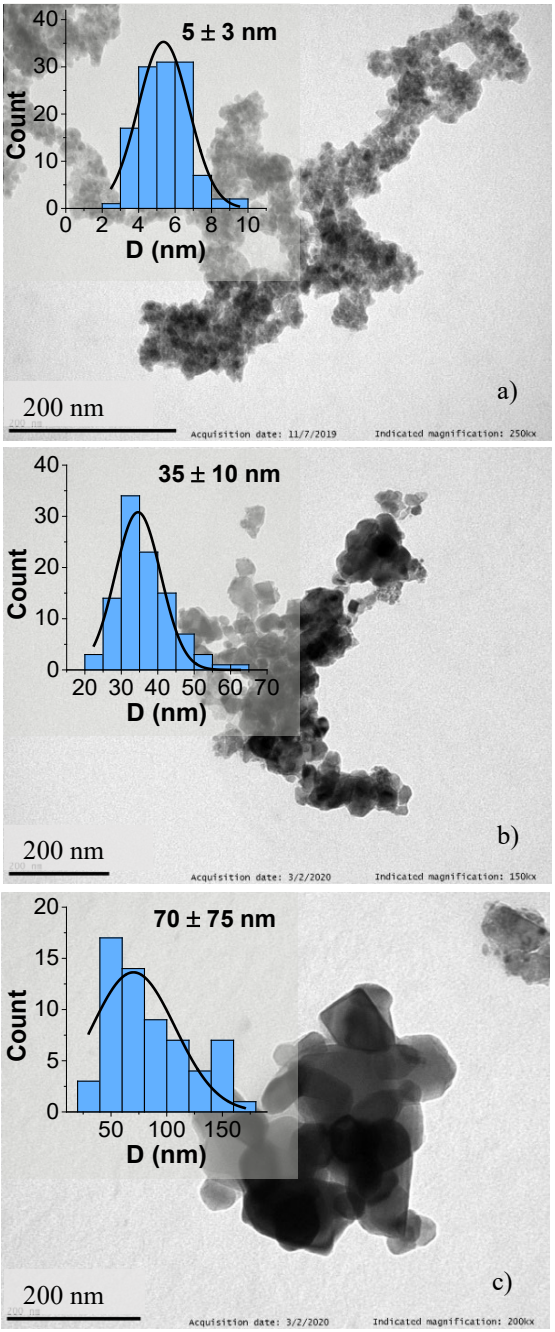

Figure 7.4. TEM images and average particle sizes of undoped (a) non-calcined TiO_2 NPs ($RTTiO_2$); (b) TiO_2 NPs calcined at 600 °C ($600TiO_2$); (c) TiO_2 NPs calcined at 800 °C ($800TiO_2$).

The Raman spectra of all undoped TiO_2 NPs were recorded and plotted in Figure 7.5. Mode assignment for anatase, rutile and brookite crystalline phases was previously reported elsewhere [52,53,54]. In this line, a total of 15 optical modes are expected from the anatase crystal space group analysis [D_{4h}^{19}, $I41/amd$, $Z=4$]. Their irreducible representation is the following [52]:

$$1\ A_{1g} + 1\ A_{2u} + 2\ B_{1g} + 1\ B_{2u} + 3\ E_g + 2\ E_u,$$

where A_{1g}, B_{1g} and E_g are Raman active; A_{2u} and E_u are infrared active; and B_{2u} is not Raman or infrared active. Thus, up to 6 lines can be expected to appear in the Raman spectrum.

At the same time, rutile also presents tetragonal structure, which belongs to the D_{4h}^{14} ($P42/mnm$, $Z=2$) space group. Again, 15 vibrational modes are expected, their irreducible representation being as follows [54]:

$$1\ A_{1g} + 1\ A_{2g} + 1\ A_{2u} + 1\ B_{1g} + 1\ B_{2g} + 2\ B_{1u} + 1\ E_g + 3\ E_u,$$

where A_{1g}, B_{1g}, B_{2g} and E_g are Raman active; A_{2u} and E_u are infrared active; and A_{2g}, and B_1u are not active in both Raman and infrared spectra. Consequently, only 4 lines associated to TiO_2 rutile phase could be detected in the Raman spectrum.

On the other hand, 69 optical modes are expected for the orthorhombic brookite phase from its D_{2h}^{15} space group ($Pbca$, $Z=8$), with the following irreducible representation [53]:

$$9\ A_{1g} + 9\ B_{1g} + 9\ B_{2g} + 9\ B_{3g} + 9\ A_{1u} + 8\ B_{1u} + 8\ B_{2u} + 8\ B_{3u},$$

where A_{1g}, B_{1g}, B_{2g} and B_{3g} are Raman active modes; B_{1u}, B_{2u} and B_{3u} correspond to infrared active modes, and A_{1u} is not active in both Raman and infrared. According to this, up to 36 lines would be expected in the Raman spectrum.

$RTTiO_2$ and $600TiO_2$ NPs exhibit Raman spectra dominated by bands associated to anatase phase, which was the main crystalline phase in good agreement with XRD results (68 and 92%, respectively). Specifically, the most intense band is centered at 144 cm^{-1} and corresponds to the E_g mode. Four additional bands out of the total six vibrational modes of anatase phase were detected for $RTTiO_2$, while the remaining five out of six were observed for

600TiO_2 sample. These characteristic Raman peaks are centered at 198 (E_g), 397 (B_{1g}), 516 (A_{1g} + B_{1g}) and 639 cm^{-1} (E_g) [52]. The presence of brookite phase was also confirmed in the RTTiO_2 NPs by two low intensity bands out of the total 36 Raman active modes, related to the reduced phase concentration, located at 319 (A_{1g}) and 364 cm^{-1} (B_{2g}) [53]. Raman peaks expected to be centered at 153 (A_{1g}) and 172 cm^{-1} (B_{1g}) seem to be overlapped by the predominant anatase band at 144 cm^{-1}. Likewise, three additional brookite Raman bands were expected to appear at 395 (B_{2g}), 407 (B_{1g}) and 640 cm^{-1} (A_{1g}), the former two being most likely the cause of the anatase peak broadening at 397 cm^{-1} for the RTTiO_2 sample.

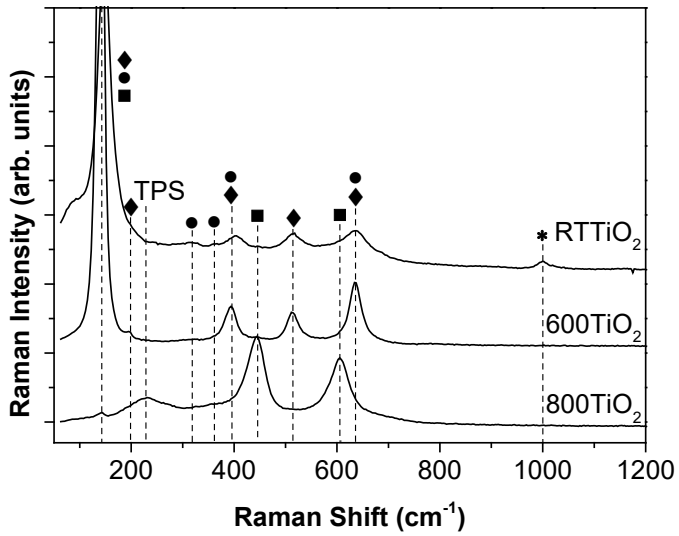

Figure 7.5. Raman spectra of undoped TiO_2 NPs before thermal treatment (RTTiO_2), and after calcination at 600 ºC and 800 ºC (600TiO_2 and 800TiO_2, respectively). ♦ anatase, ●: brookite, ■: rutile, *: urea. TPS: two-phonon scattering.

No Raman active modes from rutile phase were detected for RTTiO_2 and 600TiO_2 NPs due to its low concentration or total absence. Nevertheless, 800TiO_2 sample, in good agreement with the determined phase ratio from XRD results, presented a Raman spectrum completely dominated by bands associated to rutile phase. Specifically, three of the total four possible Raman active modes centered at 143 (B_{1g}), 447 (E_g) and 612 cm^{-1} (A_{1g}) were observed [54]. The remaining band expected to appear at 826 cm^{-1} (B_{2g}) was not detected. Additionally, a typical broad band at 247 cm^{-1} was present, related to two-phonon scattering (TPS in Figure 7.5), being a sign of the low harmonicity level in this crystalline phase [54]. Finally, and in good accord with XRD results, it

is worth noting that a broad band centered at 1002 cm^{-1}, corresponding to the NCN stretching mode of urea, was identified in the Raman spectrum of RTTiO_2 [55]. Such a band is related to the presence of urea traces from the synthesis process.

7.3.1.2. TM-doped TiO_2 samples

A second series of TiO_2 NPs doped with TM ions was prepared, since doping has been proven to be an efficient strategy to enhance the photocatalytic activity [14,15,56,57,58]. In this way, Mn and Co were selected as doping metals, with a concentration of 5% mol. Additionally, a subsequent thermal treatment at 600 ºC was applied. This moderate calcination temperature was selected to avoid the complete transformation of anatase and brookite phases to pure rutile form.

Figure 7.6 shows the XRD patterns of the TM-doped NPs. Phase identification and crystallite size estimation were performed through Rietveld refinement (Table 7.4). Both non-calcined Mn and Co-doped samples (RTMnTiO_2 and RTCoTiO_2, respectively) exhibit predominant anatase phase (≥60%), high brookite phase ratios (>35%), and small crystallite sizes (<5 nm), as expected from the low temperature synthesis process (85 ºC) [39]. Besides, an increase in the brookite ratio when compared with non-doped TiO_2 NPs was observed for both non-calcined Mn and Co-doped samples. As previously mentioned, pH is one of the parameters that modify anatase-rutile-brookite phase transition. Indeed, it has been previously reported that a higher acidity of the medium promotes the formation of brookite phase [39,59]. This is in good agreement with our results, given that metal chloride precursors containing elements with Lewis acid character (Mn and Co) were employed for the synthesis. On the other hand, samples subjected to the thermal treatment at 600 ºC (600MnTiO_2 and 600CoTiO_2) experienced an increase in the NP size related to the sintering process. In terms of crystalline phase ratios, the brookite content decreased or even disappeared after the annealing process, anatase becoming the most abundant phase (87%) for Mn-doped NPs, and the only TiO_2 phase (100%) for Co-doped NPs. An additional phase was detected in small amounts (8%) for the latter, which was assigned to $CoTiO_3$ ilmenite-type structure. The formation of this phase is related to the annealing process, given that at *ca*. 540 ºC solid-phase interactions of cobalt and titanium species occur to yield $CoTiO_3$ [60,61].

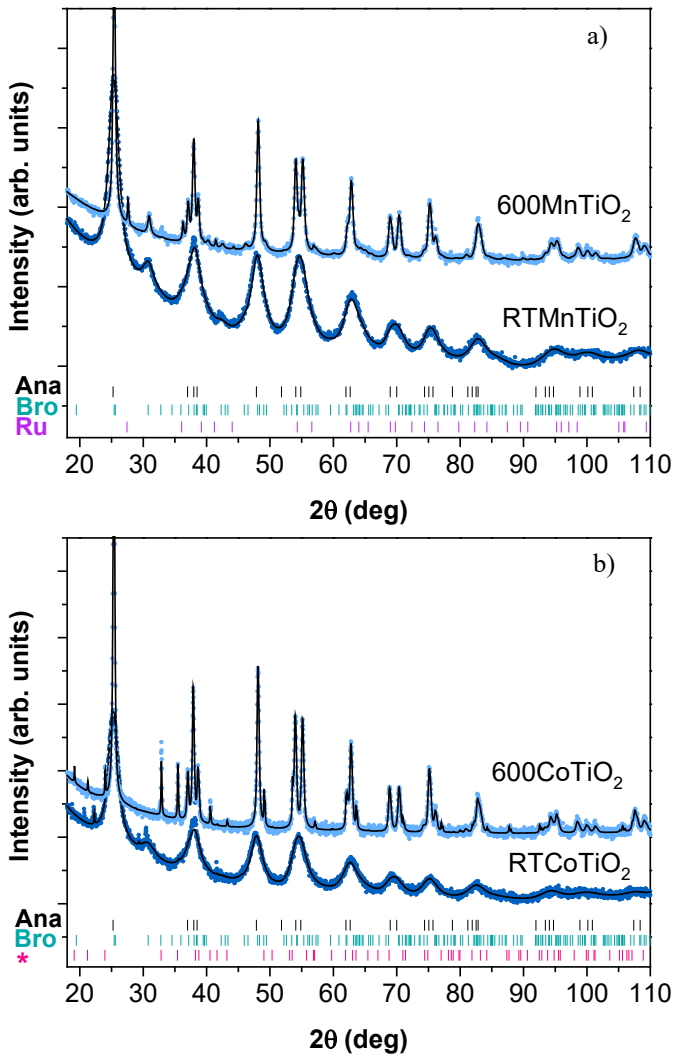

Figure 7.6. Refinement of XRD diffraction patterns of TM-doped TiO_2 NPs before and after thermal treatment at 600 ºC. a) Mn-doped NPs; b) Co-doped NPs. Ana, Bro and Ru correspond to the Bragg positions of anatase, brookite and rutile phases, respectively. Bragg positions for traces of $CoTiO_3$ phase in $600CoTiO_2$ NPs are indicated by (*).

From the Rietveld refinement of the XRD patterns, NP size was also determined (Table 7.4). Both non-calcined and calcined TM-doped NPs present slightly smaller crystallite size when compared with pure TiO_2 NPs. This trend is especially evident for the rutile phase of Mn-doped NPs annealed at 600 ºC ($600MnTiO_2$), which shows an average crystallite size of 37 nm in contrast with an average size of 59 nm for the $600TiO_2$ sample (Table 7.4). This effect has already been described by different authors. Elements such as Mn, Eu, Cu, Ag

or Fe have proven to inhibit crystal growth, and thus lead to smaller NPs [21,62,63,64,65]. On the other hand, no rutile phase was generated in the case of Co-doped NPs (600CoTiO$_2$). As previously described, in this size range (<11 nm) anatase is the most stable phase, and again brookite presents a crystallite size below the D_c. Therefore, applying a thermal treatment results in crystal growth of anatase at expense of brookite phase, *i.e.*, promoting the brookite → anatase phase transformation, thus confirming the highly size-dependent nature of the TiO$_2$ phase transformation [51].

Table 7.4. Summary of anatase/rutile/brookite ratios and sizes obtained by XRD and TEM for TM-doped TiO$_2$ NPs. Results for undoped TiO$_2$ NPs before and after thermal treatment at 600 ºC are included for comparison purposes. Ana, Ru and Bro correspond to anatase, rutile and brookite phases, respectively.

Sample	**T_{CAL} (ºC)**	**Ana:Ru:Bro**	**$Size_{Ana}$ (nm)**	**$Size_{Ru}$ (nm)**	**$Size_{Bro}$ (nm)**	**$Size_{TEM}$ (nm)**
RTTiO$_2$[a]	–	68 : – : 32	5 ± 1	–	3 ± 1	5 ± 3
600TiO$_2$	600	92 : 8 : –	30 ± 1	59 ± 1	–	35 ± 10
RTMnTiO$_2$	–	63 : 0 : 37	4 ± 1	–	3 ± 1	5 ± 2
600MnTiO$_2$	600	87 : 3.0 : 10	23 ± 1	37 ± 4	12 ± 1	30 ± 10
RTCoTiO$_2$	–	60 : 0 : 40	4 ± 1	–	2 ± 1	5 ± 2
600CoTiO$_2$[b]	600	100 : 0 : 0	27 ± 1	–	–	35 ± 20

[a] 10% urea. [b] 8% CoTiO$_3$. T_{CAL}: calcination temperature.

Figure 7.7 displays the TEM images of Mn and Co-doped TiO$_2$ NPs before and after thermal treatment at 600 ºC. As it can be observed, NPs presented a well-defined polyhedral morphology as well as an increased particle size after annealing. The NP sizes were determined from TEM images, being *ca*. 5 nm for non-calcined NPs and 30 and 35 nm for calcined Mn- and Co-doped NPs, respectively, in good agreement with the results obtained from Rietveld refinement.

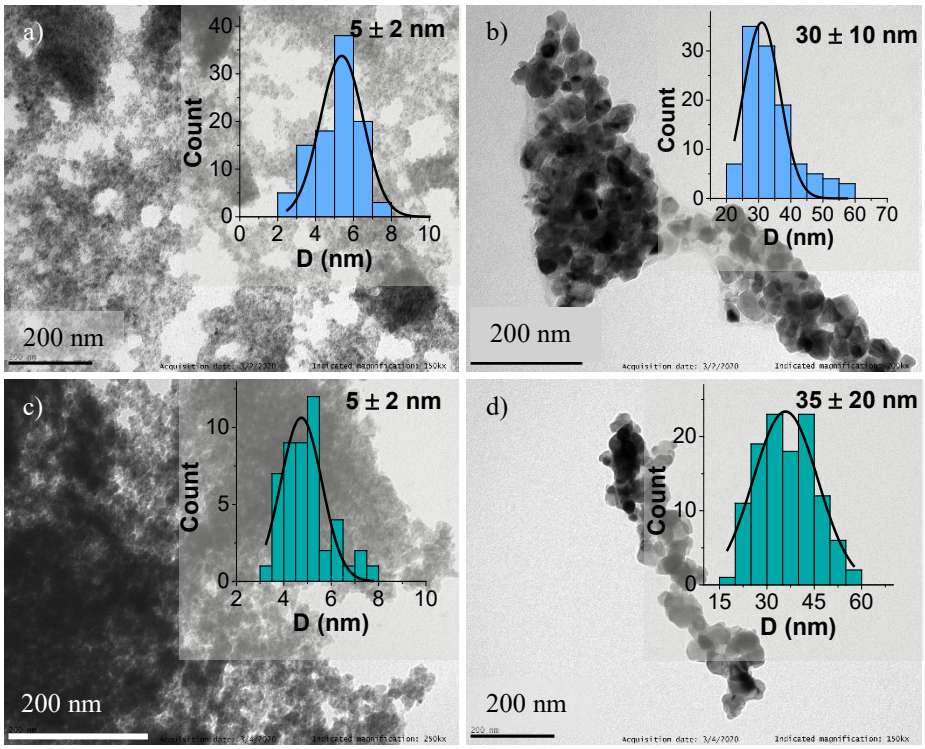

Figure 7.7. TEM images and average particle sizes of (a) non-calcined Mn-doped TiO_2 NPs ($RTMnTiO_2$); (b) Mn-doped TiO_2 NPs calcined at 600 °C ($600MnTiO_2$); (c) non-calcined Co-doped TiO_2 NPs ($RTCoTiO_2$); (d) Co-doped TiO_2 NPs calcined at 600 °C ($600CoTiO_2$).

The Raman spectra of Mn and Co-doped NPs are displayed in Figure 7.8. As expected, all Raman spectra are dominated by bands associated to anatase phase, in good agreement with XRD results (Table 7.4) and previous results from undoped samples. Specifically, the non-calcined Mn-doped NPs ($RTMnTiO_2$) presented anatase Raman bands centered at 149, 395, 514 and 631 cm^{-1} [52] (Figure 7.8a). Additionally, and due to the relatively high amount of brookite phase (>35%), the peak located at 318 cm^{-1} can be ascribed to such a TiO_2 crystalline phase [53]. As a consequence of the thermal treatment, the amount of anatase phase increased up to 87% for $600MnTiO_2$ NPs, ultimately leading to more intense anatase bands. At the same time, the brookite phase content decreased but still possible to detect by the characteristic band at 315 cm^{-1}. No rutile phase was identified in the $600MnTiO_2$ sample Raman spectrum (3%).

Similarly, both Co-doped samples ($RTCoTiO_2$ and $600CoTiO_2$) showed spectra dominated by the anatase phase (Figure 7.8b), following the previously described trend in which the intensity of these bands increased after the thermal treatment. Furthermore, in the case of $600CoTiO_2$ NPs, additional peaks were detected at 196, 263, 332 and 687 cm^{-1}. These Raman active bands correspond to the $CoTiO_3$ ilmenite structure [66], supporting the XRD fitting results.

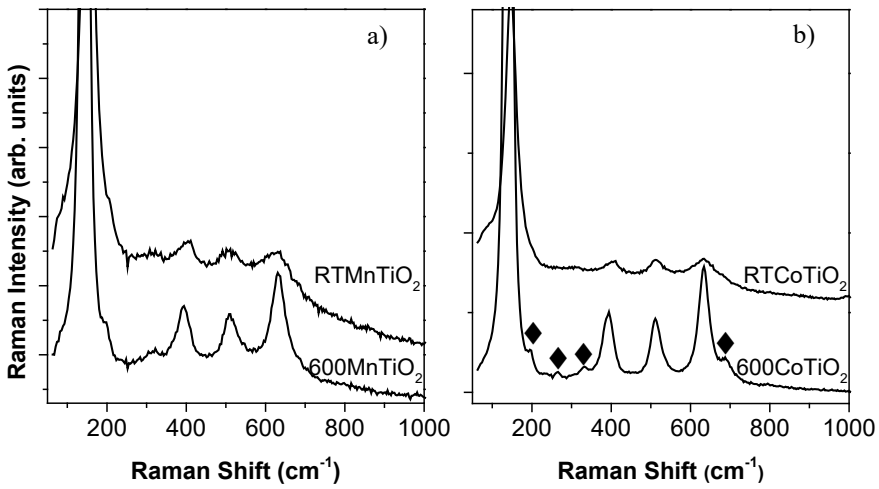

Figure 7.8. Raman spectra of TM-doped TiO_2 NPs before thermal treatment ($RTMnTiO_2$ and $RTCoTiO_2$) and after thermal treatment at 600 ºC ($600MnTiO_2$ and $600CoTiO_2$). ♦: $CoTiO_3$ ilmenite phase.

7.3.2. Optical characterization

7.3.2.1. Undoped TiO_2 samples

The optical characterization was performed by reflectance spectroscopy. Figure 7.9 displays the normalized absorption spectra of non-calcined undoped TiO_2 NPs and those of NPs calcined at different temperatures. As it can be observed, the thermal treatment had an important influence on the absorption band gap. Band gap values of the undoped NPs were determined by means of the graphical approach (Table 7.5), *i.e.*, from the intersection of the tangent line to the absorption curve and the wavelength axis [67]. Accordingly, $RTTiO_2$, $600TiO_2$ and $800TiO_2$ NPs presented average band gap energy values of 3.07 eV (404 nm), 2.93 eV (423 nm) and 2.89 eV (429 nm), respectively, thus

evidencing the band gap red-shift promoted by the anatase content increase and rutile formation arising from the thermal treatment. This red-shift of the band gap is attributed to the increase in the anatase ratio in the case of the NPs thermally treated at 600 ºC, and the formation of rutile phase upon treatment at 800 ºC [68], in good agreement with phase identification from XRD and Raman results. On the other hand, the non-calcined NPs ($RTTiO_2$) presented an additional band centered at *ca*. 1014 nm, corresponding to C-N stretching vibrations of urea traces [69,70]. After the thermal treatment this absorption band was not detected due to the removal of such a compound.

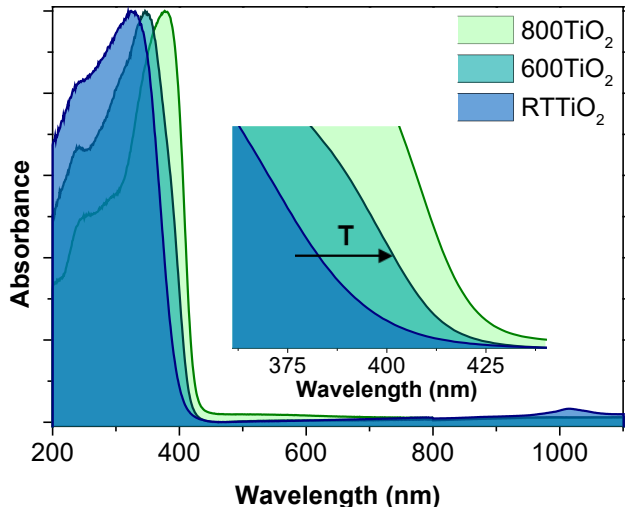

Figure 7.9. Normalized absorption spectra of undoped TiO_2 NPs.

Table 7.5. Estimated band gap values of the synthesized undoped NPs.

Entry	Photocatalyst	Band gap (eV)
1	$RTTiO_2$	3.07
2	$600TiO_2$	2.93
3	$800TiO_2$	2.89

7.3.2.2. TM-doped TiO_2 samples

Figure 7.10 shows the normalized absorption spectra of TM-doped TiO_2 NPs before and after the thermal treatment. The two main differences observed with regards to undoped NPs are: (i) red-shift of the absorption edge, and (ii)

presence of new absorption bands as a shoulder overlapping the absorption edge.

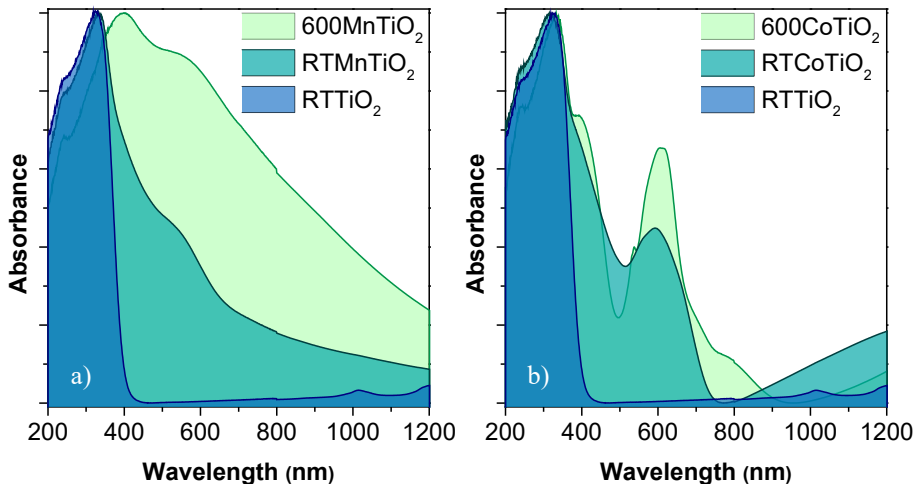

Figure 7.10. Normalized absorption spectra of (a) 5% Mn-doped TiO_2 NPs; (b) 5% Co-doped TiO_2 NPs. For comparison purposes, absorption spectra of non-calcined undoped TiO_2 NPs ($RTTiO_2$) are also included.

The latter can be ascribed to both TM ion absorption and charge-transfer interactions between doping ions and the TiO_2 CB or VB, confirming the incorporation of TM ions into the TiO_2 lattice [71,72]. Specifically, for Mn-doped TiO_2 NPs, remarkable differences are also observed comparing the spectra before and after thermal treatment ($RTMnTiO_2$ and $600MnTiO_2$, respectively). This can be attributed to the different possible oxidation states of Mn ion. It has been previously reported by means of X-ray photoelectron spectroscopy that synthesis procedures at RT promote Mn^{2+} as doping ion [18,73]. However, samples subjected to annealing processes with temperatures above 550 ºC lead to Mn^{3+} and Mn^{4+} oxidation states. In this context, Figure 7.10a shows that the TiO_2 characteristic edge at *ca*. 404 nm is shifted towards higher wavelengths for both Mn-doped samples. A remarkable red-shift of the absorption edge up to 600 nm is related to the contribution of electronic transitions of Mn ions in different oxidation states. Different Mn^{2+} bands are expected in the 400–600 nm range. Specifically, bands ascribed to the following crystal field transitions: $^6A_{1g} \rightarrow {}^4A_{1g}$, at *ca*. 420 nm, and $^6A_{1g} \rightarrow {}^4T_{2g}$, at *ca*. 500 and 610 nm. However, due to their weak intensity, such bands might be overlapped by the broad shoulder of the $^5B_{1g} \rightarrow {}^5E_g$ transition of Mn^{3+} expected at 485 nm [20]. Furthermore, a remarkable increase of absorption intensity is observed in the spectrum of the annealed Mn-doped NPs. This can

be ascribed to the presence of Mn^{4+} ions, since they present a characteristic absorption band at *ca*. 470 nm, assigned to the $^4A_{2g} \rightarrow {}^4T_{2g}$ transition [20,21]. This confirms that the calcination at 600 ºC promotes the generation of additional oxidation states when compared with the non-calcined Mn-doped NPs. Finally, the increased absorbance at wavelengths higher than 700 nm can be associated to the $^5B_{1g} \rightarrow {}^5A_{1g}$ transition of Mn^{3+} [20,21,74]. All things considered, the characterization study indicates that the annealing process not only influences crystallite size and TiO_2 phase ratio, but also plays a crucial role in the different oxidation states of Mn ions.

Conversely, Figure 7.10b displays the Co-doped NPs normalized absorption spectra, which show no remarkable changes in band shape when heating at high temperatures. This supports that Co exhibits its most stable valence, +2, which is also corroborated by the presence of a well-defined absorption band centered at 610 nm, ascribed to a *d-d* transition of Co^{2+} in octahedral coordination [23,71]. Similarly to TiO_2, Co^{2+} ions in the generated $CoTiO_3$ phase after calcination at 600 ºC also present octahedral coordination. Nevertheless, the presence of such an ilmenite phase can be inferred from the new small $Co^{2+} \rightarrow Ti^{4+}$ charge-transfer band at 537 nm of 600$CoTiO_2$ NPs, overlapping the initial broad band centered at 610 nm [75,76].

Regarding band gap values estimation, the previously employed graphical method cannot be accurately used for the prepared TM-doped NPs. This is caused by the complete overlap of the newly-generated absorption bands of the dopants with the TiO_2 absorption edge, making difficult to distinguish both contributions for band gap value determination.

In view of the results presented in this section, a potential enhancement of the photocatalytic activity of the TM-doped NPs could be associated not only with a red-shift of the energy band gap, but also with the introduction of new energy states within the TiO_2 energy band gap. Besides, in the case of Co-doped NPs, the promotion of light absorption at higher wavelengths in the Vis range could also be related to the presence of the photoactive $CoTiO_3$ phase.

7.3.3. Photocatalytic activity of transition-metal doped titania nanoparticles for methylene blue degradation

The photodegradation of MB synthetic dye in water was employed as a model reaction (Scheme 7.1) to study the photocatalytic activity of the synthetized

pure and TM-doped TiO_2 NPs, as recommended by the ISO 10678:2010 regulation [38]. Degradation of MB occurs, as described in section 6.2.1, when TiO_2 absorbs radiation of higher energy than its band gap, leading to the formation of e^-_{CB}/h^+_{VB} pairs, which generate powerful oxidizing radicals that may degrade pollutants or organic compounds such as MB.

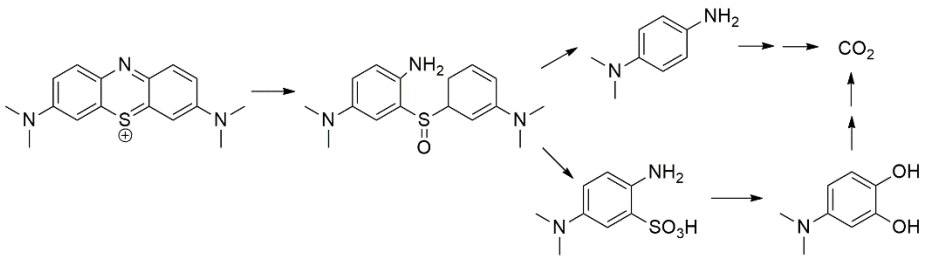

Scheme 7.1. Photocatalytic degradation route of methylene blue.

A set of catalytic experiments was carried out to study the influence of NP size, anatase/rutile/brookite ratio and TM-doping on the photocatalytic activity of TiO_2 NPs. Each of the synthesized NPs were dispersed in an aqueous solution of MB and irradiated with a UV lamp (395 nm). After a given time, the absorbance of the MB characteristic band centered at 664 ± 5 nm in the UV-Vis spectrum was employed to determine dye concentration (*C*). The photocatalytic efficiency of each type of NPs is correlated with the decomposition rate of MB, estimated by the following equation:

$$d\,(\%) = \frac{C_0 - C_t}{C_0} \cdot 100 = \frac{A_0 - A_t}{A_0} \cdot 100 \qquad \text{(eqn. 7.2)}$$

where *d* is the degradation rate, C_0 is the initial concentration of the MB solution and C_t is the concentration of the MB solution after a specific irradiation time, *t*. A_0 and A_t are the absorbance values at the maximum absorption band at time $t = 0$ and time *t*.

7.3.3.1. Undoped TiO_2 samples

Figure 7.11 shows the evolution of MB solution absorbance with time under UV irradiation in the presence of the photocatalytic undoped NPs prepared at RT and calcined at 600 and 800ºC. Table 7.6 summarizes the previously described structural information of the NPs, *i.e.*, anatase/rutile/brookite phase ratios and particle size, together with the achieved MB degradation rates.

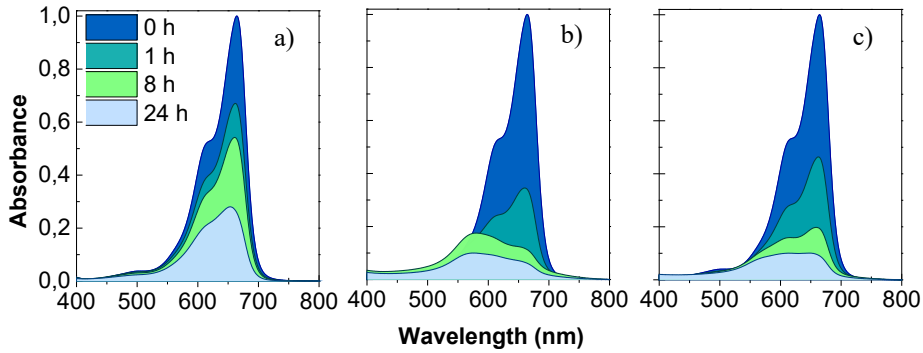

Figure 7.11. Evolution of MB solution normalized absorbance with time in a catalytic experiment mediated by undoped (a) RTTiO$_2$, (b) 600TiO$_2$, and (c) 800TiO$_2$ NPs. Conditions: MB (150 mL, 10 μM), TiO$_2$ NPs (10 mg), 22 W, λ = 395 nm, at RT.

RTTiO$_2$ NPs, which present a 68:32 anatase/brookite ratio, displayed a good catalytic performance with up to 72% MB degradation after 24 h of reaction (Figure 7.11a and Table 7.6, entry 1). Interestingly, despite the much bigger NP size after calcination at 600 ºC, 600TiO$_2$ NPs showed higher photocatalytic activity, achieving 93% MB degradation (Figure 7.11b and Table 7.6, entry 2). Firstly, this result can be attributed to an increase in the anatase crystalline phase and the formation of rutile phase upon annealing at 600 ºC, thus favoring the presumable positive anatase-rutile synergistic effect, which would reduce e^-_{CB}/h^+_{VB} recombination. Indeed, it has been previously reported that a mixture of anatase and rutile phases promotes the transference of e^-_{CB} from anatase to rutile CB, which leads to a separation of photogenerated charge carriers and ultimately reduces the e^-_{CB}/h^+_{VB} recombination, this being the major limitation in semiconductor-based photocatalysts [10,39,77]. However, there is not a clear agreement on this matter as some authors have described a 40-80% anatase phase proportion to be the optimal ratio for photooxidation by TiO$_2$ (with the remaining amount of rutile) [41], or a maximum photocatalytic activity for a 60:40 anatase/rutile ratio [40], while others claim that there is no such a synergistic effect at all between the aforementioned TiO$_2$ crystalline phases [42]. In addition, the improved photoactivity of the NPs annealed at 600 ºC could be related to their increased light absorption resulting from their band gap red-shift (3.07 and 2.93 eV for RTTiO$_2$ and 600TiO$_2$, respectively). Finally, the complete removal of remaining organic reagents from the synthesis process (10% urea in RTTiO$_2$ NPs by XRD) might have also contributed to the photocatalytic activity enhancement.

Table 7.6. Photocatalytic degradation of MB mediated by undoped TiO_2 NPs.[a] Ana, Ru and Bro correspond to anatase, rutile and brookite phases, respectively.

Sample	Ana:Ru:Bro	$Size_{Ana}$ (nm)	$Size_{Ru}$ (nm)	$Size_{Bro}$ (nm)	$Size_{TEM}$ (nm)	MB degr. (%)
$RTTiO_2$[b]	68 : 0 : 32	5 ± 1	–	3 ± 1	5 ± 3	72
$600TiO_2$	92 : 8 : 0	30 ± 1	59 ± 1	–	35 ± 10	93
$800TiO_2$	1 : 99 : 0	–	102 ± 4	–	70 ± 75	90

[a] Reagents and conditions: MB (150 mL, 10 μM), catalyst (10 mg), 22 W, λ = 395 nm, RT, 24 h. [b] 10% urea.

Annealing at 800 ºC ($800TiO_2$ NPs) led to a slight reduction of MB degradation (90%) when compared with $600TiO_2$ NPs (93%) (Figure 7.11c and Table 7.6, entry 3). This can be related to the observed remarkable decrease in the anatase phase content, given that, as previously reported, the photocatalytic activity is higher for a mixture of anatase/rutile polymorphs than for pure rutile phase [77]. Specifically, $600TiO_2$ NPs contain 92% anatase, while $800TiO_2$ NPs present 99% rutile phase. Additionally, a higher calcination temperature not only promoted almost pure rutile phase, but also the formation of much bigger NPs, which is known to be detrimental for photocatalytic activity due to the reduction of surface area [77].

Regarding the role of brookite in $RTTiO_2$ NPs, despite this phase being photocatalytically active and presenting a very small particle size, no positive contribution was observed. This could be ascribed to its larger band gap energy value (3.4 eV) when compared with the other TiO_2 crystalline phases (3.2 and 3.0 eV for anatase and rutile, respectively), thus leading to a reduced absorption of light from the excitation source.

7.3.3.2. TM-doped TiO_2 samples

The effect of TM-doping on MB degradation mediated by TiO_2 NPs was also studied. TM-doped NPs were expected to modify the TiO_2 absorption as a result of the introduction of new energy levels and the shift of the absorption edge towards higher wavelengths. At the same time, the e^-_{CB}/h^+_{VB} pair separation can be enhanced by TM ions, reducing the recombination of photogenerated charge carriers and increasing their lifetime [10,77]. Figure 7.12 presents the evolution of MB solution absorbance with time under UV irradiation in the presence of the photocatalytic TM-doped NPs prepared at RT and calcined at 600 ºC. Table 7.7 collects the resulting MB degradation rates together with the most relevant

structural features of the NPs, *i.e.*, TiO_2 crystalline phase ratios and particle size.

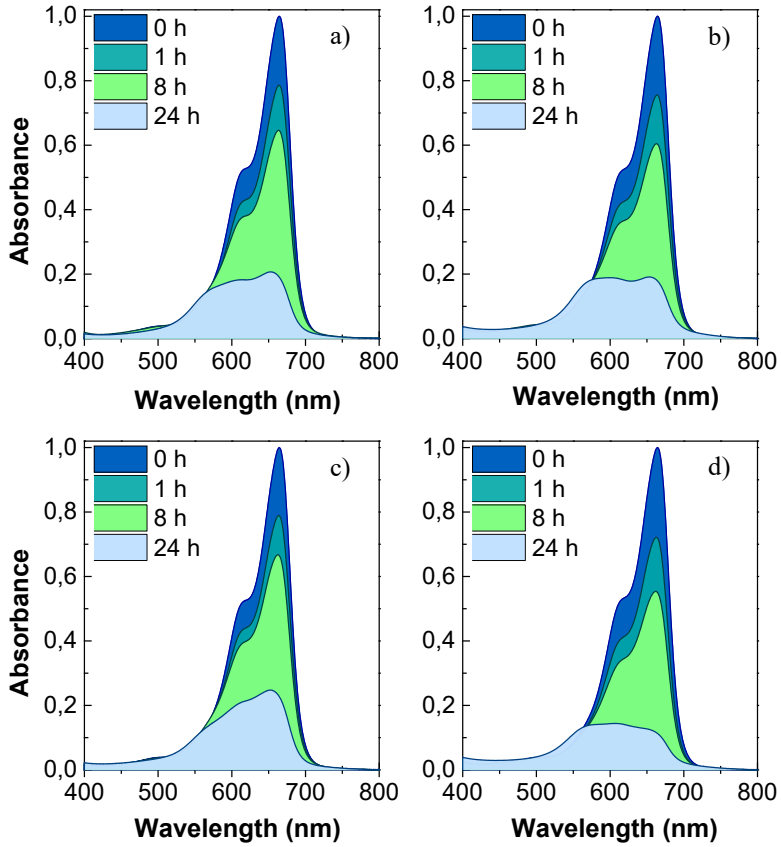

Figure 7.12. Evolution of MB solution normalized absorbance with time in a catalytic experiment mediated by a) $RTMnTiO_2$, b) $600MnTiO_2$, c) $RTCoTiO_2$, and d) $600CoTiO_2$. Conditions: MB (150 mL, 10 μM), TiO_2 NPs (10 mg), 22 W, λ = 395 nm, at RT.

In line with the obtained results from reflectance spectroscopy, an increase of 7% in the MB degradation (79%, Table 7.7, entry 3, Figure 7.12a) was achieved when using Mn-doped NPs ($RTMnTiO_2$) due to the absorption edge red-shifting (Figure 7.10a). Indeed, this improvement can be ascribed to the effect of Mn incorporation when compared with pure TiO_2 NPs ($RTTiO_2$), as both samples exhibit similar NP size and crystalline phase ratios.

The observed increase in photocatalytic activity with pure TiO_2 NPs after thermal treatment was also displayed by both Mn-doped NPs ($RTMnTiO_2$ and $600MnTiO_2$ samples) (Figures 7.12a and 7.12b), although the activity

growth was not as high as expected (Table 7.7, entries 3 and 4). In fact, pure TiO_2 NPs calcined at 600 ºC ($600TiO_2$) showed higher photocatalytic activity than Mn-doped NPs after the annealing process ($600MnTiO_2$) (93 and 82%, respectively). This could indicate that crystalline phase ratio may play a more important role than NP size for the photocatalytic activity. In this line, even though $600MnTiO_2$ sample presents smaller NPs than $600TiO_2$, the former exhibits an 87:3:10 anatase/rutile/brookite ratio, while the latter displays a 92:8 anatase/rutile ratio. Therefore, undoped TiO_2 NPs thermally treated at 600 ºC ($600TiO_2$) are the most active photocatalyst for MB degradation, indicating that there might be indeed a synergistic effect between anatase and rutile phases.

On the other hand, Co-doped TiO_2 NPs ($RTCoTiO_2$) also exhibited a slightly higher activity (75%) (Table 7.7, entry 5, Figure 7.12c) than that shown by undoped NPs ($RTTiO_2$), in good agreement with the absorption edge shift observed in Figure 7.10b. Again, annealing at 600 ºC had a positive impact on the photocatalytic activity, providing a MB degradation of 86% for $600CoTiO_2$ NPs (Table 7.7, entry 6, Figure 7.12d). Nevertheless, and as previously observed for the Mn-doped sample, pure TiO_2 NPs calcined at 600 ºC still displayed higher photocatalytic activity than Co-doped TiO_2 NPs. This result can be ascribed to the aforementioned synergistic effect, given that $600CoTiO_2$ NPs lack this required combination of anatase and rutile polymorphs (100% of pure anatase form).

Table 7.7. Photocatalytic degradation of MB mediated by TM-doped TiO_2 NPs.[a] $RTTiO_2$ and $600TiO_2$ NPs are included for comparative purposes. Ana, Ru and Bro correspond to anatase, rutile and brookite phases, respectively.

Sample	Ana:Ru:Bro	$Size_{Ana}$ (nm)	$Size_{Ru}$ (nm)	$Size_{Bro}$ (nm)	$Size_{TEM}$ (nm)	MB degr. (%)
$RTTiO_2$[b]	68 : 0 : 32	5 ± 1	–	3 ± 1	5 ± 3	72
$600TiO_2$	92 : 8 : 0	30 ± 1	59 ± 1	–	35 ± 10	93
$RTMnTiO_2$	63 : 0 : 37	4 ± 1	–	3 ± 1	5 ± 2	79
$600MnTiO_2$	87 : 3.0 : 10	23 ± 1	37 ± 4	12 ± 1	30 ± 10	82
$RTCoTiO_2$	60 : 0 : 40	4 ± 1	–	2 ± 1	5 ± 2	75
$600CoTiO_2$[c]	100 : 0 : 0	27 ± 1	–	–	35 ± 20	86

[a] Reagents and conditions: MB (150 mL, 10 μM), catalyst (10 mg), 22 W, λ = 395 nm, RT, 24 h. [b] 10% urea. [c] 7.9% $CoTiO_3$.

The results presented in this section point out the clear influence of both the anatase/rutile/brookite ratio and the presence of TM dopants on the catalytic performance of TiO_2 NPs. Specifically, the decrease of brookite content and the formation of rutile phase led to an enhancement of catalytic activity, which could be associated with the aforementioned synergistic effect between anatase and rutile phases. In addition, TM-doping also produces an improvement in the catalytic performance of TiO_2 NPs. Both the optimization of the anatase/rutile ratio and the doping with TM ions led to a shift in the absorption edge towards the visible spectral region, and thus to an increase in the activity of TiO_2 NPs.

7.4. Characterization of enamel coatings and photocatalytic activity

7.4.1. Structural characterization

The structural characterization of non-calcined NPs incorporated in enamel coatings and supported on steel sheets was performed by means of different techniques. Figure 7.13 shows the XRD patterns of the supported catalysts based on $RTTiO_2$, $RTMnTiO_2$ and $RTCoTiO_2$ NPs. Several differences can be identified from the patterns when compared with the initial NPs. On the one hand, the non-supported NPs presented broader diffraction peaks related to the small crystallite size, while supported NPs exhibited narrower peaks, expected after the thermal treatment performed during the preparation of the supported photocatalysts. On the other hand, additional peaks were detected for both non-doped and TM-doped supported samples. The vast majority of these peaks can be assigned to different phases, mainly silicates, from the mixture employed for enamel preparation. No traces of other crystalline phases were detected when doping the NPs with TM ions. Specifically, no features from $CoTiO_3$ phase were observed in the Co-doped sample, which might be related to the low amount of NPs added during the preparation of the supported catalyst.

After Rietveld refinement was carried out, phase ratios were determined and crystallite sizes were estimated (Table 7.8). All the phases related to the mixture used for the preparation of the enamel were considered together as one single non-TiO_2 phase (NTP) to roughly calculate their abundance. This NTP phase represented around the 20% content in all supported samples. Regarding the TiO_2 phases, as previously observed for non-supported NPs, the brookite phase was completely removed after the thermal

treatment applied during the preparation of the supported photocatalyst. Besides, as expected, rutile phase appeared and anatase phase ratio increased. All supported samples presented a similar anatase:rutile crystalline phase ratio of *ca*. 75:25. In addition, XRD analyses showed an increase of NP size in the supported catalysts when compared with the non-calcined original NPs (Table 7.4). This growth can be ascribed to the thermal treatment required for the preparation of the supported photocatalysts (15 min at 700 ºC).

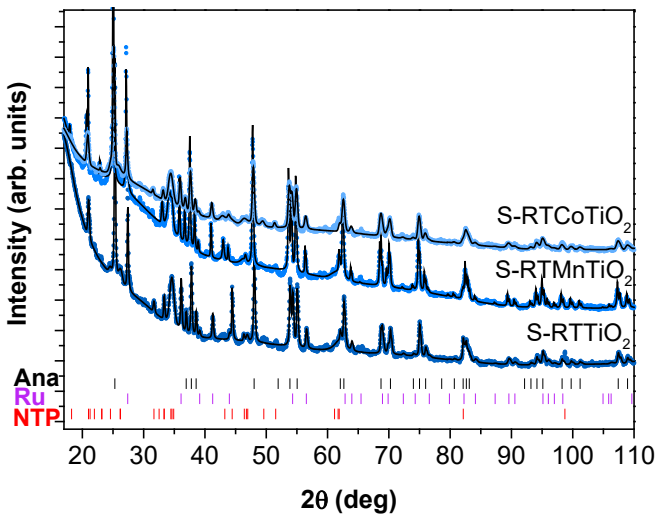

Figure 7.13. Refinement of XRD diffraction patterns of supported catalysts. Ana, Ru and NTP correspond to the Bragg positions of anatase and rutile phases, and the single phase related to the mixture used for the preparation of the enamel, respectively.

Table 7.8. Summary of TiO_2 NP sizes and anatase:rutile ratios determined by XRD of supported samples. Ana and Ru correspond to anatase and rutile phases, respectively.

Sample	**TM dopant**	**Ana:Ru**	**Size$_{Ana}$ (nm)**	**Size$_{Ru}$ (nm)**
S-RTTiO$_2$	–	72 : 28	45	44
S-RTMnTiO$_2$	5% Mn	75 : 25	42	61
S-RTCoTiO$_2$	5% Co	76 : 24	23	25

The Raman spectra of the three supported samples are displayed in Figure 7.14. The three spectra are dominated by bands corresponding to the anatase phase. Specifically, anatase Raman active peaks located at 144 (E_g), 198 (E_g), 397 (B_{1g}), 514 (A_{1g} + B_{1g}) and 639 cm^{-1} (E_g) were identified.

Additionally, a low-intensity band centered at 449 cm^{-1} was also recorded, which is associated to the E_g mode of rutile phase. As expected, the analyses of Raman spectra are in good agreement with phase determination by XRD.

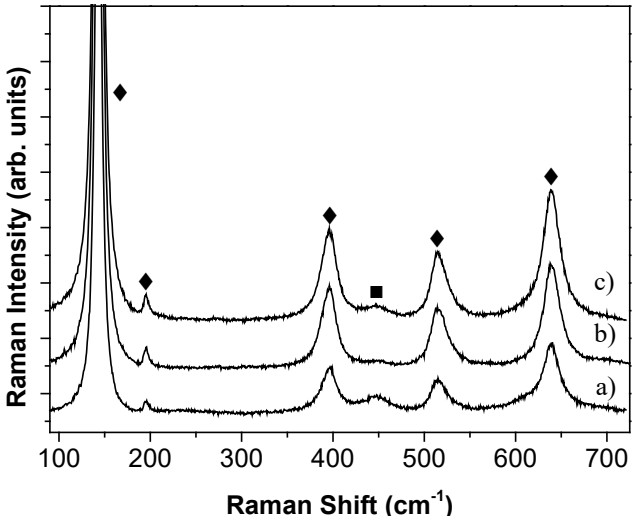

Figure 7.14. Raman spectra of active TiO_2 NPs deposited on enamel supported onto steel sheets; a) pure TiO_2 NPs (S-RTTiO$_2$), b) Mn-doped TiO_2 NPs (S-RTMnTiO$_2$), c) Co-doped TiO_2 NPs (S-RTCoTiO$_2$). ♦: anatase, ■: rutile.

7.4.2. Optical characterization

The optical characterization of the supported photocatalysts was carried out by reflectance spectroscopy. Figure 7.15a shows the absorption spectrum of the pure TiO_2-containing supported sample (S-RTTiO$_2$) and that of the original non-supported NPs (RTTiO$_2$) for comparative purposes. As it can be observed, only a slight shift of the absorption band towards the Vis region occurred after the deposition process. This shift can be ascribed to the formation of rutile phase (28%) during the thermal treatment at 700ºC required for NPs immobilization on the enamel-coated steel sheet.

On the other hand, Figure 7.15b compares the absorption spectra of the enamel samples containing RTTiO$_2$, RTMnTiO$_2$ and RTCoTiO$_2$ NPs deposited on steel sheets (S-RTTiO$_2$, S-RTMnTiO$_2$ and S-RTCoTiO$_2$ samples, respectively). No remarkable differences in terms of absorption edge values were observed for Mn and Co-doped supported NPs, in good agreement with their similar anatase:rutile ratios. Furthermore, as in the optical characterization of non-supported Mn-doped NPs, *d-d* transitions of Mn ions in different

oxidation states in the S-RTMnTiO$_2$ catalyst, arising from the applied thermal treatment at 700 ºC, were detected as a shoulder overlapping the absorption edge. In the case of S-RTCoTiO$_2$ catalyst, the *d-d* Co absorption band at 610 nm was also detected together with a small absorption band at 537 nm characteristic of the ilmenite CoTiO$_3$ phase, thus confirming the formation of a very reduced amount (non-detected by XRD) of such a phase during the aforementioned thermal treatment at 700 ºC.

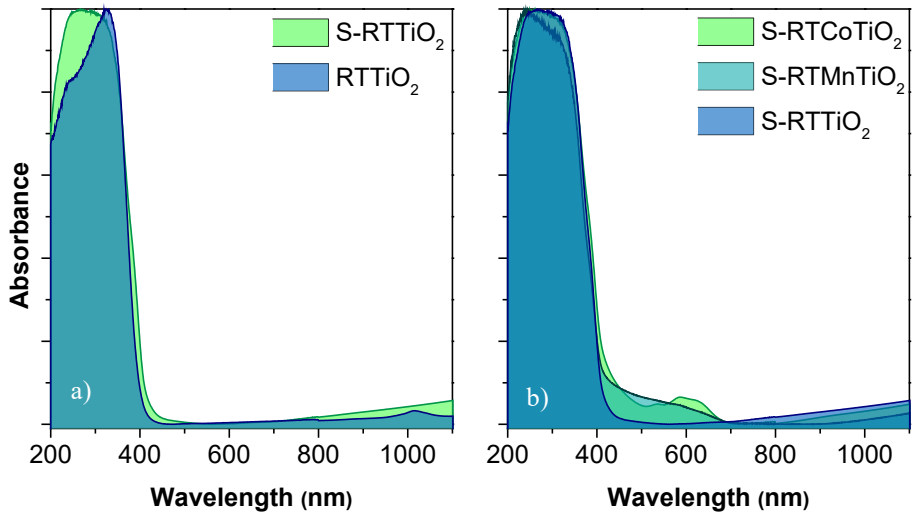

Figure 7.15. Normalized absorption spectra of a) non-supported (RTTiO$_2$) and supported (S-RTTiO$_2$) non-doped TiO$_2$ NPs; and b) pure, Mn and Co-doped supported NPs (S-RTTiO$_2$, S-RTMnTiO$_2$ and S-RTCoTiO$_2$, respectively).

7.4.3. Photocatalytic activity of supported nanoparticles on enamel coatings for methylene blue degradation

7.4.3.1 MB degradation mediated by supported catalysts

In this section, pure and TM-doped TiO$_2$-containing supported samples were studied as photocatalysts for MB degradation. The main results obtained from the experiments are presented in Figure 7.16 and Table 7.9. After 8 h of reaction, 16% MB degradation (54% at 24 h) was observed using the supported sample based on undoped NPs as photocatalyst (S-RTTiO$_2$). By comparison, TM-doped samples displayed very different results. Firstly, the Mn-doped photocatalyst (S-RTMnTiO$_2$) showed a decrease in activity, providing only 9% MB degradation after 8 h of reaction (35% at 24 h). However, a remarkable increase in the MB degradation was observed for the Co-doped photocatalyst

(S-RTCoTiO$_2$) when compared with the pure TiO$_2$ supported sample (from 16% up to 35% after 8h of reaction). Since the three samples exhibited similar anatase/rutile ratios (Table 7.9), the different results on the photocatalytic activity can be attributed to both TM-doping and NP size. In this line, the improved performance of the Co-doped photocatalyst can be related to its small crystallite size when compared with the undoped sample, and to the red-shift of the absorption edge caused by TM-doping. On the other hand, the Mn-doped sample was the least active photocatalyst, which could be associated with the higher crystallite size of rutile phase in such a material.

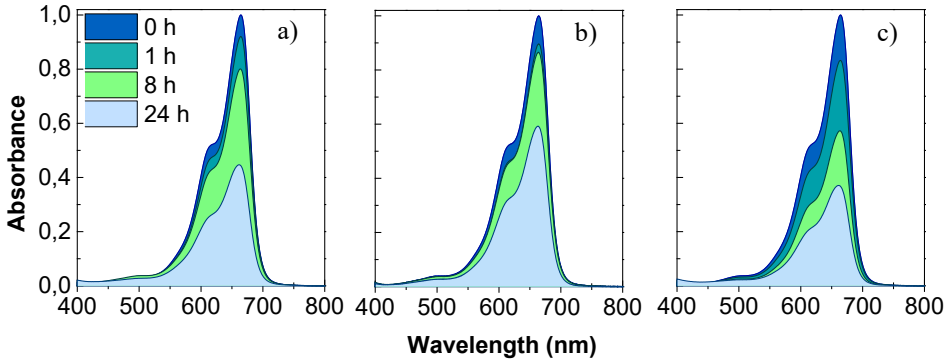

Figure 7.16. Evolution of MB solution normalized absorbance with time in a catalytic experiment mediated by (a) S-RTTiO$_2$, (b) S-RTMnTiO$_2$, and (c) S-RTCoTiO$_2$. Conditions: MB (150 mL, 10 μM), catalyst (5 × 5 cm^2), 22 W, λ = 395 nm, at RT.

Table 7.9. Photocatalytic degradation of MB mediated by TiO$_2$ NPs deposited on enamel supported onto steel sheets.[a] Ana and Ru correspond to anatase and rutile phases, respectively.

Sample	**Ana:Ru**	**Size$_{Ana}$ (nm)**	**Size$_{Ru}$ (nm)**	**MB degradation (%)**	
				8 h	**24 h**
S-RTTiO$_2$	72 : 28	45	44	16	54
S-RTMnTiO$_2$	75 : 25	42	61	9	35
S-RTCoTiO$_2$	76 : 24	23	25	35	55

[a] Reagents and conditions: MB (100 mL, 10 μM), catalyst (5 × 5 cm2), 22 W, λ = 395 nm, RT.

7.4.3.2. Recyclability

The TM-doped supported photocatalysts were selected to study the recyclability of the prepared surfaces. These were reactivated by irradiation with the LED lamp for 48 h between successive cycles. Figure 7.17 displays a substantial reduction of photocatalytic activity in the third cycle (Table 7.10), which may be attributed to a gradual loss of supported NPs as a result of the repeated catalytic cycles, thus indicating that the supported photocatalysts show a limited potential for recyclability.

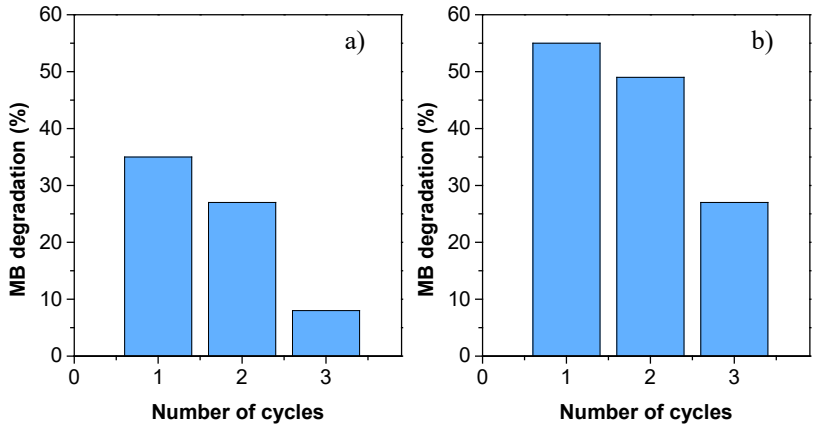

Figure 7.17. Reuse of a) S-RTMnTiO$_2$ and b) S-RTCoTiO$_2$ in the degradation of MB. Conditions: MB (150 mL, 10 μM), catalyst (5 x 5 cm^2), 22 W, λ = 395 nm, at RT.

Table 7.10. Reuse of S-RTMnTiO$_2$ and S-RTCoTiO$_2$ in the degradation of MB.

	MB degradation (%)		
Sample	**Cycle 1**	**Cycle 2**	**Cycle 3**
S-RTMnTiO$_2$	35	27	8
S-RTCoTiO$_2$	55	49	27

Even though the results reported herein might seem moderate when compared with others described in the literature for TiO$_2$ NPs supported on glazed surfaces [26,27,28,32,35,36] or contained in enamels [29,31,34], it is important to note that: (i) the supported photocatalysts prepared in this Thesis contain only 5% wt. TiO$_2$, and (ii) the experiments were carried out under near-Vis light (λ= 395 nm) with a low power LED lamp (22 W). In this line, the

photocatalytic activity could be certainly improved using a sunlight source with light intensity of *ca*. 500 lux. Thus, this photocatalytic system could be a potential candidate for applications such as indoor and outdoor construction elements like floorings, walls, tunnels, or subway panels.

7.5. Concluding remarks

The main conclusions obtained along this chapter are the following:

- The relevance and positive effect of both the appropriate anatase/rutile ratio and TM-doping has been demonstrated for photocatalytic applications of TiO_2 NPs.
- The thermal treatment has been proven to increase the initial anatase ratio and to form the rutile phase, leading to an activity enhancement attributed to a synergistic effect between these two crystalline phases.
- TM-doping has been demonstrated as an efficient strategy to improve the catalytic performance of the system, ascribed to the promoted displacement of the absorption edge to the Vis region.
- TiO_2 NPs have been successfully incorporated into an enamel surface onto stainless-steel sheets, showing good photocatalytic behavior. As in the case of the non-supported NPs, an influence of TM-doping has been observed, the Co-doped photocatalyst being the most efficient for MB degradation.
- The TiO_2 NPs-based enamel coatings display promising properties for potential industrial applications such as self-cleaning surfaces and NO_x photodegradation. Furthermore, the introduction of TM dopants has been demonstrated to promote Vis light absorption, boosting their photoactivity taking advantage of solar radiation.

References

1 Balbuena, J.; Cruz-Yusta, M.; Sánchez, L. Nanomaterials to combat NO_X pollution. *J. Nanosci. Nanotechnol*. **2015**, *15*, 6373–6385.

2 Ebele, A. J.; Abou-Elwafa Abdallah, M.; Harrad, S. Pharmaceuticals and personal care products (PPCPs) in the freshwater aquatic environment. *Emerg. Contam*. **2017**, *3*, 1–16.

3 Li, J.; Liu, H.; Chen, J. P. Microplastics in freshwater systems: a review on occurrence, environmental effects, and methods for microplastics detection. *Water Res.* **2018**, *137*, 362–374.

4 Serpone, N. Heterogeneous photocatalysis and prospects of TiO_2-based photocatalytic deNOxing the atmospheric environment. *Catal*. **2018**, *8*, 553.

5 Prasad, M. N. V.; Shih, K. *Environmental materials and waste: resource recovery and pollution prevention*. Academic Press Elsevier, 2016.

6 Gnanasekaran, L.; Hemamalini, R.; Saravanan, R.; Ravichandran, K.; Gracia, F.; Gupta, V. K. Intermediate state created by dopant ions (Mn, Co and Zr) into TiO_2 Nanoparticles for degradation of dyes under visible light. *J. Mol. Liq*. **2016**, *223*, 652–659.

7 Verbruggen, S. W. TiO_2 photocatalysis for the degradation of pollutants in gas phase: from morphological design to plasmonic enhancement. *J. Photochem. Photobiol*. **2015**, *24*, 64–82.

8 Paz, Y. Application of TiO_2 photocatalysis for air treatment: patents' overview. *Appl. Catal. B* **2010**, *99*, 448–460.

9 Petronella, F.; Truppi, A.; Ingrosso, C.; Placido, T.; Striccoli, M.; Curri, M. L.; Agostiano, A.; Comparelli, R. Nanocomposite materials for photocatalytic degradation of pollutants. *Catal. Today* **2017**, *281*, 85–100.

10 Pelaez, M.; Nolan, N. T.; Pillai, S. C.; Seery, M. K.; Falaras, P.; Kontos, A. G.; Dunlop, P. S. M.; Hamilton, J. W. J.; Byrne, J. Anthony.; O'Shea, K.; Entezari, M. H.; Dionysiou, D. D. A review on the visible light active titanium dioxide photocatalysts for environmental applications. *Appl. Catal.* **2012**, *125*, 331–349.

11 Ajmal, A.; Majeed, I.; Malik, R. N.; Idriss, H.; Nadeem, M. A. Principles and mechanisms of photocatalytic dye degradation on TiO_2 based photocatalysts: a comparative overview. *RSC Adv*. **2014**, *4*, 37003–37026.

12 Truppi, A.; Petronella, F.; Placido, T.; Striccoli, M.; Agostiano, A.; Curri, M.; Comparelli, R. Visible-light-active TiO_2-based hybrid nanocatalysts for environmental applications. *Catal*. **2017**, *7*, 100.

13 Kaur, R.; Singla, P.; Singh, K. Transition metals (Mn, Ni, Co) doping in TiO_2 nanoparticles and their effect on degradation of diethyl phthalate. *Int. J. Environ. Sci. Technol*. **2017**, *15*, 2359–2368.

14 Choi, W.; Termin, A. M.; Hoffmann, M. R. J. The role of metal ion dopants in quantum-sized TiO_2: correlation between photoreactivity and charge carrier recombination dynamics. *Phys. Chem*. **1994**, *98*, 13669–13679.

15 Chen, J.; Yao, M.; Wang, X. Investigation of transition metal ion doping behaviours on TiO_2 nanoparticles. *J. Nanopart. Res*. **2008**, *10*, 163–171.

16 Chen, J.; Qiu, F.; Xu, W.; Cao, S.; Zhu, H. Recent progress in enhancing photocatalytic efficiency of TiO_2-based materials. *Appl. Catal. A: Gen*. **2015**, *495*, 131–140.

17 Karuppasamy, P.; Nisha, N. R. N.; Pugazhendhi, A.; Kandasamy, S.; Pitchaimuthu, S. An investigation of transition metal doped TiO_2 photocatalysts for the enhanced photocatalytic decoloration of methylene blue dye under visible light irradiation. *J. Environ. Chem. Eng*. **2021**, *9*, 105254–105254.

18 Birlik, I.; Dagdelen, D. Synergistic effect of manganese and nitrogen codoping on photocatalytic properties of titania nanoparticles. *Bull. Mater. Sci*., **2020**, *43*, 85.

19 Kuzmicheva, G. M.; Savinkina, E. V.; Obolenskaya, L. N.; Zubavichus, Y. V.; Murzin, V.; Podbelskiy, V. V.; Sadovskaya, N. V. Synthesis of Mn-sensitized TiO_2 nanoparticles: influence of sequence of reagents on phase composition and photocatalytic activity. *J. Nanopart. Res*. **2015**, *17*, 406.

20 Velu, S.; Shah, N.; Jyothi, T. M.; Sivasanker, S. Effect of manganese substitution on the physicochemical properties and catalytic toluene oxidation activities of Mg–Al layered double hydroxides. *Microporous Mesoporous Mater*. **1999**, *33*, 61–75.

21 Pérez-Larios, A.; Hernández-Gordillo, A.; Morales-Mendoza, G.; Lartundo-Rojas, L.; Mantilla, A.; Gómez, R. Enhancing the H_2 evolution from water–methanol solution using Mn^{2+}–Mn^{+3}–Mn^{4+} redox species of Mn-doped TiO_2 sol–gel photocatalysts. *Catal. Today* **2016**, *266*, 9–16.

22 Sadanandam, G.; Lalitha, K.; Kumari, V. D.; Shankar, M. V.; Subrahmanyam, M. Cobalt doped TiO_2: a stable and efficient photocatalyst for continuous hydrogen production from glycerol:water mixtures under solar light irradiation. *Int. J. Hydrog. Energy* **2013**, *38*, 9655–9664.

23 Ding, Y.; Xu, X.; Gan, Z.; Xiong, R.; Liu, H. Extension of the optical absorption of TiO_2 nanoparticles to visible light region by doping with cobalt. *Solid State Phenom*. **2011**, *181-182*, 348–351.

24 Ganesh, I.; Gupta, A. K.; Kumar, P. P.; Chandra Sekhar, P. S.; Radha, K.; Padmanabham, G.; Sundararajan, G. Preparation and characterization of Co-doped TiO_2 materials for solar light induced current and photocatalytic applications. *Mater. Chem. Phys*. **2012**, *135*, 220–234.

25 Samet, L.; Ben Nasseur, J.; Chtourou, R.; March, K.; Stephan, O. Heat treatment effect on the physical properties of cobalt doped TiO_2 sol–gel materials. *Mater. Charact*. **2013**, *85*, 1–12.

26 Sirirerkratana, K.; Kemacheevakul, P.; Chuangchote, S. Color removal from wastewater by photocatalytic process using titanium dioxide-coated glass, ceramic tile, and stainless steel sheets. *J. Clean. Prod*. **2019**, *215*, 123–130.

27 Ke, S.; Cheng, X.; Wang, Q.; Wang, Y.; Pan, Z. Preparation of a photocatalytic $TiO_2/ZnTiO_3$ coating on glazed ceramic tiles. *Ceram. Int*. **2014**, *40*, 8891–8895.

28 Murugan, K.; Subasri, R.; Rao, T. N.; Gandhi, A. S.; Murty, B. S. Synthesis, characterization and demonstration of self-cleaning TiO_2 coatings on glass and glazed ceramic tiles. *Prog. Org. Coat*. **2013**, *76*, 1756–1760.

29 Jiang, W.; Wang, Y.; Gu, L. Influence of TiO_2 film on photo-catalytic property of enamels. *J. Non-Cryst. Solids* **2007**, *353*, 4191–4194.

30 Yoo, S.-J.; Lee, S.-I.; Kwak, D.-H.; Kim, K.-G.; Hwang, K.-J.; Lee, J.-W.; Hwang, U.-Y.; Park, H.-S.; Kim, J.-O. Photocatalytic degradation of methylene blue and acetaldehyde by TiO_2/glaze coated porous red clay tile. *Korean J. Chem. Eng*. **2008**, *25*, 1232–1238.

31 Morelli, S.; Pérez, R.; Querejeta, A.; Muñoz, J.; Lusvarghi, L.; Gualtieri, M. L.; Bolelli, G.; Grande, H.-J. Photocatalytic enamel/TiO_2 coatings developed by electrophoretic deposition for methyl orange decomposition. *Ceram. Int*. **2018**, *44*, 16199–16208.

32 Machida, M.; Norimoto, K.; Kimura, T. Antibacterial activity of photocatalytic titanium dioxide thin films with photodeposited silver on the surface of sanitary ware. *J. Am. Ceram. Soc*. **2004**, *88*, 95–100.

33 Cuce, E.; Cuce, P. M.; Riffat, S. TiO_2 nano-coated thin film PV glazing with superior thermal resistance, self-cleaning, electricity generation and adaptive optical control. *Int. J. Low-Carbon Technol*. **2021**, *17*, 130–139.

34 Baltes, L.; Patachia, S.; Tierean, M.; Ekincioglu, O.; Ozkul, H. M. Photoactive glazed polymer-cement composite. *Appl. Surf. Sci*. **2018**, *438*, 84–95.

35 Marcos, P. S.; Marto, J.; Trindade, T.; Labrincha, J. A. Screen-printing of TiO_2 photocatalytic layers on glazed ceramic tiles. *J. Photochem. Photobiol. A* **2008**, *197*, 125–131.

36 Raimondo, M.; Guarini, G.; Zanelli, C.; Marani, F.; Fossa, L.; Dondi, M. Photocatalytic, highly hydrophilic porcelain stoneware slabs. *IOP Conf. Ser.: Mater. Sci. Eng*. **2011**, *18*, 222022.

37 Lusvardi, G.; Barani, C.; Giubertoni, F.; Paganelli, G. Synthesis and characterization of TiO_2 nanoparticles for the reduction of water pollutants. *Materials* **2017**, *10*, 1208.

38 ISO 10678:2010, *Fine ceramics (advanced ceramics, advanced technical ceramics) – Determination of photocatalytic activity of surfaces in aqueous medium by degradation of methylene blue.*

39 Hu, Y.; Tsai H.-L.; Huangk, C.-L. Effect of brookite phase on the anatase–rutile transition in titania nanoparticles. *J. Eur. Ceram. Soc*., **2003**, *23*, 691–696.

40 Su, R.; Bechstein, R.; Sø, L.; Vang, R. T.; Sillassen, M.; Esbjörnsson, B.; Palmqvist, A.; Besenbacher, F. How the anatase-to-rutile ratio influences the photoreactivity of TiO_2. *J. Phys. Chem. C*, **2011**, *115*, 24287–24292.

41 He, J.; Du, Y.-e.; Bai, Y.; An, J.; Cai, X.; Chen, Y.; Wang, P.; Yang, X.; Feng, Q. Facile formation of anatase/rutile TiO_2 nanocomposites with enhanced photocatalytic activity. *Molecules*, **2019**, *24*, 2996.

42 Ma, R.; Chen, T. Checking the synergetic effect between anatase and rutile. *J. Phys. Chem. C*, **2019**, *123*, 19479–19485.

43 Ibhadon, A. O.; Fitzpatrick, P. Heterogeneous photocatalysis: recent advances and applications. *Catal*. **2013**, *3*, 189–218.

44 Byrne, C.; Subramanian, G.; Pillai, S. C. Recent advances in photocatalysis for environmental applications. *J. Environ. Chem. Eng*. **2018**, *6*, 3531–3555.

45 Di Paola, A.; Bellardita, M.; Palmisano, L. Brookite, the least known TiO_2 photocatalyst. *Catal*. 2013, 3, 36–73.

46 Manzoli, M.; Freyria, F. S.; Blangetti, N.; Bonelli, B. Brookite, a sometimes under evaluated TiO_2 polymorph. *RSC Adv*. **2022**, *12*, 3322–3334.

47 Kandiel, T. A.; Robben, L.; Alkaim, A.; Bahnemann, D. Brookite versus anatase TiO_2 photocatalysts: phase transformations and photocatalytic activities. *Photochem. Photobiol. Sci*. **2013**, *12*, 602–609.

48 Zang, H.; Banfield, J. Understanding polymorphic phase transformation behavior during growth of nanocrystalline aggregates: insights from TiO_2. *J. Phys. Chem. B* **2000**, *104*, 3481-3487.

49 Ye, X.; Sha, J.; Jiao, Z.; Zhang, L. Thermoanalytical characteristic of nanocrystalline brookite-based titanium dioxide. *NanoStructured Materials* **1997**, *8*, 919–927.

50 Li, J.-G.; Ishigaki, T. Brookite→rutile phase transformation of TiO_2 studied with monodispersed particles. *Acta Mater*. **2004**, *52*, 5143–5150.

51 Zhu, K.-R.; Zhang, M.-S.; Hong, J.-M.; Yin, Z. Size effect on phase transition sequence of TiO_2 nanocrystal. *Mater. Sci. Eng. A* **2005**, *403*, 87–93.

52 Ohsaka, T.; Izumi, F.; Fujiki, Y. Raman spectrum of anatase, TiO_2. *J. Raman Spectrosc.* **1978**, *7*, 321–324.

53 Tompsett, G. A.; Bowmaker, G. A.; Cooney, R. P.; Metson, J. B.; Rodgers, K. A.; Seakins, J. M. The Raman spectrum of brookite, TiO_2 (*Pbca*, *Z*=8). *J. Raman Spectrosc*. **1995**, *26*, 57–62.

54 Porto, S. P. S.; Fleury, P. A.; Damen, T. C. Raman spectra of TiO_2, MgF_2, ZnF_2, FeF_2, and MnF_2. *Phys. Rev*. **1967**, *154*, 522–526.

55 Frost, R. L.; Kristof, J.; Rintoul, L.; Kloprogge, J. T. Raman spectroscopy of urea and urea-intercalated kaolinites at 77 K. *Spectrochim. Acta, Part A* **1999**, *56*, 1681–1691.

56 Zhou, M.; Yu, J.; Cheng, B. J. Effects of Fe-doping on the photocatalytic activity of mesoporous TiO_2 powders prepared by an ultrasonic method. *J. Hazard. Mater*. **2006**, **137**, 1838–1847.

57 Yu, J.; Xiang, Q.; Zhou, M. Preparation, characterization and visible-light-driven photocatalytic activity of Fe-doped titania nanorods and first-principles study for electronic structures. *Appl. Catal. B* **2009**, *90*, 595–602.

58 Devi, L. G.; Kumar, S. G. Influence of physicochemical– electronic properties of transition metal ion doped polycrystalline titania on the photocatalytic degradation of indigo carmine and 4-nitrophenol under UV/solar light. *Appl. Surf. Sci*. **2011**, *257*, 2779–2790.

59 Bakardjieva, S.; Stengl, V.; Szatmary, L.; Subrt, J.; Lukac, J.; Murafa, N.; Niznansky, D.; Cizek, K.; Jirkovsky, J.; Petrova, N. Transformation of brookite-type TiO_2 nanocrystals to rutile: correlation between microstructure and photoactivity. *J. Mater. Chem*. **2006**, *16*, 1709–1716.

60 Vinogradov, A. V.; Vinogradov, V. V.; Gerasimova, T. V.; Agafonov, A. V. Low-temperature sol–gel synthesis of crystalline $CoTiO_3$ coatings without annealing. *J. Alloys Compd*. **2012**, *543*, 172–175.

61 Ha, C.A.; Nguyen, D.T.; Nguyen, T. Green fabrication of heterostructured $CoTiO_3/TiO_2$ nanocatalysts for efficient photocatalytic degradation of cinnamic acid. *ACS Omega* **2022**, *7*, 40163−40175.

62 Pal, M.; Pal, U.; Jiménez, J. M. G. Y.; Pérez-Rodríguez, F. Effects of crystallization and dopant concentration on the emission behavior of TiO_2:Eu nanophosphors. *Nanoscale Res. Lett*. **2012**, *7*, 1.

63 Sahu, M.; Biswas, P. Single-step processing of copper-doped titania nanomaterials in a flame aerosol reactor. *Nanoscale Res. Lett*. **2011**, *6*, 441.

64 Chao, H. E.; Yun, Y. U.; Xingfang, H. U.; Larbot, A. Effect of silver doping on the phase transformation and grain growth of sol-gel titania powder. *J. Eur. Ceram. Soc*. **2003**, *23*, 1457–1464.

65 Ali, T.; Tripathi, P.; Azam, A.; Raza, W.; Ahmed, A. S.; Ahmed, A.; Muneer, M. Photocatalytic performance of Fe-doped TiO_2 nanoparticles under visible-light irradiation. *Mater. Res. Express*, **2017**, *4*, 015022.

66 Shilpy, M.; Ehsan, M. A.; Ali, T. H.; Hamid, S. B. A.; Ali, Md. E. Performance of cobalt titanate towards H_2O_2 based catalytic oxidation of lignin model compound. *RSC Adv*. **2015**, *5*, 79644–79653.

67 Pradeep, T. Determination of the band gap of semiconductor nanoparticles. In: *Textbook of nanoscience and nanotechnology*. McGraw Hill Education, 2012.

68 Lan, Y.; Lu, Y.; Ren, Z. Mini review on photocatalysis of titanium dioxide nanoparticles and their solar applications. *Nano Energy* **2013**, *2*, 1031–1045.

69 Piasek, Z.; Urbański, T. The infra-red absorption spectrum and structure of urea. *Bull. Acad. Pol. Sci., Sér. Sci. Chim*. **1962**, *10*, 113–120.

70 Fischer, P. H. H.; McDowell, C. A. The infrared absorption spectra of urea-hydrocarbon adducts. *Can. J. Chem*. **1960**, *38*, 187–193.

71 Umebayashi, T; Yamaki, T.; Itoh, H.; Asai, K. Analysis of electronic structures of 3d transition metal-doped TiO_2 based on band calculations. *J. Phys. Chem. Solids* **2002**, *63*, 1909–1920.

72 Peng, B.; Meng, X.; Tang, F.; Ren, X.; Chen, D.; Ren, J. General synthesis and optical properties of monodisperse multifunctional metal-ion-doped TiO_2 hollow particles. *J. Phys. Chem. C* **2009**, *113*, 20240–20245.

73 Zhang, W.; Zhou, W.; Wright, J. H.; Kim, Y. N.; Liu, D.; Xiao, X. Mn-doped TiO_2 nanosheet-based spheres as anode materials for lithium-ion batteries with high performance at elevated temperatures. *ACS Appl. Mater. Interfaces* **2014**, *6*, 7292–7300.

74 Baldi, M.; Milella, F.; Gallardo-Amores, J. M.; Busca, G. A study of Mn-Ti oxide powders and their behaviour in propane oxidation catalysis. *J. Mater. Chem*. **1998**, *8*, 2525–2531.

75 Qu, Y.; Zhou, W.; Fu, H. Porous cobalt titanate nanorod: a new candidate for visible light-driven photocatalytic water oxidation. *ChemCatChem* **2013**, *6*, 265–270.

76 Ye, R.; Fang, H.; Zheng, Y.-Z.; Li, N.; Wang, Y.; Tao, X. Fabrication of $CoTiO_3$/G-C_3N_4 hybrid photocatalysts with enhanced H_2 evolution: Z-scheme photocatalytic mechanism insight. *ACS Appl. Mater. Interfaces* **2016**, *8*, 13879–13889.

77 Hanaor, D. A. H.; Sorrell, C. C. Review of the anatase to rutile phase transformation. *J. Mater. Sci*. **2010**, *46*, 855–874.

8

Rare-earth and transition-metal doped titania nanoparticles for CO_2 photoreduction

This chapter describes the fabrication and subsequent use of pure, RE-doped and TM-RE-co-doped TiO_2 NPs as catalysts for the photoreduction of CO_2 to alcohols. Doping strategies have demonstrated to be an effective approach to increase the photocatalytic activity of metal oxide semiconductors. Therefore, RE and TM ions have been introduced within the TiO_2 lattice to enhance alcohol production rates in the photoreduction of CO_2 as part of a collaboration project with the CITIMAC and the Chemical and Biomolecular Engineering Departments of the University of Cantabria. An in-depth structural and optical characterization of the prepared TiO_2-based nanocatalysts has been performed. Afterwards, the synthesized NPs have been evaluated as photocatalysts for CO_2 reduction to alcohols, namely methanol and ethanol, within a planar optofluidic microreactor.

The main goals of this chapter are:

1. To synthesize pure, RE-doped and TM-RE-co-doped photocatalytically active TiO_2 NPs.
2. To carry out an in-depth structural and optical characterization of the photocatalytically active TiO_2 NPs.
3. To perform CO_2 photoreduction experiments mediated by the catalysts based on pure, RE-doped and TM-RE-co-doped TiO_2 NPs.
4. To study the structural and optical stability of the catalytic materials after the photoreduction process.

8.1. State of the art

The increased atmosphere pollution levels caused by intensive exploitation of fossil fuels has become one of the most urgent environmental problems to overcome [1,2]. Particularly, the concentration of atmospheric CO_2, the main contributor to the greenhouse effect, has reached a global average concentration of 420 ppm in October 2023, supporting the observed increasing trend [3]. To mitigate climate change harmful effects, different strategies for CO_2 remediation have been studied. Among them, Carbon Capture and Utilization (CCU) is an interesting alternative in which CO_2 is considered as a resource instead of a waste [4,5]. This approach shows several benefits, such as: i) the use of CO_2 as zero-cost feedstock for the production of fuels and chemicals, ii) non-toxic products or residue generation, and iii) zero carbon emission [6,7,8,9].

CO_2 activation and transformation can be carried out by means of numerous methods, such as biological, thermochemical, electrochemical, or photocatalytic conversion, to name a few [10,11,12]. In particular, CO_2 photoreduction is a very interesting strategy that takes place under soft conditions and uses sunlight as only energy input [13,14]. The first photocatalytic reduction of CO_2 was reported in 1979 [15], in which different organic compounds such as formaldehyde, methyl alcohol, methane or formic acid were generated using various semiconductors as catalysts. Since then, a wide range of semiconductor-based catalysts have been employed under illumination with different light wavelengths. Among them, TiO_2 is the most popular semiconductor catalyst due to its remarkable photocatalytic activity, high stability, non-toxicity, environmentally friendly character, and low price [16]. Nevertheless, as outlined in Chapter 6, TiO_2 shows a reduced absorption capacity in the Vis spectral range resulting from its wide band gap, which is an important constraint for its potential application in industry [17,18]. To overcome this limitation, doping with TM or RE ions represents an interesting strategy to increase the photocatalytic activity by introducing new energy levels between the VB and the CB of the semiconductor [17].

Regarding RE elements, Ce-doping has shown to increase the photoactivity of TiO_2 in the Vis range owing to the generation of new states within the band gap. However, Ce^{4+} can also act as a scavenger capturing e^-_{CB}, thus reducing the photoactivity. Therefore, achieving an appropriate introduction of Ce^{3+} while avoiding the formation of Ce^{4+} is crucial to reduce

recombination rate and increase the e^-_{CB}/h^+_{VB} pair lifetime [19,20]. Considering doping with TM elements, Cu-doped photocatalysts are especially efficient for the photoreduction of CO_2 to alcohols [21,22,23]. Like for Ce, the introduction of Cu increases light absorption in the Vis region. Besides, the presence of different oxidation states, specifically Cu^0, Cu^+ and Cu^{2+}, has been described to be beneficial for the photoactivity [24,25]. Nevertheless, there is no clear agreement on the role of each species on such a mechanism [26,27]. Interestingly, the vast majority of studies describe the use of metallic Cu deposited over the semiconductor surface [28,29,30,31]. Conversely, when Cu is incorporated within the semiconductor structure, Cu^+/Cu^{2+} ions replace Ti^{4+}, creating O-vacancies charge compensation, which act as additional adsorption sites for species as CO_2 [27]. Besides, doping makes possible the homogeneous incorporation of isolated Cu ions, avoiding the formation of single Cu particles or aggregates, and hence boosting the separation and mobility of e^-_{CB}/h^+_{VB} pairs [26]. In this context, the implementation of TM-RE-co-doping strategies has experienced an increasing interest due to the remarkable activity and selectivity achieved in certain photocatalytic reactions, such as CO_2 conversion [32,33]. Some of the most relevant features of this approach include: i) enhancement of absorption at different wavelength ranges in the Vis region; ii) promotion of electron conductivity, resulting from metal-metal and metal-semiconductor interactions; and iii) boost of redox reactions due to the increased availability of different catalytic sites [34,35]. In addition, it should be noted that additional parameters such as morphology, oxidation state or surface structure of the catalyst play a crucial role in the CO_2 photoreduction process [36,37].

Among the products formed during CO_2 reduction, compounds with two or more carbon atoms (C2+) are highly desirable in comparison with those with a single carbon (C1), since C2+ present both wider industrial use and higher added value [38,39]. In this sense, ethanol is of great interest from the industrial point of view as it presents numerous applications in the fields of chemistry, medicine, healthcare, food, or agriculture [40]. Accordingly, it is essential to overcome the low efficiency of ethanol production in the photocatalytic CO_2 reduction and to increase the selectivity towards this product [38].

8.2. Fabrication of supported catalysts and photoreduction set-up

Pure, RE-doped and TM-RE-co-doped TiO_2 NPs have been synthesized by the hydrothermal method described in section 2.1.2. After an exhaustive structural and optical characterization, the obtained NPs have been deposited onto porous carbon paper supports to evaluate their performance as catalysts in the photoreduction of CO_2 to methanol and ethanol.

8.2.1. Synthesis of rare-earth and transition metal doped titania nanoparticles

Undoped, Ce-doped and Cu-Ce co-doped TiO_2 NPs were prepared following the hydrothermal method described by Oskam et *al*. [41]. An acidified aqueous solution (pH 1) was prepared by adding nitric acid (63%, 433 μL) to distilled water (185 mL). Then, TTIP (50 mmol) was dropped into the solution under vigorous agitation. The mixture was heated up to 85 ºC to reduce the volume to *ca*. 50 mL. The resulting mixture was transferred to a Teflon-lined stainless-steel autoclave, which was sealed, and heated up at 240 ºC for 2 h. Afterwards, the precipitate was washed three times with ethanol to remove remaining traces of reagents, and then resuspended in ethanol to be dried in a stove at 80 ºC overnight. For Ce-doped and Cu-Ce co-doped TiO_2 NPs, stoichiometric amounts of cerium(III) nitrate hexahydrate and copper(II) nitrate trihydrate were dissolved in the acidified aqueous solution prior to TTIP addition.

8.2.2. Fabrication of supported catalysts

As described in section 2.5.2, the immobilization of the photoactive TiO_2 NPs onto porous carbon paper supports was carried out by dispersion of the sample in a mixture of Nafion and isopropanol. After sonication, the resulting mixture was airbrushed over the carbonaceous support, which was originally covered by a paper mask with a square hole of 1 cm^2. Deposition was performed at 100 ºC to promote the complete evaporation of the solvent, and a total mass of NPs per electrode of 2 $mg \cdot cm^{-2}$ was set.

8.2.3. CO_2 photoreduction equipment

As described in section 2.6.2, the photocatalytic activity of the supported NPs for light-driven conversion of CO_2 into alcohols was evaluated using a tailor-

made designed planar optofluidic microreactor equipped with a reaction microchamber. The photoactive electrodes were sandwiched between two transparent polymethylmethacrylate plates and a stainless-steel plate on the top, as depicted in Figure 8.1. Such surfaces were placed in the reaction microchamber and irradiated with UV (peak at 365 nm) or Vis (peak at 450 nm) LED lights with a light intensity of E = 5 $mW \cdot cm^{-2}$. CO_2 photoreduction experiments were carried out in continuous mode by duplicate for 180 min under ambient conditions, where a CO_2 saturated 0.5 M $KHCO_3$ aqueous solution was supplied to the microchamber with a peristaltic pump at a flow rate of 100 $\mu L \cdot min^{-1}$.

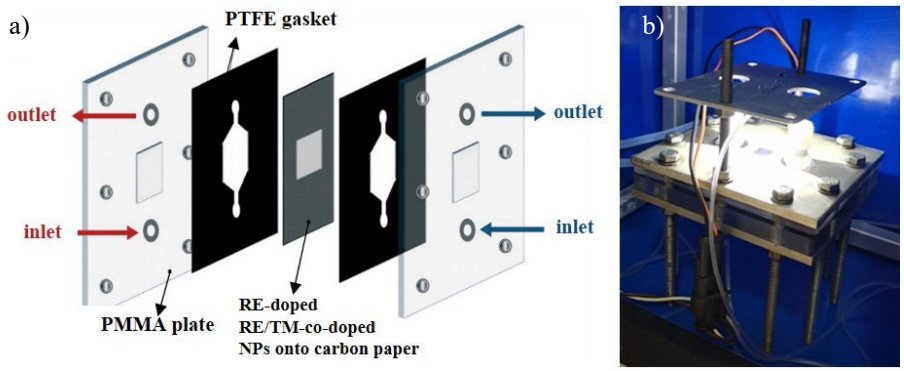

Figure 8.1. a) Internal components of the optofluidic microreactor. b) Planar optofluidic microreactor illuminated with Vis LED lights.

8.3. Structural and optical properties of nanoparticles

Prior to performing the CO_2 photoreduction experiments, an in-depth structural and optical characterization of the pure, RE-doped and TM-RE-co-doped TiO_2 NPs were carried out. ICP-AES and XPS techniques were used for elemental and oxidation state determination of the doping species, respectively. In addition, XRD, TEM and Raman spectroscopy were employed for crystalline phase identification, particle size estimation and morphology assessment. Finally, reflectance spectroscopy measurements were performed to study the effect of dopants on TiO_2 absorption band gap.

8.3.1. Structural characterization

Cu and Ce concentration determination was performed by ICP-AES. The obtained results and sample nomenclature to be used along the chapter are presented in Table 8.1.

Table 8.1. Composition and nomenclature of undoped, RE and TM-RE-co-doped TiO_2 NPs prepared via hydrothermal method. Elemental contents were determined by ICP-AES.

Photocatalytic material	**Ce content (atom.%)**	**Cu content (atom.%)**	**Nomenclature**
TiO_2	–	–	TiO_2
Ce-TiO_2	0.75	–	Ce0.75
	1.27	–	Ce1.27
	2.81	–	Ce2.81
Cu-Ce-TiO_2	0.11	0.11	Cu0.11Ce0.11
	0.15	0.35	Cu0.35Ce0.15
	0.12	0.61	Cu0.61Ce0.12

Figure 8.2 shows the XPS spectra of Ti, Ce, Cu and N for Ce0.75 and Cu0.35Ce0.15 NPs. The shape and position of Ti 2p peaks ($2p_{3/2}$ and $2p_{1/2}$: 458 and 464 eV, respectively) agree with those reported for TiO_2 by the National Institute of Standards and Technology in its Standard Database for XPS [42]. Low intensity peaks located at 471 and 478 eV in both samples are satellite peaks attributed to Ti(IV) oxidation state. Ce0.75 NPs presented peaks at 885 and 904 eV corresponding to $3d_{5/2}$ and $3d_{3/2}$ levels of Ce(III). However, the presence of Ce(IV) at low concentrations cannot be completely ruled out. Furthermore, a peak at 407 eV and ascribed to N 1s level was detected. This peak fits the expected position of nitrate (NO_3^-) ion (407-408 eV), which suggests that remaining traces of this species were present in Ce0.75 NPs. Additionally, it is noteworthy to remark that the XPS analysis of such NPs provided a 0.73% Ce content, in good agreement with ICP-AES results (Table 8.1). Regarding Cu0.35Ce0.15 NPs, the presence of Ce was hardly inferred from the peak placed at 885 eV ($3d_{5/2}$), while that expected for the $3d_{3/2}$ level could not be extracted from the background contribution. The presence of Cu was also confirmed through XPS by the peak at 931 eV ($2p_{3/2}$). Nevertheless,

the oxidation state of Cu could not be determined due to its low intensity and absence of satellite peaks.

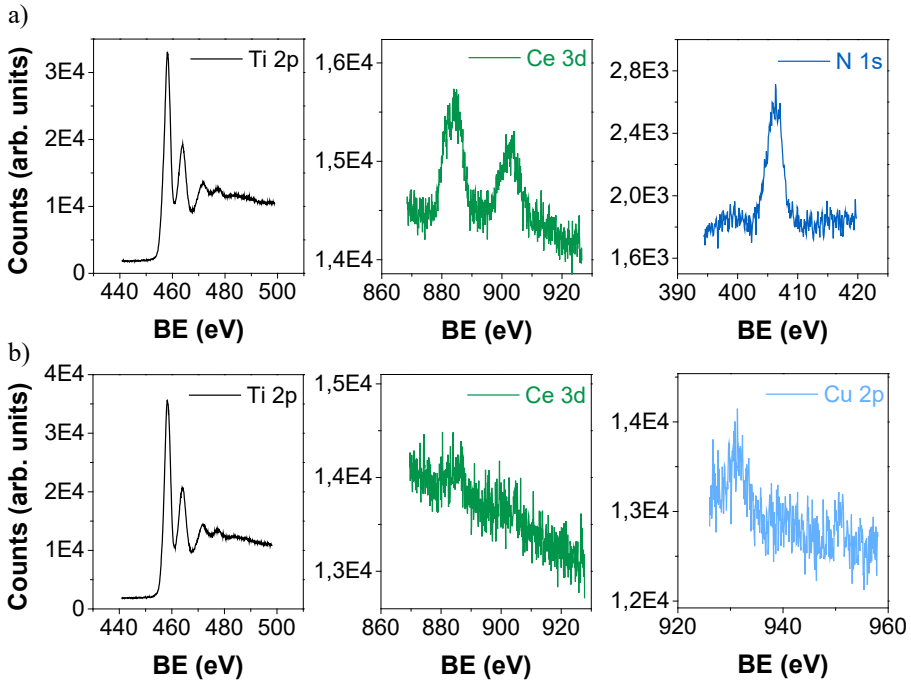

Figure 8.2. XPS spectra of a) Ce0.75, and b) Cu0.35Ce0.15 NPs.

XRD patterns of undoped, doped and co-doped TiO_2 NPs are displayed in Figure 8.3. As it can be observed from the summarized results in Table 8.2, anatase and brookite were the main crystalline phases for all synthesized NPs owing to the low-temperature preparation process [43]. In addition, some samples showed traces of rutile form (< 3%). Specifically, for Ce-doped samples, the highest dopant concentration led to a larger particle size in the brookite phase, while that of anatase was not affected within experimental uncertainty (Table 8.2, entries 2-4). This effect has been previously attributed to the larger radius of rare earth ions when substituting Ti, thus causing lattice distortion [19,44]. A slight shift of diffraction peaks towards higher 2θ angles was also observed with increasing Ce concentration. It is well known that the introduction of dopants with larger ionic radii into the lattice promotes a shift to lower angles, which is also associated with lattice distortion [26,45,46]. However, as previously described, since the ionic radii of Ce^{3+} and Ce^{4+} (0.103 nm and 0.093 nm, respectively) are remarkably larger than that of Ti^{4+} (0.064 nm) [46], the introduction of Ce as doping agent within the TiO_2 lattice may

also induce perturbations and strain energy accumulation in the crystalline phase, leading to a displacement towards higher angles [46,47,48,49].

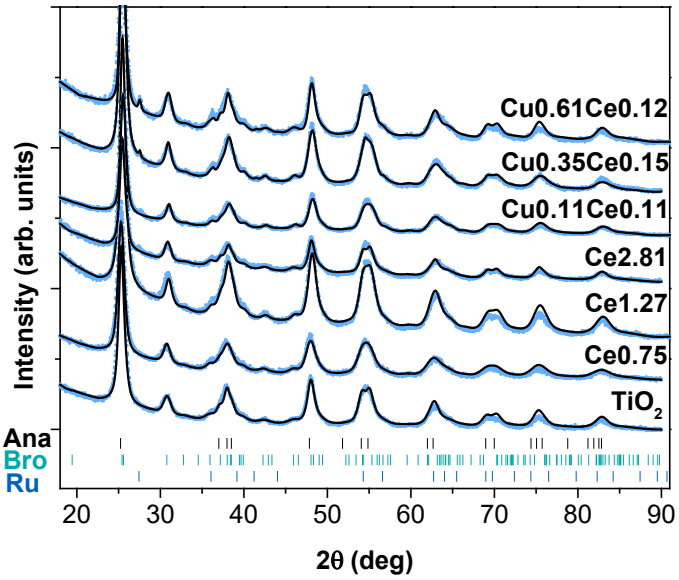

Figure 8.3. Refinement of XRD diffraction patterns of undoped, doped, and co-doped TiO_2 NPs. Ana, Bro and Ru correspond to the Bragg positions of anatase, brookite and rutile phases, respectively.

Likewise, Cu-Ce-co-doped NPs experienced a slight increase in the brookite crystallite size for higher Cu concentrations, while anatase size remained stable. Besides, the formation of a small amount of rutile was observed in co-doped NPs with a Cu concentration above 0.35% (Table 8.2, entries 5-7). Specifically, Cu0.61Ce0.12 NPs presented the largest particle size and the highest rutile content, which may be related to the phase stability of TiO_2 crystalline forms. As previously described in Chapter 7, numerous authors have discussed the main influencing factors controlling the anatase-brookite-rutile transformation mechanism, particle size being one of the most critical elements [41]. In this sense, anatase is the most stable phase when particle size is below 11 nm, in good agreement with results shown in Table 8.2. Therefore, an increase in the anatase crystallite size usually leads to a lower concentration of such a form, promoting the formation of brookite and rutile phases with larger average crystallite sizes, as observed in Cu0.61Ce0.12 NPs (Table 8.2, entry 7). These two phases are the most stable in the 11-35 nm size range, and above 35 nm [50], respectively. On the other hand, no traces of Cu or Ce oxides were detected in the XRD patterns. Nevertheless, the presence of reduced

concentrations of such species below the detection limits of XRD cannot be discarded [20].

Table 8.2. Summary of anatase/brookite/rutile ratios and sizes obtained by XRD and TEM for undoped, doped, and co-doped TiO_2 NPs. Ana: anatase, Bro: brookite, Ru: rutile.

Entry	Photocatalyst	Ana:Bro:Ru	$Size_{Ana}$ (nm)	$Size_{Bro}$ (nm)	$Size_{TEM}$ (nm)
1	TiO_2	70:30:0	9 ± 2	19 ± 4	7 ± 2
2	Ce0.75	63:37:0	10 ± 2	11 ± 2	7 ± 3
3	Ce1.27	77:23:0	11 ± 1	11 ± 1	8 ± 3
4	Ce2.81	63:37:0	9 ± 1	25 ± 4	11 ± 3
5	Cu0.11Ce0.11	64:36:0	13 ± 1	10 ± 1	10 ± 3
6	Cu0.35Ce0.15	68:31:1	12 ± 1	9 ± 1	9 ± 3
7	Cu0.61Ce0.12	57:40:3	15 ± 1	19 ± 4	11 ± 2

Figure 8.4 shows representative TEM images of the prepared undoped, doped and co-doped TiO_2 NPs. The observed average particle sizes are in good agreement with those obtained from the refined XRD patterns (Table 8.2). Additionally, the NPs exhibited a well-defined polyhedral morphology.

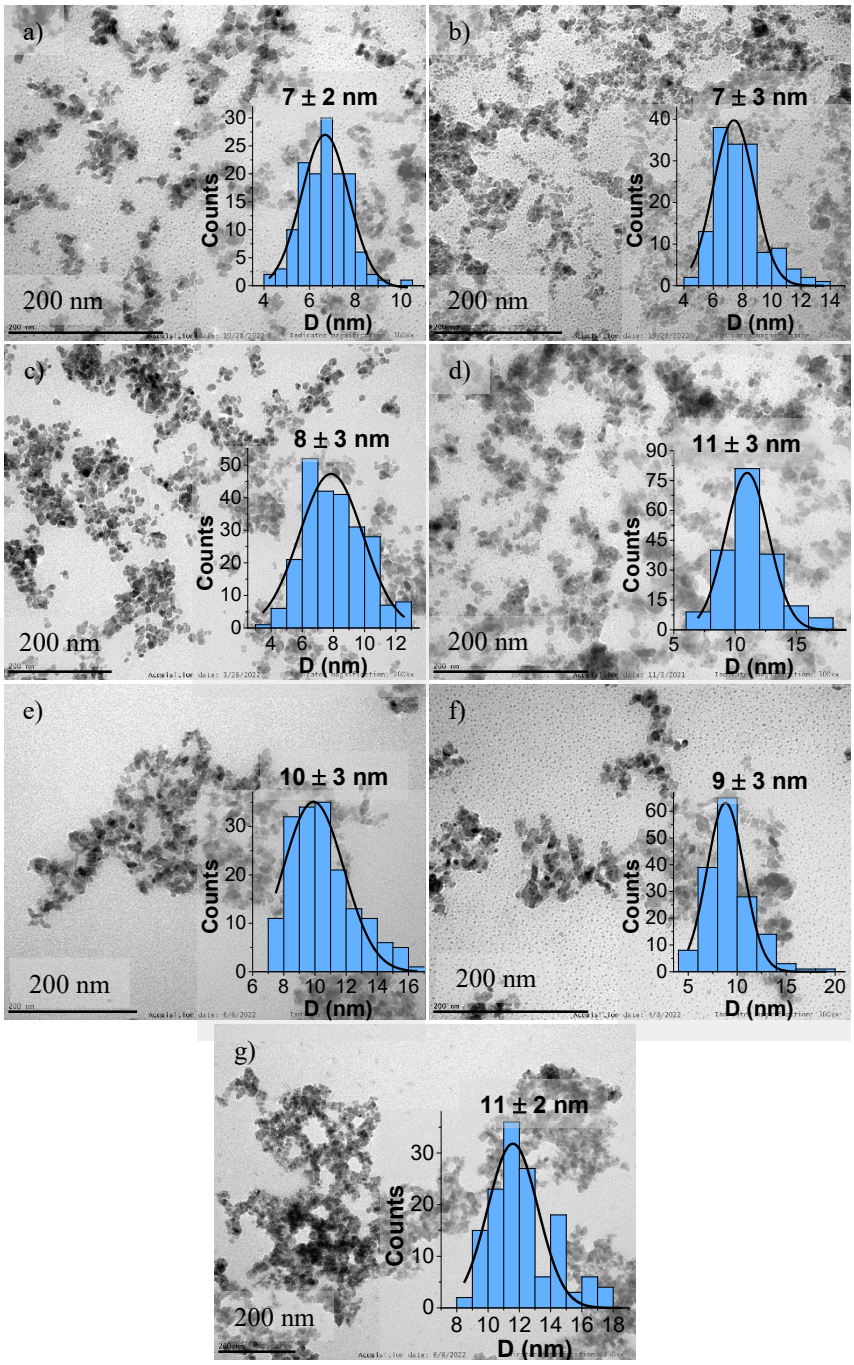

Figure 8.4. TEM images and average particle sizes of a) undoped, b) Ce0.75, c) Ce1.27, d) Ce2.81, e) Cu0.11Ce0.11, f) Cu0.35Ce0.15, g) Cu0.61Ce0.12 TiO_2 NPs.

The structural characterization was also performed by means of Raman spectroscopy. The obtained spectra are displayed in Figure 8.5. All of them are dominated by the strong band centered at 144 cm^{-1} (E_g), which is attributed to the anatase form as it is the main phase, in good agreement with XRD results. The remaining five out of the total six characteristic vibrational modes of anatase phase were observed for all the synthesized samples. Specifically, these bands are centered at 198 (E_g), 397 (B_{1g}), 516 (A_{1g} + B_{1g}) and 639 cm^{-1} (E_g) [51]. On the other hand, the presence of brookite phase was confirmed by the bands detected at 247 (A_{1g}), 320 (A_{1g}), 366 (B_{2g}), 395 (B_{2g}), 452 (B_{3g}) and 640 cm^{-1} (A_{1g}) [52]. No contribution from the four possible Raman active modes of rutile form located at 143, 447, 612 and 826 cm^{-1} was detected due to its absence or reduced concentration [53].

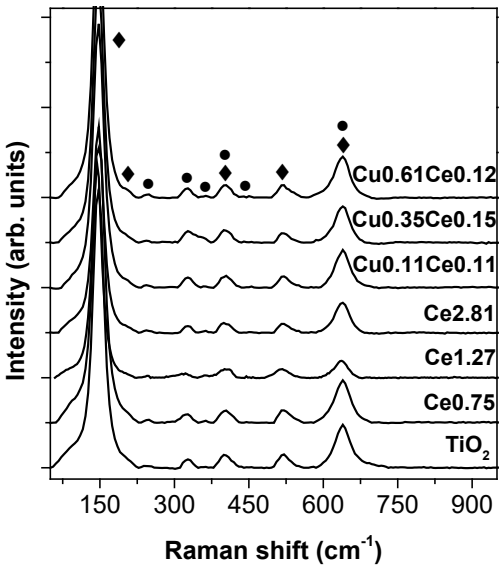

Figure 8.5. Raman spectra of pure, Ce-doped and Cu-Ce co-doped TiO_2 NPs. ♦ anatase, ●: brookite.

8.3.2. Optical characterization

Reflectance spectroscopy was employed to carry out the optical characterization of the synthesized NPs. First, the effect of Ce-doping on the TiO_2 NPs absorption band gap was studied. Figure 8.6a shows the normalized absorption spectra of pure and Ce-doped NPs. Band gap values were determined by means of the graphical approach (Table 8.3) as described in

section 7.3.2 [54]. Specifically, pure TiO_2 NPs exhibit a band gap energy value of 3.14 eV (395 nm). Clearly, as expected, Ce-doped TiO_2 NPs displayed a red-shifting towards the Vis region with increasing Ce concentration, which is associated to the generation of new energy levels within the band gap [45,55]. Specifically, Ce-doped samples (0.75%, 1.27% and 2.81% mol) presented 2.64 (469 nm), 2.62 (473 nm) and 2.67 eV (473 nm) band gap energy values, respectively, in contrast with the 3.14 eV (395 nm) value obtained for pure TiO_2 NPs, thus evidencing a decrease of band gap values due to the formation of a new Ce^{3+}/Ce^{4+} band and oxygen defect states generated from the interaction between the dopant ion and TiO_2 [56]. In this sense, it has been previously reported that the introduction of Ce ions within the TiO_2 lattice may induce a charge transfer transition between the TiO_2 valence band and the 4*f* electron of Ce^{3+} [45, 57], thus playing a relevant role in the generation of e^-_{CB}/h^+_{VB} pairs under Vis light irradiation, as described by Xie [58] and Yan [59].

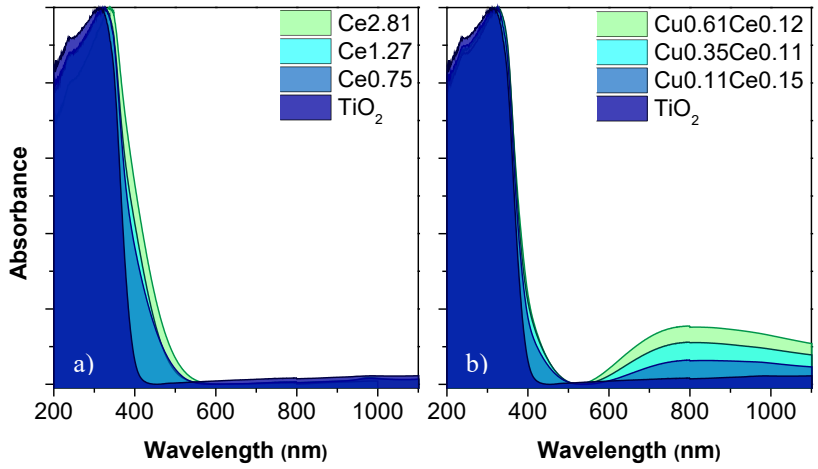

Figure 8.6. Normalized absorption spectra of a) pure and Ce-doped TiO_2 NPs, b) pure and Cu-Ce co-doped TiO_2 NPs.

Secondly, the effect of Cu concentration on Cu-Ce co-doped TiO_2 NPs was studied, as represented in Figure 8.6b. Only a slight shift of the TiO_2 absorption band was observed because of the reduced Ce content ($\leq$ 0.15%). Specifically, the absorption edge was estimated to be centered at *ca*. 373 nm for the three co-doped samples regardless of the Cu content, being close to that for undoped TiO_2 NPs, *i.e.*, 366 nm. Accordingly, the calculated band gap energy values of Cu-Ce co-doped TiO_2 NPs are hardly different from that obtained for pure TiO_2 NPs, *ca*. 3 eV *vs* 3.14 eV, respectively. Interestingly, a

new band in the Vis region between 600 and 800 nm was observed, which is ascribed to *d-d* transitions of Cu^{2+} in octahedral O_h or tetragonally distorted D_{4h} symmetry [60]. The intensity of such a band increases at higher Cu concentrations. Therefore, the use of Cu-Ce co-doped TiO_2 NPs for Vis-light-driven photocatalytic reactions is a very interesting strategy as a consequence of this enhanced absorption in the 600-800 nm spectral range.

Table 8.3. Estimated band gap values of the synthesized pure, Ce-doped and Cu-Ce co-doped TiO_2 NPs.

Entry	Photocatalyst	Band gap (eV)
1	TiO_2	3.14
2	Ce0.75	2.64
3	Ce1.27	2.62
4	Ce2.81	2.60
5	Cu0.11Ce0.11	3.01
6	Cu0.35Ce0.15	2.99
7	Cu0.61Ce0.12	2.94

8.4. Photocatalytic activity of synthesized nanoparticles

8.4.1. Effect of Ce content on the photocatalytic reduction of CO_2 to alcohols

Initially, the effect of Ce content on the photoreduction of CO_2 to alcohols catalyzed by TiO_2 NPs was studied. Specifically, the photoactivity of pure TiO_2 NPs was compared with those of Ce0.75, Ce1.27 and Ce2.81 doped NPs under different light sources, UV and Vis LEDs, in the optofluidic microreactor. The obtained results for the photoreduction of CO_2 to methanol and ethanol are shown in Figure 8.7 and Table 8.4.

It should be noted that very small quantities of formic acid (HCOOH) were also observed in the liquid phase, while the gas phase was not analyzed as previous experiments mediated by TiO_2-based catalysts in the same experimental setup showed that only traces of CO and CH_4, which represent an almost negligible fraction (AQY < 0.05), were generated [61,62]. Additionally, blank experiments where no alcohol production was detected were performed

in the absence of illumination or CO_2, thus confirming that both methanol and ethanol are obtained through the photocatalytic reduction of CO_2.

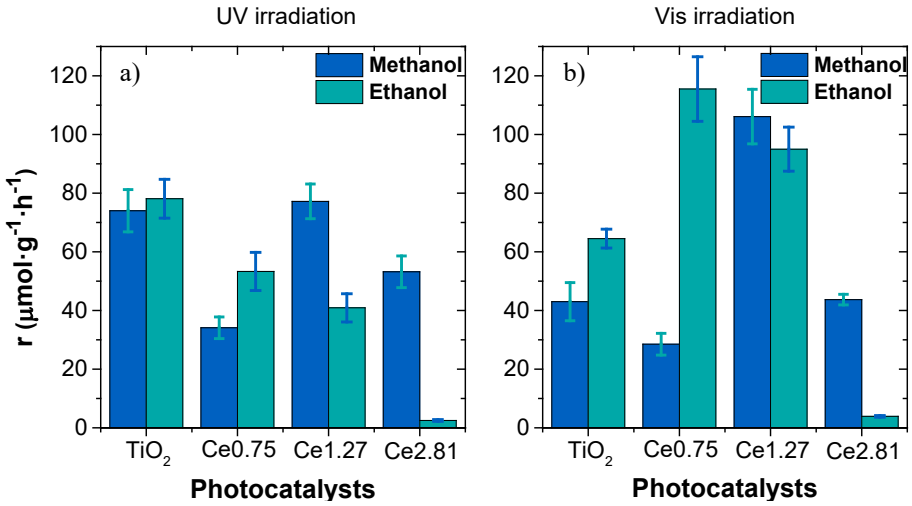

Figure 8.7. Reaction rates for methanol and ethanol production from photoreduction of CO_2 catalyzed by pure and Ce-doped TiO_2 NPs under a) UV and b) Vis light irradiation.

Table 8.4. Results for the continuous photoreduction of CO_2 in the optofluidic microreactor using supported pure and Ce-doped TiO_2 NPs as catalysts under UV and Vis light irradiation (5 $mW \cdot cm^{-2}$).

Photocatalyst	**Light Source**	**r (µmol·g^{-1}·h^{-1})**		**AQY (%)**	
		CH_3OH	**C_2H_5OH**	**CH_3OH**	**C_2H_5OH**
TiO_2	UV	74 ± 7	78 ± 6	1.6	3.4
	Vis	43 ± 6	65 ± 3	0.8	2.3
Ce0.75	UV	34 ± 4	53 ± 6	0.8	2.3
	Vis	29 ± 4	116 ± 11	0.5	4.1
Ce1.27	UV	77 ± 6	41 ± 5	1.7	1.8
	Vis	106 ± 9	95 ± 7	1.9	3.4
Ce2.81	UV	53 ± 5	2.5 ± 0.3	1.2	0.1
	Vis	44 ± 2	4.0 ± 0.3	0.8	0.1

r: production rate of alcohols; AQY: apparent quantum yield

Under UV irradiation, no improvement in the production of any of the alcohols was observed upon doping with Ce (Figure 8.7a). Only Ce1.27 photocatalyst showed a slight increase in methanol generation when compared

with the pure TiO_2 NPs, while the rest of Ce-doped catalysts displayed lower alcohol production rates. These low production rates can be ascribed to the introduction of Ce as dopant, as the Ce-doped samples exhibit similar crystallite TiO_2 phase ratios and close average NP sizes, except for the brookite phase in Ce2.81 TiO_2 NPs. The progressive reduction of alcohol generation with increasing Ce concentration can be related with the formation of Ce^{4+} impurities, these acting as traps and recombination centers. On the other hand, it can be observed that Ce-doping led to a change in product selectivity towards methanol when irradiated with UV light. Indeed, an accused decrease in ethanol generation as a function of Ce concentration was noted, which can be attributed to a lower activity when a reduced number of e^-_{CB}/h^+_{VB} pairs is generated. As a result, the formation of ethanol, which is a more electron-demanding product, is severely handicapped, thus changing the selectivity of the reaction towards the most favored compounds, *i.e.*, methanol [38].

Interestingly, when irradiating with Vis light, a remarkable improvement of alcohol production rates was observed for Ce-doped catalysts (Figure 8.7b). Specifically, Ce0.75 and Ce1.27 NPs provided increased ethanol, and both ethanol and methanol generation rates, respectively. The former led to a 79% increase in ethanol formation (116 $\mu mol \cdot g^{-1} \cdot h^{-1}$, AQY = 4.1%) when compared with pure TiO_2 NPs (65 $\mu mol \cdot g^{-1} \cdot h^{-1}$, AQY = 2.3%), while the latter displayed 146% and 47% increase in methanol and ethanol production, respectively (methanol: 106 $\mu mol \cdot g^{-1} \cdot h^{-1}$, AQY = 1.9%; ethanol: 95 $\mu mol \cdot g^{-1} \cdot h^{-1}$, AQY = 3.4%). In this sense, a Ce content of 0.75% mol is the optimum concentration for maximizing ethanol production by photoreduction of CO_2 under Vis light, while 1.27% mol Ce concentration provided high methanol and ethanol production rates, although the latter was lower than that obtained using Ce0.75 NPs as catalyst. Both catalysts showed remarkably high conversion rates, exceeding the average values reported in the literature for ethanol production under Vis light [9,40]. In addition, Ce0.75 NPs provided 80% selectivity towards ethanol, which results of great interest from the industrial perspective. These results can be ascribed to the aforementioned absorption edge red-shifting related to Ce-doping, increasing light absorption in the Vis range, and therefore confirming the importance of the absorption band position.

However, as observed when using an UV light source, a further increase in Ce concentration, *i.e.*, Ce2.81 NPs, led to a decrease in alcohol production and to a change in product selectivity. Indeed, ethanol was the main product when Ce0.75 NPs were employed as catalyst (116 $\mu mol \cdot g^{-1} \cdot h^{-1}$, AQY

= 4.1%), while it was scarcely produced when the Ce load was increased up to 2.81% mol (4 $\mu mol \cdot g^{-1} \cdot h^{-1}$, AQY = 0.1%). In addition, Ce2.81 NPs provided a lower methanol production rate than Ce0.75 and Ce1.27 NPs, although remarkably higher selectivity towards this product. In this sense, both trends, lower activity and product selectivity change, can be ascribed to the possible formation of Ce^{4+} ions at higher Ce concentrations. Despite the lack of understanding about the main factors that drive the observed selectivity, it has been previously described that catalytic reactions involving higher number of e^- and H^+ promote C2+ products [38]. Accordingly, while the incorporation of Ce^{3+} in the Ti^{4+} site may generate extra e^-_{CB}/h^+_{VB} pairs available for redox reactions, substitutional Ce^{4+} would not change the Ce-doped TiO_2 properties significantly. Therefore, the control of Ce^{3+}/Ce^{4+} ratio in the TiO_2 host lattice plays an important role in the ultimate photocatalytic performance. In addition, Ce^{4+} ions can also act as traps and recombination centers, which is strongly detrimental for the catalytic activity [57], and might avoid the formation of a more challenging product as ethanol, in line with the observed results.

8.4.2. Effect of Cu content in Cu-Ce co-doped TiO_2 NPs on the photocatalytic reduction of CO_2 to alcohols

After studying the influence of Ce concentration on the photocatalytic activity of the NPs, the effect of Cu content as co-doping strategy was assessed, as it was observed that Cu provides an additional absorption band in the Vis region. Consequently, the photoactivity of co-doped catalysts was evaluated using uniquely Vis light as excitation source. It is important to point out that for co-doped NPs only 0.11, 0.35 and 0.61% mol Cu and up to 0.15% mol Ce could be incorporated into the TiO_2 lattice, in contrast to the larger concentrations achieved in the single-doped NPs. Figure 8.8 displays the reaction rates for both methanol and ethanol production by photoreduction of CO_2 catalyzed by the Cu-Ce co-doped NPs. Table 8.5 shows the effect of Cu concentration on the photoreduction of CO_2 catalyzed by different co-doped TiO_2 samples with similar Ce content. Pure TiO_2 and Ce0.75 NPs are also included for comparative purposes.

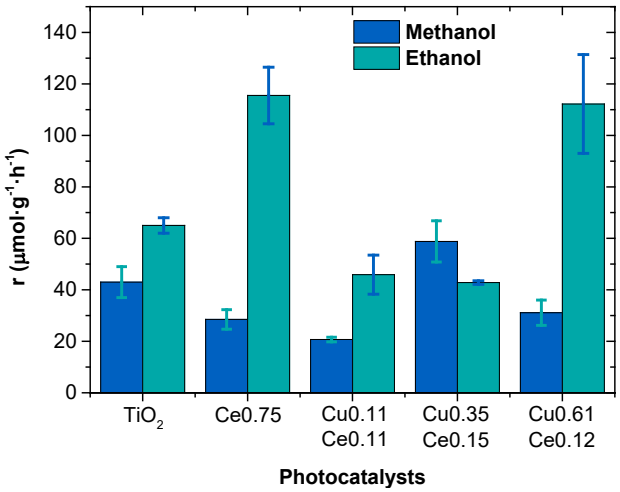

Figure 8.8. Reaction rates for methanol and ethanol production from photoreduction of CO_2 catalyzed by pure, Ce-doped (0.75%) and Cu-Ce co-doped TiO_2 NPs under Vis light irradiation.

Table 8.5. Results for the continuous photoreduction of CO_2 in the optofluidic microreactor using supported Cu-Ce-co-doped TiO_2 NPs as catalysts under Vis light irradiation (5 mW·cm^{-2}).

Photocat. material	**r (µmol·g^{-1}·h^{-1})**		**AQY (%)**	
	CH_3OH	**C_2H_5OH**	**CH_3OH**	**C_2H_5OH**
TiO_2	43 ± 6	65 ± 3	0.8	2.3
Ce0.75	29 ± 4	116 ± 11	0.5	4.1
Cu0.11Ce0.11	21 ± 1	46 ± 8	0.4	1.6
Cu0.35Ce0.15	59 ± 8	43 ± 1	1.0	1.5
Cu0.61Ce0.12	31 ± 5	112 ± 19	0.6	4.0

No general improvement on alcohol production rates was observed for co-doped samples when compared to pure and Ce-doped TiO_2 NPs, which can be mainly attributed to the reduced inclusion of doping ions within the TiO_2 structure. However, a slight increase in methanol production rate was achieved when using Cu0.35Ce0.15 NPs as photocatalyst, surpassing those of TiO_2 and Ce0.75 NPs. Therefore, 0.35% mol seems to be the optimal Cu content for methanol production. This positive effect of Cu-doping on methanol generation has been previously described in the literature [61,63,64]. Besides, it has also been reported that simultaneous doping with Cu and Ce boosts the photoreduction of CO_2 to methanol when compared with purely Cu-doped

samples [65]. Interestingly, a further increase in the Cu content up to 0.61% (Cu0.61Ce0.12 NPs) led to a remarkable promotion of ethanol production, achieving a slightly higher production rate than that obtained with Ce0.75 catalyst (112 $\mu mol \cdot g^{-1} \cdot h^{-1}$, AQY = 4.0%, vs 116 $\mu mol \cdot g^{-1} \cdot h^{-1}$, AQY = 4.1%, respectively).

8.4.3. Stability of NP-based photoactive surfaces after the CO_2 photoreduction process

Long-term stability of the photocatalyst under light irradiation is one of the most relevant aspects for potential practical application in industry [66,67]. Therefore, in line with the results obtained for the photoreduction of CO_2 to alcohols, Ce0.75 NPs were selected as the most suitable catalyst due to not only their remarkably high ethanol production rate but also their noteworthy selectivity towards this compound, up to 80%, under Vis light. Accordingly, the evolution of ethanol and methanol production rates was studied for Ce0.75 NPs during 6 h (Table 8.6), as represented in Figure 8.9. The production rates of both alcohols, ethanol and methanol, followed a pseudo-stable behavior, where only slight differences were noted between the initial and final rates of the experiment. Specifically, the ethanol production rate only decreased by 5% after 6 h of continuous photoreduction process, while that of methanol improved by 19% regarding the initial quantity, both values being close to the experimental error.

It is worth mentioning that the Ce-doped and Cu-Ce co-doped TiO_2 NPs described herein display a generally superior photocatalytic performance in terms of alcohol production rates when compared with other Cu-TiO_2-based photocatalysts reported in the literature [61]. Furthermore, the NPs synthesized in this Thesis not only provided improved results in the photoreduction of CO_2 to alcohols but also gave stable yields after up to 6 h of continuous operation, in contrast with other Cu-TiO_2-based catalysts, which show deactivation after a certain time [61]. Therefore, this enhanced alcohol production under Vis light may be attributed to the introduction of Ce within the TiO_2 crystalline structure, leading to the increased light absorption in this spectral range. It should also be noted that numerous Cu-doped TiO_2 systems have been reported in the literature. However, for a similar Cu content, they display much lower production rates than the Cu-Ce co-doped TiO_2 NPs presented in this Thesis [68,69,70,71], supporting the synergistic effect between Ce and TiO_2 in the photoreduction of CO_2 under Vis light.

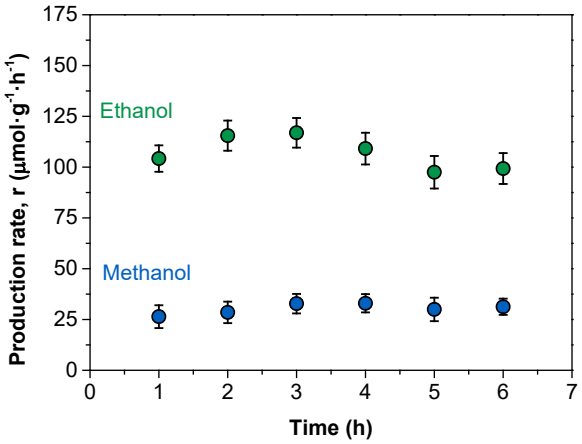

Figure 8.9. Evolution of long-term alcohol production rates using Ce0.75 NPs as catalyst. Blue dots: methanol; green dots: ethanol.

Table 8.6. Long-term alcohol production rates for the continuous photoreduction of CO_2 in the optofluidic microreactor using supported Ce0.75 NPs as catalysts under Vis light irradiation (5 mW·cm^{-2}).

		Time (h)					
		1	**2**	**3**	**4**	**5**	**6**
r (µmol·g^{-1}·h^{-1})	Methanol	26 ± 6	28 ± 5	33 ± 5	33 ± 4	30 ± 6	31 ± 4
	Ethanol	104 ± 6	115 ± 7	117 ± 7	97 ± 8	99 ± 8	99 ± 7

Additionally, the Ce0.75 sample was structurally characterized by XRD and Raman spectroscopy after the continuous photoreduction process in the optofluidic microreactor to study its stability. Figure 8.10 displays the XRD patterns of the initial Ce0.75 NPs in powder form and upon deposition over carbon paper before and after the photoreduction process. The bare carbon paper pattern is also included for comparison purposes. As it can be seen, peaks from the carbon paper overlap those from the deposited NPs due to their reduced concentration (2 mg of TiO_2 NPs powder). Nevertheless, some of the characteristic original peaks of anatase phase can still be identified at 38, 48 and 62˚, demonstrating the stability of the catalyst along the photoreduction process.

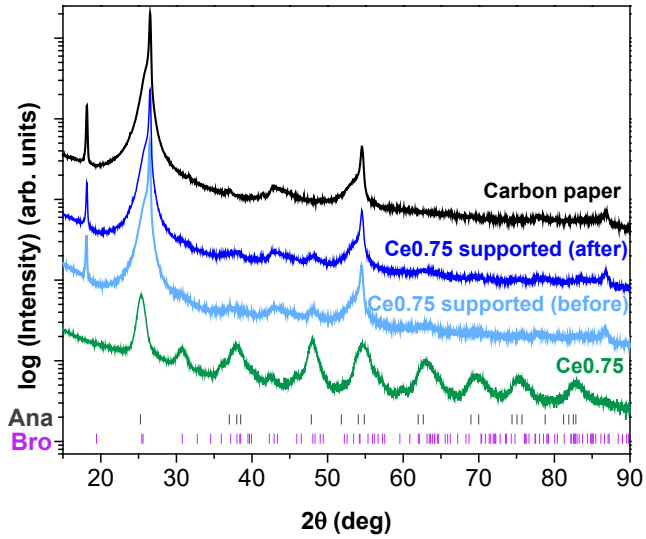

Figure 8.10. XRD patterns of the initial Ce0.75 NPs powder (green), NPs supported over carbon paper before and after the photoreduction process (light and dark blue, respectively), and the bare carbon paper (black). Ana and Bro correspond to the Bragg positions of anatase and brookite phases, respectively.

Finally, Figure 8.11 shows the Raman spectra of Ce0.75 NPs before and after deposition over carbon paper. Most peaks detected in the Raman spectrum of the initial NPs powders were identified after their immobilization and the photoreduction process. No changes in band positions were noted, highlighting the stability of the catalyst after prolonged use. Specifically, bands ascribed to the anatase phase centered at 198 (E_g), 397 (B_{1g}), 516 (A_{1g} + B_{1g}) and 639 cm^{-1} (E_g) were detected. Additionally, the brookite phase was also identified by the presence of its characteristic bands at 247(A_{1g}), 320 (A_{1g}), 366 (B_{2g}), 395 (B_{2g}), 452 (B_{3g}) and 640 cm^{-1} (A_{1g}). As expected, no contribution from the rutile phase was observed. The remarkable decrease in intensity observed for the supported NPs (note the scaling factor) in comparison with the initial NPs powder is due to the low concentration of NPs required for the catalytic process.

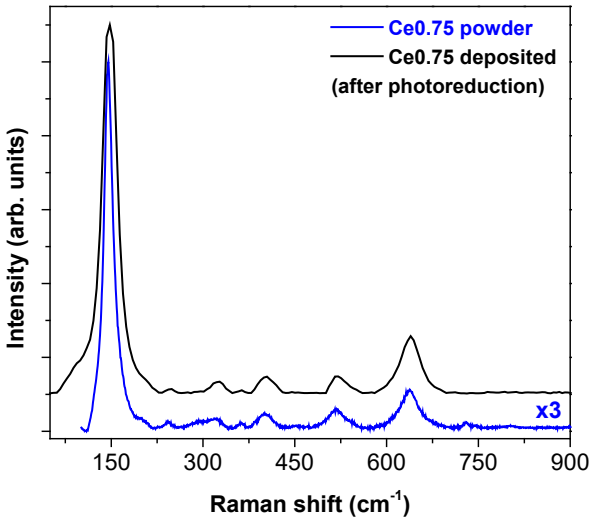

Figure 8.11. Raman spectra of Ce0.75 NPs powder (blue) and NPs supported over carbon paper after the photoreduction process (black).

8.5. Concluding remarks

The main conclusions obtained along this chapter are the following:

- Pure, Ce-doped and Cu-Ce co-doped TiO_2 photocatalytically active NPs have been prepared by a simple hydrothermal method with different Cu and Ce concentrations. Diverse structural and optical techniques have been used to characterize the synthesized materials.
- The obtained NPs have been employed as catalysts for the photoreduction of CO_2 to alcohols, demonstrating the relevance and positive effect of Ce-doping on the catalytic activity.
- NPs doped with 0.75% mol Ce concentration have displayed the highest CO_2 photoreduction rate among the prepared catalysts, leading to an ethanol production rate of 116 $\mu mol \cdot g^{-1} \cdot h^{-1}$ under Vis light. Additionally, this catalyst has provided the best selectivity towards ethanol (80%), such a product being of great interest for industrial purposes.
- NPs doped with 1.27% mol Ce concentration have also provided high production rates of both methanol and ethanol, displaying similar

selectivity for the two compounds. A further increase in the Ce content, *i.e.*, 2.81% mol, has proven to be detrimental for ethanol production.

- Simultaneous Cu and Ce incorporation as co-doping strategy has not provided an enhanced photoactivity, which can be attributed to the reduced inclusion of the doping species.
- The synthesized NPs have exhibited long-term stability under Vis light irradiation, showing maintained activity after 6 h of continuous operation.
- The immobilization of NPs on the porous support and their structural stability after the photoreduction experiments have been corroborated by XRD and Raman spectroscopy.
- The catalytic performance of Ce0.75 NPs presented in this Thesis is amongst the highest reported to date for ethanol production under Vis light.
- The demonstrated stability along time of the developed catalysts proves their suitability for industrial applications. Specifically, the immobilized NPs described in this chapter display a remarkable performance under continuous flow, which requires greater complexity than slurry batch photoreactors. In addition, the obtained results could be further improved by using a sunlight-like energy source.

References

1 Balbuena, J.; Cruz-Yusta, M.; Sánchez, L. Nanomaterials to combat NO_x pollution. *J. Nanosci. Nanotechnol*. **2015**, *15*, 6373–6385.

2 Letcher, T. M. *Climate Change (Third Edition): Observed impacts on planet Earth*. Elsevier, 2021.

3 NOAA Global Monitoring Laboratory: trends in atmospheric carbon dioxide. https://gml.noaa.gov/ccgg/trends/global.html (accessed October 26th, 2023).

4 Habisreutinger, S. N.; Schmidt-Mende, L.; Stolarczyk, J. K. Photocatalytic reduction of CO_2 on TiO_2 and other semiconductors. *Angew. Chem. Int. Ed*. **2013**, *52*, 7372–7408.

5 Tseng, I.; Chang, W.; Wu, J. C. S. Photoreduction of CO_2 using sol–gel derived titania and titania-supported copper catalysts. *Appl. Catal. B Environ*. **2002**, *37*, 37–48.

6 Merino-Garcia, I.; Alvarez-Guerra, E.; Albo, J.; Irabien, A. Electrochemical membrane reactors for the utilisation of carbon dioxide. *Chem. Eng. J*. **2016**, *305*, 104–120.

7 Endrődi, B.; Bencsik, G.; Darvas, F.; Jones, R.; Rajeshwar,K.; Janáky, C. Continuous-flow electroreduction of carbon dioxide. *Prog. Energy Combust. Sci*. **2017**, *62*, 133–154.

8 Sabri, M. A.; Al Jitan, S.; Bahamon, D.; Vega, L. F.; Palmisano, G. Current and future perspectives on catalytic-based integrated carbon capture and utilization. *Sci. Total Environ*. **2021**, *790*, 148081.

9 Shehzad, N.; Tahir, M.; Johari, K.; Murugesan, T.; Hussain, M. A critical review on TiO_2 based photocatalytic CO_2 reduction system: strategies to improve efficiency. *J. CO_2 Util*. **2018**, *26*, 98–122.

10 Centi, G.; Quadrelli, E. A.; Perathoner, S. Catalysis for CO_2 conversion: a key technology for rapid introduction of renewable energy in the value chain of chemical industries. *Energy Environ. Sci*. **2013**, *6*, 1711–1731.

11 Merino-Garcia, I.; Tinat, L.; Albo, J.; Alvarez-Guerra, M.; Irabien, A.; Durupthy, O.; Vivier, V.; Sánchez-Sánchez, C. M. Continuous electroconversion of CO_2 into formate using 2 nm tin oxide nanoparticles. *Appl. Catal. B Environ*. **2021**, *297*, 120447.

12 Ochedi, F. O.; Liu, D.; Yu, J.; Hussain, A.; Liu, Y. Photocatalytic, electrocatalytic and photoelectrocatalytic conversion of carbon dioxide: a review. *Environ. Chem. Lett*. **2021**, *19*, 941–967.

13 Navarro-Jaén, S.; Virginie, M.; Bonin, J.; Robert, M.; Wojcieszak, R.; Khodakov, A. Y. Highlights and challenges in the selective reduction of carbon dioxide to methanol. *Nat. Rev. Chem*. **2021**, *5*, 564–579.

14 Angulo-Ibáñez, A.; Perfecto-Irigaray, M.; Merino-Garcia, I.; Luego, N.; Goitandia, A. M.; Albo, J.; Aranzabe, E.; Beobide, G.; Castillo, O.; Pérez-Yáñez, S. Metal-organic aerogels based on titanium(IV) for visible-light conducted CO_2 photoreduction to alcohols. *Mater. Today Energy* **2022**, *30*, 101178.

15 Inoue, T.; Fujishima, A.; Konishi, S.; Honda, K. Photoelectrocatalytic reduction of carbon dioxide in aqueous suspensions of semiconductor powders. *Nature* **1979**, *277*, 637–638.

16 Ma, Y.; Wang, X.; Jia, Y.; Chen, X., Han, H.; Li, C. Titanium dioxide-based nanomaterials for photocatalytic fuel generations. *Chem. Rev*. **2014**, *114*, 9987–10043.

17 Etacheri, V.; Di Valentin, C.; Schneider, J.; Bahnemann, D.; Pillai, S. C. Visible-light activation of TiO_2 photocatalysts: advances in theory and experiments. *J. Photochem. Photobiol., C* **2015**, *25*, 1–29.

18 Ibhadon, A.; Fitzpatrick, P. Heterogeneous photocatalysis: recent advances and applications. *Catalysts* **2013**, *3*, 189–218.

19 Ma, T. Y.; Cao, J. L.; Shao, G.S.; Zhang, X. J.; Yuan, Z. Y. Hierarchically structured squama-like cerium-doped titania: synthesis, photoactivity, and catalytic CO oxidation. *J. Phys. Chem. C* **2009**, *113*, 16658–16667.

20 hua Xu, Y.; rong Chen, H.; xian Zeng, Z.; Lei, B. Investigation on mechanism of photocatalytic activity enhancement of nanometer cerium-doped titania. *Appl. Surf. Sci*. **2006**, *252*, 8565–8570.

21 Chen, Z.; Wang, T.; Liu, B.; Cheng, D.; Hu, C.; Zhang, G.; Zhu, W.; Wang, H.; Zhao, Z. -J.; Gong, J. Grain-boundary-rich copper for efficient solar-driven electrochemical CO_2 reduction to ethylene and ethanol. *J. Am. Chem. Soc*. **2020**, *142*, 6878–6883.

22 Karapinar, D.; Creissen, C. E.; Rivera de la Cruz, J. G.; Schreiber, M. W.; Fontecave, M. Electrochemical CO_2 reduction to ethanol with copper-based catalysts. *ACS Energy Lett*. **2021**, *6*, 694–706.

23 Albo, J.; Alvarez-Guerra, M.; Castaño, P.; Irabien, A. Towards the electrochemical conversion of carbon dioxide into methanol. *Green Chem*. **2015**, *17*, 2304–2324.

24 Assadi, M. H. N.; Hanaor, D. A. H. The effects of copper doping on photocatalytic activity at (101) planes of anatase TiO_2: a theoretical study. *Appl. Surf. Sci*. **2016**, *387*, 682–689.

25 Amorós-Pérez, A.; Cano-Casanova, L.; Lillo-Ródenas, M. A.; Román-Martínez, M. C. Cu/TiO_2 photocatalysts for the conversion of acetic acid into biogas and hydrogen. *Catal. Today* **2017**, *287*, 78–84.

26 Gonell, F.; Puga, A.V.; Julián-López, B.; García, H.; Corma, A. Copper-doped titania photocatalysts for simultaneous reduction of CO_2 and production of H_2 from aqueous sulfide. *Appl. Catal. B Environ*. **2016**, *180*, 263–270.

27 Bhattacharyya, K.; Mane, G. P.; Rane, V.; Tripathi, A. K.; Tyagi, A. K. Selective CO_2 photoreduction with Cu-doped TiO_2 photocatalyst: delineating the crucial role of Cu-oxidation state and oxygen vacancies. *J. Phys. Chem. C* **2021**, *125*, 1793–1810.

28 Liu, L.; Gao, F.; Zhao, H.; Li, Y. Tailoring Cu valence and oxygen vacancy in Cu/TiO_2 catalysts for enhanced CO_2 photoreduction efficiency. *Appl. Catal. B Environ*. **2013**, *134-135*, 349–358.

29 Liu, C.; Iyemperumal, S. K.; Deskins, N. A.; Li, G. Photocatalytic CO_2 reduction by highly dispersed Cu sites on TiO_2. *J. Photonics Energy* **2016**, *7*, 012004.

30 Chen, B.-R.; Nguyen, V.-H.; Wu, J. C. S.; Martin, R.; Kočí, K. Production of renewable fuels by the photohydrogenation of CO_2: effect of the Cu species loaded onto TiO_2 photocatalysts. *Phys. Chem. Chem. Phys*. **2016**, *18*, 4942–4951.

31 Liu, M.; Qiu, X.; Miyauchi, M.; Hashimoto, K. Cu(II) oxide amorphous nanoclusters grafted Ti^{3+} self-doped TiO_2: an efficient visible light photocatalyst. *Chem. Mater*. **2011**, *23*, 5282–5286.

32 Farsinezhad, S.; Sharma, H.; Shankar, K. Interfacial band alignment for photocatalytic charge separation in TiO_2 nanotube arrays coated with CuPt nanoparticles. *Phys. Chem. Chem. Phys*. **2015**, *17*, 29723–29733.

33 Kang, Q.; Wang, T.; Li, P.; Liu, L.; Chang, K.; Li, M.; Ye, J. Photocatalytic reduction of carbon dioxide by hydrous hydrazine over Au-Cu alloy nanoparticles supported on $SrTiO_3/TiO_2$ coaxial nanotube arrays. *Angew. Chemie - Int. Ed*. **2015**, *54*, 841–845.

34 Kavitha, R.; Kumar, S. G. Review on bimetallic-deposited TiO_2: preparation methods, charge carrier transfer pathways and photocatalytic applications. *Chem. Pap*. **2020**, *74*, 717–756.

35 Gao, W.; Jin, R.; Chen, J.; Guan, X.; Zeng, H.; Zhang, F.; Guan, N. Titania-supported bimetallic catalysts for photocatalytic reduction of nitrate. *Catal. Today* **2004**, *90*, 331–336.

36 Guzmán, H.; Russo, N.; Hernández, S. CO_2 valorisation towards alcohols by Cu-based electrocatalysts: challenges and perspectives. *Green Chem*. **2021**, *23*, 1896–1920.

37 Zhang, L.; Merino-Garcia, I.; Albo, J.; Sánchez-Sánchez, C. M. Electrochemical CO_2 reduction reaction on cost-effective oxide-derived copper and transition metal–nitrogen–carbon catalysts. *Curr. Opin. Electrochem*. **2020**, *23*, 65–73.

38 Albero, J.; Peng, Y.; García, H. Photocatalytic CO_2 reduction to C^{2+} products. *ACS Catal*. **2020**, *10*, 5734–5749.

39 Boltersdorf, J.; Forcherio, G. T.; McClure, J. P.; Baker, D. R.; Leff, A. C.; Lundgren, C. A. Visible light-promoted plasmon resonance to induce “hot” hole transfer and photothermal conversion for catalytic oxidation. *J. Phys. Chem. C* **2018**, *122*, 28934–28948.

40 Li, D.; Hao, C.; Liu, H.; Zhang, R.; Li, Y.; Guo, J.; Vilancuo, C. C.; Guo, J. Photocatalytic CO_2 conversion to ethanol: a concise review. *Catalysts* **2022**, *12*, 1549.

41 Oskam, G.; Nellore, A.; Penn, R. L.; Searson, P. C. The growth kinetics of TiO_2 nanoparticles from titanium(IV) alkoxide at high water/titanium ratio. *J. Phys. Chem. B* **2003**, *107*, 1734–1738.

42 *NIST X-ray Photoelectron Spectroscopy Database, NIST Standard Reference Database Number 20*, National Institute of Standards and Technology, Gaithersburg MD, 20899, 2000. (Accessed 05-06-2023).

43 Hu, Y.; Tsai, H. -L.; Huang, C. -S. Effect of brookite phase on the anatase–rutile transition in titania nanoparticles. *J. Eur. Ceram. Soc*. **2003**, *23*, 691–696.

44 Zhao, X. P.; Yin, J. B. Preparation and electrorheological characteristics of rare-earth-doped TiO_2 suspensions. *Chem. Mater*. **2002**, *14*, 2258–2263.

45 Ali, K.A.; Abdullah, A. Z.; Mohamed, A. R. Visible light responsive TiO_2 nanoparticles modified using Ce and La for photocatalytic reduction of CO_2: effect of Ce dopant content. *Appl. Catal. A Gen*. **2017**, *537*, 111–120.

46 Amritha, A.; Sundararajan, M.; Rejith, R. G.; Mohammed-Aslamm, M. A. La-Ce doped TiO_2 nanocrystals: a review on synthesis, characterization and photocatalytic activity. *SN Appl. Sci*. **2019**, *1*, 1441

47 Khan, M. A. M.; Nain, P.; Ahmed, J.; Ahamed, M.; Kumar, S. Characterization and photocatalytic performance of hydrothermally synthesized Cu-doped TiO_2 NPs. *Opt. Mat*. **2022**, *133*, 112983.

48 López, R.; Gómez, R.; Llanos, M. E. Photophysical and photocatalytic properties of nanosized copper-doped titania sol–gel catalysts. *Catal. Tod*. **2009**, *148*, 103–108.

49 Sun, X.; Liu, H.; Dong, J.; Wei, J.; Zhang, Y. Preparation and characterization of Ce/N-Codoped TiO_2 particles for production of H_2 by photocatalytic splitting water under visible light. *Catal Lett*. **2010**, *135*, 219–225.

50 Zang, H.; Banfield, J. Understanding polymorphic phase transformation behavior during growth of nanocrystalline aggregates: insights from TiO_2. *J. Phys. Chem. B* **2000**, *104*, 3481–3487.

51 Ohsaka, T.; Izumi, F.; Fujiki, Y. Raman spectrum of anatase, TiO_2. *J. Raman Spectrosc*. **1978**, *7*, 321–324.

52 Tompsett, G. A.; Bowmaker, G. A.; Cooney, R. P.; Metson, J. B.; Rodgers, K.A.; Seakins, J.M. The Raman spectrum of brookite, TiO_2 (Pbca, Z=8). *J. Raman Spectrosc*. **1995**, *26*, 57–62.

53 Porto, S.P.S.; Fleury, P.A.; Damen, T.C. Raman spectra of TiO_2, MgF_2, ZnF_2, FeF_2, and MnF_2. *Phys. Rev*. **1967**, *154*, 522–526.

54 Pradeep, T. Determination of the band gap of semiconductor nanoparticles. In: *Textbook of nanoscience and nanotechnology*. McGraw Hill Education, 2012.

55 Liu, C.; Tang, X.; Mo, C.; Qiang, Z. Characterization and activity of visible-light-driven TiO_2 photocatalyst codoped with nitrogen and cerium. *J. Solid State Chem.* **2008**, *181*, 913–919.

56 Chen, S. W.; Lee, J. M.; Lu, K. T.; Pao, C. W.; Lee, J. F.; Chan, T. S.; Chen, J. M. Band-gap narrowing of TiO_2 doped with Ce probed with X-ray absorption spectroscopy. *Appl. Phys. Lett*. **2010**, *97*, 2–5.

57 Worayingyong, A.; Sang-urai, S.; Smith, M.F.; Maensiri, S.; Seraphin, S. Effects of cerium dopant concentration on structural properties and photocatalytic activity of electrospun Ce-doped TiO_2 nanofibers. *Appl. Phys. A* **2014**, *117*, 1191–1201

58 Xie, J.; Jiang, D.; Chen, M.; Li, D.; Zhu, J.; Lü, X.; Yan, C. Preparation and characterization of monodisperse Ce-doped TiO_2 microspheres with visible light photocatalytic activity. *Colloids Surf., A* **2010**, *372*, 107–114.

59 Yan, N.; Zhu, Z.; Zhang, J.; Zhao, Z.; Liu, Q. Preparation and properties of Ce-doped TiO_2 photocatalyst. *Mater. Res. Bull*. **2012**, *47*, 1869–1873.

60 Praliaud, H.; Mikhailenko, S.; Chakar, Z.; Primet, M. Surface and bulk properties of Cu-ZSM-5 and Cu/Al_2O_3 solids during redox treatments. Correlation with the selective reduction of nitric oxide by hydrocarbons. *Appl. Catal. B Environ*. **1998**, *16*, 359–374.

61 Albo, J.; Qadir, M. I.; Samperi, M.; Fernandes, J. A.; de Pedro, I.; Dupont, J. Use of an optofluidic microreactor and Cu nanoparticles synthesized in ionic liquid and embedded in TiO_2 for an efficient photoreduction of CO_2 to methanol. *Chem. Eng. J*. **2021**, *404*, 126643.

62 Albo, J.; García, G. Enhanced visible-light photoreduction of CO_2 to methanol over Mo_2C/TiO_2 surfaces in an optofluidic microreactor. *Chem. Eng*. **2021**, *6*, 304–312.

63 Izadpanah Ostad, M.; Niknam Shahrak, M.; Galli, F. Photocatalytic carbon dioxide reduction to methanol catalyzed by ZnO, Pt, Au, and Cu nanoparticles decorated zeolitic imidazolate framework-8. *J. CO_2 Util*. **2021**, *43*, 101373.

64 Xi, H.; Xu, Y.; Zou, W.; Ji, J.; Cai, Y.; Wan, H.; Dong, L. Enhanced methanol selectivity of CuO/TiO_2 photocatalytic CO_2 reduction: synergistic mechanism of surface hydroxyl and low-valence copper species. *J. CO_2 Util.* **2022**, *55*, 101825.

65 Luo, D.; Bi, Y.; Kan, W.; Zhang, N.; Hong, S. Copper and cerium co-doped titanium dioxide on catalytic photo reduction of carbon dioxide with water: experimental and theoretical studies. *J. Mol. Struct*. **2011**, **994**, 325–331.

66 Das, R.; Das, K.; Ray, B.; Vinod, C. P.; Peter, S. C. Green transformation of CO_2 to ethanol using water and sunlight by the combined effect of naturally abundant red phosphorus and Bi_2MoO_6. *Energy Environ. Sci*. **2022**, *15*, 1967–1976.

67 Tian, Z. -Y.; Kong, L. -H.; Wang, Y.; Wang, H.; Wang, Y.; Yao, S.; Lu, T. -B.; Zhang, Z. -M. Construction of low-cost Z-scheme heterostructure Cu_2O/PCN for highly selective CO_2 photoreduction to methanol with water oxidation. *Small* **2021**, *17*, 2103558.

68 Wang, W. -N.; Park, J.; Biswas, P. Rapid Synthesis of Nanostructured $Cu–TiO_2–SiO_2$ composites for CO_2 photoreduction by evaporation driven self-assembly. *Catal. Sci. Technol.* **2011**, *1*, 593.

69 Liu, D.; Fernández, Y.; Ola, O.; Mackintosh, S.; Maroto-Valer, M. M.; Parlett, C. M. A.; Lee, A. F.; Wu, J. C. S. On the impact of Cu dispersion on CO_2 photoreduction over Cu/TiO_2. *Catal. Commun*. **2012**, *25*, 78–82.

70 Xiong, Z.; Xu, Z.; Li, Y.; Dong, L.; Wang, J.; Zhao, J.; Chen, X.; Zhao, Y.; Zhao, H.; Zhang, J. Incorporating highly dispersed and stable Cu^+ into TiO_2 lattice for enhanced photocatalytic CO_2 reduction with water. *Appl. Surf. Sci*. **2020**, *507*, 145095.

71 Rodríguez, V.; Camarillo, R.; Martínez, F.; Jiménez, C.; Rincón, J. High-pressure synthesis of rGO/TiO_2 and rGO/TiO_2/Cu catalysts for efficient CO_2 reduction under solar light. *J. Supercrit. Fluids* **2021**, *174*, 105265.

9

Conclusions

This chapter summarizes the most relevant conclusions reached throughout this Thesis. An in-depth description of them can be found at the end of each chapter.

1. Regarding the development of $Y_2O_3:Pr^{3+}$ NPs for optical applications, the election of the synthesis method has proven to play a crucial role in both the final structural and luminescent properties of the obtained material. Specifically, all the tested procedures have provided NPs with pure cubic crystalline phase, but differing in size and morphology, these features being highly dependent on the fabrication strategy. $^1D_2$ emission from the two available crystallographic sites for Pr^{3+} in the Y_2O_3 host matrix has been detected in all samples, while no emission from the ^3P_J manifold was observed, as previously described for sesquioxides. The emission lifetime has been employed as a comparative parameter to enhance the optical performance of $Y_2O_3:Pr^{3+}$ NPs. It has been tuned and optimized, displaying an improvement of *ca*. 25% for the NPs prepared by solvothermal method regarding the longest decay lifetime reported in the literature.

2. PLD has demonstrated its suitability to fabricate optically active composites consisting of embedded $Y_2O_3:Pr^{3+}$ NPs. Thin films with different thicknesses have been prepared by modifying the number of deposition cycles and their respective positions during such, the latter confirming the high directionality of the employed technique. The structural and optical properties of the NPs have been optimally preserved after the encapsulation between pure cubic Y_2O_3 thin films as confirmed by different techniques, namely XRD, luminescence and time-resolved spectroscopy. Thus, the developed NPs-based composites hold a great potential for applications in the field of optics, such as waveguiding.

3. Concerning the catalytic applications of TiO_2 NPs, a synergistic effect between anatase and rutile crystalline phases has been confirmed to increase the photocatalytic activity. Likewise, TM-doping has proven to have a positive effect by inducing a red shift of the absorption edge of the catalyst, thus increasing the photoactivity of the material. Specifically, the introduction of TM dopants such as Mn or Co has promoted light absorption of the NPs in the Vis region. Additionally, the preparation of NPs-based enamel coatings has demonstrated to be a promising approach for diverse potential industrial applications. These prepared photoactive surfaces have shown good photocatalytic activity for MB dye degradation. Specifically, the Co-doped NPs-based enamel coating have exhibited the most efficient photocatalytic response, yielding up to 35% MB degradation after 8 h (55% after 24h), in contrast with 16% and 9% (54% and 35% after 24 h) shown by non-doped and Mn-doped surfaces, respectively. These results have been attributed to the reduced NP size in the Co-doped surfaces and the effect of the dopant ion.

4. The introduction of Ce as dopant within the lattice of TiO_2 NPs has demonstrated to be an effective strategy to carry out the photocatalytic reduction of CO_2 to alcohols. Ce concentration has proven to play an important role in both alcohol production rate and product selectivity. 0.75% and 1.27% mol Ce concentrations have yielded remarkable alcohol production rates of both ethanol and methanol. Interestingly, the lowest studied concentration (0.75% mol Ce) has provided the highest ethanol production rate (116 $\mu mol \cdot g^{-1} \cdot h^{-1}$) and the maximum selectivity towards such a product under Vis irradiation (80%), this being of great interest for industrial applications. However, a further increase in Ce concentration has turned out to be detrimental for the photoactivity of the NPs, leading to a very low ethanol production. Simultaneous introduction of Cu and Ce as dopants has proven to have little effect on the photoactivity of the system. Indeed, it has not been possible to introduce the desired dopant concentrations, which might have hindered the expected improvement of production rates. The stability of the immobilized catalysts has also been demonstrated, since the NPs have exhibited a stable photoactivity during continuous operation and an entire structural integrity, as corroborated by different characterization techniques.

Table A.1. Symmetry assignment of the Raman peaks observed for Y_2O_3: Pr^{3+} (0.1% mol) NPs synthesized by the different methods, together with the peaks position (ω) and width (FWHM), both in cm^{-1}. In bold the most intense Raman peak.

Mode	**Combustion**		**Molten salt**		**Sol-gel Pechini**		**Homogeneous precipitation**		**Solvothermal**	
	ω	**FWHM**	**ω**	**FWHM**	**ω**	**FWHM**	**ω**	**FWHM**	**ω**	**FWHM**
T_g	105.3	3.8	–	–	–	–	–	–	105.2	3.6
T_g	114.9	12.4	–	–	115.7	5.5	–	–	114.6	3.5
T_g	128.3	3.4	128.9	1.7	128.4	2.9	128.3	3.4	128.6	2.8
T_g	137.3	4.0	137.9	53.7	–	–	–	–	137.8	3.0
A_g	160.4	3.9	160.4	4.2	160.4	4.2	159.9	4.3	160.7	3.3
E_g	192.6	4.4	193.5	2.3	193.0	3.0	192.1	6.0	192.4	4.6
T_g	234.1	1.7	–	–	–	–	–	–	234.3	1.5
T_g	–	–	288.4	29.8	287.7	19	285.3	16.5	290.5	5.1
T_g	316.2	5.9	315.5	2.8	316.2	5.1	315.8	4.4	316.5	3.8
T_g+E_g	326.0	8.2	329.4	5.4	328.7	8.8	328.4	10.3	329.4	6.3
T_g	**376.4**	**6.8**	**376.3**	**6.1**	**376.4**	**5.9**	**375.9**	**6.5**	**376.5**	**5.3**
A_g	430.1	6.8	429.6	5.8	429.9	7.9	429.8	7.6	431.4	9.1
T_g	468.0	9.5	468.1	8.2	467.5	11.2	467.3	10.6	468.2	9.0
T_g	591.9	11.6	592.1	13.7	591.5	14.9	590.2*	18.3	591.6	12.3

Appendix B

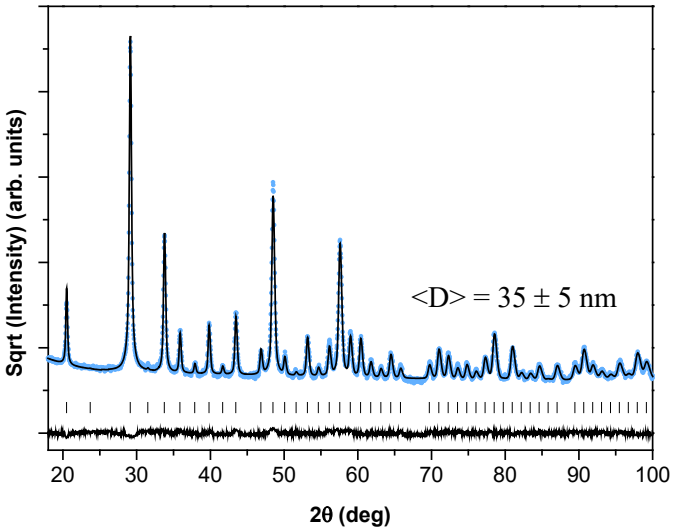

Figure B.1. Rietveld refinement of XRD diffraction patterns of $Y_2O_3:Pr^{3+}$ (0.1% mol) NPs prepared through **combustion method** after annealing at 900 ºC for 4 h. Vertical lines correspond to c-Y_2O_3 Bragg reflections. The average NP diameter <D> is also depicted.

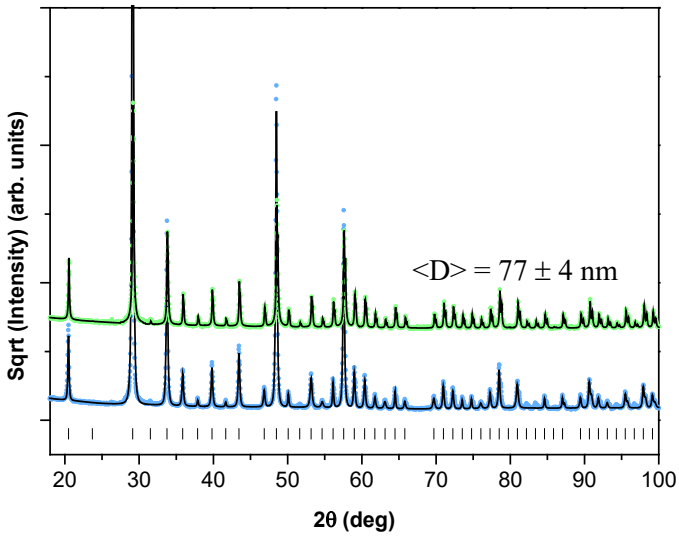

Figure B.2. Rietveld refinement of XRD diffraction patterns of $Y_2O_3:Pr^{3+}$ (0.1% mol) NPs prepared through **molten salt** method, after 5 (blue) and 10 (green) washing cycles. Vertical lines correspond to c-Y_2O_3 Bragg reflections. The average NP diameter <D> is also depicted.

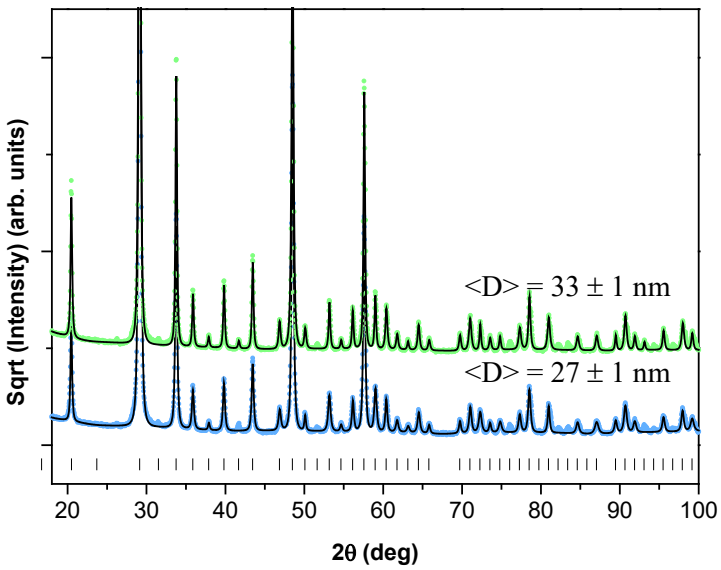

Figure B.3. Rietveld refinement of XRD diffraction patterns of Y_2O_3:Pr^{3+} (0.1% mol) NPs prepared through **sol-gel Pechini method** using citric acid as chelating agent, and treating the NPs at 800 ºC for 16 h (blue) and 24 h (green). The average NP diameter <D> is also depicted.

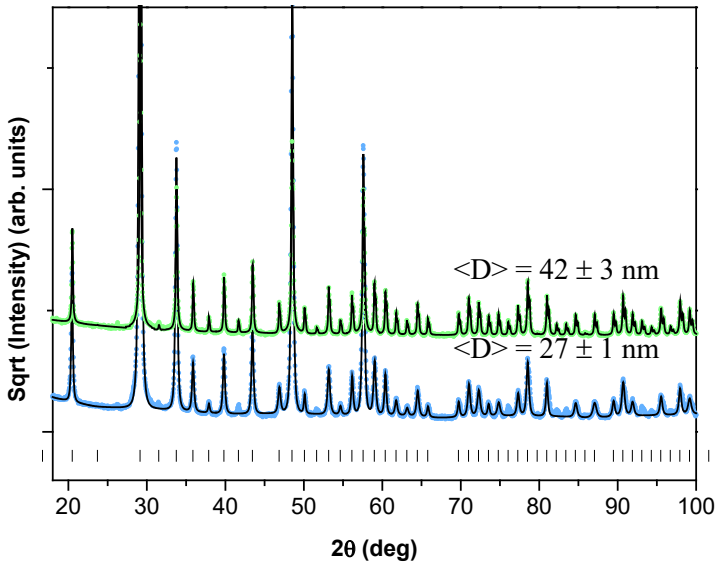

Figure B.4. Rietveld refinement of XRD diffraction patterns of Y_2O_3:Pr^{3+} (0.1% mol) NPs prepared through **sol-gel Pechini method** using citric acid as chelating agent, and treating the NPs at 800 ºC (blue) and 900 ºC (green) for 16 h. The average NP diameter <D> is also depicted.

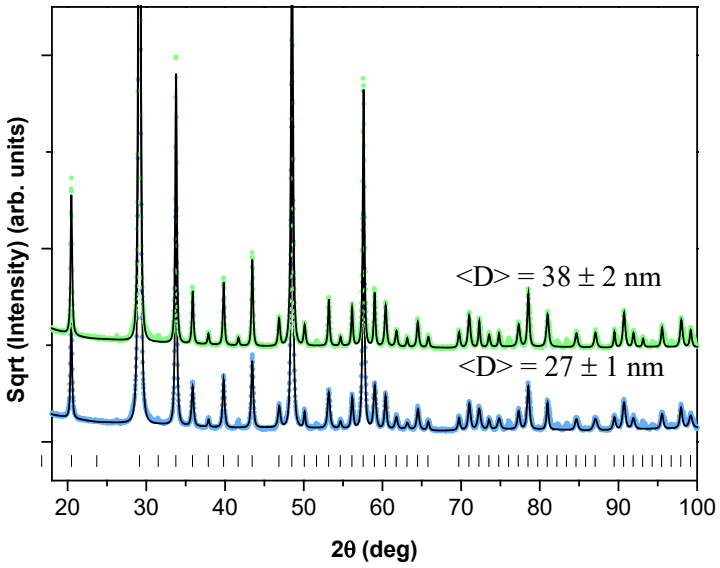

Figure B.5. Rietveld refinement of XRD diffraction patterns of Y_2O_3:Pr^{3+} (0.1% mol) NPs prepared through **sol-gel Pechini method** using citric acid (blue) and EDTA (green) as chelating agents, and treating the NPs at 900 ºC for 16 h. The average NP diameter <D> is also depicted.

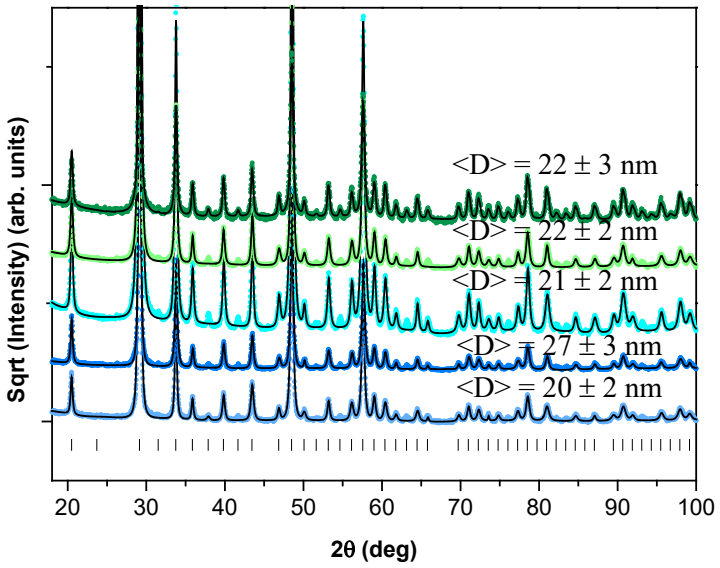

Figure B.6. Rietveld refinement of XRD diffraction patterns of Y_2O_3:Pr^{3+} (0.1% mol) NPs prepared through **homogeneous precipitation method** using a urea concentration of 1.35 (light blue), 0.46 (dark blue), 2.31 (cyan), 3.93 (light green), and 4.16 mol/L (dark green). The average NP diameter <D> is also depicted.

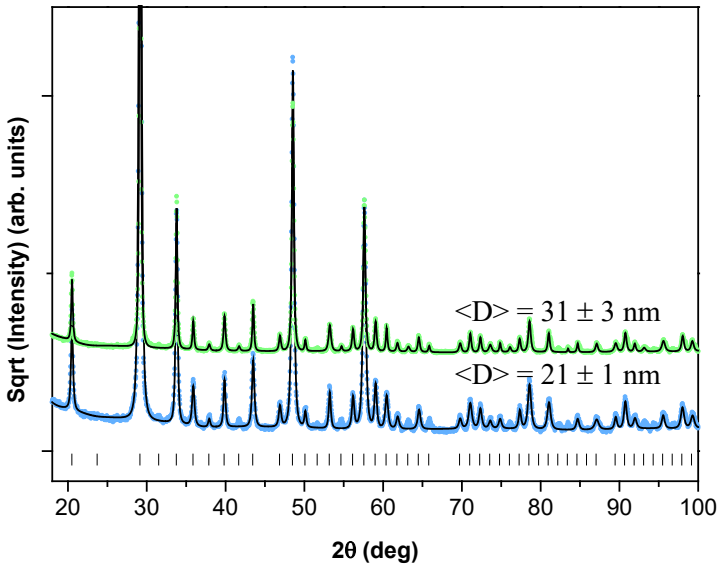

Figure B.7. Rietveld refinement of XRD diffraction patterns of Y_2O_3:Pr^{3+} (0.1% mol) NPs prepared through **solvothermal method** at 180 ºC, using EG, RE precursors (5.04 mmol), and treating the NPs at 800 ºC (blue) and 900 ºC (green) for 4 h. The average NP diameter <D> is also depicted.

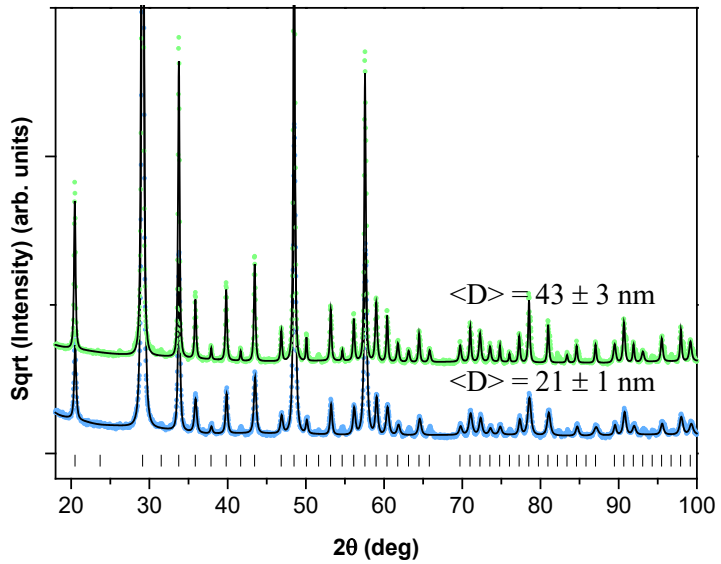

Figure B.8. Rietveld refinement of XRD diffraction patterns of Y_2O_3:Pr^{3+} (0.1% mol) NPs prepared through **solvothermal method** at 180 ºC, using EG, RE precursors (5.04 mmol, blue; 10.07 mmol, green), and treating the NPs at 800 ºC for 4 h. The average NP diameter <D> is also depicted.

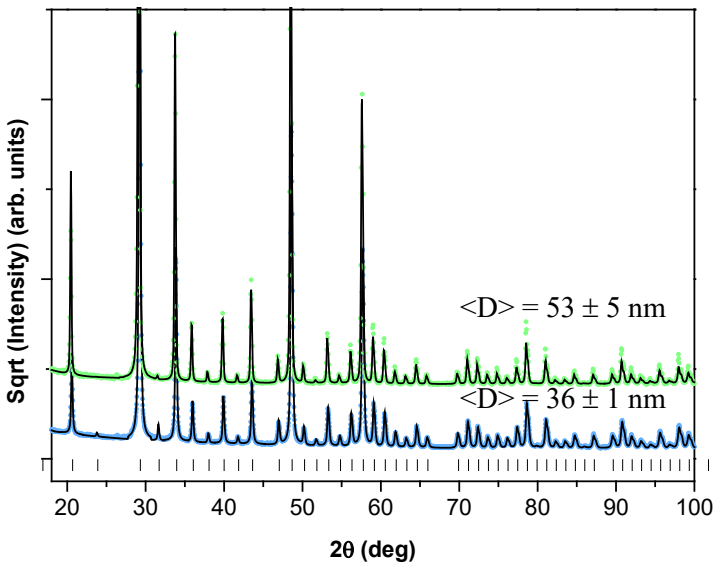

Figure B.9. Rietveld refinement of XRD diffraction patterns of $Y_2O_3:Pr^{3+}$ (0.1% mol) NPs prepared through **solvothermal method** at 220 ºC, using EG, RE precursors (5.04 mmol), and treating the NPs at 900 ºC (blue) and 1000 ºC (green) for 4 h. The average NP diameter <D> is also depicted.

Abbreviation list

AQY	apparent quantum yield
C1	one-carbon compounds
C2+	multi-carbon compounds
CB	conduction band
CCU	carbon capture and utilization
COF	covalent organic framework
e^-_{CB}	photo-excited electron
EDTA	ethylenediaminetetraacetic acid
E_g	band gap energy
EG	ethylene glycol
eq	equivalent
EtOH	ethanol
FS	fused silica
FWHM	full width at half the maximum height
h^+_{VB}	photo-generated hole
IR	infrared
MB	methylene blue
min	minute
MO	magnesium oxide
MP-AES	microwave plasma-atomic emission spectroscopy
NIR	near infrared
NP	nanoparticle

NTP	non-TiO_2 phase
o.n.	overnight
PLD	pulsed laser deposition
PMT	photomultiplier
PTFE	polytetrafluoroethylene
RE	rare earth
RT	room temperature
SC	sapphire C
SR	sapphire R
T_{CAL}	calcination temperature
t_{CAL}	calcination time
TEM	transmission electron microscopy
TM	transition metal
T_R	reaction temperature
t_R	reaction time
TTIP	titanium isopropoxide
UV	ultraviolet
VB	valence band
Vis	visible
WLED	white light emitting diode
XPS	X-ray photoelectron spectroscopy
XRD	X-ray diffraction

List of publications

1. **Diego-Rucabado, A.**; Candela, M.T.; Aguado, F.; González, J.; Rodríguez, F.; Valiente, R.; Martín-Rodríguez, R.; Cano, I. A comparative study on luminescence properties of Y_2O_3:Pr^{3+} nanocrystals prepared by different synthesis methods. *Nanomaterials* 2020, 10, 1574.

2. **Diego-Rucabado, A.**; Candela, M.T.; Aguado, F.; González, J.; Gómez, E.; Valiente, R.; Cano, I.; Martín-Rodríguez, R. Photocatalytic activity of undoped and Mn- and Co-doped TiO_2 nanocrystals incorporated in enamel coatings on stainless steel. *React. Chem. Eng*. 2021, 6, 2376–2390.

3. Jäger, M.; Müller, R.; Kobelke, J.; Wondraczek, K.; Valiente, R.; **Diego-Rucabado, A.**; Cano, I.; Aguado, F.; Gluch, J.; Kinski, I.; Dorosz, D.; Kochanowicz, M. Nanocrystal-doped fibres using glass powder doping – towards new laser transitions in fibre lasers. *Conference on Lasers and Electro-Optics Europe & European Quantum Electronics Conference (CLEO/Europe-EQEC)* 2021.

4. **Diego-Rucabado, A.**; Segura, A.; Aguado, F.; Pollnau, M.; Valiente, R.; Martín-Rodríguez, R.; Cano, I. Pr^{3+}-doped Y_2O_3 nanocrystals embedded in Y_2O_3 thin films as a sandwich-like structure prepared by pulsed laser deposition. *J. Lumin*. 2022, 252, 119378.

5. Dorosz, D.; Kochanowicz, M.; Lesniak, M.; Müller, R.; Lorenz, M.; Kobelke, J.; Wondraczek, K.; Valiente, R.; **Diego-Rucabado, A.**; Cano, I.; Aguado, F.; Gluch, J.; Kinski, I.; Jäger, M. Glass powder doping of nanocrystal-doped fibres – Challenges and results. *Proc. SPIE 12142, Fiber Lasers and Glass Photonics: Materials through Applications III* 2022, 12142.

6. Candela, M.T.; Aguado, F.; **Diego-Rucabado, A.;** González, J.A.; Valiente, R. Non-resonant energy transfer from Eu^{3+} to Yb^{3+} in C-type and B-type $(Eu_{1-x}Yb_x)_2O_3$ nanocrystals. *J. Alloys Compd*. 2022, 921, 166043.

7. **Diego-Rucabado, A.**; Merino-García, I.; Espeso, J.I.; González, J.; Arce, B.; Valiente, R.; Beobide, G.; Cano, I.; Martín-Rodríguez, R.; de Pedro, I.; Albo, J. Visible-light-active Ce-doped and Cu−Ce-codoped TiO_2 nanocrystals and optofluidics for clean alcohol production from CO_2. *ACS Sustainable Chem. Eng*. 2023, 11, 13260–13273.

Grants and projects

The author of this Thesis thanks financial support from the European Community through the Future and Emerging Technologies (FET) project NCLas (Proposal: 829161).

Grants received to participate in nanoscience and spectroscopy meetings and conferences are as well acknowledged:

- International Conference on Nanomaterials Applied to Life Sciences NALS 2022 (Santander, Spain, 2022).
- International Workshop on Advanced Spectroscopy and Optical Materials, University of Gdansk (Gdansk, Poland, 2022).
- XVIth International Conference on Molecular Spectroscopy (ICMS 2022). Photoluminescence in Rare Earths: Photonic Materials and Devices (PRE'22-Poland) Workshop (Szczawnica, Poland, 2022).
- IV Minisimposio Nanomedicina 2023, Grupo de Nanomedicina de Idival (Santander, Spain, 2023).
- Glass and Light Engineering Seminar as part of the International Day of Light, Bialystok University of Technology (Online, Bialystok, Poland, 2023).
- International Summer School on Rare-Earth-Doped Optical Materials: Synthesis, Characterization, and Applications to Lasers, AGH University of Science and Technology (Krakow, Poland, 2023).

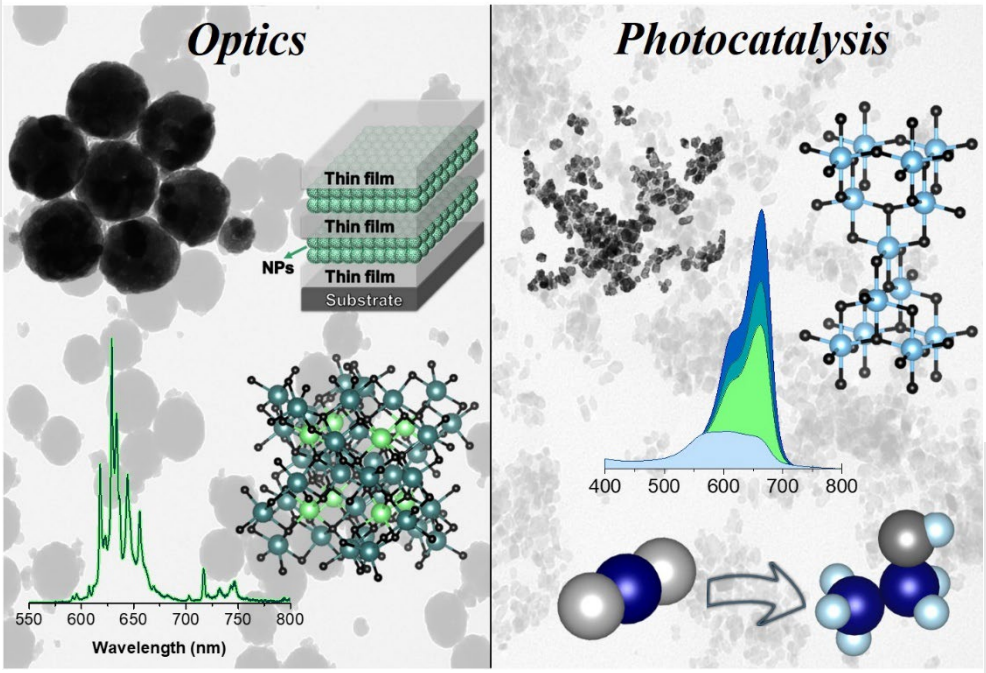

Esta Tesis tiene por objeto el estudio de la potencial aplicación de nanopartículas basadas en óxidos metálicos en los campos de la óptica y la fotocatálisis, empleando iones de tierras raras y de metales de transición como dopantes. En la primera parte de la Tesis, dedicada a materiales ópticos, se ha realizado un estudio exhaustivo del efecto de los diferentes métodos de síntesis sobre las características ópticas de las nanopartículas de óxido de itrio dopadas con praseodimio obtenidas y se han fabricado composites ópticamente activos a partir de estas mediante la técnica de deposición por láser pulsado para su posible uso como guía de ondas. En la segunda parte de la Tesis, enfocada en materiales fotocatalíticos, se han desarrollado recubrimientos de esmalte sobre láminas de acero vitrificado para su aplicación en la degradación de contaminantes ambientales Por otro lado, se ha evaluado la actividad catalítica de nanopartículas de óxido de titanio dopadas con elementos de tierras raras y co-dopadas con elementos de tierras raras y metales de transición en la fotoreducción de dióxido de carbono a alcoholes.

This Thesis aims to study the potential applications of metal oxide nanoparticles in the fields of optics and photocatalysis, using rare earth and transition metal ions were as dopant species. The first part of this Thesis, devoted to optical materials, is focused on the effect of the synthesis procedures on the optical performance of the obtained Pr-doped yttrium oxide nanoparticles and the fabrication of nanoparticle-based optical composites for waveguide applications by means of pulsed laser deposition technique. The second part of this Thesis, focused on photocatalytic materials, covers the preparation of transition-metal-doped titanium oxide nanoparticle-based enamel coatings on stainless-steel sheets for pollutant degradation purposes and the catalytic performance of rare-earth-doped and transition metal/rare earth co-doped titanium oxide nanoparticles has been evaluated for the photoreduction of carbon dioxide to alcohols.

UC UNIVERSIDAD DE CANTABRIA
Escuela de Doctorado